

UNCLASSIFIED

AD NUMBER

AD415681

LIMITATION CHANGES

TO:

Approved for public release; distribution is unlimited.

FROM:

Distribution authorized to U.S. Gov't. agencies and their contractors;
Administrative/Operational Use; 30 JUN 1963.
Other requests shall be referred to Army Electronics Research and Development Laboratory, Fort Monmouth, NJ.

AUTHORITY

ECOM ltr dtd 1 Dec 1965

THIS PAGE IS UNCLASSIFIED

UNCLASSIFIED

AD **415681**

DEFENSE DOCUMENTATION CENTER

FOR

SCIENTIFIC AND TECHNICAL INFORMATION

CAMERON STATION, ALEXANDRIA, VIRGINIA



UNCLASSIFIED

NOTICE: When government or other drawings, specifications or other data are used for any purpose other than in connection with a definitely related government procurement operation, the U. S. Government thereby incurs no responsibility, nor any obligation whatsoever; and the fact that the Government may have formulated, furnished, or in any way supplied the said drawings, specifications, or other data is not to be regarded by implication or otherwise as in any manner licensing the holder or any other person or corporation, or conveying any rights or permission to manufacture, use or sell any patented invention that may in any way be related thereto.

DISCLAIMER NOTICE

THIS DOCUMENT IS THE BEST
QUALITY AVAILABLE.

COPY FURNISHED CONTAINED
A SIGNIFICANT NUMBER OF
PAGES WHICH DO NOT
REPRODUCE LEGIBLY.

415681

CATALOGED BY DDC 415681

AS AD No. _____

FUEL CELL

RESEARCH & DEVELOPMENT

ION EXCHANGE MEMBRANE FUEL CELL
REPORT NUMBER 2

CONTRACT NUMBER DA-36-039-AMC-00095(E)
TASK NO. OST 7776.11.001.38.00
ARPA ORDER NUMBER 80

SECOND SEMI-ANNUAL TECHNICAL REPORT
JANUARY 1, 1963 - JUNE 30, 1963
DATE OF CONTRACT: 1 OCTOBER 1962
AMOUNT: \$198,880.00

U.S. ARMY ELECTRONICS RESEARCH AND DEVELOPMENT LABORATORY
FORT MONMOUTH, NEW JERSEY

DIRECT ENERGY CONVERSION OPERATION
GENERAL  ELECTRIC
LYNN, MASS.

DDC
RECEIVED
SEP 7 1963
RESOLVED
JISIA D

ION EXCHANGE MEMBRANE FUEL CELL

REPORT NO. 2

CONTRACT NUMBER DA-36-039-AMC-00095(E)

TECHNICAL GUIDELINES EPP NO. 58238 OF JULY 17, 1962

TASK NO. OST 7776. 11.001. 38.00

ARPA ORDER NO. 80

SECOND SEMI-ANNUAL TECHNICAL REPORT

JANUARY 1, 1963 - JUNE 30, 1963

OBJECT: RESEARCH ON ION-EXCHANGE MEMBRANE FUEL CELLS

REPORT PREPARED BY:

Henri J. R. Maget
Henri J. R. Maget

REPORT APPROVED BY:

E. A. Oster
E. A. Oster

The work performed under this contract was made possible by the support of the Advanced Research Project Agency under Order Number 80, through the United States Army Electronics Research and Development Laboratory.

TABLE OF CONTENTS

| | | <u>PAGE</u> |
|------|--|-------------|
| 1.0 | PURPOSE | 1 |
| 2.0 | ABSTRACT | 4 |
| 3.0 | PUBLICATIONS, LECTURES, REPORTS AND CONFERENCES | 7 |
| 4.0 | FACTUAL DATA | 8 |
| 4.1 | TASK I - INTERFACE STRUCTURE AND INTERFACIAL PROPERTIES OF IEM/ELECTRODE SYSTEMS | 8 |
| 4.2 | TASK II - WATER TRANSPORT IN ION EXCHANGE MEMBRANES | 31 |
| 4.3 | TASK III - KINETIC STUDY OF THE ELECTROCHEMICAL OXYGEN (AIR) REDUCTION | 39 |
| 4.4 | TASK IV - HEAT AND MASS TRANSFER INVESTIGATIONS OF THE AIR- BREATHING I. E. M. FUEL CELL | 81 |
| 4.4A | (ADDITION TO TASK IV) - AN OPTIMIZING CONTROL DEVICE FOR USE IN LABORATORY EVALUATION OF HYDROGEN-AIR FUEL CELL OPERATION | 107 |
| 4.5 | TASK V - DESIGN PARAMETERS AFFECTING AIR-OPERATED I. E. M. FUEL CELLS | 114 |
| 4.6 | APPENDIXES | 130 |
| 5.0 | CONCLUSIONS | 198 |
| 6.0 | NEXT INTERVAL | 200 |
| 7.0 | KEY PERSONNEL | 201 |
| 8.0 | LITERATURE REFERENCES | 205 |
| 9.0 | CONTRACT DISTRIBUTION LIST | 209 |
| 10.0 | GENERAL ELECTRIC DISTRIBUTION LIST | 213 |

1.0

PURPOSE

The work undertaken under this contract and presented in this Report is related to research investigations to contribute to the development of air-breathing fuel cells based on ion exchange membranes as "solid" electrolytes.

Technical guidelines EPP No. 58238 of the contract were defined as follows:

1. These Technical Guidelines cover the requirements for the investigation of hydrogen-oxygen ion exchange membrane fuel cells. These guidelines further cover limited investigations of fuels other than hydrogen which show practical and economical feasibility with respect to military applications.
2. The objective of these investigations is to improve the power density and lifetime characteristics of ion exchange membrane fuel cell power supplies for ground power applications. Cells utilizing fuels other than hydrogen shall also be investigated. Emphasis shall be placed on the improvement of ion exchange membrane fuel cell technology and a systematic understanding of the phenomena observed. This effort should lead to an increase in the state of the art which will allow the design of improved fuel cell power sources to meet groundpower requirements with a known reliability.
3. The Contractor shall conduct the necessary investigations leading to the establishment of an analytical model expressing factors determining fuel cell performances. This model shall be used to further improve the overall operating performance of the ion exchange membrane fuel cell. The Contractor shall perform the following experimental and theoretical studies:
 - a. Determine the factors causing ion exchange membrane oxygen electrode performance to decrease when operating on convected ambient air as the source of oxygen. Work will be directed toward obtaining optimum air electrode performance.
 - b. Conduct fuel cell performance and life studies, using new improved cation exchange membrane materials. Emphasis shall be placed on structures which improve ionic conductance, physical properties, and stability.

1.0

PURPOSE (Cont'd)

- c. Complete a study of factors determining the membrane's water balance.
- d. Investigate factors influencing electrode-electrolyte coupling to produce low electrode polarization. This work shall be directed toward optimization of ion exchange membrane electrodes.
- e. Investigate fuels other than hydrogen in ion exchange membrane fuel cells. These fuels shall be restricted to those found by other investigators to work such as dissolved liquid fuels in acid electrolytes. Emphasis shall be given to determining the Faradaic efficiency, main reactions, and causes of anode polarizations. Studies of the methanol ion exchange membrane cell shall be included in these investigations.

The initial experimental program started in October 1962, and approved on November 1, 1962, is considered compatible with the Technical Guidelines.

The following TASK organization was adopted:

TASK I: Interface Structure and Interfacial Properties of IEM/Electrode Systems

- 1. Isotropic Characteristics of an Ion Exchange Membrane.
- 2. Ion Exchange Membrane/Electrode Morphology.
- 3. Interfacial Bonding Forces.

TASK II: Water Transport Across Ion Exchange Membranes

- 1. Water Permeability.
- 2. Electro-osmotic Water Transport.
- 3. Water Gradients in Membranes.

TASK III: Kinetic Study of Electrochemical Oxygen Reduction at Variable Oxygen Partial and Total Pressures

- 1. Electrode Reproducibility.
- 2. Variables Affecting Reaction Rates.
- 3. Transient Rate Measurements.
- 4. Steady-State Rate Measurements.

1.0

PURPOSE (Cont'd)

TASK IV: Heat and Mass Transfer Investigations of the Air-Breathing IEM Cell and Battery

1. Over-all Mass Transfer Processes.
2. Detailed Mechanism.
3. Temperature Distribution and Profile.
4. Property Measurements.
5. Analytical Model.
6. Life Testing.

TASK V: Design Parameters Affecting Air-Operated IEM Fuel Cells

1. Performance Data as Related to Water Transport.
2. Systems Evaluation for Product Water Conservation.
3. Air Electrode for Constant Water Removal.
4. Air Electrode Configuration and Geometry.
5. Cell-Stack Operation.

TASK VI: Ion Exchange Membranes

1. New Ion Exchange Membrane Materials.
2. Materials Properties.

Postponed TASK VII: IEM Methanol Fuel Cell

1. Methanol Transport through IEM.
2. Rate of Methanol Oxidation in Solution.
3. Reduction of Cathodic Electrode-Poisoning.
4. Reaction Rates of Intermediate Products.

This Report presents experimental work regarding TASKS I, II, III, IV and V.

ABSTRACT

During the contract period from January 1, 1963 to June 30, 1963, experimental work has been conducted on membranes and interface membrane/electrolyte properties. Reaction rates for the electrochemical oxygen reduction as well as heat and mass transfer studies have yielded interesting results regarding air-breathing fuel cell electrodes. The reported results suggest a continued effort of the proposed program throughout the remaining contract period.

1. The study of the IEM-electrode interface by optical microscopy, capacity and adhesion measurements has yielded results regarding type, quality and nature of the electrolyte-electrode bond. Surface contact between the two media rather than interfacial penetration has been observed. The presence of a fluorocarbon-type wet-proofing agent has shown to be effective as a water-rejecting medium and generates stronger binding, resulting practically in better resistance to thermal or mechanical degradation by cycling processes, between membrane and electrode.
2. Hydraulic transport rates in IEM, important in the overall water transport processes (heat and mass transfer, thermal convective processes, rates of evaporation in presence and absence of forced gas flow, etc...) have yielded values for permeability ranging from 1.3 to $25 \cdot 10^{-8} \text{ cm}^3\text{-cm/cm}^2\text{-sec. atm.}$ at room temperature. These transport rates are largely dependent on ion exchange capacity, and corrections for tortuosity factors have allowed the derivation of a generalized equation for all IEC's. Transport rates are temperature-dependent and yield reduced activation energies for diffusion of about 3-4000 cal/mole. Diffusion coefficients at room temperature, as determined from the corrected permeabilities, have yielded $D \approx 2 \cdot 10^{-5} \text{ cm}^2/\text{sec.}$
3. Limiting current densities for cathodic oxygen reduction on IEM-Pt black type electrolyte-electrode systems are quasi-linearly dependent on oxygen partial pressure, for the binary system O_2/N_2 , in the absence of convective flow. At room temperature, limiting current densities for air are about 130 Ma/cm^2 . These current densities can be increased by forced gas flow over the electrode.

ABSTRACT (Cont'd)

In air-breathing channels of defined geometry current-potential characteristics are position-dependent and can be formulated quantitatively from relationships describing local limiting current densities. Channel-edge currents can become appreciably larger than center-channel currents (2-3 times for channel-height/length ratios of 1/20 to 1/40). Diffusional resistances (defined as dE/dI) can be predicted from calculated local limiting currents, assuming gas diffusion controlled rates. Dependence on channel length, height and diffusion coefficient is shown. Experimental results are compared to derived equations. Under defined flow rate conditions, local diffusion polarization is appreciably reduced, and already at low flow rates, quasi-uniform current distributions can be observed, resulting practically in cell operation near limiting currents.

4. The success of cell operation at high current densities depends essentially on the study and design of the air electrode. A new design of an air electrode current collector based on the requirement that oxygen and water partial pressures as well as temperatures should be as uniform as possible in order to operate at uniform current densities and this at uniform rates (oxygen diffusion, water removal, etc...) has resulted in single cell operation under steady state conditions of 60 amps/ft² at D.C. voltages about 0.65 volt. This result represents an appreciable improvement over experimental data reported under earlier contracts. In fact, room temperature air-operated fuel cells can now be expected to extend the range of current densities up to 100 amps/ft² (at about 50 watts/ft²).
5. Overall heat and mass transfer investigations, including determination of effective thermal conductivities and effective diffusion coefficients for the porous catalytic layer, as well as measurements of rates of water removal separated in thermal contribution by Joule effect and mass transport contribution by diffusion to bulk gas stream will allow the attempt for quantitative description of the transport processes.

ABSTRACT (Cont'd)

6. The realization of the importance of major parameters, i.e. oxygen partial pressure, water partial pressure, electrode temperature, etc., resulting in surface uniformity regarding reaction rates, heat and mass transfer rates, has yielded various conceptual designs. Consideration has been given to a system recycling large volumes of air and operating at near-saturated conditions. A considerable fraction of the overall heat transferred from the device is removed through the anode. Such a design, in essence, quite different from the concept regarding the modified air electrode current collector, allows for a broad approach to battery design aimed at the multitude of applications based on air-operation.
7. A design for air-operated fuel cells control has yielded a simple control device based on a signal input corresponding to positive or negative rates of variation of cell internal resistance. Air flow modulation allowing for changes of rates of water transport from the electrode surface insure constancy of internal cell resistance and of cell voltage. Such a control device will allow cell operation under largely variable environmental conditions, without appreciable variations of cell power density.

3.0 PUBLICATIONS, LECTURES, REPORTS AND CONFERENCES

3.1 Work planning Conference with Contracting Officer, Fort Monmouth, N. J.

A review meeting of the work accomplished on the contract up to mid-January 1963 was held at the USAELRDL, Fort Monmouth, N. J., on January 25, 1963. The attendance included Messrs. S. Bartoch, H. Hunger and J. Perry of the USAELRDL and Messrs. A. Glenn, T. K. Johnson, H. Maget and E. A. Oster of the Direct Energy Conversion Operation of General Electric.

3.2 Work Planning Conference at the DECO Fuel Cell Laboratory, Lynn, Mass.

During the review meeting of February 21, 1963, held at the DECO Fuel Cell Laboratory, Lynn, Mass., the major investigators associated with the contract program presented experimental results and planned work to Mr. S. Bartoch of the USAELRDL, Fort Monmouth, N. J.

Mr. A. Daniel of the USAELRDL, Fort Monmouth, New Jersey, visited the DECO Fuel Cell Laboratory on April 15, 1963. DECO attendance included Messrs. D. W. Craft, T. K. Johnson, E. A. Oster and H. Maget. During the meeting, the status of the technical program as well as planned experimental work were discussed.

3.3 Power Sources Conference Presentation

At the Fuel Cell Batteries Meeting of the Seventeenth Annual Power Sources Conference held on May 22, 1963, Dr. H. Maget presented a short, prepared note regarding some experimental results obtained under the present contract, as well as the improvements in power capabilities of IEM Air Breathing Fuel Cells.

4.0 FACTUAL DATA

4.1 TASK I

INTERFACE STRUCTURE AND INTERFACIAL PROPERTIES OF IEM/ELECTRODE SYSTEMS

S. J. Krumbein

4.1.1 Introduction

Fabrication of an ion-exchange membrane (IEM) fuel cell results in the formation of a new interfacial zone, comprising the boundary region between the electrode and the IEM electrolyte. The importance of this interface is known from the dependence of the cell's operational characteristics on the methods used for combining the two phases; as well as by the great effort that has been expended in developing optimum manufacturing procedures.

As pointed out in the first semi-annual progress report, the amount of work accomplished in the general realm of solid-solid interfaces has been quite meager when compared to the considerable published literature on other facets of surface chemistry. This observation is particularly pertinent to the complex series of interfacial regions inherent in IEM fuel cell components; and is due, no doubt, to their relative experimental inaccessibility when contrasted with classically well-defined, partly fluid interfacial systems. Primary emphasis was, therefore, placed on the development and evaluation of representative experimental techniques.

4.1.2 Impedance Measurements

4.1.2.1 Introduction: As discussed in a previous report (2) the measured capacitance of an IEM fuel cell component at high frequencies is assumed to be related to the resultant of a complex parallel circuit of different RC ratios, but free from practically all faradaic effects. Although the magnitude of these limiting capacitance values will be far below the "true" ones (8) they should, nevertheless, serve as a comparative measure of the relative double layer capacities for the different IEM/electrode systems. Hence, if it were possible to maintain all other cell parameters constant, (viz. catalyst loading, fabrication conditions, electrode thickness, etc.) much could be learned regarding relative surface areas and roughness of the interfacial region from dependence of the measured impedance values on certain of these properly-chosen experimental variables.

4.0 FACTUAL DATA (Cont'd)

4.1.2.2 Experimental Techniques and Procedures

General: The program in progress during this report period was pursued with an eye towards evaluating the feasibility of obtaining meaningful data on the fuel cell interphases by the A. C. impedance technique. In particular, an effort was made to characterize the experiment by attempting to identify the particular interface or interfaces being measured and resolving them into their individual components.

Two "conducting" interfaces in the IEM fuel cell can be visualized 1) the metal/aqueous solution boundary within the porous electrode and 2) the metal/IEM interfacial region with the measured capacitance being affected by both. Since these two components are essentially in parallel, the relation

$$C = f(I) + g(m) \quad (I-1)$$

can be written, where I refers to the IEM/metal interface and m is the amount of electrode material (e. g. platinum black) per unit geometric area. For electrodes of identical relative composition and porosity, g (m) might be identified with km (i. e. direct proportionality), as a first order of approximation, so that equation (I-2) could be simplified to:

$$C = km + f(I) \quad (I-2)$$

In the course of this program two experimental techniques for eliminating the g (m) -- or km -- term were tried. These were:

1. Varying the amount of liquid electrolyte (dilute pH4 sulfonic acid solution) in the (porous) electrode phase by slowly passing dry nitrogen through the cell's gas compartments. As drying progresses, the effective metal/liquid interfacial area will decrease; and the measured double layer capacitance should drop accordingly. It was postulated that the capacitance would finally decrease to a low, but finite, limiting value corresponding to the IEM interface, since this region was not expected to dry out at the same rate as the bulk electrode.

2. The catalyst loading (i. e. the thickness of the electrode) was varied but all other conditions were held constant. By this means, variations in impedance values with total surface area of the platinum could be observed and, if found to be regular, could be extrapolated to zero catalyst loading (Eqn. I-1) to eliminate the bulk electrode term. The success of the method hinges on the possibility of fabricating reprodu-

FACTUAL DATA (Cont'd)

cible cell configurations whose only variable is the amount of electrode material (of constant composition and porosity) pressed onto the membrane. A correlary condition is the need for temporal reproducibility so that cells made at different times can be compared.

Procedure: - In order to avoid some of the ambiguities of assymetrical geometries (2, 3) when using the bridge technique, all measurements were limited to back-to-back parallel configurations; where the measured geometrical areas would be symmetrically disposed and (unless otherwise specified) of approximately identical character. For this purpose, cells were fabricated by pressing identical electrode discs onto both sides of 3" x 5" ion-exchange membranes--each of which was designed to fit into the smaller half of a 4-compartment test fixture. The fixture itself is described in detail in a previous report (Figure 23 of Reference (1) and was found particularly useful due to the ease with which it could be adapted to both flooding and drying conditions.

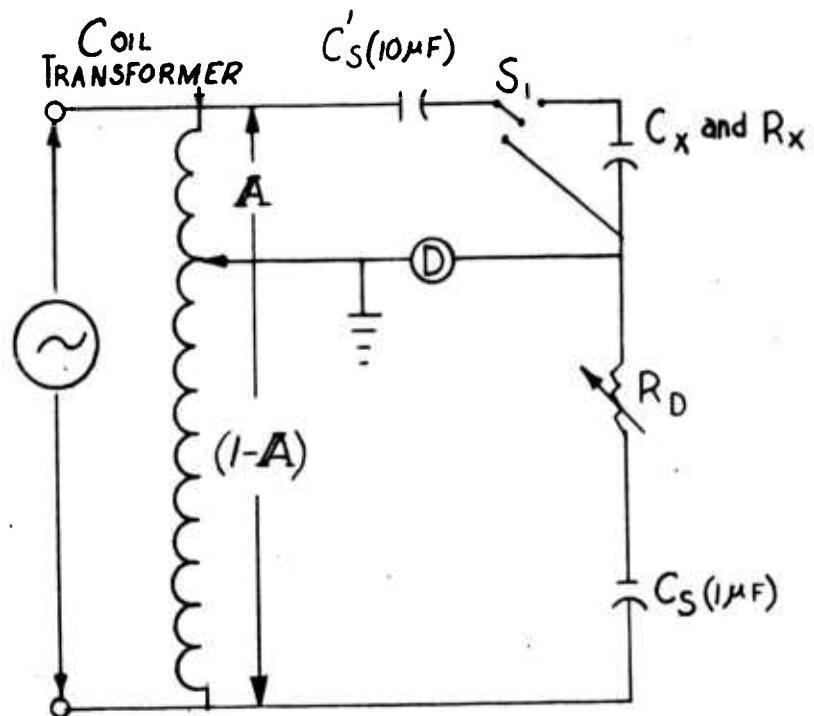
All the impedance determinations were run with the variable ratio-transformer bridge, developed by the Electrical and Physical Standards Operation of General Electric's Advanced Technology Laboratory (6). Difficulties were encountered at the outset due to large inductive residuals of the circuit components at the high frequencies used. With modifications and refinements in both measuring procedure and circuitry, however, it became possible to obtain an accuracy of 10% at 10,000 CPS when encountering capacitance values up to 3,000 μ F (7).

This was accomplished by the use of the substitution technique of Hillhouse and Kline, provided for by the modified circuitry of Figure I-1. In practice, the experimental fixture, containing the leads and current-collector screens (i. e. with C_x shorted by switch, S_1), was placed in a fixed geometric position with respect to the circuit; and resistance and transformer-ratio values (A_0 or $1-A_0$) were obtained at all frequencies of interest. The experimental cell was then placed in the fixture and another set of resistance and transformer-ratio values (A_1 or $1-A_1$) obtained. If care was taken to keep the relative geometric relationships of all the circuit components fixed during these two operations, the experimental capacitance, C_x , could be calculated by the relation

$$C_x = \frac{C_s(1-A_1^c)(1-A_0^c)}{(A_1^c - A_0^c) [1 - \omega^2(L_s + L_d)]} \quad (I-3)$$

where C_s is the "standard" capacitor (of 1μ F), A_1^c and A_0^c are the corrected (for inductance) A_1 and A_0 values, and L_s and L_d are the

SCHEMATIC OF VARIABLE RATIO-TRANSFORMER
BRIDGE CIRCUITRY



Fuel Cell Lab
DECO - G. E. Co.
Lynn, Mass.

FIGURE I-1'

Semi-Annual Summary
Report #2
Contract DA-36-039-
AMC-00095(E)
S. Krumbein 6/30/63

4.0 FACTUAL DATA (Cont'd)

inductive residuals of the "standard circuit" and of the balancing resistors respectively. One should also note that neither the exact magnitude of C_g' nor that of the inductive residuals of the test circuit (L_x) need to be known, provided they remain constant.

In most cases, the high resolution of the method, together with the low C_g/C_x ratios generally encountered in our measurements (≤ 0.01), enables the use of the approximate relation

$$\Delta A \equiv (A_1^c - A_0^c) \simeq \frac{C_s}{C_x} (1 - A_0')^2 \quad (I-4)$$

(where A_0' is an average of the A_0^c values from 2 to 10 Kilocycles), since $A/(1-A)$ was very close to 0.1 at practically all frequencies. One could then be justified in drawing up calibration curves for direct "readout" of capacity from the calculated ΔA values.

4.1.2.3 Results: -

1. Drying the cell, by passing "dry" nitrogen gas at low pressure (2-5 psi) through the small gas compartments of the test fixture, produced a continuous drop in capacitance, coupled with a rise in the measured cell resistance. In the initial stages of the drying procedure, the cell was observed to recover (with respect to its impedance parameters) when the gas flow was stopped, but continued passage of N_2 eventually resulted in capacitance values below $1 \mu F/cm^2$ and a related resistance increase of several orders of magnitude. During this latter stage, a slight tendency toward recovery was also observed -- manifested by very small increases in capacity--due, probably, to longitudinal diffusion of water from the "electrode-less" portion of the ion-exchange membrane.

2. Impedance measurements under "normal" wet conditions were generally conducted with the cell's gas compartments flooded with dilute (pH 4) sulfuric acid solution, so as to eliminate ambiguities connected with the position of the liquid level in the electrode phase. Under these conditions, the electrode surfaces were at a potential of approximately 1.0V (versus NHE); based upon measurements made against two large (3-5/8" diameter) back-to-back, "built-in" hydrogen reference electrodes (cf. Figure 22 of Reference (1)) of similar composition.

4.0 FACTUAL DATA (Cont'd)

The first set of experimental determinations -- all of which were performed with cells fabricated from 0.005 inch thick GPS^{***} membranes -- appeared to indicate direct variation of capacitance (at constant frequency) with electrode loading. That this result was fortuitous was shown by later measurements on the same cells. Tables I-1 and I-2 not only indicate that the capacity changed with time, but that these changes themselves were not reproducible; although they were, for the most part, in the general direction of increasing capacitance and resistance.

TABLE I-1

Constant-Frequency Impedance Characteristics of IEM Fuel Cell Configurations.

| Cell No. ** | Electrode Loading gm/cm ² | Date Made | Date Run 1963 | C _{5Kc} F/cm ² | R _{5Kc} Approximately , ohms |
|----------------|--|--------------|---------------------|---------------------------------------|---|
| 37 | 0.025 | 1/3/63 | 1/31 | 215 | 0.17 |
| 30 | 0.021 | 12/21/62 | 1/17 | 155 | 0.73* |
| 36 | 0.013 | 12/24/62 | 1/31 | 85 | 0.15 |
| | | | 4/26 | 92 | 0.45 |
| 32 | 0.0074 | 12/21/62 | 1/16 | 78 | 1.39* |
| | | | 1/31 | 111 | 0.97 |
| | | | 4/25 | 311 | 1.05 |

* Not flooded during these two runs. The cells had been soaked in pH4 (H₂SO₄) just prior to being placed in the fixture, however.

** All cells in table are based on GPS membranes of 0.005 inch thickness.

*** In this text GPS will represent grafted polystyrene sulfonic acid.

4.0 FACTUAL DATA (Cont'd)

TABLE I-2

Constant-Frequency Impedance Characteristics of IEM Fuel Cell Configurations

| Cell No. * | Electrode Loading gm/cm ² | Date Made 1963 | Date Run 1963 | C F/cm ² | | R |
|-------------------|--|----------------------|---------------------|------------------------------------|------|--------|
| | | | | 5Kc | 8Kc | 5-10Kc |
| 57 | 0.029 | 3/18 | 3/22 | 680 ⁺ ₃ **** | 495 | 0.20 |
| 51-1 | 0.016 ₅ ** | 3/11 | 3/21 | 686 ⁺ ₁ | 485 | 0.14 |
| | | | 3/22 | 800 ⁺ ₄ | 630 | 0.19 |
| 53 | 0.015 ^{**} | 3/12 | 3/21 | 845 ⁺ ₃ | 610 | 0.14 |
| 50 | 0.009 ₅ | 3/8 | 4/26 | 1168 ⁺ ₃₈ | 940 | 0.21 |
| 54 | 0.008 ₅ | 3/13 | 3/21 | 862 ⁺ ₀ | 675 | 0.18 |
| | | | 3/21 | 788 ⁺ ₀ | 600 | 0.20 |
| | | | 4/25 | 1190 ⁺ ₁₈ | 1030 | 0.26 |
| 56 | 0.005 | 3.14 | 3/22 | 385 ⁺ ₂ | 278 | 0.32 |
| | | | 4/26 | 500 ⁺ ₁₀ | 412 | 0.62 |
| 59 ^{***} | 0.009 | 3/19 | 3/22 | 322 ⁺ ₃ | 249 | 0.38 |

* All cells (except No. 59) in this table are based on GPS membranes of 0.010 inch thickness.

** Electrodes for No. 51-1 and 53 were made with 7 mil and 10 mil decals respectively; No. 51-1 was, therefore, of greater compactness.

*** PSS membrane

**** Average deviation

FACTUAL DATA (Cont'd)

Measurements were also obtained with pre-pressed electrode configurations. These were either applied with heat and pressure to the membrane, so that the resulting cell was outwardly no different from those of Table I-1 and I-2, or else consisted of individual discs (1-5/8" diameter and 0.005 inches thick) containing about 0.065 gms/cm² of catalyst; and held against the IEM by simple mechanical pressure of the current collectors.

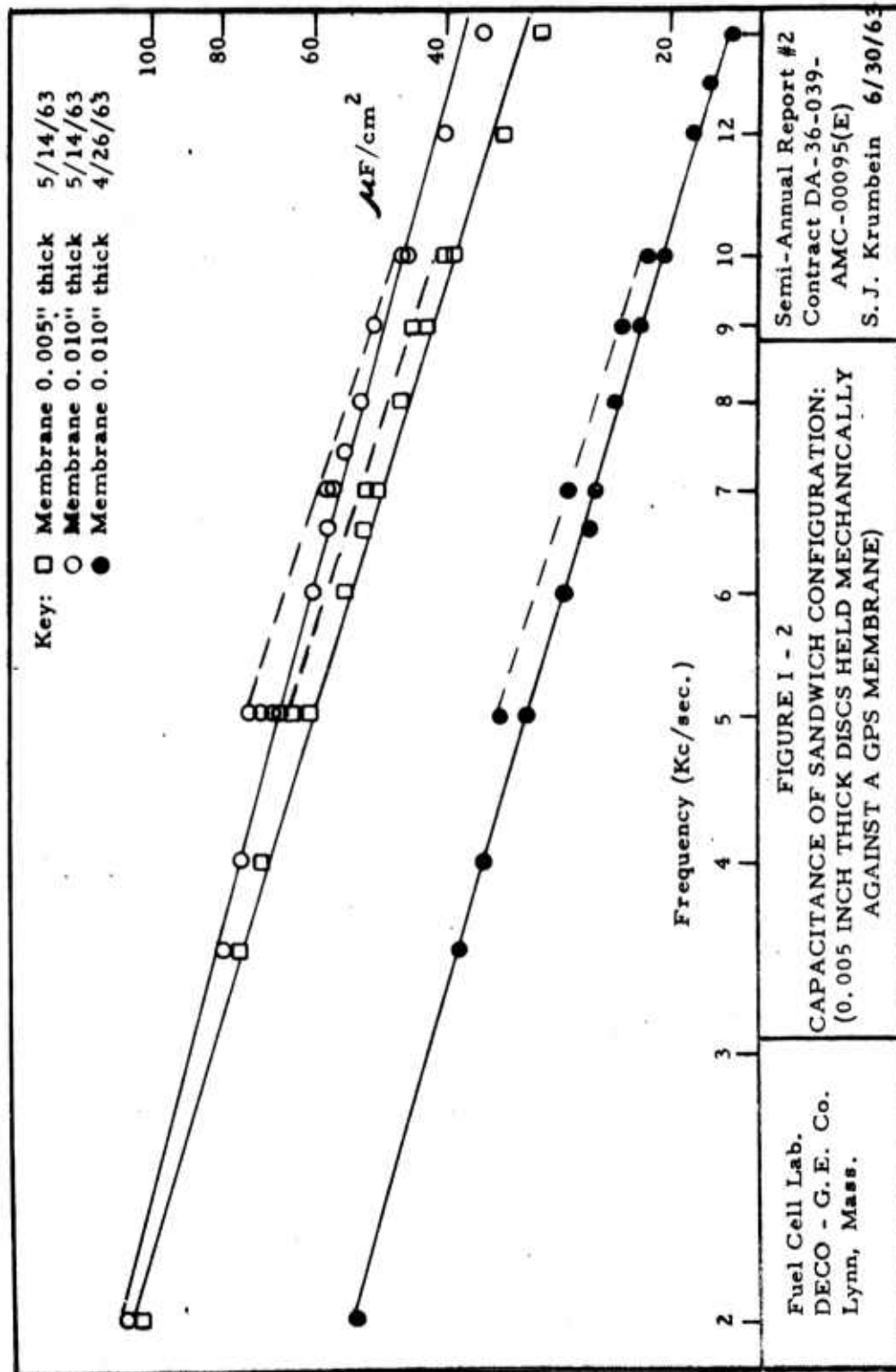
The former (with a 0.005 inch thick GPS membrane) yielded capacitance values of approximately the same magnitude as those of Table I-1, but showed definite tendencies towards increasing capacitance and decreasing resistance over the half-hour period of the actual determinations (from low to high frequencies and back -- cf. Figure I-2). The latter, however, gave lower capacity values but a greater tendency for change -- both in between runs (as in Tables I-1 and I-2) and during the course of the experimental series. These changes were always toward higher capacities and lower resistance, and are illustrated, to a certain extent, by the broken lines of figure I-2.

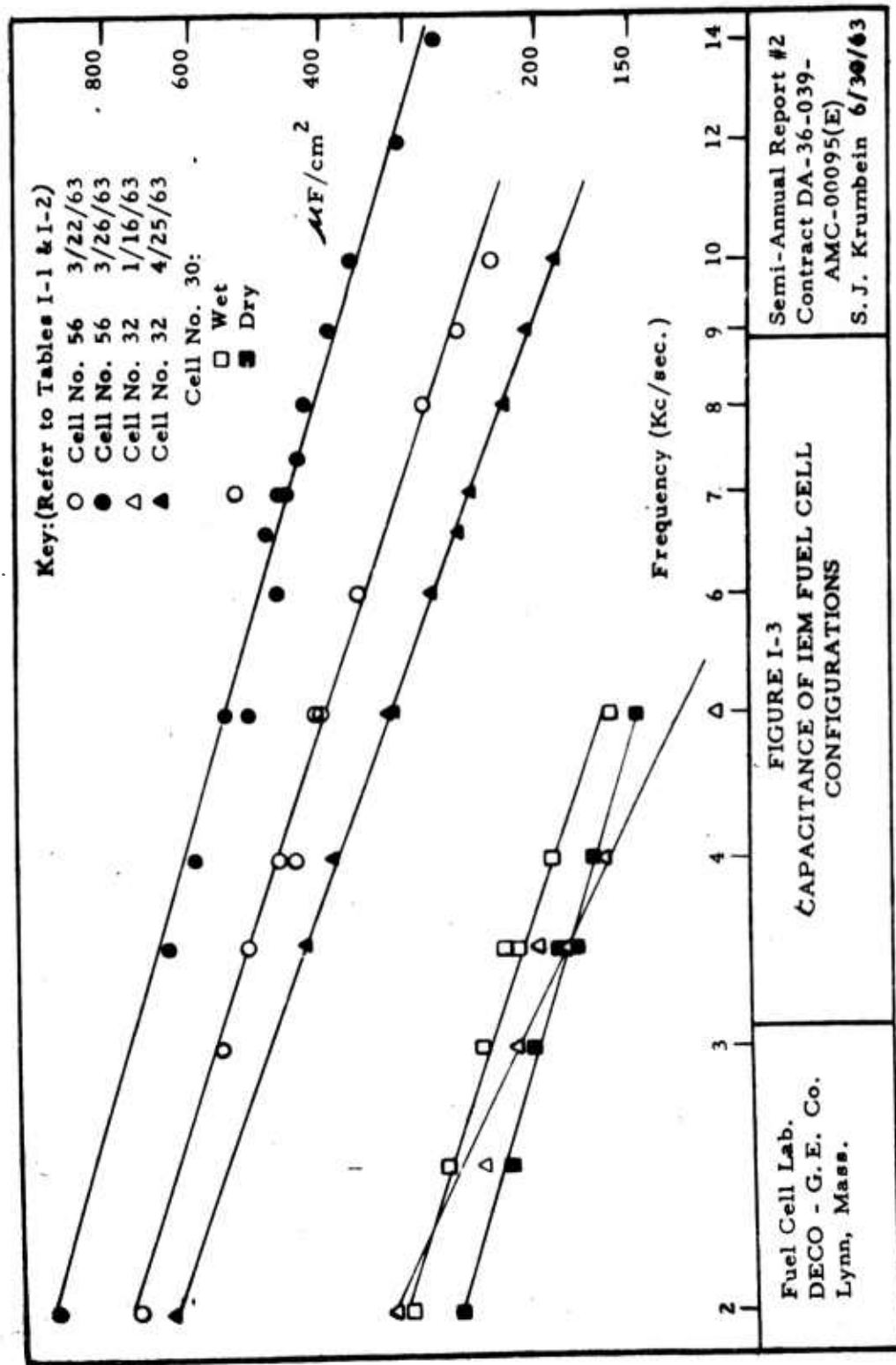
Auxiliary determinations were conducted with the same two GPS membrane types, but with platinum foil discs (1-5/8 inches diameter and 0.001 inch thickness) in place of the pre-pressed electrodes. Although time-dependence during the measurements was similar, the measured capacitance values were found to be between 6 and 8 $\mu\text{F}/\text{cm}^2$, for both types of membrane, over the same frequency range as above.

3. Variations of capacity with frequency were virtually independent of all experimental parameters; and was shown to be so even during early stages of drying (Figure I-3). The logarithmic equivalents of this typical hyperbolic dependence is illustrated by the plots of Figures I-2 and I-3.

4.1.2.4 Discussion and Conclusions:

1. The capacitance values are apparently a relative measure of the "active", non-wetproofed, interfacial area between the platinum black and aqueous phases (Figure I-4). This would include only those regions of free platinum surface which are in electrolytic contact, through the aqueous phase, with the ion exchange membrane (i.e. not in blocked pores). As such, the measurements could not differentiate between the platinum surfaces within the bulk porous electrode phase and those directly adjoining the membrane material. This was experimentally corroborated by the comparatively





FACTUAL DATA (Cont'd)

fast attainment of water equilibrium between IEM and electrode -- as shown by the tendency toward recovery of the impedance parameters during the drying experiment -- so that the assumptions of Section 4.1.2.2 would appear to have been incorrect.

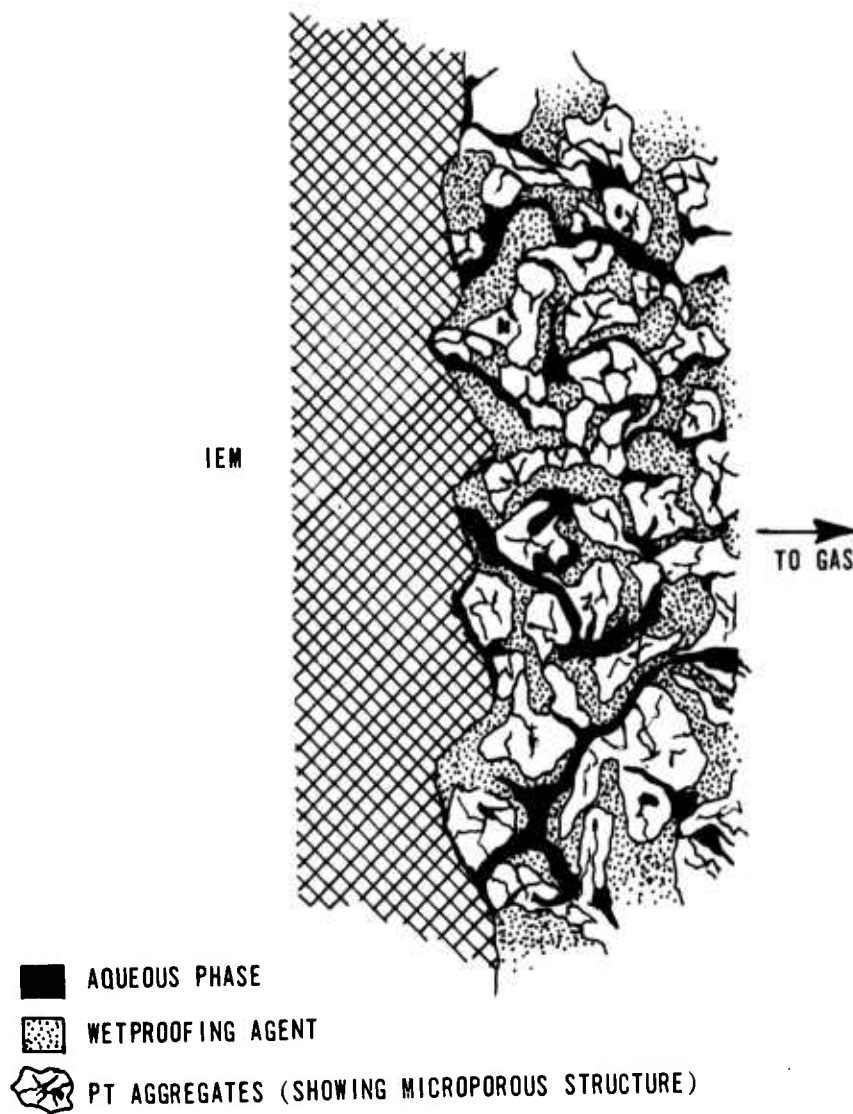
2. Capacitance values were time-dependent, but the magnitude of the changes could not be reproducibly related to known experimental parameters. Considerable change occurred even when the cells were stored under conditions which would preclude drying out. Judging from the odor released when the water-tight bags were opened (after a month or more), these changes may be partly associated with membrane degradation. Since the observed time-dependence was generally in the direction of increasing capacitance, any effect due to degradation products adsorbed onto the platinum surface (a process that has long been known (18) to lower the double-layer capacity) would appear to have been masked by the directionally opposite effects of structural changes in the experimental cell.

Degradation of the membrane, as well as shrinkage and swelling (see Task II), would, however, tend to produce distortions and/or separations between the IEM surface and parts of the electrode material, with resultant changes in the interfacial area. Of equal importance would be the gradual release of the original compressional stresses (probably aided by water absorption) in the porous electrodes -- especially those that had been applied, in the powder form, directly to the IEM (Tables I-1 and I-2). This would lead to an increase in the open pore network connecting with the membrane surface (Figure I-4), with a concomitant increase in the total area of active platinum/water interface.

Some degree of evidence for this hypothesis can be seen from the capacity values of cells No. 51-1 and 53 (Table I-2). The electrodes of both had approximately the same loading factor, but differed considerably in their compactness during the pressing stage of cell fabrication -- so that initial capacitance values for cell No. 51-1 were considerably below those for No. 53. In the next day's run (with soaking in-between), however, values quite close to the latter were produced,

* Figure I-4 represents one opinion of the electrode structure in the region adjacent to the IEM. It is intended only as a pictorial aid to the discussion, and should not be considered a scale model representation of the true cross-section.

TWO DIMENSIONAL REPRESENTATION OF POSSIBLE ELECTRODE
STRUCTURE AT THE IEM INTERFACE



Fuel Cell Laboratory
DECO - G.E. Co.
Lynn, Mass.

FIGURE I-4

Semi-Annual Summary
Report #2
Contract DA-36-039-
AMC-00095(E)
S. Krumbein 6/30/63

4.0

FACTUAL DATA (Cont'd)

indicating a comparatively rapid opening up of the pore structure (cf. the two separate runs of cell No. 54).

Figure I - 2 indicates that some such effect may have also occurred with the pre-pressed electrode discs, after having been soaked in the aqueous solution for some time. It should be noted, in this context, that different 0.010-inch thick membrane samples were used in May and April, so that the great differences between the two months' runs -- and the small effect of substituting a 0.005-inch thick membrane -- was chiefly due to differences in the electrodes themselves. The effect of water on the porosity is also suggested by the short-time changes in this figure, the points on the dashed lines being those obtained at the end of each series of runs.

3. The results of this phase suggest the use of the impedance technique in determining aging and/or time-dependent operational effects occurring at the IEM/electrode interface. Determination of relative interfacial areas and other structural parameters of different IEM fuel cells, however, can, at best, only be of a qualitative nature; unless improved fabrication and storage procedures can be developed for assuring better microscopic reproducibility.

4.1.3 Adhesion Measurements

4.1.3.1 Theory:

A program has been undertaken to determine the relative adhesion existing between the catalyst and membrane phases of IEM fuel cells. The method adopted for initial evaluation was that developed by Heavens (9) and, later, put on a semi-theoretical basis by Benjamin and Weaver (10). Photograph I-1 illustrates the complete experimental setup, including a modified form of Heavens-type apparatus built in our laboratory. This is seen to consist essentially of a horizontal beam with a weight-pan in its center and a smoothly rounded point at its end. Samples are drawn across a flat table, directly under the "point", so that the latter travels across the metal (i.e. electrode) surface. Weights are added to the pan after each run, until -- at a certain critical weight -- the film should be cleanly stripped from the surface.

The theory of the experiment is based upon the work of Bowden and Tabor (11, 12) on the adhesional theory of friction; under which Amonton's second law acquires the form

$$F_r = Ws/p \quad (I-5)$$

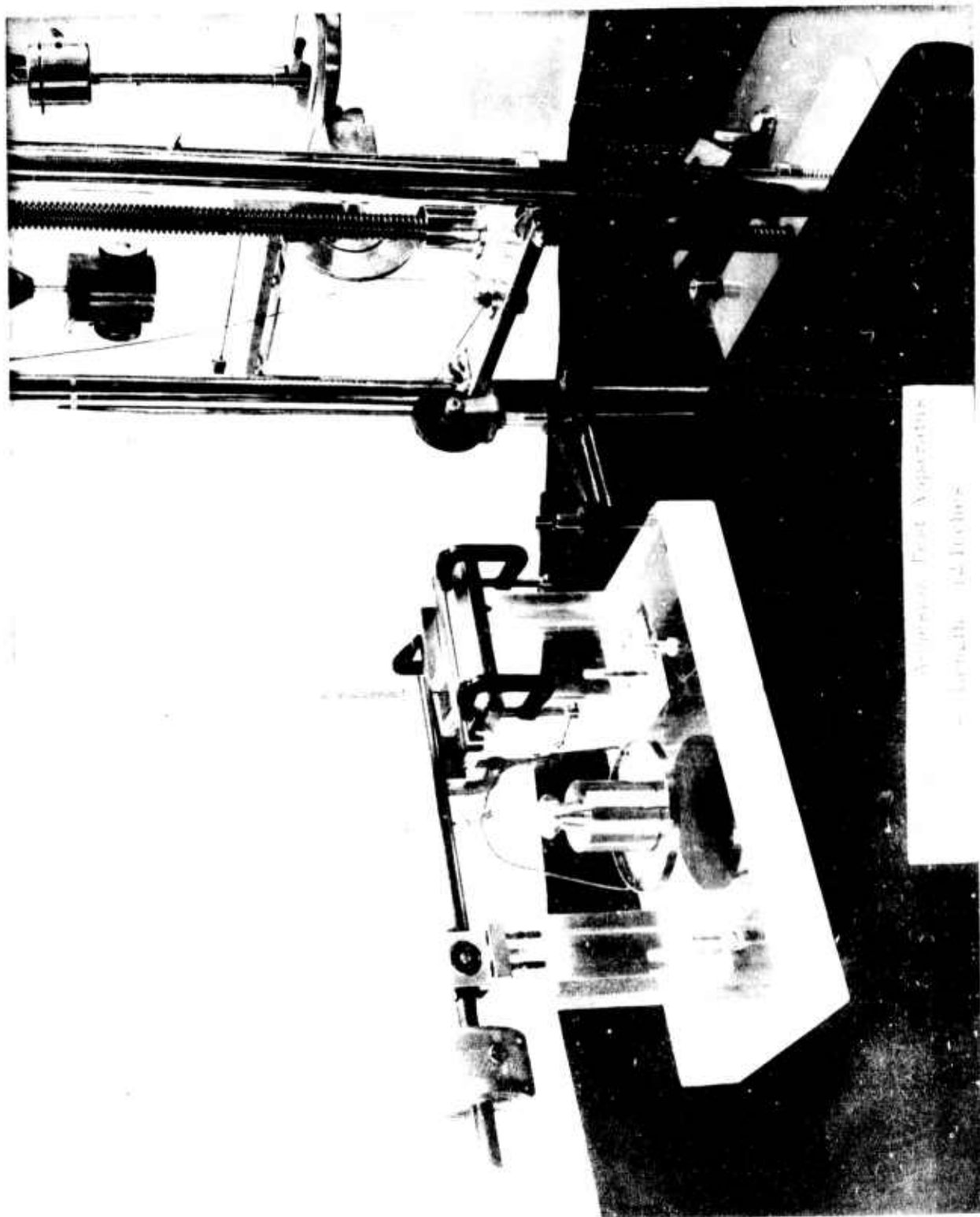


Photo I-1
-21-

A 12604

FACTUAL DATA (Cont'd)

where F_r is the frictional force, W the normal load, and p the yield pressure of the softer material, while s is the force per unit area, acting in a direction tangential to the interface, which is required to shear the adhesive bonds.

It has been shown (10), however, that the "critical" vertical forces obtained with the Heavens apparatus are determined, primarily, by the properties of the film/substrate interface. The hard point (or ball) is assumed to slide over the metal film for increasing loads, up to the point where deformation of the substrate causes a loosening of the film. The load at which the deformation occurs can be related to the yield pressure of the substrate (11) by

$$W = Ap \quad (I-6)$$

where A is the area of contact between the (hard) ball or point and the softer substrate.

Any effect of the metal film is assumed to be negligible provided its thickness is much less than the ball's radius, so that the former can readily be deformed to the contour of the indentation. The maximum shearing forces between this film and the substrate surface would then be expected to occur at the lip of the indentation. It is here that the adhesive bonds would be initially broken by the critical vertical load; and the horizontal motion of the indenter would merely serve to push the sheared film aside.

From equation (I-6) and analysis of forces (including these two assumptions) Benjamin and Weaver (10) have shown that the shearing force (per unit area) could be expressed as:

$$F = \frac{W^{1/2} P}{(\pi r^2 P - W)^{1/2}} \quad (I-7)$$

where r is the radius of curvature of the indenter and P is now the deformation or indentation hardness of the substrate.

It is seen that, for identical substrate materials (identical ion-exchange membranes, in our case), comparative measurements of adhesion can be obtained from the vertical load, W , alone; although this parameter will also be a function of the fraction of the interfacial area on which actual IEM-electrode bonding has taken place. The hardness of the substrate, P , must be known, however, before one can calculate the shearing forces. This was determined for both thick GPS and PSS*

* non cross-linked sulfonated polystyrene

4.0

FACTUAL DATA (Cont'd)

membranes by measuring the apparent compressive yield stress, Y , by standard technique (15), and applying the relation (13)

$$P = cY$$

(I-8)

where c is between 2.5 and 3. The lower value was chosen, as proposed by Benjamin and Weaver, and the experimental value of P was found to be approximately 11 Kg/mm^2 for the fluorocarbon based GPS membrane, which can be compared to the value of 11.5 Kg/mm^2 measured directly by King and Tabor on pure Kel-F (12). Experimental compressive yield stress values for the PSS membrane were not reproducible, but appeared to average about 3 Kg/mm^2 -- for an apparent indentation hardness of 7.5 Kg/mm^2 .

4.1.3.2 Experimental:

In addition to the assumptions that were specified in Section 4.1.3.1, certain other assumptions and experimental conditions must be met for the theory to be tenable.

1. The indentation hardness, P , of the substrate must not change significantly with W or the time of actual contact with the indenter. Approximate constancy of P has been found by King and Tabor (14) over a 10 to 40-second range of "loading" time -- with the least changes for the shorter times. Nevertheless, it was found advisable to make all measurements at constant horizontal pulling speed with a Dillon Universal Tester (Photograph I - 1), so as to eliminate any additional unknown parameters from the comparative measurements. A speed of 0.075 cm/sec was chosen, corresponding to a far shorter contact time than the lowest -- and most accurate -- loading time of these authors.
2. The mechanical integrity of the bulk substrate material must not change during the experiment. The substrate must remain flat so that the applied horizontal and vertical forces will subtend a constant, known angle (preferably one of 90 degrees). Likewise, the other bulk properties of the material should also be unaffected by what is happening at its upper surface. The thickness of the piece must, therefore, be considerably greater than the ball radius, especially for our fairly soft IEM materials. This factor, together with the necessity for examining the scratches by transmitted light, required rather artificial fuel cell configurations, consisting of a thick membrane with the electrode material on only one side.

4.0

FACTUAL DATA (Cont'd)

3. Equation (I - 7), in the form

$$W = \frac{\pi r^2 P F^2}{P^2 + F^2} \quad (I-9)$$

indicates that the critical load, W, is directly proportional to r^2 . Moreover, the variation of W with F (assuming constant P)

$$\frac{dW}{dF} = \frac{2\pi r^2 P^3 F}{(P^2 + F^2)^2} \quad (I-10)$$

shows that, with soft substrate materials, reproducible points of comparatively large radius of curvature will be required in order to obtain sufficient precision and ease of measurement. Experimental indentors were consequently made from precision bearing balls, rigidly fixed to threaded standard stock (see Photograph I - 8 in Appendix I - 1).

4.1.3.3 Results and Discussion:

1. Significant differences were found in the vertical load required to strip electrode materials of different formulations from a specially prepared, air-dried, 1/8-inch GPS membrane. Pure platinum black required a load of about 900 grams (for a 1/64-inch diameter tungsten-carbide, ball-bearing "point"), while a platinum black - TFE (Tetrafluoro Ethylene) mixture remained adherent, over most of the test area, at loads exceeding 1200 grams. When the pieces were soaked in water just prior to the measurement, the required load was considerably reduced for the pure metal electrode, whereas no significant changes were observed for the fluorocarbon mixture. On the other hand, PSS substrates, with the same platinum/TFE electrodes, yielded lower critical force values -- which decreased still further under wet conditions.

These results were obtained with fairly uniform electrode coatings; and are summarized in Table I - 3.

TABLE I - 3

Vertical Loads and Shearing (Adhesional) Forces
For IEM/Electrode Systems.

| <u>IEM Substrate</u> | <u>Electrode Composition</u> | <u>Condition of piece</u> | <u>W (Kg)</u> | <u>F (10⁸ dynes/cm²)</u> |
|----------------------|------------------------------|---------------------------|---------------|--|
| GPS | Pure Pt | Dry | 0.9 | 15 |
| | | Wet | 0.6 | 10 |
| GPS | Pt/TFE | Dry | 1.2 | 28 |
| | | Wet | 1.2 | 28 |
| PSS | Pt/TFE | Dry | 0.7 | 13* |
| | | Wet | 0.4 | 6* |

* Based upon "average" values of poorly-defined indentation hardness.

2. Where the electrode material was applied unevenly to the membrane-- due to local differences in preparation and pressing -- the "critical" vertical weight varied with apparent thickness of the layer. In fact, by applying a 900 gram weight over various portions of this electrode it was possible to obtain a set of "contour" lines ranging from strong to weak (completely stripped) regions. Since previous theoretical and experimental work (10) has shown that the critical load -- for an ideally coherent coating -- should be independent of film thickness, the observed adhesion versus thickness dependence would appear to reflect an increase in adhesive bond density (between the IEM and the aggregated electrode material) with thickness.

3. Micrographs of "stripped" grooves from this type of sample are shown in Photograph I-2 for the 900-gram load, as well as in Photograph I-3 for a 600-gram weight on a region of weak bonding. In addition, Photograph I-9 (see Appendix I-1) shown the furrow resulting from the 1200-gram critical load that was required for a uniformly-pressed Pt/TFE electrode (Table I - 3). Under reflected light, most of the stripped material was found to have been removed from the inner lips of the furrow -- thereby pointing up the applicability of the underlying theory (10)-- and pushed to the sides as fairly large pieces (photograph I-10; Appendix I-1).

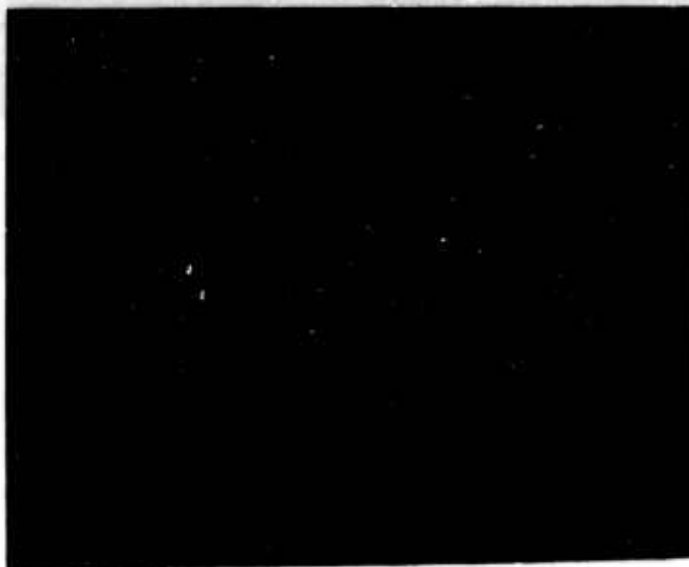


Photo I-2
Trans.
Light



Photo I-3
Trans.
Light

Fuel Cell Laboratory
DECO - G.E. Co.
Lynn, Mass.

Photos I-2 and I-3
Micrographs of
Adhesion Test
Grooves (X200)

Semi-Annual Summary
Report #2
Contract DA-36-039-
AMC-00095(E)
S. Krumbein 6/30/63

As shown by the three previous photographs, not all the electrode material was ploughed to the side after the initial adhesive bonds were broken. Instead, some remained imbedded in the bottom of the groove, the quantity of such "debris" increasing with the critical vertical load and its associated adhesive forces. That this effect is related to the nature of the adhesive bonding can be seen by comparing these pictures to those for the pure platinum black electrode. Photograph I-4 (a close-up to Photograph I-11 of the Appendix) shows the removal of a much greater amount of material-- by an 800-gram weight-- from the bottom of the furrow, with whole sections of electrode cleanly stripped away. Moreover, prior soaking of the piece in water served to accentuate this effect, resulting in an almost completely clean scratch (with 700 grams; Photograph I-5).

4. The motion of the indenter, once it had penetrated to the membrane surface, was of the "stick-slip" (13) variety. This is clearly revealed in Photographs I-4, I-11, and (to a lesser extent) I-2; and is to be expected for the fluorocarbon based GPS membrane used (14). This behavior tended to give way to a partial penetration of the "point" into the material even when dry (Photograph I-12, showing another part of the same groove as I-11); and led, in some cases, to actual jamming of the point when the substrate was wet. The latter effect is illustrated in Photograph I-13 of Appendix I-1 for another section of the same scratch as I-5. Under reflected light (Photograph I-14), this path of the indenting ball into the membrane can be easily followed as a black "finger", with the ploughed-up catalyst at the furrow's edges revealing a comparatively non-aggregated structure (Photograph I-10).

5. The problem of jamming under wet conditions was especially critical with the non-crosslinked PSS substrates, even when coated with the same platinum black/TFE mixture. In many cases, the hole became so deep that the "Dillon Tester" had to be stopped and reversed to avoid snapping the pulley-cord; and the ball-point pulled out by hand.

The low cohesional strength of the membrane and its extreme softness under load was also responsible for the tendency of the indenter to strip some of the underlying substrate material along with the electrode layer. This took place even when the test piece was not pre-soaked; and would appear to cast doubt on the applicability of the method (along with its underlying assumptions) to PSS membranes.



Photo I-4
Trans.
Light
(X200)



Photo I-5
Trans.
Light
(X80)

Fuel Cell Laboratory
DECO - G.E. Co.
Lynn, Mass.

Photos I-4 and I-5
Micrographs of
Adhesion Test
Grooves

Semi-Annual Summary
Report #2
Contract DA-36-039-
AMC-00095(E)
S. Krumbein 6/30/63

4.0 FACTUAL DATA (Cont'd)

It might also be mentioned that these pieces tended to warp when dry; and that relatively prolonged air-drying (i.e. during the measurement) tended to produce local blistering and loosening of the electrode layer.

6. The effect of polymeric binders on the cohesional characteristics of the electrode is illustrated by the reflected-light micrographs of some grooves made with less than the critical load. Photograph I-6 was made by 950 grams on a platinum black/TFE electrode, and shows a groove whose surface is little different in appearance from that of an unscratched electrode. On the other hand, a scratch made on a platinum black electrode (Photograph I-7) by 500 grams reveals a series of deep cracks, at right angles to the groove, even though the unscratched surface is no different from Photograph I-6. It should also be noted that the "unstripped" grooves in Pt/TFE material on PSS substrates gave the same appearance as that for the GPS membrane (Photograph I-6).

4.1.3.4 Conclusions:

The importance of polymeric binders, such as the polyolefines and their halogenated homologues, as wetproofing agents for porous electrodes has long been recognized (4, 5). More recently, a definite parallel was demonstrated in this laboratory (2) between optimum fuel cell characteristics and maximum contact angle -- as a function of the relative composition of platinum black and Teflon TFE binder. The results just reported -- using these same model materials -- have now shown that hydrophobic binders can serve the additional function of acting as adhesive agents between the catalyst and ion-exchange membrane.

This empirical view of the triply-functional character of "electrode binders" or "wetproofing agents" can be best understood in the light of the very recent work of Sharpe and Schonhorn (21) on the adsorption theory of adhesion. According to their proposal (which is outlined briefly in Appendix I-2), there exists a one-to-one correspondence between thermodynamic spreading and strong adhesion, so that the operational condition for strong adhesion can be shown to be identical with Zisman's wetting relation (20),

$$\gamma_c \gg \gamma_L \quad (I-11)$$

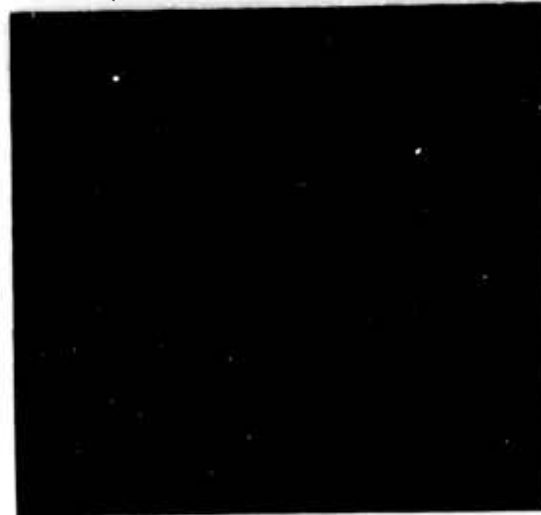


**Photo I-6
Reflected
Light**

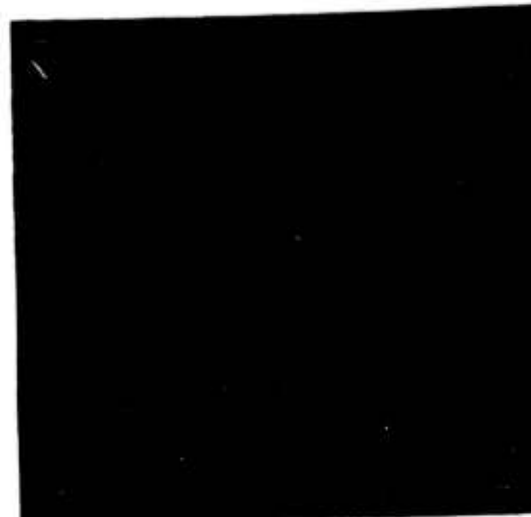


**Photo I-7
Reflected
Light**

Fuel Cell Laboratory
DECO - G. E. Co.
Lynn, Mass.

**Photos I-6 and I-7
Micrographs of
Adhesion Test
Grooves (X300)**

Semi-Annual Summary
Report #2
Contract DA-36-039-
AMC-00095(E)
S. Krumbein 6/30/63

4.0

FACTUAL DATA (Cont'd)

The critical surface tension, γ_c , of a solid has been defined by Zisman (19) as the maximum surface tension that a liquid, L, can possess in order to just wet that particular solid. Materials with lower surface tensions would then be expected to make good adhesives for such solids -- provided they could be applied in fluid form. This latter condition arises from the fundamental mechanism of simple adhesion, which is postulated (21) as being almost exclusively due to Van der Waals forces, and, therefore, only operative over very small distances.

It can now be seen that the very same property that makes a material a good "wetproofing" agent while solid (i. e. its low surface free energy) also serves to make it a good adhesive when it is caused to undergo a certain amount of flow. In practice, this is accomplished by the high pressures and moderately high temperatures applied during fabrication, so that Teflon TFE ($\gamma_c = 18.5$)^{*}, for example, would not only act as an adhesive between the high surface-energy, platinum black particles (cohesional or "cementing" agent) but also between the latter and the low surface-energy ($\gamma_c = 33$)^{*}, fluorocarbon based, solid substrate. In this context, one might also note that, whereas the softening point of Teflon TFE is almost twice that of the base fluorocarbon, its static yield pressure, at 20°C, (5.3Kg/mm²) is less than one-half that of the latter (14). It is, therefore, not surprising that the large vertical forces encountered in our measurements -- of the order of 10³Kg/mm²-- should be expected to cause individual platinum/Teflon aggregates that are directly under the ball-point (i. e. at the bottom of the groove) to adhere even more strongly to the substrate (compare Photographs I-2, I-3, and I-11 with Photographs I-4 and I-5).

4.1.3.5 Future Work

Further work is anticipated on this phase of the Program, for the purpose of testing our conclusions with hydrophobic binders possessing critical surface tension values midway between those of TFE and the base fluorocarbon. Determinations might also be attempted with similar electrodes containing Teflon FEP ($\gamma_c = 16$) as binders.

* All γ_c values are based on those of Zisman and co-workers (19, 20).

4.0 FACTUAL DATA (Cont'd)

4.2 TASK II

WATER TRANSPORT IN ION EXCHANGE MEMBRANES

J. R. Boyack

4.2.1 Introduction

Water transport phenomena are important in ion exchange membrane fuel cell technology because of the strong dependence of membrane conductivity on water content and also from the standpoint of controlling the water balance in the entire operating unit.

The driving forces which affect water transport are electric potential gradients, water activity gradients, hydrodynamic pressure gradients, and temperature gradients. The first of these has been treated quite extensively in the literature, (23), (24), (25), (26), (27) but there has been little done concerning the others, (28).

The objective of this task is to obtain additional knowledge in the areas mentioned above. Reported here are experimental results from the measurement of the hydrodynamic permeabilities of a series of polystyrene sulfonic acid membranes of various ion exchange capacities.

4.2.2 Experimental Procedure

The flux of water through the membrane under a pressure gradient was determined using a Stabin osmometer, (29). The cell was fitted with ion exchange membranes, filled with water and placed in a bath of water. Pressure was applied through the capillary tube and the flux determined by observing the movement of the meniscus in the capillary as a function of time. Membranes used were polystyrene sulfonic acid having ion exchange capacities of 1.65, 1.80, and 2.15 meq/g. The membranes were allowed to equilibrate with water at the temperature used for at least sixteen hours before a determination was made.

Membrane water content was measured by weighing after blotting off surface water of a membrane strip which had been equilibrated with water at the temperature in question. The dry weight was measured after drying the strip in an oven at 110°C.

4.0 FACTUAL DATA (Cont'd)

4.2.3 Experimental Results

The curves obtained by plotting the volume of water which had passed through the membrane vs. the time measured from application of the pressure generally had the form depicted in Figure II-1. After the induction period of from five to thirty minutes, the plots became linear. The water flux was calculated from the slope of the linear portion of the curve. The induction period shown in Figure II-1 did not always occur. A few of the plots were linear right from the beginning. The time of the induction period was characteristic in a general way of the membrane and the temperature used, but varied sometimes over wide limits.

The water flux through the membranes was in all cases a linear function of the applied pressure as can be seen from Figure II-2. Table II-1 summarizes the permeabilities obtained, along with other calculated parameters to be discussed below. The permeabilities were calculated from the least squares slopes of the plots in Figure II-2.

4.2.4 Discussion

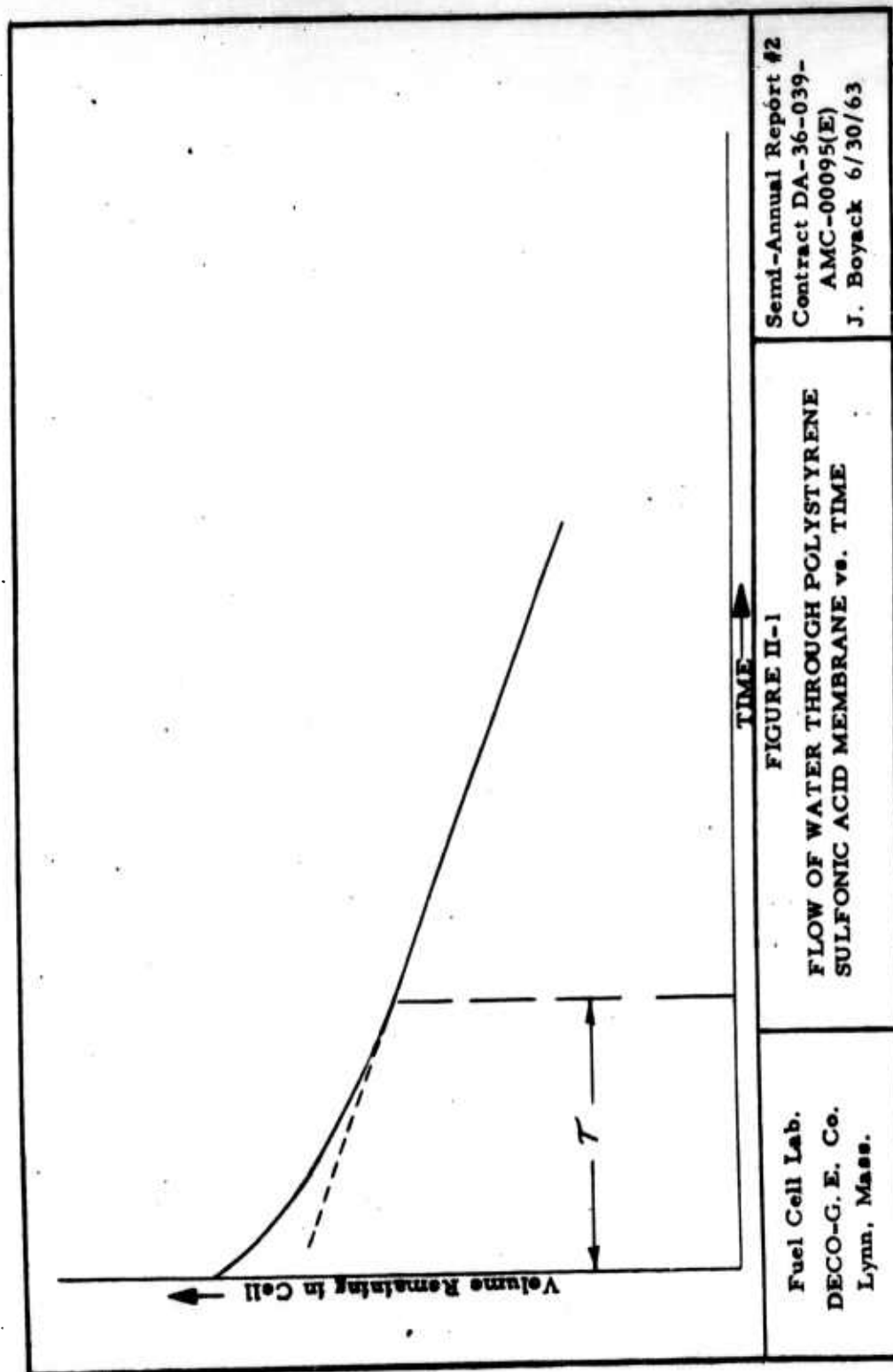
There are two mechanisms which may contribute to flow of water through a membrane under a pressure gradient: (1) diffusional transport, in which molecules move as single units and the influence of the pressure is to raise the water activity on one side of the membrane, and (2) convection, in which bulk flow of groups of molecules occurs in the membrane pores. In most membrane systems, both mechanism contribute to the total flux.

The flux, J , of water through a membrane is given by

$$J = D \, dc/dx + P_h \, \Delta p/t \quad (\text{II-1})$$

where D is the diffusion coefficient, dc/dx the concentration gradient, P_h the hydraulic permeability, Δp the pressure difference between the two sides of the membrane, and t the membrane thickness. The ratio of the water activities, a_1 and a_0 , at the two faces of the membrane is

$$a_1/a_0 = \exp \left(\frac{\bar{V} \Delta p}{RT} \right) \quad (\text{II-2})$$



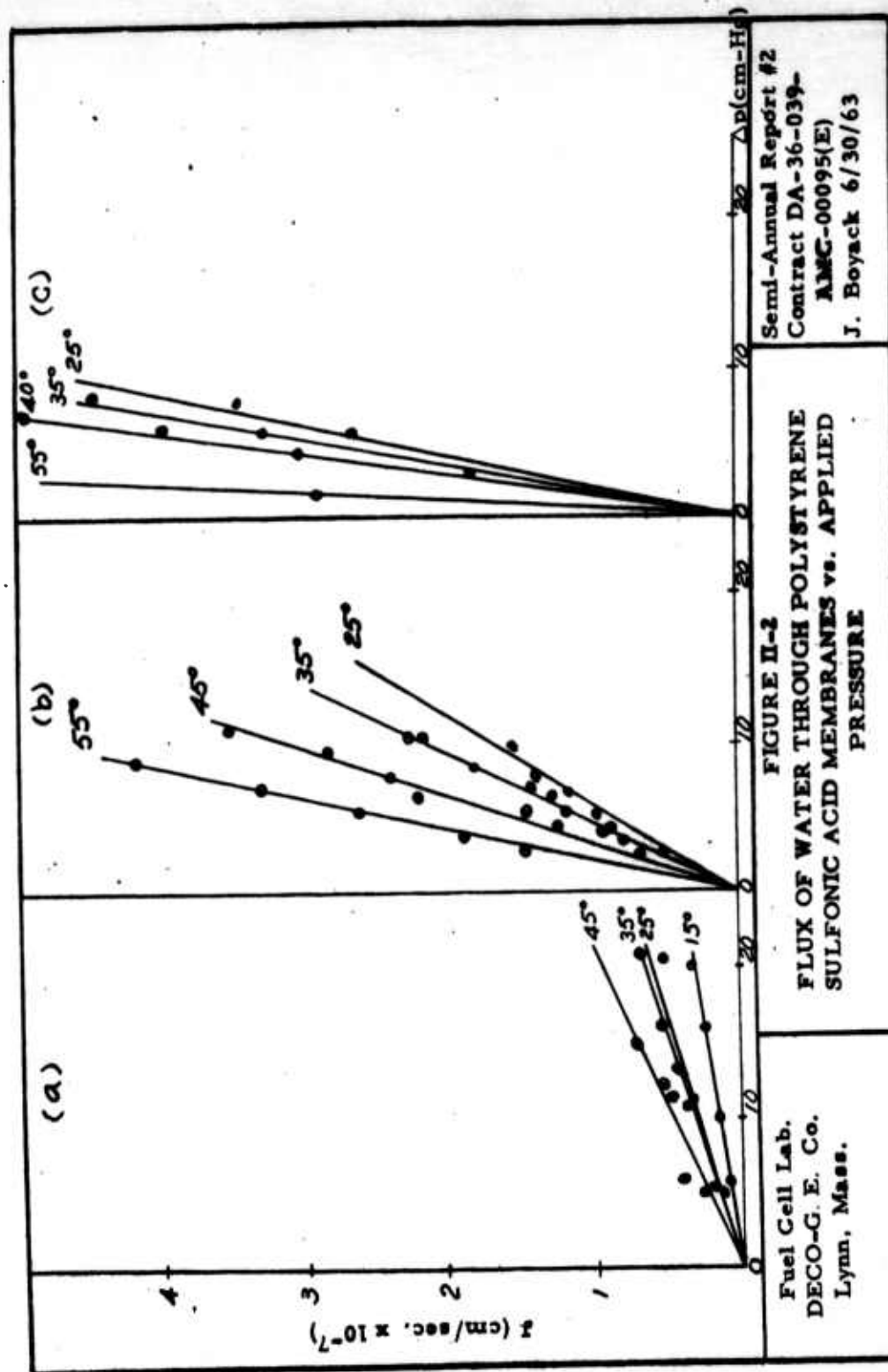


TABLE II-1: Water Transport In Polystyrene Sulfonic Acid Membranes

| I.E.C. (meq./g) | Temp. (°C) | Water Content (Volume %) | Permeability (cm ² /atm sec.) x10 ⁶ | Diffusion Coefficient (cm ² /sec.) x10 ⁶ | Diffusion Permeability (cm ² /atm sec.) (cm ² /atm sec.) x10 ⁶ | Tortu- osity | Normalized Permeability (cm ² /atm, sec.) x10 ⁶ | Normalized Diffusion Co- efficient (cm/sec. x 10 ⁵) |
|--------------------|---------------|-----------------------------------|---|---|---|-----------------|--|--|
| 1.65 | 15 | 28.2 | 7.71 x 10 ⁻⁹ | | | 6.1 | 1.0 | |
| | 25 | 30.9 | 1.34 x 10 ⁻⁸ | | | 5.5 | 1.3 | |
| | 35 | 32.4 | 1.727 x 10 ⁻⁸ | | | 5.2 | 1.4 | |
| | 45 | 34.9 | 2.42 x 10 ⁻⁸ | 1 | 2 x 10 ⁻¹⁰ | 4.7 | 1.6 | 2 |
| 1.80 | 25 | 53.8 | 9.24 x 10 ⁻⁸ | 4 | 1 x 10 ⁻⁹ | 2.7 | 1.3 | 3 |
| | 35 | 56.9 | 1.208 x 10 ⁻⁷ | 5 | 2 x 10 ⁻⁹ | 2.5 | 1.3 | 3 |
| | 45 | 57.8 | 1.861 x 10 ⁻⁷ | 2 | 6 x 10 ⁻¹⁰ | 2.5 | 2.0 | 1 |
| | 55 | 60.3 | 3.03 x 10 ⁻⁷ | 3 | 1 x 10 ⁻⁹ | 2.3 | 2.7 | 2 |
| 2.15 | 25 | 64.9 | 2.47 x 10 ⁻⁷ | 2 | 9 x 10 ⁻¹⁰ | 2.1 | 1.7 | 1 |
| | 35 | 66.3 | 3.12 x 10 ⁻⁷ | 3 | 1 x 10 ⁻⁹ | 2.0 | 1.9 | 1 |
| | 40 | 69.2 | 4.00 x 10 ⁻⁷ | 6 | 3 x 10 ⁻⁹ | 1.9 | 2.1 | 2 |
| | 55 | 74.2 | 1.78 x 10 ⁻⁶ | 14 | 7 x 10 ⁻⁹ | 1.7 | 6.8 | 4 |

FACTUAL DATA (Cont'd)

where \bar{V} is the molal volume of water, R is the gas constant, and T the absolute temperature. Assuming equal water activity coefficients at the two faces gives

$$C_1 - C_0 = C_0 \left[\exp \frac{(\bar{V} \Delta P)}{RT} - 1 \right] \approx \frac{C_0 \bar{V} \Delta P}{RT} \quad (\text{II-3})$$

Replacement of dc/dx by $(C_1 - C_0)/t$ yields

$$J = \left(D \frac{C_0 \bar{V}}{RT} + P_h \right) \frac{\Delta p}{t} \quad (\text{II-4})$$

or

$$P_a = D \frac{C_0 \bar{V}}{RT} + P_h \quad (\text{II-5})$$

where P_a is the measured apparent permeability.

The induction period shown in Figure II-1 which occurred in the majority of cases may be associated with the diffusion coefficient of water in the membrane. The diffusion coefficient can be calculated approximately from (30)

$$D = 0.42 \frac{t^2}{\tau} \quad (\text{II-6})$$

where τ is the time required to reach steady state conditions.

As mentioned before, τ varied widely in a range of $\pm 30\%$ from the average value for a given set of conditions. Nevertheless, Eq. (II-6) yields order of magnitude values for D , which are tabulated in Table II-1.

The first term in Eq. (II-5) represents the contribution of the diffusional mechanism to the total observed permeability. Table II-1 shows values for this term under the heading "Diffusion Permeability." Comparison with the measured permeability shows that only about 1% of the total flow is by this mechanism.

In migrating through the polymer matrix, the water is forced to follow a tortuous path. One may define a tortuosity factor, T , as

$$T = t'/t \quad (\text{II-7})$$

FACTUAL DATA (Cont'd)

where t' is the actual average distance traveled in migrating through the thickness of the membrane. A simple theory presented by Mackay and Meares (31) gives the tortuosity as

$$T = (1 + \theta) / (1 - \theta) \quad (\text{II-8})$$

where $\theta = 1 - C_0$ is the fraction of the space filled by polymer. A normalized permeability, P_N and a normalized diffusion coefficient, D_N , are given by

$$P_N = P_a (T^2 / C_0) \quad (\text{II-9})$$

and

$$D_N = D T^2 \quad (\text{II-10})$$

P_N and D_N are the values which would be expected if all purely geometric effects of the polymer matrix were absent. These quantities also appear in Table II-1. One should note that the D_N are all very close to the self diffusion coefficient of water, which is 2 to 5×10^{-5} cm^2/sec . (32) over the temperature range considered. The geometric effect of the matrix also accounts for most of the variation in permeability of the three membranes. Since hydraulic flow resistance is a function of the square of the effective average pore radius, this would seem to indicate that the pore size in the three membranes is about the same with differences in swelling reflecting differences in the number of pores.

If P_N is assumed to obey the relationship

$$P_N = P_N^0 e^{-\Delta E^\ddagger / RT} \quad (\text{II-11})$$

A plot of $\log P_N$ vs. $1/T$ yields a straight line, the slope of which determines the activation energy, ΔE^\ddagger . For the three membranes studied here, these plots are linear except for the points at 55°C . The activation energies obtained are 2700, 3900, and 3100 cal./mole for I. E. C.'s of 1.65, 1.80 and 2.15 meq./g. l, respectively. These values are close to the activation energy for viscous flow of water, which is 3700 cal/mole. (33)

The above considerations show that the concept of tortuosity is a valid one in dealing with these systems and that Eq. (II-8) is useful in correlating membrane transport phenomena.

4.0 FACTUAL DATA (Cont'd)

4.2.5 Future Work

Data on electro-osmotic water transport is insufficient to report at this time. Work on this part of the program will be accelerated soon. In addition, vapor permeabilities and hydrodynamic permeabilities of other membrane systems will be determined.

4.0 FACTUAL DATA (Cont'd)

4.3 TASK III

KINETIC STUDY OF THE ELECTROCHEMICAL OXYGEN (AIR) REDUCTION

H. J. R. Maget

4.3.1 Introduction

Rates of cathodic oxygen reduction, that is cell currents, are dependent on partial pressures of the oxidant if rate-controlling steps involve the concentration or partial pressure of oxygen. This is likely to be observed since reaction rates will be either liquid film or gas diffusion controlled. However, cases can arise where removal of the reaction product may be hindered by slow transport processes, thus resulting in, possibly, appreciable lower rates. This could be the case of water removal from the catalyst surface of an oxygen electrode. If local current densities are either dependent on partial pressures of oxygen or water, it will become necessary to establish relationship predicting such local current densities and to design electrode geometries favorable to uniform current distribution, and as a result uniform distribution of the main influential variables affecting oxygen electrode performance.

The ultimate goal, that is, quantitative description of current-voltage relationships for an IEM/electrode structure as a function of main variables, can be attained from experimental studies, including at least:

- the determination of limiting current densities
- an attempt to establish the rate-controlling process for known electrode structures in the current density range corresponding to 0.85 - 0.5 volts
- the derivation of relationships describing the current-voltage behavior over practical operational ranges

Experimental results, as well as the equations derived to predict limiting local current densities for purely gas-diffusion controlled processes have been obtained during this period and will be discussed in the following three sections.

4.0 FACTUAL DATA (Cont'd)

4.3.2 Influence of oxygen partial pressure on limiting current densities of the oxygen/IEM electrode-electrolyte system.

4.3.2.1 Introduction

In establishing over-all oxygen electrode capabilities for fuel cell application, one of the important variables is the limiting current density. Although these limiting currents are not simply dependent on some limited parameters, i. e. electrode activity, electrode structure, electrolyte properties, local temperatures, anisotropic current density distribution, etc . . . , actual measurements are valuable if some reproducible characteristics can be controlled, i. e. catalytic activity, electrode structure, electrolyte properties. Thus, measurements are valuable for a specifically designed system. Such a system has been chose to be a Pt black electrode associated with a cationic exchange membrane as electrolyte. Measurements have been restricted essentially to room temperature operation, and to some specific humidity conditions.

4.3.2.2 Experimental Equipment and Procedures

Partial as well as limiting currents were obtained by applying manually set voltages by means of 300 and 2000 ma potentiostats. A Luggin capillary/SCE system is used as the reference electrode, the capillary tip being tightly held against the membrane. Such reference electrodes have been described and discussed elsewhere, (1). Due to the limited current output of the initially available potentiostat, and to expected high limiting currents at high partial pressures of oxygen, the circular wet-proofed electrodes had apparent areas of either 0.33 or 0.70 cm² (Figure III-1). These electrodes could be operated for forced flow conditions (Figure III 1 B-1) or as self-breathing device (Figure III 1 B-2). Larger wet-proofed electrodes (3.88 cm²) were operated as self breathing device in an enclosed environment in absence of forced flow and currents were measured by means of an 2000 mA Wenking potentiostat. Currents were recorded for short periods of time on a Leeds and Northrup Co. Speedomax G Recorder at chart speeds of about 30 cm/min. It was hoped that surface conditions regarding water partial pressure and accumulation would be unchanged during such short time intervals. Conditions surrounding the electrode were kept constant by placing the device into a constant temperature and humidity chamber (Aminco Climate-Lab). Electrode surface temperatures were measured by a fine Pt-Pt/Rh thermocouple, inserted into the electrode catalyst layer.

4.0

FACTUAL DATA (Cont'd)

Complete polarization curves could be obtained by this procedure and steady-state currents evaluated by extrapolation of current time curves to $t = 0$. Steady or quasi-steady state currents could be obtained approximately 15-25 seconds after the applied potential.

4.3.2.3 Experimental Results

Current Decay

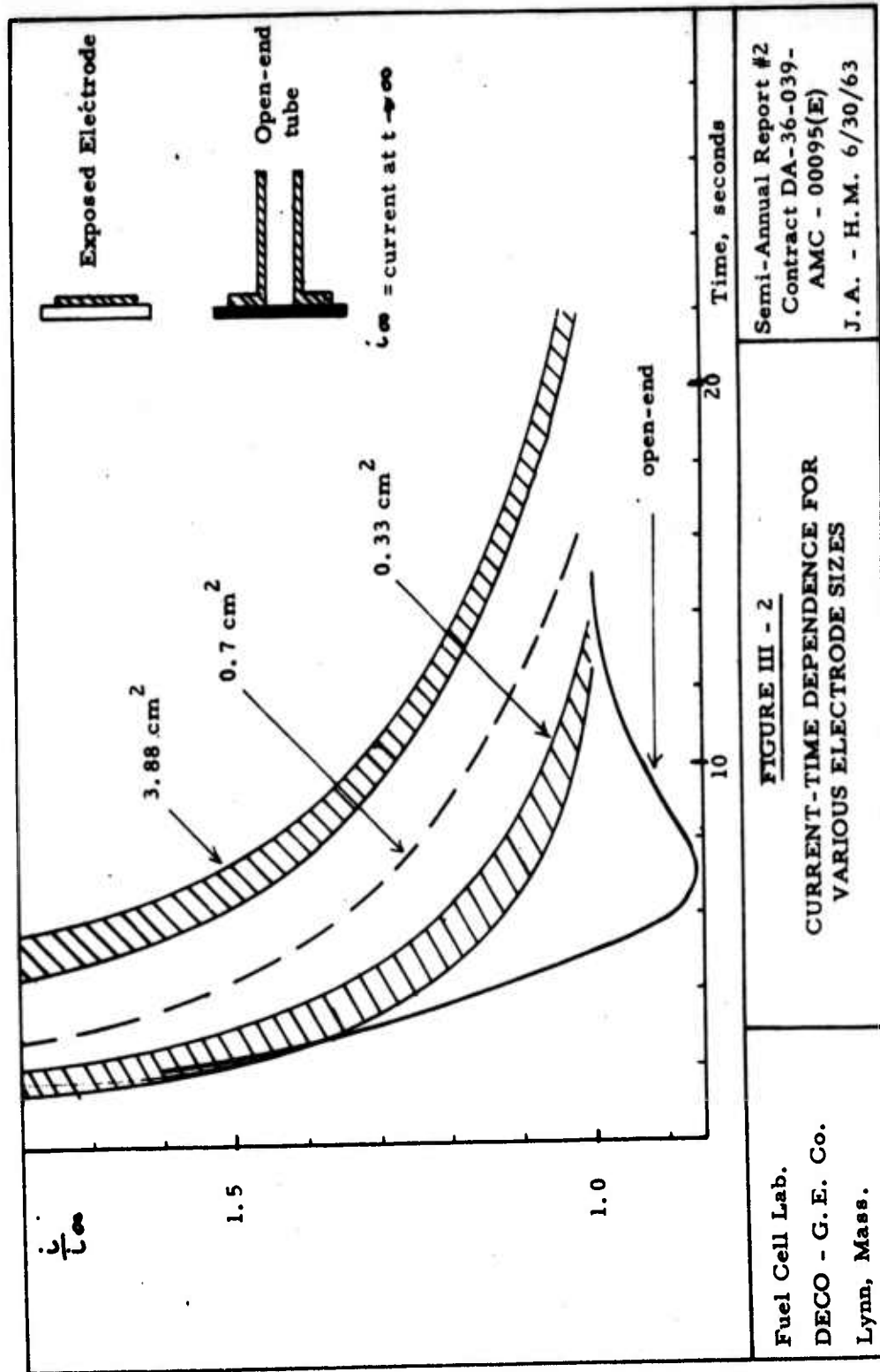
All experimental results obtained by applying fixed potentials displayed initially large "surge" currents. However, currents would decay rather rapidly, to steady state or quasi-steady state values. Steady state values reported in the following figures represent extrapolated values to $t = 0$ of the linear current-time functions. As expected, currents would increase with increased applied potentials up to certain limiting currents.

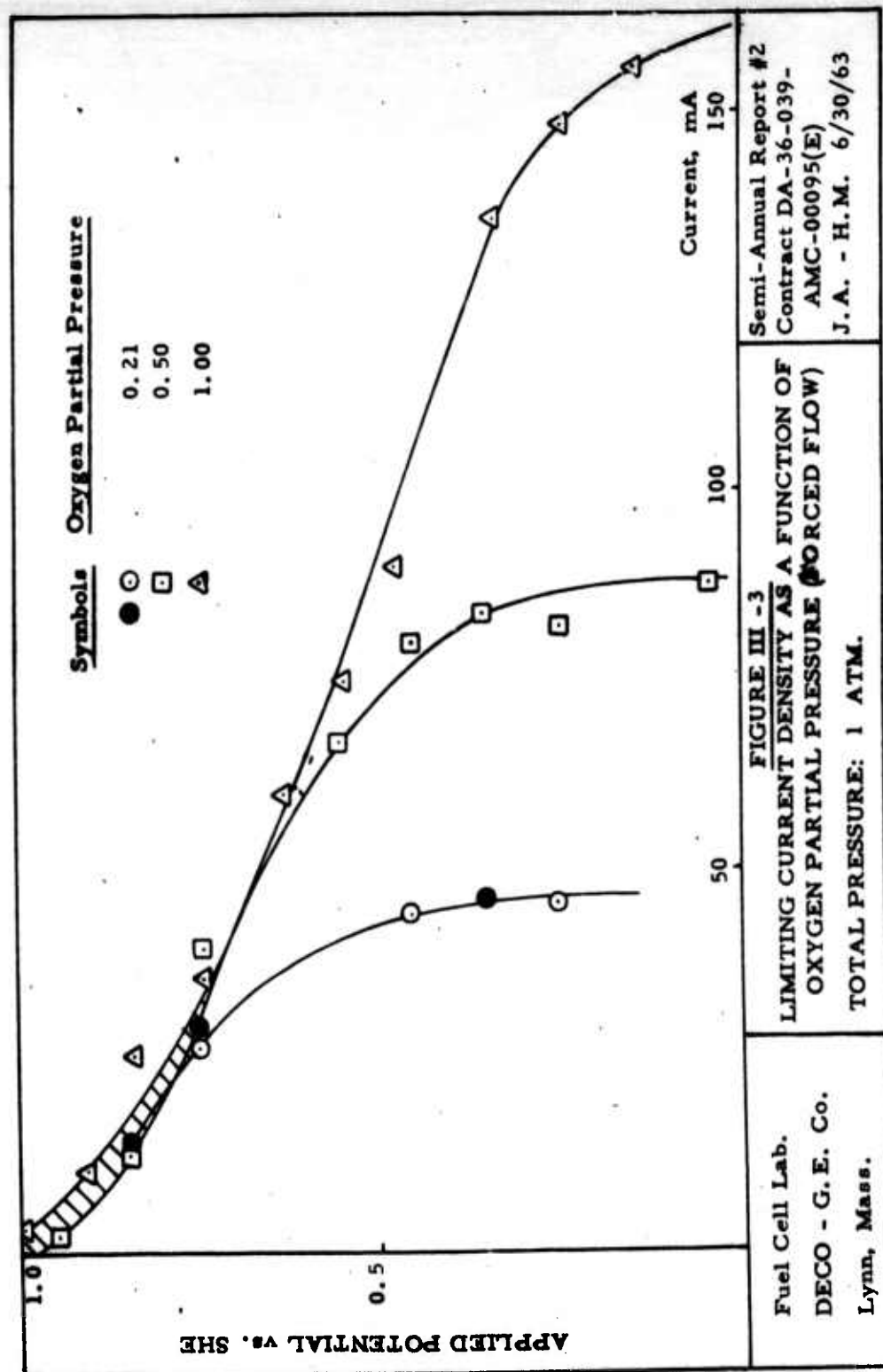
Attempts to correlate experimental results on the basis of classical equations for diffusional processes have not been successful. However, as represented in Figure III-2, rates of current decay seem to be dependent on electrode size, suggesting possibly contribution of radial diffusional processes over the electrode surface or in other words possibly variable diffusion layer thicknesses dependent on electrode geometry. An attempt to obtain analytical solution for purely gas diffusional processes will be discussed later. Current decays for open-end tube as represented in Figure III-2 suggest an induction period before steady state conditions are observed. This result could be obtained if the open-end tube creates initially a barrier to high diffusion rates followed by establishment of steady state conditions.

Electrode Polarization and Limiting Currents.

A. Forced Gas Flow Conditions

Limited experimental data are available for large flow rates over electrodes according to configuration 1B-1 (Figure III-1). These results indicate influence of gas flow as compared to self-breathing device. Such differences are associated with diffusional processes at the electrode surface. This phenomenon will be discussed in greater detail in the study of channel geometry influences. Limiting currents for air, 50 O₂/50N₂ and oxygen at 27°C and 1 atm. total pressure can be determined from Figure III-3. The following results were obtained:





FACTUAL DATA (Cont'd)

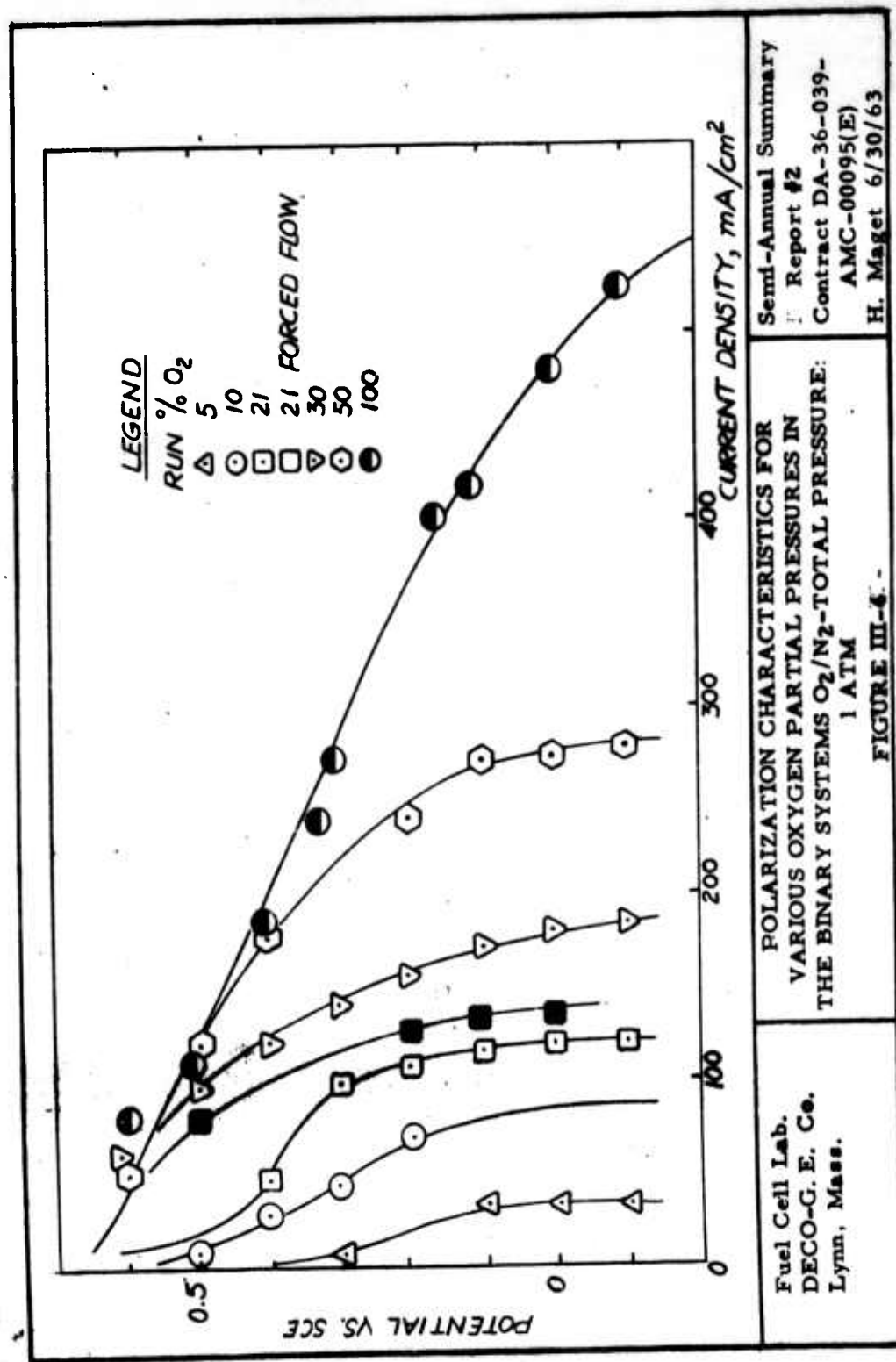
| Partial Pressure of Oxygen P_{O_2} | Limiting current $\text{mA/cm}^2, i_L$ | i_L/P_{O_2} |
|---|---|---------------|
| 0.21 | 140 | 670 |
| 0.50 | 260 | 520 |
| 1.00 | 540 | 540 |

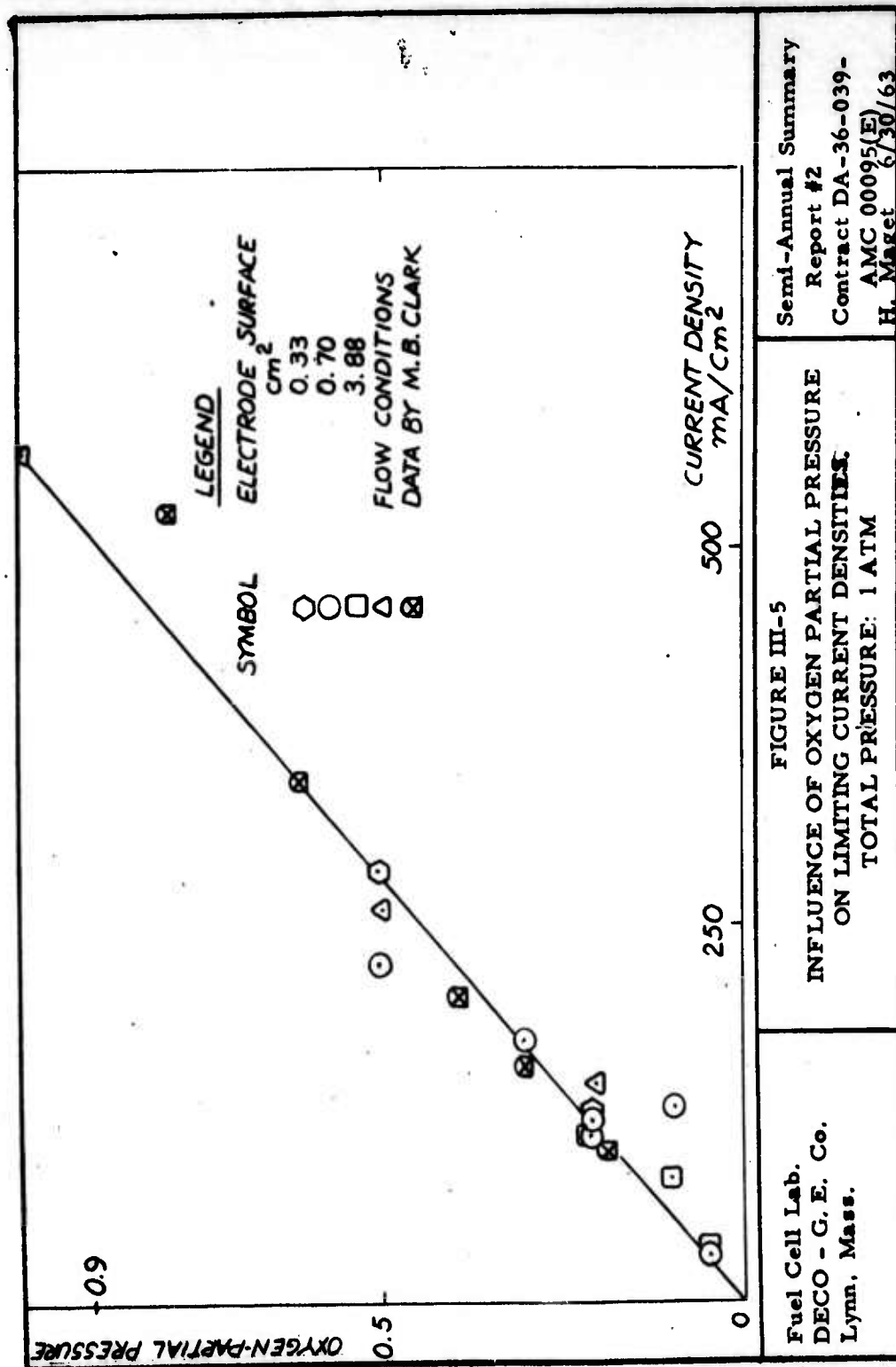
These results allow the following observations: 1) up to about 70 mA/cm^2 , the polarization curves behave almost identically and independently of the oxidant partial pressure and 2) limiting current densities are nearly proportional to oxygen partial pressures.

B. Self-Breathing Electrodes:

Since gas flow conditions are doubtlessly very influential on limiting current densities, most experimental results have been associated with non-flow conditions, on so-called self-breathing electrodes, configuration 1B-2 (Figure III-1). Results for air electrode polarization are reported in Figure III-4, where initially appreciable polarization can be observed only for low oxygen partial pressure and where air operated electrode under flow conditions yield results comparable to higher oxygen partial pressures for current densities up to about 70 mA/cm^2 . Figure III-5 represents quasi-linearity between limiting current densities and oxygen partial pressures. These results were obtained for three electrode sizes: 0.33, 0.70 and 3.88 cm^2 corresponding to electrode radii of 0.33, 0.47 and 1.1 cm, respectively.

Recent results reported by M. B. Clark, in the literature (34) on the influence of oxygen partial pressure on limiting current densities for carbon electrodes, indicate large deviation from linear relationships between i_L and P_{O_2} . In these alkaline electrolytes limiting current densities are about 2 times larger than for IEM, viz. 1200 mA/cm^2 against 550 mA/cm^2 for pure oxygen. However, limiting current densities are quasi-linear with P_{O_2} up to about 0.61 atm. and are identical to results obtained for the Pt black - IEM system. Since the compared systems are quite different, similitude in experimental results suggest a gas-diffusion controlled process, and deviation from such a mechanism in the case of pure oxygen.





4.0 FACTUAL DATA (Cont'd)

Influence of Electrode Temperature

Temperature effects have not been systematically investigated. However, for all measurements, fine-wire Pt/Pt-Rh thermocouples have been placed in the Pt-black electrodes and temperatures have been recorded. Qualitatively, temperature effects are appreciable, and limiting currents can double for temperature changes from about 25 to 60°C. Practically, this may suggest fuel cell operation under conditions such that heat transfer would allow electrode surface temperature elevations up to conditions compatible with membrane stability.

4.3.2.4 Influence of Total Pressure on Rates of Oxygen Reduction

Since total gas pressure is expected to affect limiting currents in a gas-diffusion controlled process (influence on the diffusion coefficient, partial pressure gradient) as well as in a liquid film controlling process (influence on the gas solubility, partial pressure gradients) experimental results were obtained to describe such affects with air at total pressures up to about 8 atm.

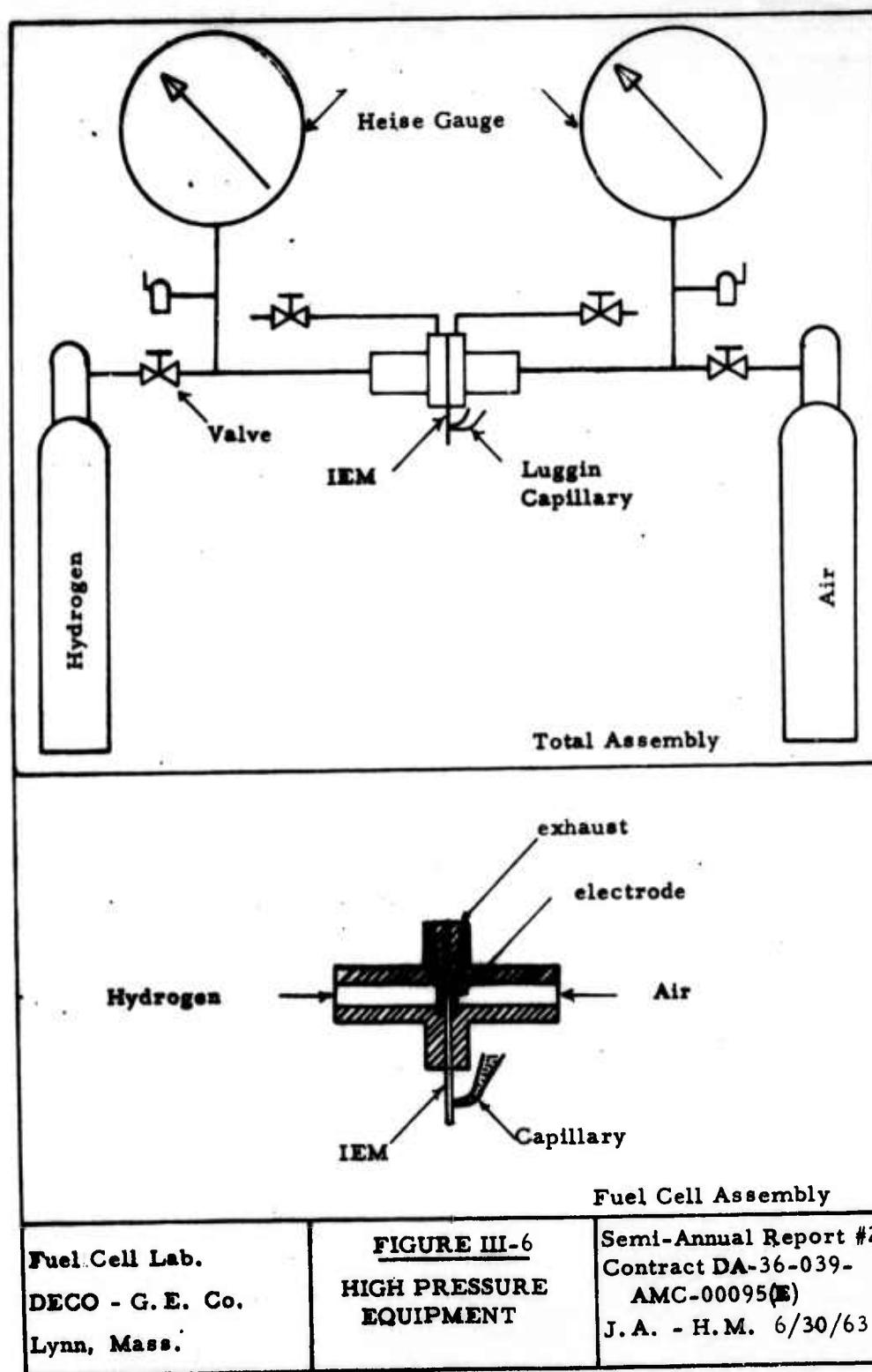
4.3.2.4.1 Experimental Equipment and Procedures.

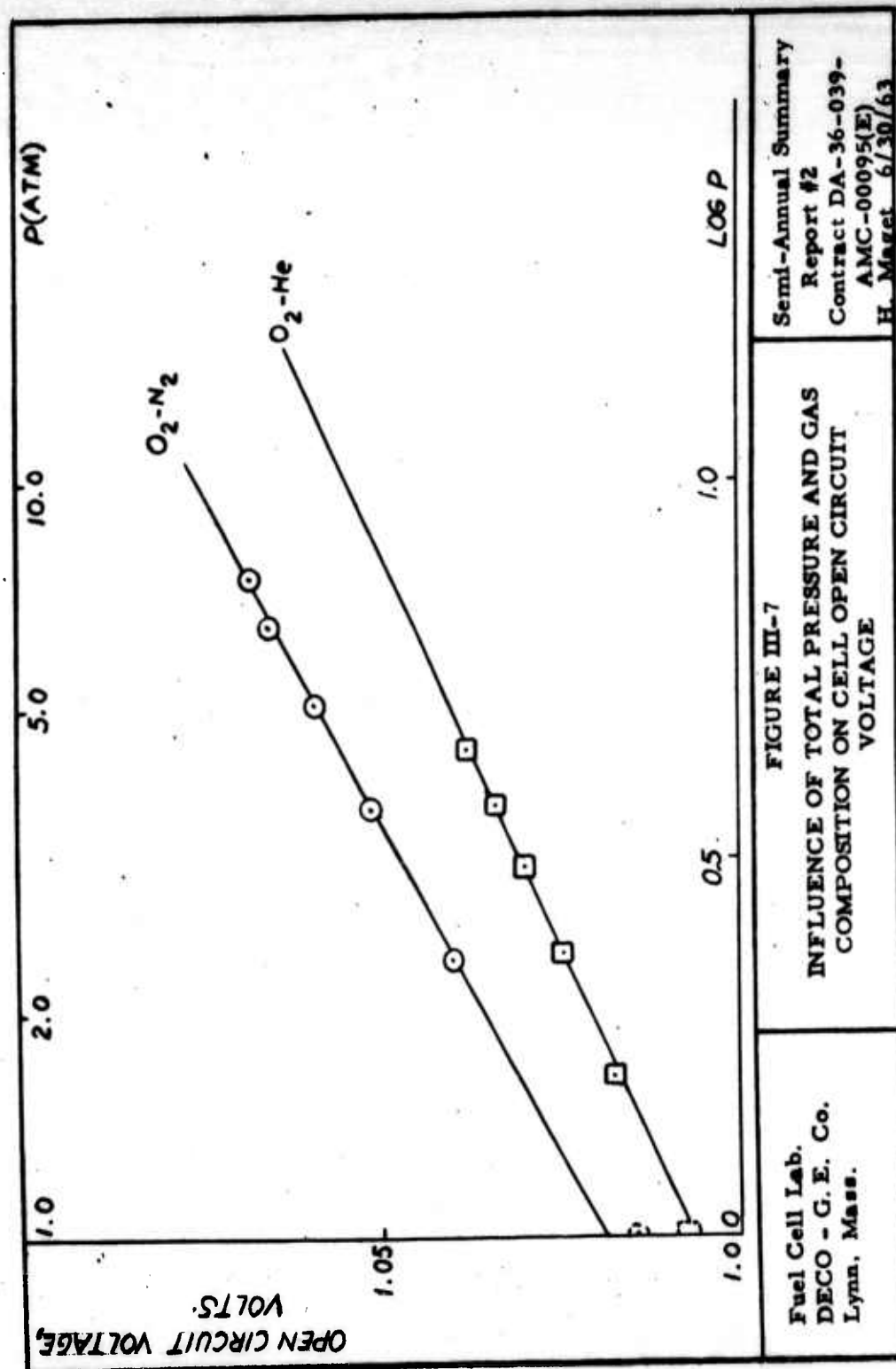
The experimental apparatus represented schematically in Figure III-6, was designed for operation up to 10 atm. total gas pressure. Gases were allowed to enter the two compartments at a rate such that pressure differences across the membranes were always less than 0.3 atm during pressurizing. Pressures could be read within 0.01 atm. By proper manipulation of exhaust valves, air was allowed to flow over the electrode at the operating pressure. A Luggin Capillary/SCE system was used as reference electrode. Such reference electrodes have been described elsewhere (1). The circular wet-proofed electrodes had an apparent area of 0.33 cm². Time-dependent currents were recorded at chart speeds up to 30 cm/min., for various potentials applied manually by means of a 2000 mA Wenking potentiostat.

4.3.2.4.2 Experimental Results

Open Circuit Voltage

Open circuit voltages recorded on the same complete fuel cell as a function of total pressure and for two gas composition are represented in Figure III-7. A logarithmic function of total pressure vs. OC/V





Semi-Annual Summary
Report #2
Contract DA-36-039-
AMC-00095(E)
H. Maget 6/30/63

FIGURE III-7
INFLUENCE OF TOTAL PRESSURE AND GAS
COMPOSITION ON CELL OPEN CIRCUIT
VOLTAGE

Fuel Cell Lab.
DECO - G. E. Co.
Lynn, Mass.

4.0

FACTUAL DATA (Cont'd)

yields linear relations for both systems, suggesting the following pressure dependence in the case of air:

$$E = E_0 + 0.056 \log P \quad (\text{III-1})$$

where

$$E = OC/V$$

$$E_0 = OC/V \text{ at } P = 1$$

P = gas pressure in atm. at the air cathode and H_2^+ anode

Limiting Current Densities

On Ag in acidic and neutral media, Krasilschchikov (35) has shown the relationship:

$$i = -\lambda_- [O_2] e^{-\frac{(1-\alpha)F}{RT} \epsilon} \quad (\text{III-2})$$

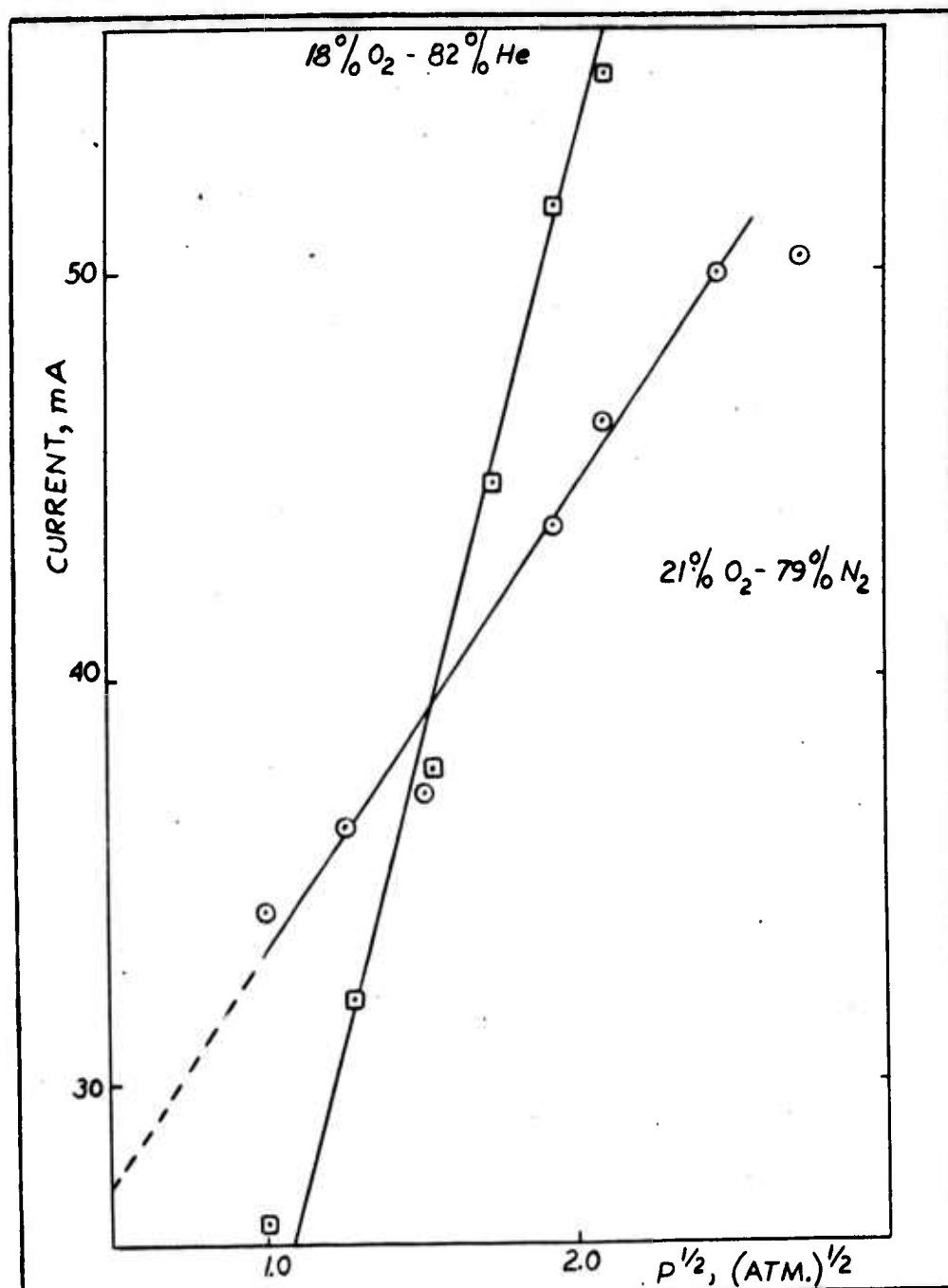
(where $\alpha = 0.5$) to hold between 0.21-70 atm. This result was supported by Winkelmann (36) for bright Pt. M. B. Clark (34) reports linear relationships between i_L and P^{-1} , (inverse of total pressure). Results obtained on IEM/Pt black systems have yielded linear relationship between i_L and \sqrt{P} . The slope for 21% O_2 -79% N_2 , Figure III-8, correspond to $0.011 \text{ Amp-atm}^{-1/2}$. In order to show possible effects of bulk diffusion coefficients, a binary gas system was chosen displaying much larger diffusion coefficient, i. e. $0.75 \text{ cm}^2/\text{sec.}$ at 27°C for $He-O_2$ (37) as compared to $0.25 \text{ cm}^2/\text{sec.}$ (38) for N_2-O_2 mixtures. Since diffusion coefficients are inversely proportional to total pressure and nearly independent on gas composition, the slope of $0.030 \text{ Amp. -atm}^{-1/2}$ for O_2 -He could be expected as compared to air. Although general trends in variations of limiting currents can be explained, it remains mandatory to obtain quantitative interpretations.

4.3.2.5 Discussion

Equations derived in Appendix III-1 for rate-controlled diffusional processes in the gas bulk, i. e.

$$I = 4\pi n F D b c^0 \sum_{m=1} \frac{1}{\lambda_m} \quad (\text{III-22})$$

INFLUENCE OF TOTAL PRESSURE ON LIMITING CURRENTS
FOR TWO BINARY GAS SYSTEMS-ELECTRODE SURFACE: 0.32cm²



Fuel Cell Lab.
DECO - G. E. Co.
Lynn, Mass.

FIGURE III-8

Semi-Annual Summary
Report #2
Contract DA-36-039-
AMC-00095(E)
H. Maget 6/30/63

4.0

FACTUAL DATA (Cont'd)

for gas-controlled diffusion in the pores

$$I(\text{pore}) = 4\pi nFD_e b c_o \sum_{m=1}^{\infty} \frac{\cosh(\lambda_m h/b) - 1}{\lambda_m \sinh(\lambda_m h/b)} \quad (\text{III-27})$$

and for liquid phase controlled diffusion:

$$I = nFS(D_e c_o i_o / k)^{1/2} e^{\frac{\alpha_n F}{RT} \eta} \quad (\text{III-35})$$

yield results too large to justify a process described by Eqn. III-22. However, rate-controlled processes in the pores could be either gas diffusion-controlled (Eqn. III-27) and will depend essentially on D_e and b , if (h/b) is large, or liquid film controlled, to become dependent on $D_e^{1/2}$ and the gas solubility $C_o^{1/2}$ in the thin film. It is not possible, presently, to make a definite distinction between these two transport mechanisms in order to explain experimental results. However, it will be shown in the case of oxygen (air) reduction in restricted channels that bulk diffusional processes may become small enough to justify observed local limiting current densities as compared to more complex pore-diffusion controlled transport rates.

4.3.3 Self-Breathing Air Electrodes4.3.3.1 Introduction:

Since it may be considered as a fact that "... fuel cells must be made to operate on air before commercial applications can be contemplated", (39) and since it has been shown previously that limiting current are essentially proportional to oxygen partial pressure in the oxidant stream, it becomes imperative to measure and possibly understand polarization losses incurred in practical air electrodes. Such losses could be minimized by compressing the air. However, compressors could only be justified for "fuel cells with power output of the order of 100-200KW" (39). For smaller unit to be operated at atmospheric pressure, careful air channel and air electrode design will be required in order to minimize diffusion polarization.

The purpose of the present work was to obtain experimental results and interpretation to explain polarization in channels of defined geometry and to establish influential parameters which would affect electrode performance. In order to establish applicability of a self-breathing air electrode, viz. without forced convective air-flow, for low current densities, experimental investigations were started on straight

4.0 FACTUAL DATA (Cont'd)

air channels. Furthermore, since such a self-breathing electrode had to operate away from limiting currents, in order to minimize diffusion polarization, additional work for forced flow (at various air flow rates) was conducted in straight air channels.

4.3.3.2 Experimental Equipment

Partial as well as limiting currents were obtained by applying manually set voltages by means of a 300 Ma Wenking potentiostat. A Luggin Capillary/SCE system is used as the reference electrode, the capillary tip being tightly held against the membrane. Such reference electrodes have been discussed and described elsewhere(1).

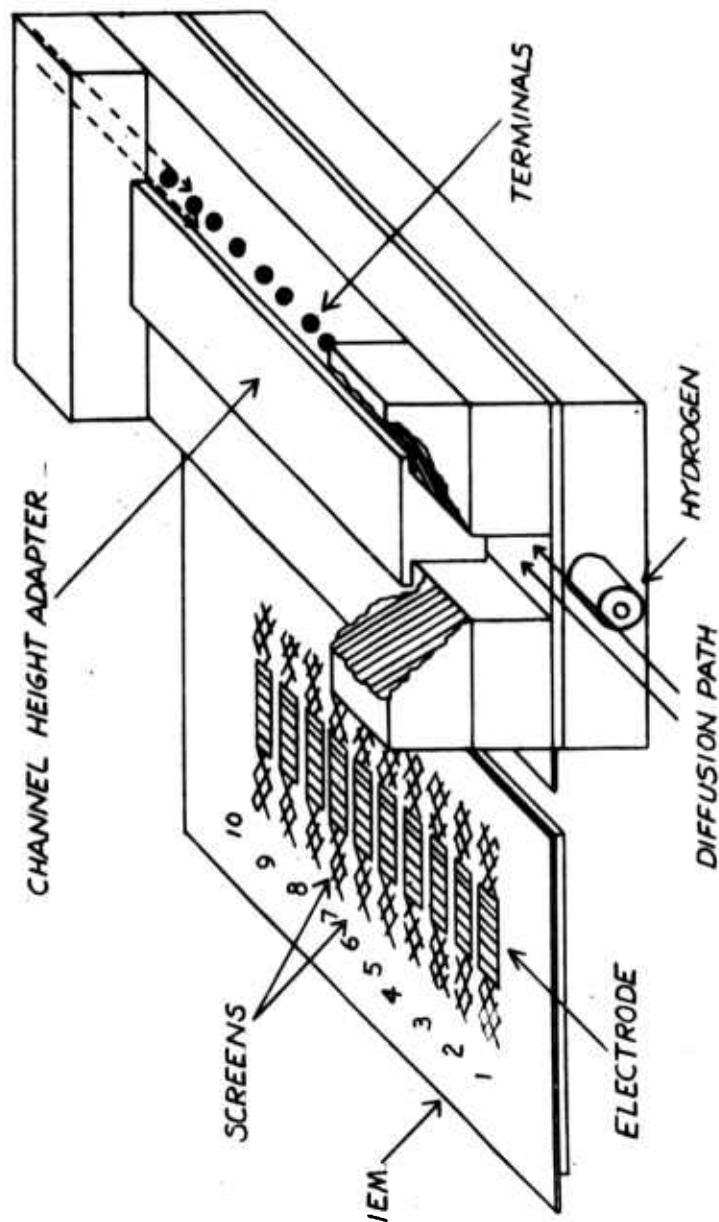
Additional investigations were undertaken for galvanostatic measurements. The equipment is represented in Figure III-9. Identical reference electrodes were used.

All experimental work was conducted on air channels 2-1/2" long and 1/2" wide. Channel height could be varied by changing a removable Lucite bar placed on the channel top. Thus, channel heights could be 1/16, 1/8, 1/4 and 1/2". The channel was mounted on an air electrode and placed in a large Lucite box in order to avoid small air flow sweeps over the air electrode.

In order to determine local current densities, the air electrode was manufactured by placing ten parallel electrode/screen strips on a GPS-Ion Exchange Membrane. (Electrode position is described in Figure III-9.) Gaps of 1/16" between electrodes allowed for electrical insulation of the various electrodes. Electrode dimensions were 1/2" x 3/16" with an actual area of $0.60 \pm 0.05 \text{ cm}^2$. The IEM extended out of the channel for reference potential measurements and stainless rods contacted the screens for current pick-up.

The counter electrode (H₂-electrode) was prepared in a similar manner. Catalytic electrodes faced each other across the electrolyte (membrane).

The two ends of the self-breathing channel were open, thus displaying planar symmetry on either side of the channel center cross-section. Closing one channel end actually corresponded to doubling the channel length.



Semi-Annual Summary
Report #2
Contract DA-36-039-
AMC-00095(E)
H. Maget 6/30/63

FIGURE III-9
EXPERIMENTAL DEVICE FOR MEASUREMENTS
OF LOCAL CURRENTS IN AIR CHANNELS OF
VARIABLE GEOMETRY

Fuel Cell Lab.
DECO - G.E. Co.
Lynn, Mass.

4.0 FACTUAL DATA (Cont'd)

4.3.3.3 Experimental Results

1. Individual Electrode Polarization

Experimental electrode polarizations are presented in Figures III-10 and III-11 for various channel heights. The following general observation regarding these figures can be made:

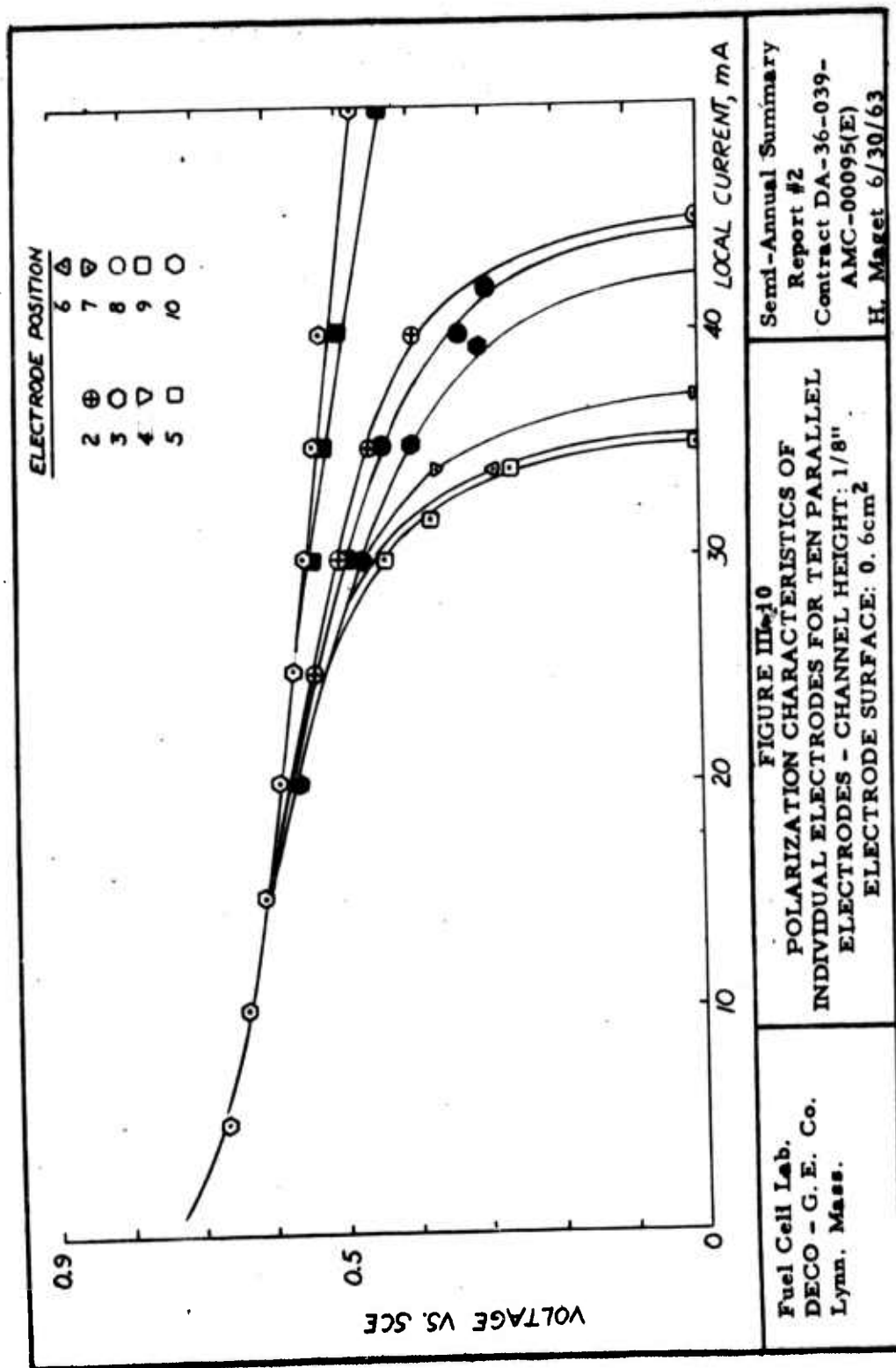
a. polarization characteristics are almost identical for all electrodes for current densities up to about 25 ma/cm^2 for a channel height of $1/8''$, although the initial slope of the I-V curves are not all identical.

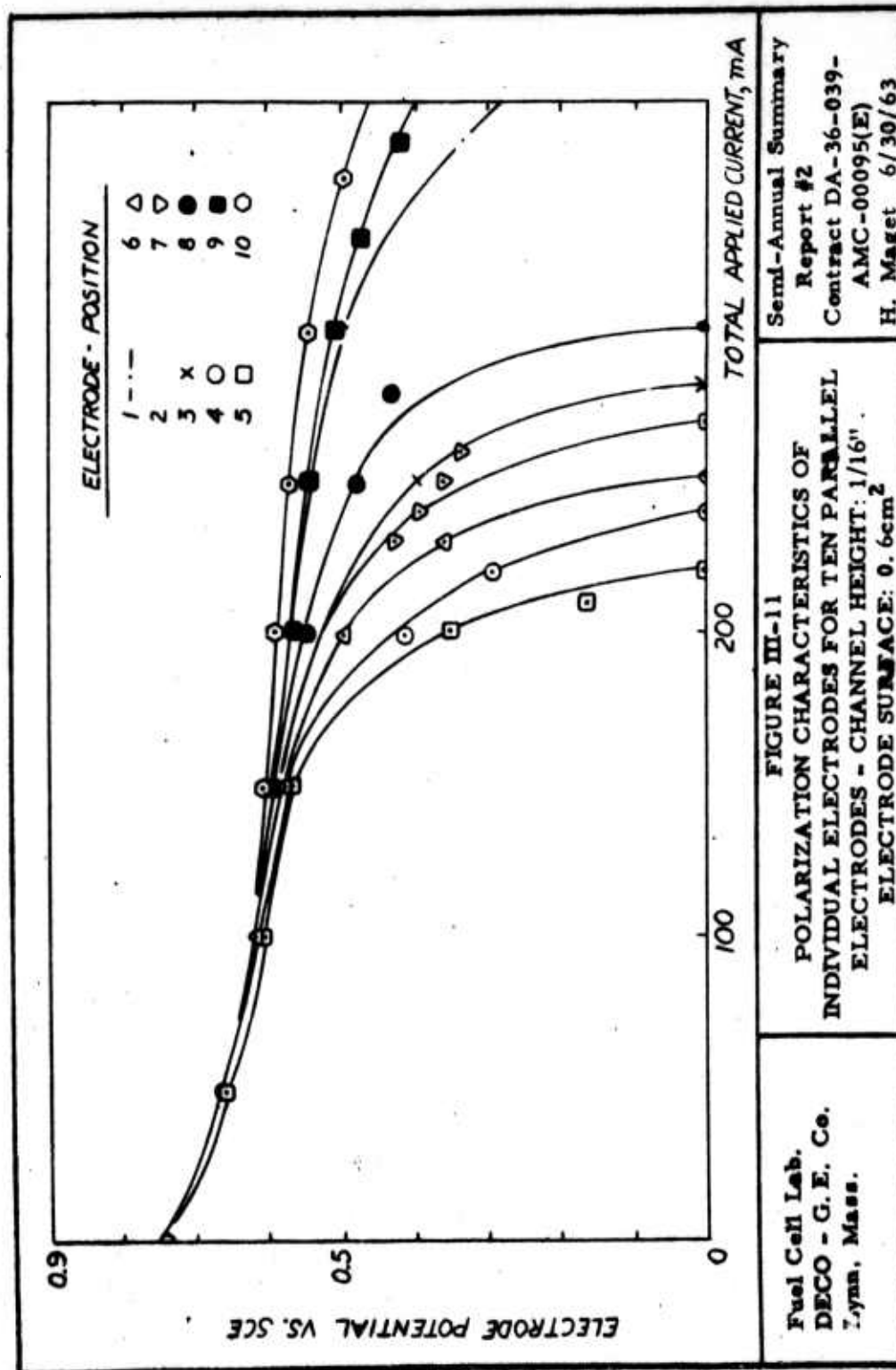
b. limiting currents are larger (in essence the limiting current for exposed electrodes) for terminal electrodes (1 and 10) than other electrodes and limiting currents decrease harmoniously from terminal to central electrodes.

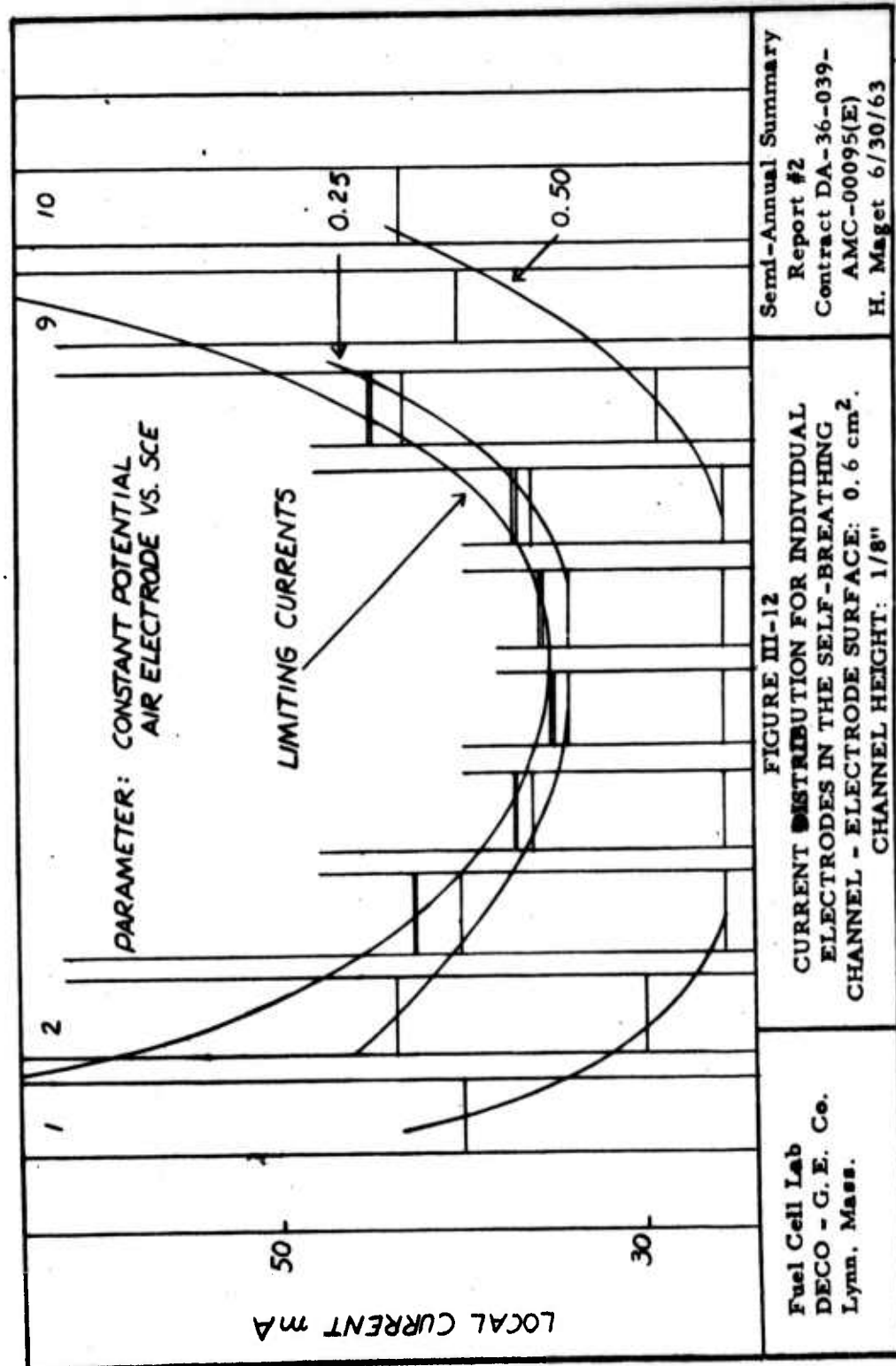
c. central electrodes 5 and 6 display minima in current densities as expected from consideration of central planar symmetry.

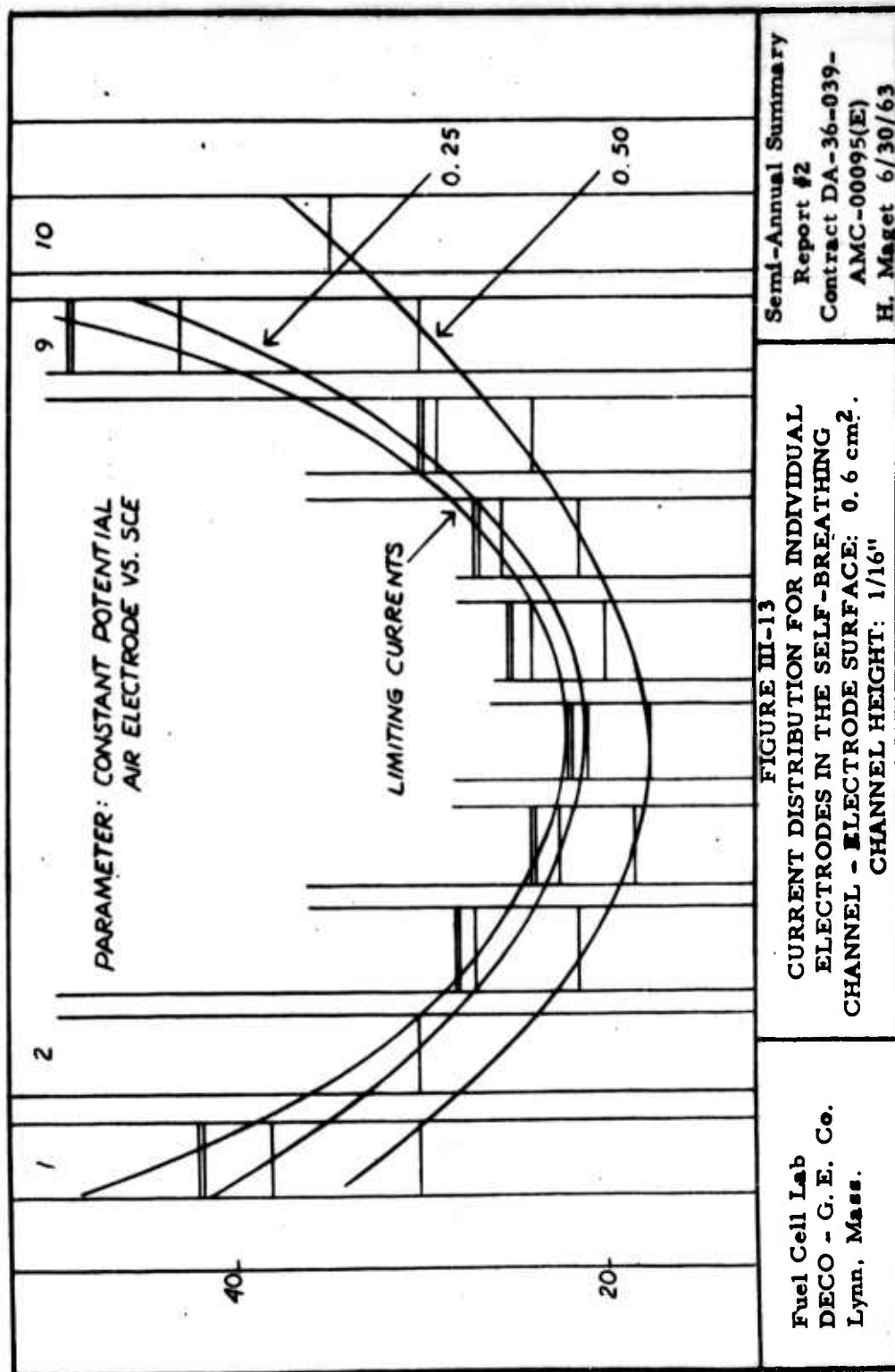
d. channel height affects performance to a large degree, i. e. limiting currents for inner electrodes are 22mA and 35mA for channel heights of $1/16''$ and $1/8''$ respectively. These current densities, i. e. 37 and 60 Ma/cm^2 , correspond to oxygen partial pressures of about 0.07 and 0.1, respectively. No appreciable polarization is observable for channel height $\geq 0.64 \text{ cm}$ ($1/4''$).

e. for identical polarization potentials (as determined for polarization curves) current density distributions display minima for inner electrodes and can be extrapolated to edge values of limiting currents as determined from previous measurements. Strictly speaking, these current densities cannot be described from Figures III-10 and III-11. However, the partial pressure of oxygen in the channel would not be too greatly affected at higher current corresponding to limit currents of the edge electrodes. Results would be affected greatly at the edge electrodes, let's say electrodes 1 and 2 and their corresponding symmetrical position. Current density distributions for channel heights of $1/8$ and $1/16''$ for various applied potentials are represented in Figures III-12 and III-13. Edge currents (about 80mA) can become 2 to 4 times larger than center channel currents, but display much more uniform distribution for lower electrode polarization, i. e. 0.5 volts vs. SCE for $1/8''$ channel.









Interpretation of Individual Polarization Curves

Current potential behavior for the investigated systems can be represented by the following Figures:

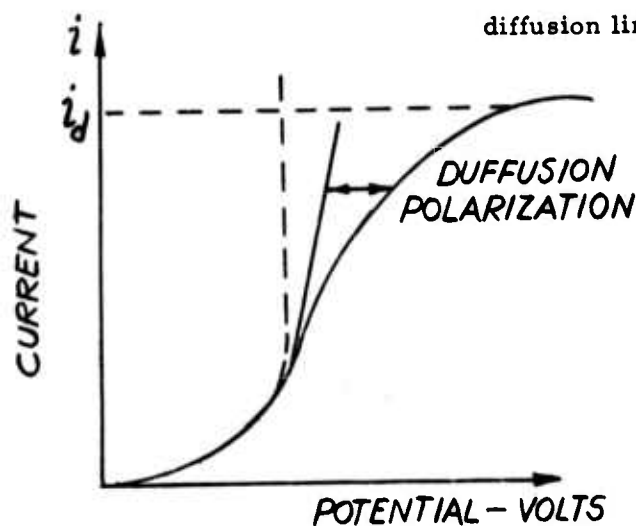


FIGURE A

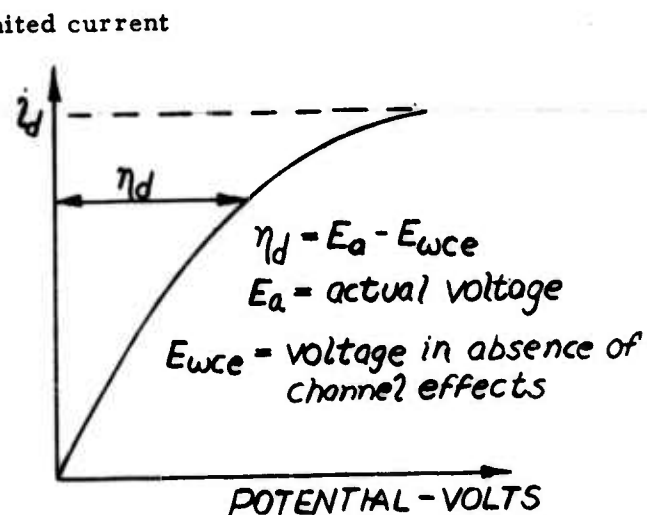


FIGURE B

Figure A represents polarization characteristics as observed in absence of diffusion polarization (probably activation polarization, in absence of ohmic contribution, which are generally eliminated). Figure B represents strictly diffusion polarization terms in absence of other possible polarization.

Polarization characteristics can be represented by the equation:

$$\left(1 - \frac{i}{i_L}\right) = e^{\alpha(E^0 - E)} \quad (\text{III-3})$$

where i and i_L represent actual and limiting currents, respectively; $\alpha = \frac{nF}{RT}$, E^0 = reference potential in absence of channel polarization, $E^0 - E = \eta_d$

$$\ln(1 - i/i_L) = \alpha(E^0 - E) = \alpha\eta_d \quad (\text{III-4})$$

By differentiation:

$$\frac{dE}{di} = \frac{1}{\alpha i_L (1 - i/i_L)} \quad (\text{III-5})$$

with

$$\left(\frac{dE}{di}\right) \rightarrow \infty \text{ as } i \rightarrow i_L$$

and

$$R_d = \left(\frac{dE}{di}\right)_{i=0} = \frac{1}{\alpha i_L} \quad (\text{III-6})$$

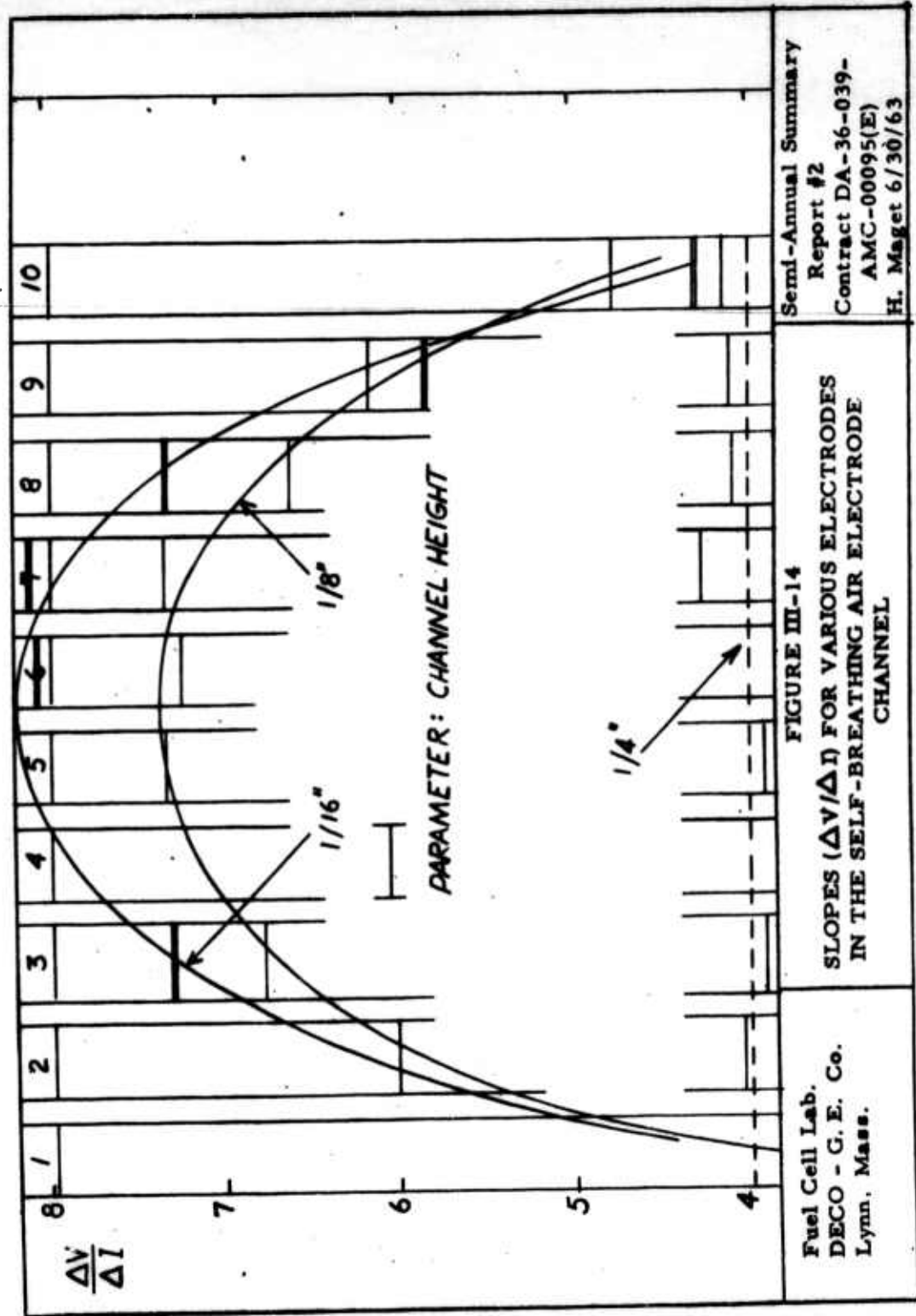
Since $i_L(x)$ displays a monotonous decrease up to channel center, equation III-6 is expected to display an increase from channel edge to center. Figure III-14 represents smoothed experimental results for 1/4, 1/8 and 1/16" channel heights. Since no additional position-dependent polarization was observed for $y_0 = 1/4"$, the value of $R_d = 4$ was chosen as reference systems resistance to obtain a relationship between channel-induced diffusion resistance $R_d(x)$ and $i_L(x)$. Now, in equation III-6, the slope (dE/di) defined as diffusional resistance becomes dependent of α and i_L . (If i_L can be determined analytically and since α represents defined constants, (dE/di) is defined.) Equation III-6, if represented by $\left(\frac{1}{i_L}\right) / \left(\frac{\Delta V}{\Delta i}\right)_{\text{exp}}$ should yield a constant value, determining α .

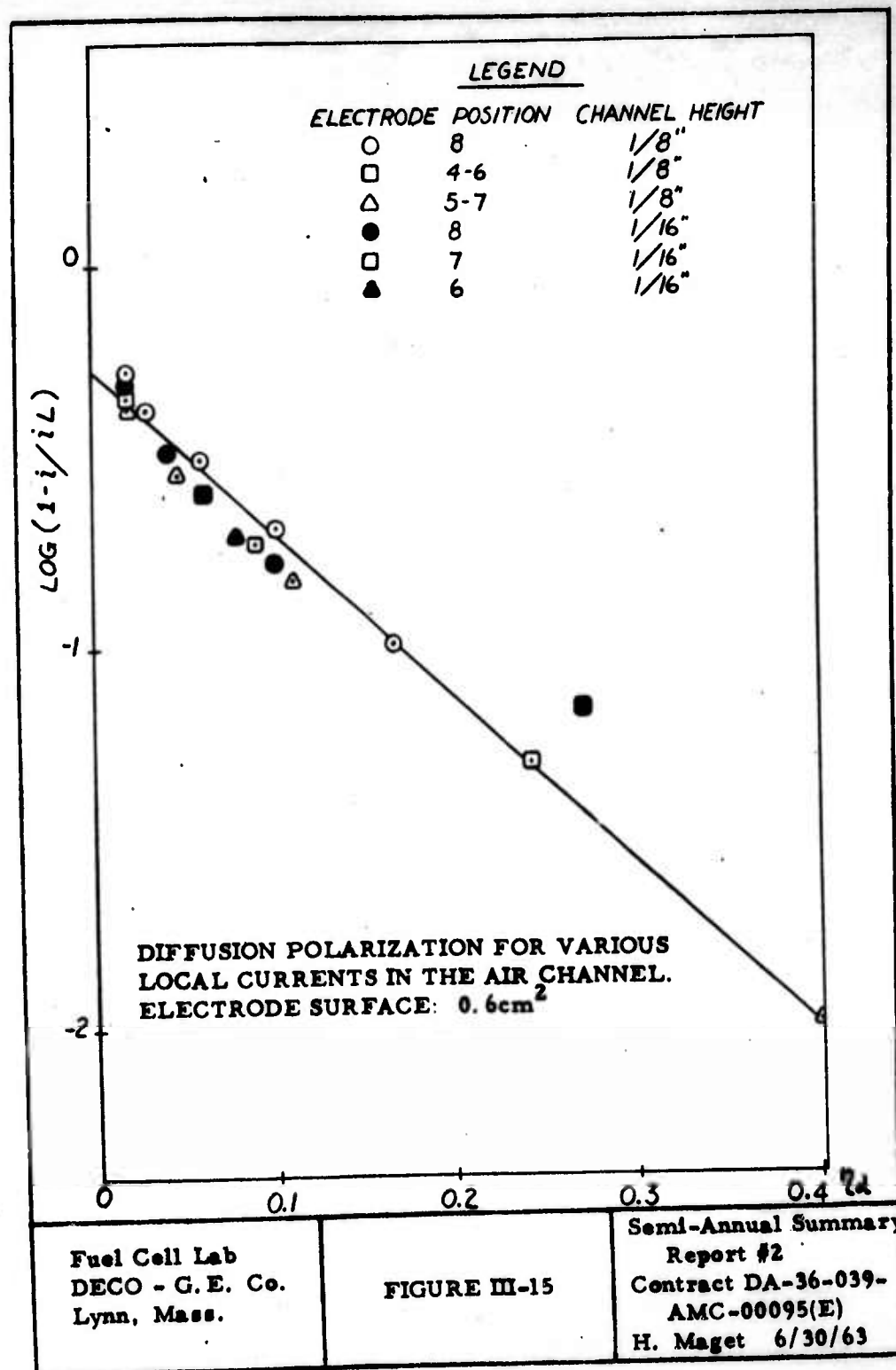
. $\Delta V/\Delta i$ representing the diffusional resistance should display:

- a. no diffusional resistance at the edges, at least as related to electrode geometry
- b. maximum diffusional resistance for center electrodes
- c. increased resistance for reduced channel cross-section.

Experimental results regarding these observations are represented in figure III-15 for channel heights of 1/8 and 1/16", and different electrode positions.

Table III-1 represents results obtained for 1/8" and 1/16" channel heights.





4.0

FACTUAL DATA (Cont'd)

TABLE III-1

Determination of α from experimental data

| Electrode Position | Limiting Current, i_L Amps | $\frac{1}{i_L}$ (Amps) ⁻¹ | $\left(\frac{\Delta V}{\Delta I}\right)_{\text{exp.}}$ (ohm) | $\left(\frac{\Delta V}{\Delta I}\right)^{-R}$ (ohm) | $\frac{1}{(\Delta V/\Delta I - R)}$ (Volt) ⁻¹ |
|------------------------------------|------------------------------------|---|---|--|---|
| <u>Channel Height</u> <u>1/16"</u> | | | | | |
| 1 | 0.041 | - | - | - | - |
| 2 | - | - | - | - | - |
| 3 | 0.028 | 35.8 | 7.3 | 3.3 | 10.8 |
| 4 | 0.024 | 41.7 | 7.8 | 3.8 | 11.0 |
| 5 | 0.022 | 45.5 | 8.2 | 4.2 | 10.8 |
| 6 | 0.025 | 40.0 | 8.1 | 4.1 | 9.8 |
| 7 | 0.027 | 38.0 | 7.9 | 3.9 | 9.7 |
| 8 | 0.030 | 33.3 | 7.3 | 3.3 | 10.1 |
| 9 | 0.050 | 20.0 | 6.1 | 2.1 | 9.6 |
| 10 | - | - | - | - | Average $\alpha = 10.2$ |
| <u>Channel Height</u> <u>1/8"</u> | | | | | |
| 1 | - | - | - | - | - |
| 2 | 0.045 | 22.2 | 6.0 | 2.0 | 11.1 |
| 3 | 0.043 | 23.2 | 6.7 | 2.7 | 8.6 |
| 4 | 0.037 | 27.0 | 7.1 | 3.1 | 9.0 |
| 5 | 0.035 | 28.6 | 7.3 | 3.3 | 8.7 |
| 6 | 0.035 | 28.6 | 7.3 | 3.3 | 8.7 |
| 7 | 0.037 | 27.0 | 7.1 | 3.1 | 9.0 |
| 8 | 0.044 | 22.7 | 6.8 | 2.8 | 8.2 |
| 9 | - | - | - | - | - |
| 10 | - | - | - | - | Average $\alpha = 9.0$ |

Evaluation of the Limiting Current.

The analytical evaluation of i_L (K) will allow to describe the polarization curves means of Equation III-6. Local limiting currents can be evaluated by solving Laplace's equation, providing transport by convection is considered to be negligible. Detailed calculations are presented in Appendix III-2.

The concentration distribution for oxygen and water in the channel are represented by:

$$C_{O_2} = C^0 \left[1 - \sum_{n=1}^{\infty} A_n \sin \alpha_n x (\cosh \alpha_n y - \tanh \alpha_n y_0 \sinh \alpha_n y) \right] \quad \text{(III-7)}$$

and

$$C_w = \sum_{n=1}^{\infty} A_n \sin \alpha_n x \left[\frac{g(T) - f(T) \cosh \alpha_n y_0}{\sinh \alpha_n y_0} \sinh \alpha_n y - f(T) \cosh \alpha_n y \right] \quad \text{(III-8)}$$

where C_{O_2} and C_w represent local concentration of oxygen and water.

C^0 = oxygen partial pressure at channel inlets.

$g(T)$ and $f(T)$ represent partial pressures of water under equilibrium conditions at $y = y_0$ and $y = 0$, respectively.

y_0 = channel height

$$A_n = \frac{(-1)^{n-1}}{b \alpha_n} \quad \text{and} \quad \alpha_n = \frac{n\pi}{2b}$$

Local current densities can be evaluated from:

$$j(x) = -n'FD \left. \frac{dC_{O_2}}{dy} \right|_{y=0} \quad \text{(III-9)}$$

and total channel current from:

$$I = \int_S j(x) ds = W \int_0^{2b} j(x) dx \quad \text{(III-10)}$$

I = total channel current

$j(x)$ = local current density

W = channel width

Equations can be derived for diffusion of oxygen or water vapor through the ternary gas system.

4.0

FACTUAL DATA (Cont'd)

Calculated local current densities, thus become:

$$j(x)_{O_2} = \frac{8n'FD_0C^0}{b} \sum_{n=1,3..} \sin \alpha_n x \tanh \alpha_n y_0 \quad (III-11)$$

and:

$$j(x)_w = \frac{2n'FD_w h(T)}{b} \sum_{n=1,3..} \sin \alpha_n x \left[\frac{1 - \cosh \alpha_n y_0}{\sinh \alpha_n y_0} \right] \quad (III-12)$$

where:

- n' = number of equivalent/mole ($n' = 4$ for O_2 and $n' = 2$ for H_2O)
- F = Faraday constant = 96,500
- D = Diffusion constant of species i in the gas medium
- $2b$ = Channel length (6.35cm)
- y_0 = Channel height 0.32 and 0.16 cm

Equation III-12 has been obtained for $g(T) = f(T) = h(T)$

Application to specific environmental conditions

For operation with air, equation III-11 becomes:

$$j(x)_{O_2} = 0.235 \sum_{n=1,3} \sin \left(n\pi \frac{x}{2b} \right) \tanh \left(n\pi \frac{y_0}{2b} \right) \quad (III-13)$$

$$j(x)_w = 0.031 \sum_{n=1,3} \sin \left(n\pi \frac{x}{2b} \right) \left[\frac{1 - \cosh \alpha_n y_0}{\sinh \alpha_n y_0} \right] \quad (III-14)$$

Equation III-13 and III-14 are based on

$$D_{O_2} = 0.21 \text{ cm}^2/\text{sec}$$

$$D_w = 0.29 \text{ cm}^2/\text{sec}$$

$$h(T) = 30\text{mmHg (vapor pressure of water at } 30^\circ\text{C)}$$

Some calculated data are presented in Table III-2 for a channel height of $1/16'' = 0.16 \text{ cm}$.

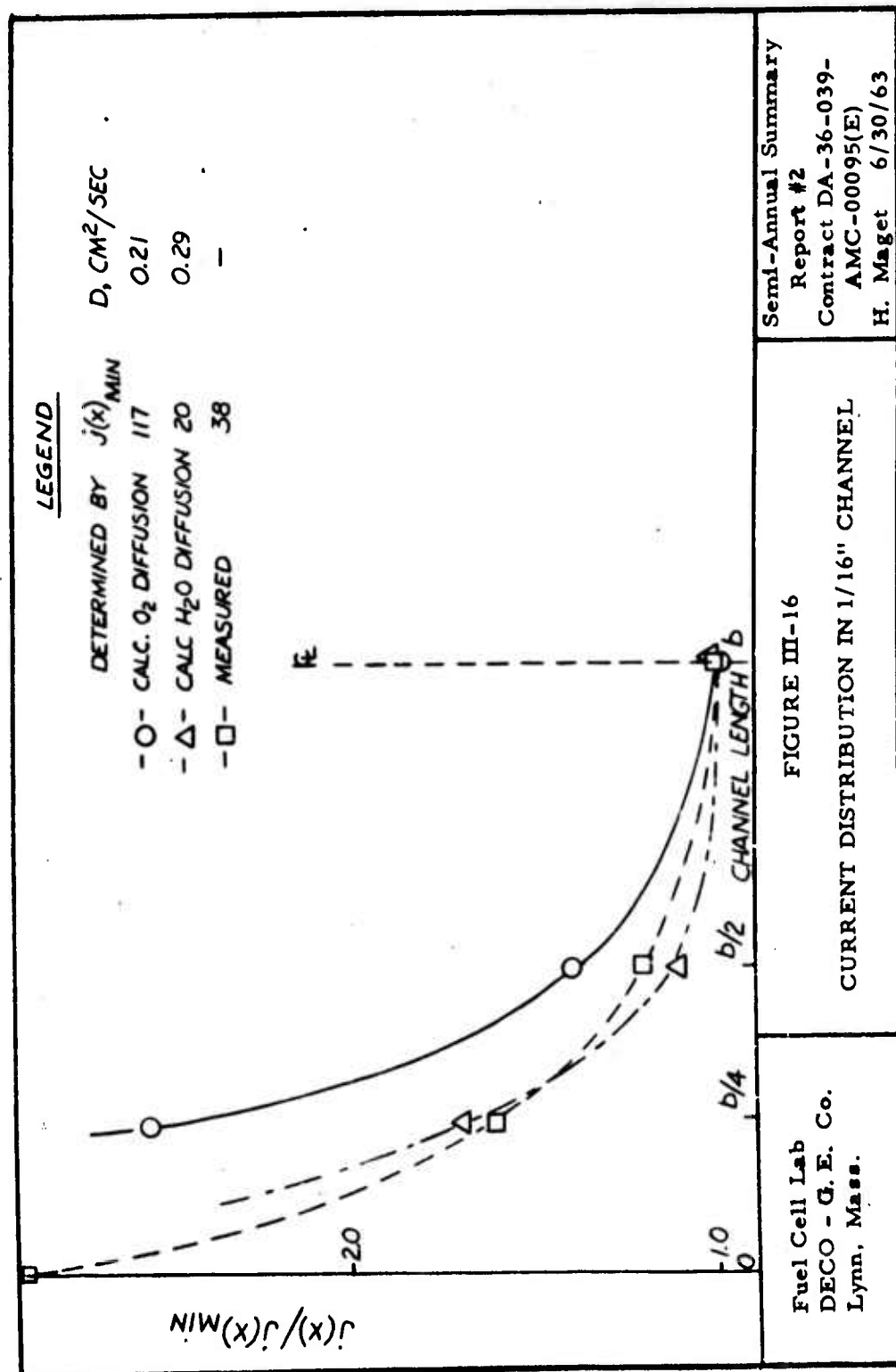
4.0 FACTUAL DATA (Cont'd)

TABLE III-2

Local Current Density for 1/16" Channel Height

| | Position | Local Current Density $j(x)$ in mA/cm ² | $j(x)/j(x) \text{ min.}$ | Minimum Current Density $j(x) \text{ min.}$ |
|------------------|----------|---|--------------------------|---|
| Oxygen Diffusion | b | 117 | 1.0 | |
| | b/2 | 163 | 1.41 | 117 |
| | b/4 | 298 | 2.5 ^c | |
| Water Diffusion | b | 20 | 1.0 | |
| | b/2 | 22 | 1.1 | 20 |
| | b/4 | 35 | 1.7 | |
| Measured | b | 38 | 1.0 | |
| | b/2 | 44 | 1.2 | 38 |
| | b/4 | 61 | 1.6 | |
| | 0 | 110 | 2.9 | |

Calculated and experimental results are presented in Figure III-16 for the 1/16" channel and for fixed diffusion coefficients. Data can be represented fairly well by assuming a water diffusion-controlled process.



4.0 FACTUAL DATA (Cont'd)

4.3.3.4 Discussion

Restriction of channel cross-section, i.e. of y_o , may result in appreciable reduction in gas-phase transport rates. In fact, these rates may be calculated from purely gas-diffusion controlled processes. In channel where forced air flow rates may be small, unfavorable current density distributions may also be encountered. Such conditions and results will be discussed in section 4.3.4. The results also suggest reduction of channel length (for defined y_o) in an attempt to maintain quasi-uniform oxygen partial pressure and surface temperature. The results indicate applicability of self-breathing electrodes up to about 25 mA/cm^2 (at ambient temp.) in a design where air-electrodes would be disposed face-to-face and separated by air-channels such that $y_o \geq 1/4''$. Better current distribution may also be expected for disc-shaped electrodes, by careful selection of the channel-gap/electrode-radius ratio. The stability of such a design would require additional investigations related to heat and mass transfer processes.

4.3.4 Current distribution in air-breathing electrode channels under forced flow conditions.

4.3.4.1 Introduction

Experimental results and interpretation presented under the title: "Self-Breathing Air Electrodes" apply strictly to non-flow conditions and represent limiting conditions, since fuel cells operating under high current drains, will be subjected to air flowing over the electrodes. Other limiting conditions would correspond to infinite flow rates of air, insuring identical oxygen partial pressure over the electrode. However, such operating conditions can not be realized, although approached, under practical flow conditions. In fact, in the case of the IEM air-operated cathode, air flow rates have to be adjusted in order to remove product water, and only product water, lest the membrane water would decrease, generating non-uniform surface and bulk conditions, very detrimental to proper operation of the complete system.

In order to measure, analyze and possibly interpret effects of air flow rates on local current densities in air-breathing channels, additional work was conducted on the channels discussed earlier. Air-flow rates were maintained at low Reynolds number, i.e. in all cases less than 20.

4.0 FACTUAL DATA (Cont'd)

4.3.4.2 Experimental Equipment

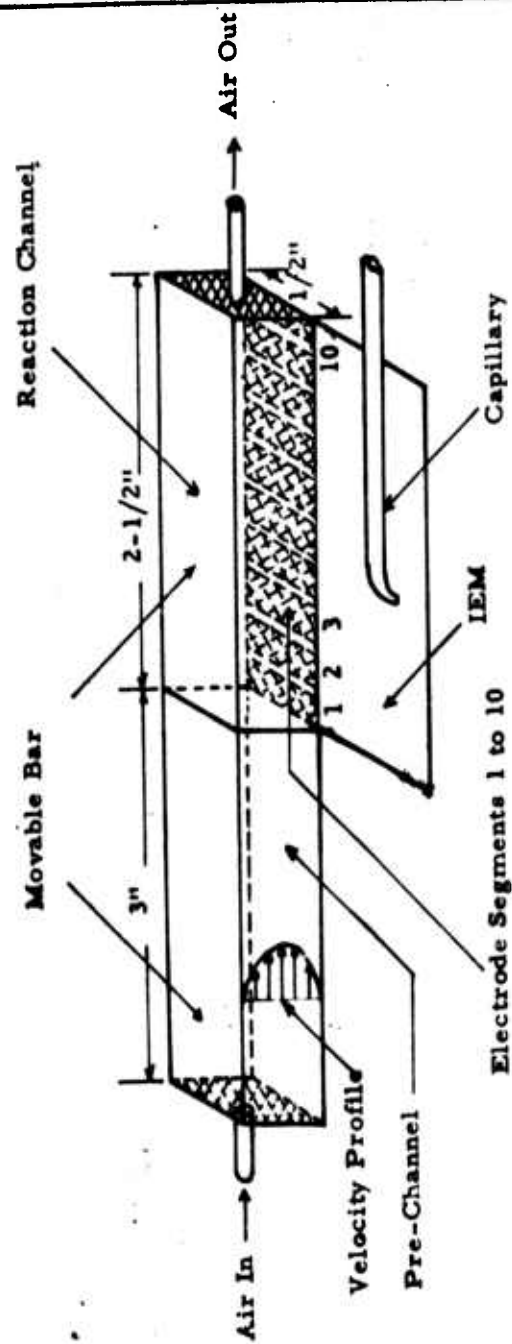
Partial and limiting currents were measured indirectly by galvanostatic measurements. A Luggin Capillary/SCE system was used as reference electrode, the capillary tip being tightly held against the membrane. The experimental equipment is represented in figures III-17 and III-18. Air channels are 2-1/2" long and 1/2" wide. Channel height can be varied by moving a Lucite bar placed on the channel top. Channel heights could be 1/16, 1/8, 1/4 and 1/2". The channel was mounted on an air electrode. In order to avoid appreciable entrance effects due to possible turbulence, the air velocity profile was generated in a channel similar to the reaction channel, and had a total length of 3". (See figure III-17). The air electrode was prepared by placing ten parallel electrode/screen strips on a GPS - Ion Exchange Membrane. The IEM extended out of the channel for reference potential measurements. The counter-electrode was prepared in a similar manner. One channel end (exhaust O₂/N₂mixture) was closed. This may affect currents at channel end because of local turbulence. In the case of open exhaust channel, end-effects were observed, corresponding to oxygen back diffusion, thus to higher local currents. Flow rates for in-conditions were measured with calibrated flow-meters and for small flow rates with a soap-bubble displacement technique.

The assembled experimental set-up is represented schematically in figure III-18.

4.3.4.3 Experimental Procedures:

Under galvanostatic conditions (for currents limited to 700 ma, corresponding to current densities of 116 ma/cm²), and for steady-state operation, local cell potentials were measured for various flow conditions. In order to show effect of air flow and to account for convective processes, similar results were obtained in absence of forced flow. The presence of the pre-channel reduces gas diffusion to electrode #1, allowing for small local currents, whereas if reaction channel end is open to the atmosphere, back-diffusion of oxygen is occurring, even at low air flow rates, thus displaying higher local current densities in position 10 as compared to electrode #1.

4.3.4.4 Experimental Results:



Semi-Annual Report #2
Contract DA-36-039-
AMC-00095(E)
J.A. - H. M. 6/30/63

FIGURE III-17

FUEL CELL FOR THE STUDY OF FLOW
RATE INFLUENCE ON POLARIZATION

Fuel Cell Lab.
DECO - G.E. Co.
Lynn, Mass.

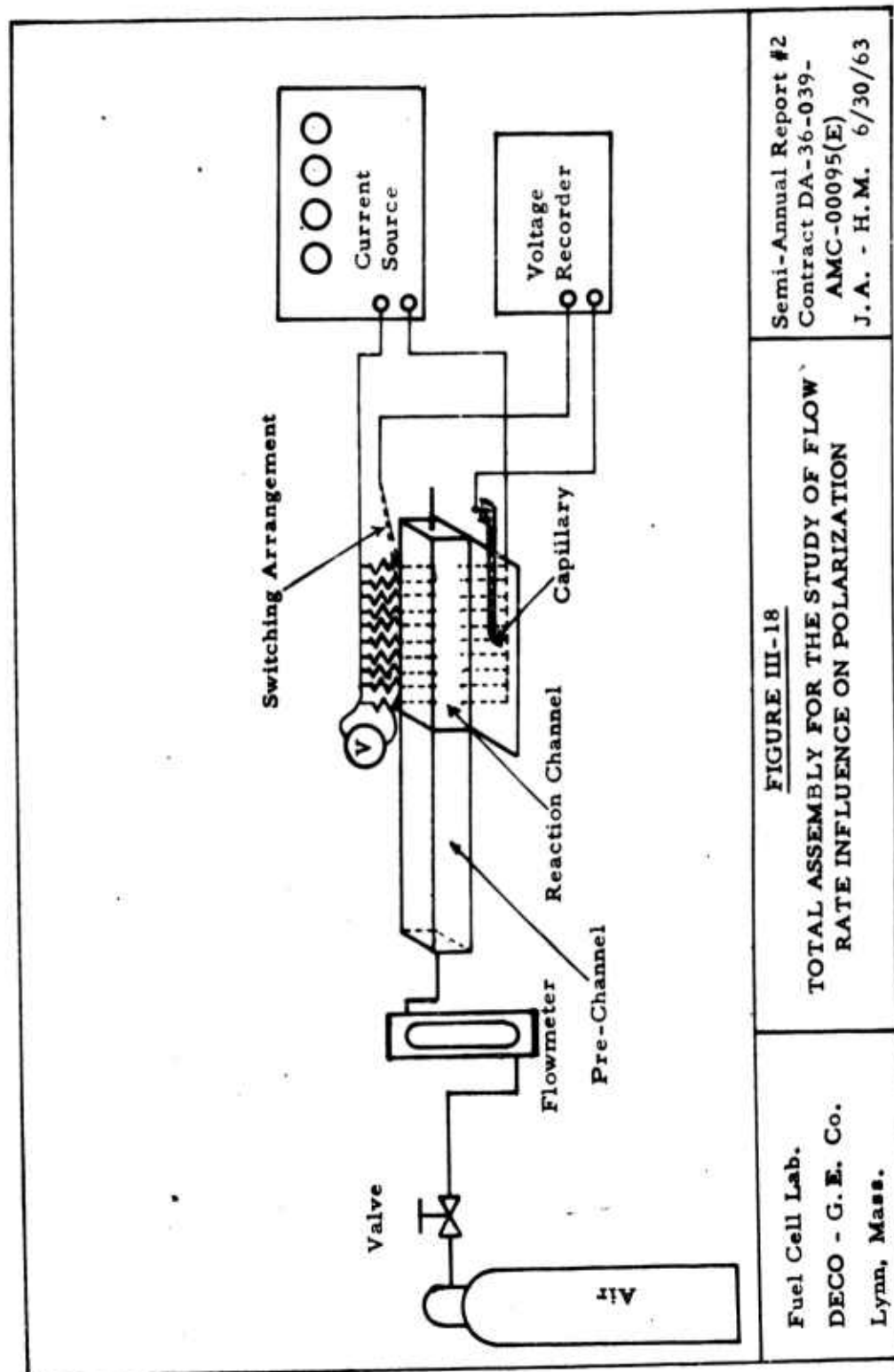


FIGURE III-18

TOTAL ASSEMBLY FOR THE STUDY OF FLOW
RATE INFLUENCE ON POLARIZATION

Fuel Cell Lab.
DECO - G. E. Co.
Lynn, Mass.

Semi-Annual Report #2
Contract DA-36-039-
AMC-00095(E)
J.A. - H.M. 6/30/63

Polarization Characteristics

Polarization characteristics for individual electrodes in the reaction channel are represented in figure III-19 for individual cases as related to electrode position, air flow rates and channel geometry. On the basis of limiting currents observed for flow conditions over electrodes, total channel limiting current should be about 800 mA, corresponding to 16 cc/min. of air flowing through the channel. Current distributions are reported for flow rates from 1 to 60 cc/min., or linear velocities of 0.08 to 1.0 cm/sec. for 1/16" channel height. In figure III-19 it appears that appreciable stoichiometric reaction air flow rates are required to avoid limiting currents smaller than edge limiting currents observed on electrode #1 already at low flow rates.

Limiting Currents:

Figure III-20 represents limiting currents (normalized with respect to the limiting current at $x = 0$) as a function of position and air inlet conditions. These results were obtained from polarization characteristics as described by figure III-19 and extrapolated to $(i_L/i_{L,0}) = 1$ for electrodes near air inlet channel.

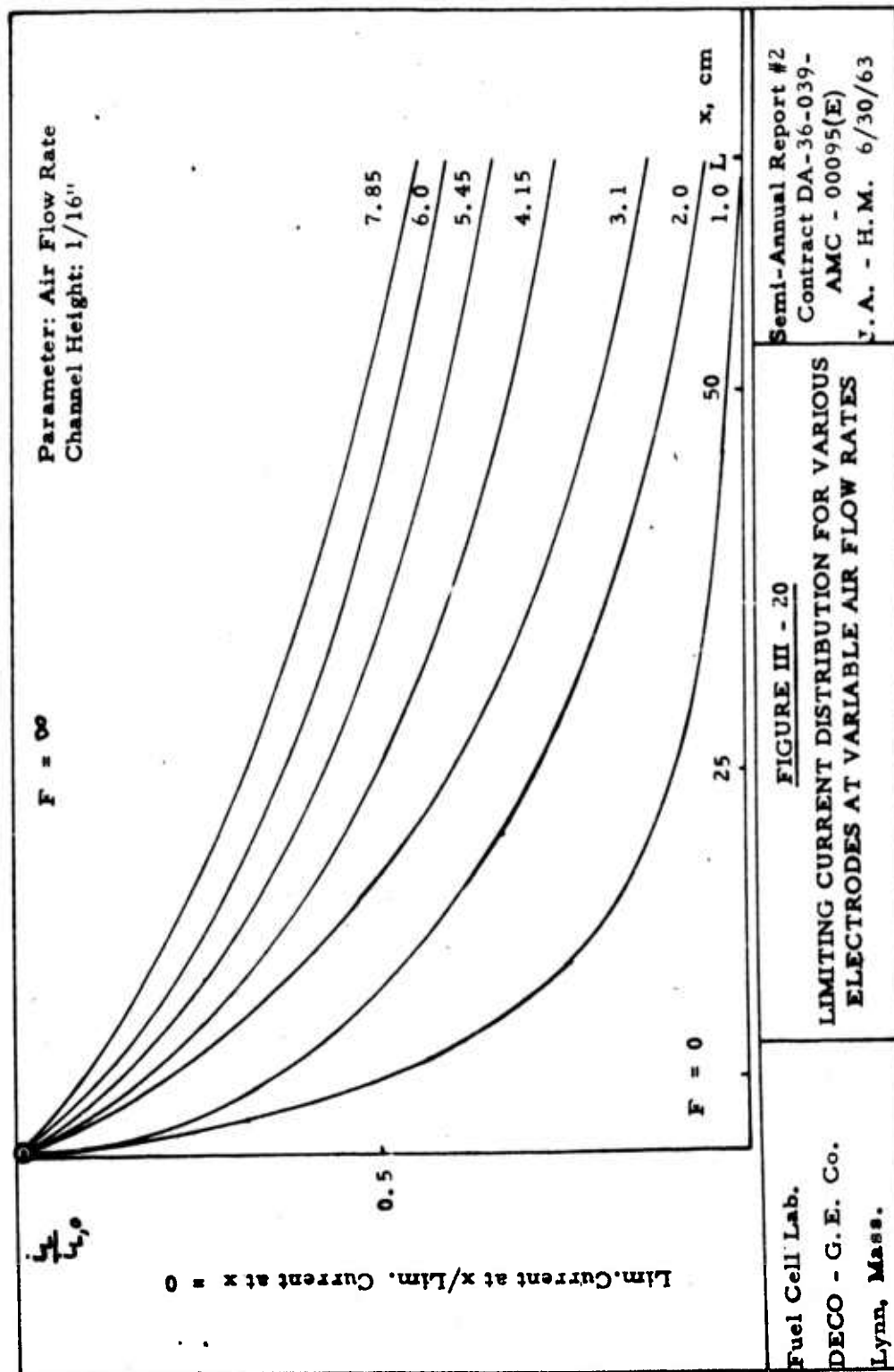
On the assumption that these limiting currents can be derived from gas phase diffusion processes, an attempt has been made to solve differential equations descriptive of the process, considering defined boundary conditions. (For details of the derivation, see Appendix III-3).

On the basis of a simplified (approximately correct near the electrode surface) linear velocity profile, it was possible to derive a relation describing limiting currents i_L as a function of position (x in cm), gas flow rates (Q in cm^3 air/sec.), channel height (y_0 in cm), gas bulk concentration (c_0 in moles/ cm^3), channel width ($W = \text{const.}$ in cm) and diffusion coefficient (D in $\text{cm}^2/\text{sec.}$).

$$i_L(x) = 2nFD^{2/3}W^{-1/3}c_0\left(\frac{Q}{xy_0^3}\right)^{1/3} \quad (\text{III-15})$$

If Eqn. III-15 is normalized by dividing by $i_L(x=0) \approx 130 \text{ ma/cm}^2$, a linear relationship should be obtained for the log. function, i. e.

$$\log \frac{i_L(x)}{i_L(0)} = \log A + \log \left(\frac{Q}{xy_0^3} \right)^{1/3} \quad (\text{III-16})$$



FACTUAL DATA (Cont'd)

Experimental results reported in figure III-21 for $y_0 = 0.16$ cm, air flow rates varying from 1.0 to 6.9 cm³/sec. and to electrode positions, i.e. #1, 2 and 5, yield a linear function with slope equal to 2. The specific extrapolated conditions $(Q/xy_0^3) = 1$, yields $\log A = -1.0$ from figure III-21 whereas the calculated value from eqn. III-15 corresponds to $\log A = 0.76$.

Presently, experimental results suggest the application of a semi-empirical relationship defined as

$$\frac{i_L(x)}{i_L(0)} = 4.10^3 D^{2/3} W^{-1/3} C_0 \left(\frac{Q}{xy_0^3} \right)^{2/3} \quad (\text{III-17})$$

Description of the polarization curves

As in Section 4.3.4.2 (on "Self-Breathing Air Electrodes", regarding diffusion polarization), the polarization curves can be completely described, if in eqn. III-3,

$$\left(1 - \frac{i}{i_L} \right) = e^{\alpha \eta_d} \quad (\text{III-3})$$

limiting current $i_L(x)$ can be analytically derived and if the value of α can be empirically established or evaluated from its physico-chemical significance. However, in this case, $i_L(x)$ is not only position-dependent, but also dependent on air flow rates and gas properties. In principle, all experimental results for various flow conditions and channel geometrics could be correlated by eqn. III-3. A plot of:

$$\log \left[1 - \frac{i}{i_L} \right] \text{ vs. } \alpha \eta_d \quad (\text{III-4})$$

should yield linear relationship as shown in figure III-22, with slope $\alpha = -11.0$. Experimental results reported in figure III-22 are related to two channel geometries (1/8" and 1/16") and two electrode positions (#5 and #8). Data scattering is not unexpected, since diffusion polarization η_d is obtained from actual observed potentials and potentials observed for air - operated cathode in absence of channel effects, i.e. very high air flow rates. Voltage scattering can also occur because of initial rest potential variation and dissimilitude in the various electrode segments in the channel. Significance of α has been discussed in Section 4.3.3.3, and values obtained for forced flow conditions are comparable to $\alpha = 10.2$ and 9.0 for channel heights of 1/16 and 1/8", respectively, in the case of self-breathing electrodes.

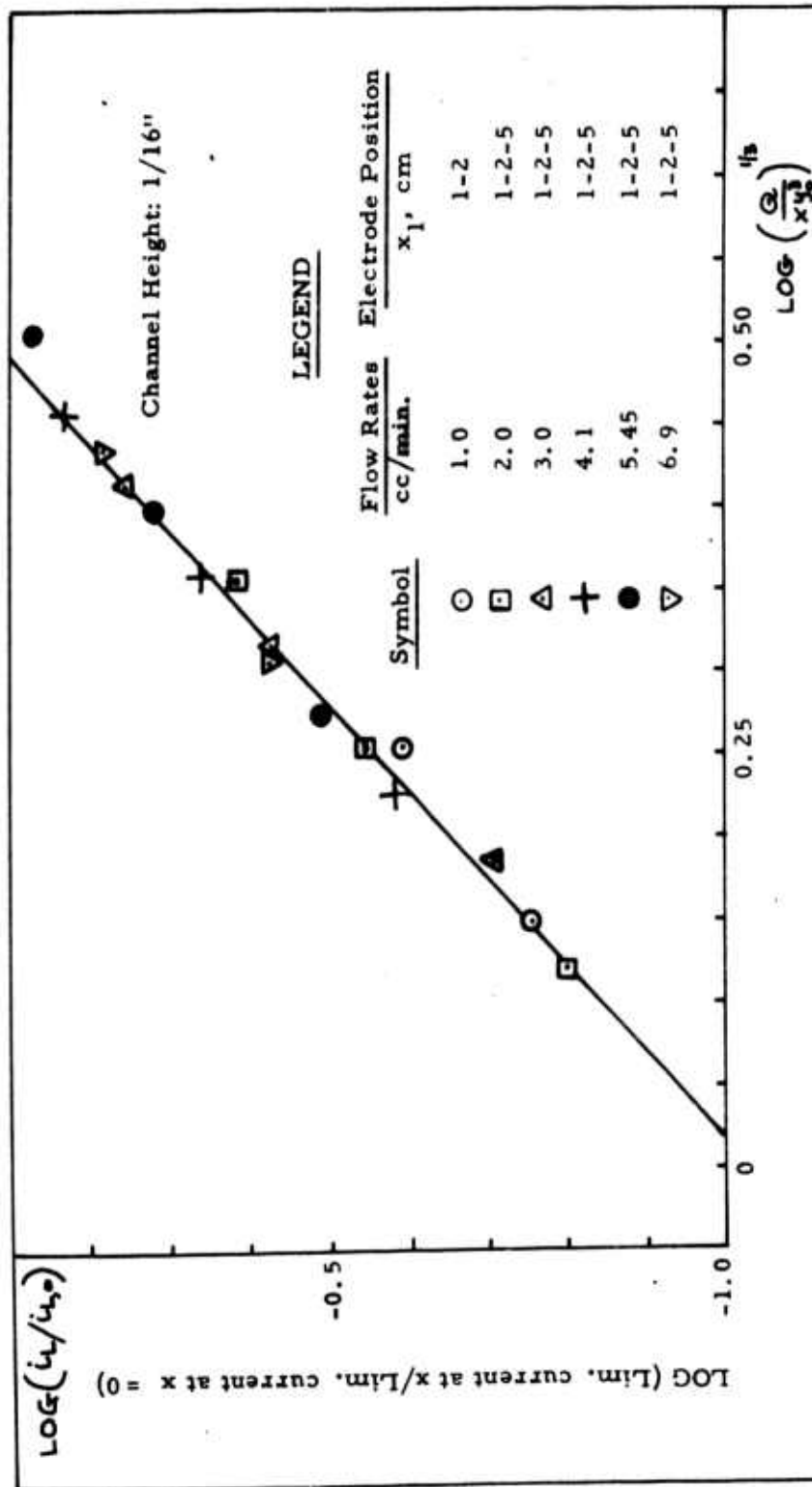
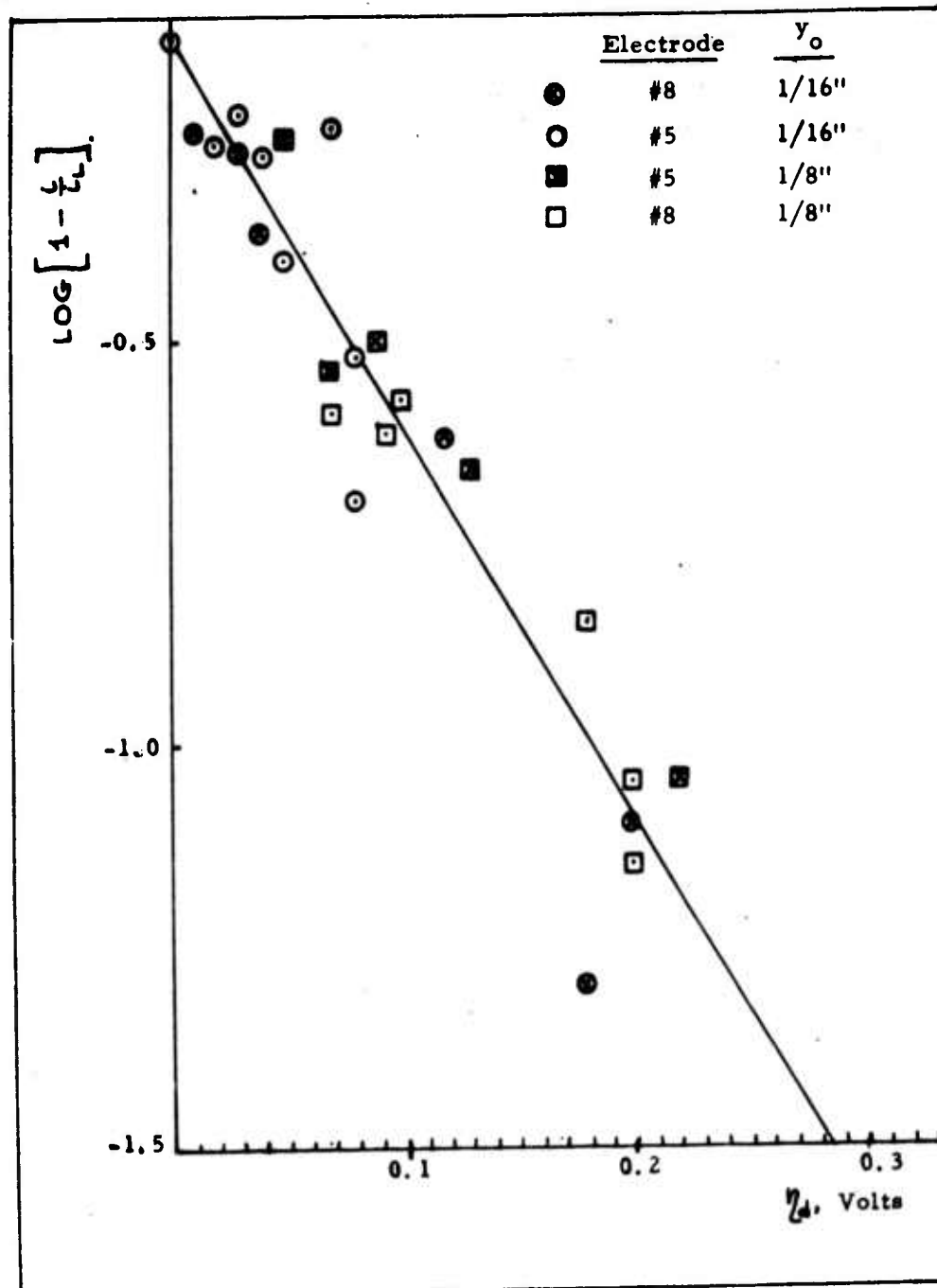


FIGURE III - 21
INFLUENCE OF AIR FLOW RATE AND CHANNEL
GEOMETRY ON LIMITING CURRENTS

Fuel Cell Lab.
DECO - G.E. Co.
Lynn, Mass.

Semi-Annual Report #2
Contract DA-36-039-
AMC - 00095(E)
J.A. - H.M. 6/30/63



Fuel Cell Lab.
DECO - G. E. Co.
Lynn, Mass.

FIGURE III-22
RELATION BETWEEN
LOCAL CURRENT AND
DIFFUSION POLARI-
ZATION.

Semi-Annual Report #2
Contract DA-36-039
AMC - 00095(E)
J. A. - H. M. 6/30/63

4.0

FACTUAL DATA (Cont'd)

In view of the previous discussion, the following semi-empirical relationship can be used to describe polarization characteristics in channels

$$i(x) = 4.10^3 i_L(0) D^{2/3} W^{-1/3} C_0 \left(\frac{Q}{xy_0^3} \right)^{2/3} \left\{ 1 - e^{-\frac{\alpha_0 F \eta d}{RT}} \right\} \quad (\text{III-18})$$

where $i = \text{Amp/cm}^2$,

$i_L(0)$ = limiting current density (Amp/cm^2) in absence of channel effects, and $\alpha_n = 0.28$.

In addition to I-V relationships, approximate equations to describe oxidant concentration distribution can be used in relation to local current densities:

$$\frac{C}{C_0} = 1 - \frac{i}{nFD C_0} \left(\frac{gx}{N} \right)^{1/3} \left[\frac{e^{-\pi^3}}{\Gamma(2/3)} - \pi \left\{ 1 - \frac{\Gamma(2/3, \pi^3)}{\Gamma(2/3)} \right\} \right] \quad (\text{III-19})$$

when $\pi = 0$;

$$\frac{C_{\text{wall}}}{C_0} = 1 - \frac{i}{nFD C_0} \left(\frac{gx}{N} \right)^{1/3} \frac{1}{\Gamma(2/3)} \quad (\text{III-88})$$

leading to the limiting current expression (Appendix III-3), when $C_{\text{wall}} = 0$, i.e. $i = i_L$

4.3.4.5 Conclusion:

Experimental results and analytical result interpretation have shown the importance of channel geometry for air-operated current collectors and channels. Appreciable diffusion polarization and poor current density distribution can only be avoided for high air flow rates if long air channels are to be used. Designs should take care of all influential variables, suggesting large channel height or better yet, small air channel length to obtain good PO_2 distribution. These observations are specially true for operation near limiting currents. For fractional parts of i_L , i.e. $0.5 i_L$, flow rates $\gg 2$ times stoichiometric rates for i_L are sufficient to obtain quasi-uniform rate distributions.

Air electrode can operate near i_L for very high flow rates for short channels. These limiting currents can then be increased by increasing electrode surface temperature and/or oxidant total pressure, if the partial pressure is to be maintained constant.

4.0 FACTUAL DATA (Cont'd)

Over-all Heat and Mass Transport processes will, of course, be affected by suggested designs. New designs are discussed in Task IV, where experimental results regarding modified air current collectors are presented.

4.4 TASK IV

HEAT AND MASS TRANSFER INVESTIGATIONS OF THE AIR-BREATHING I. E. M. FUEL CELL

J. P. Dankese

4.4.1 Introduction:

Substantially all of the necessary data for a heat and mass transfer analysis and possible correlation are available. Since the heat transfer data reduction and analysis are not completed, the results of this work will be reported in the Final Report.

Included in this report are descriptions and photographs of the experimental apparatus and fuel cell hardware; the performance characteristics of the new design air electrode current collector; the results of a mass transfer analysis which included bulk gas, pore, and gas-liquid diffusion mechanisms; a comparison of the water transport and evaporation rates for a "GPS" I. E. M. fuel cell membrane and pure water; an empirical equation for the effect of air velocity on the rate of water transport and evaporation for a "GPS" I. E. M. fuel cell with and without electrochemical reaction; and, finally possible over-all mass transfer correlating relationships.

4.4.2 Experimental Apparatus and Procedure

4.4.2.1 A. I. E. M. Fuel Cell Hardware

1. Perforated Metal Screen

Perforated metal screens made by a photo-etching process are used. This screen may be made from any metal desired, but for the experimental investigations reported herein, the materials were Carpenter 20 Cb stainless steel and molybdenum. The practical ranges of screen thickness, hole diameter, and percentage flow area for fuel cell applications appear to be 0.003 to 0.010 in. and 5 to 50%, respectively. The range of the number of holes per geometric square inch of screen area is then about 160 to 18,000. The screens used in the experimental

FACTUAL DATA (Cont'd)

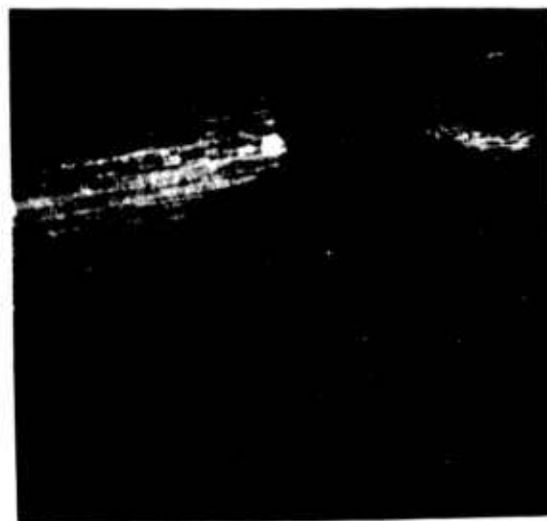
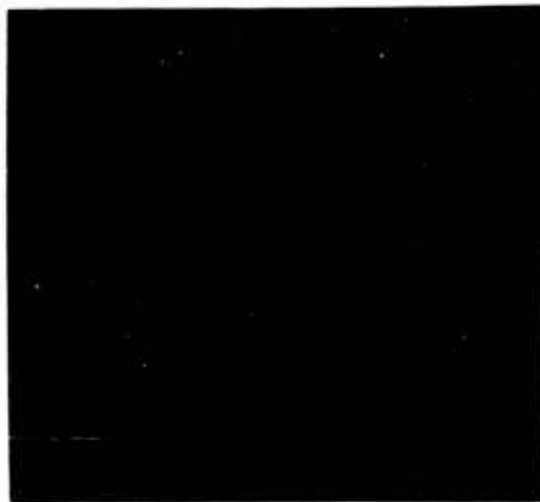
work were 0.005 in. thick, had a hole diameter of 0.005 in., and contained from 2000 to 15,000 holes per in². The percent flow areas were from 10% to 35%.

Representative cross-sectional profiles of perforated metal sheets are shown in Photograph IV-1. The top profile represents the 35% flow area screen with 0.005 in. holes and an inlet to throat diameter ratio of about 2.5 to 1. The bottom profile represents a ratio of 3.5 to 1, a percent flow area of 11% for a 0.0075" screen thickness. The holes are smooth, without burrs, and are streamlined with convergent-divergent, convergent, and divergent nozzle type shapes.

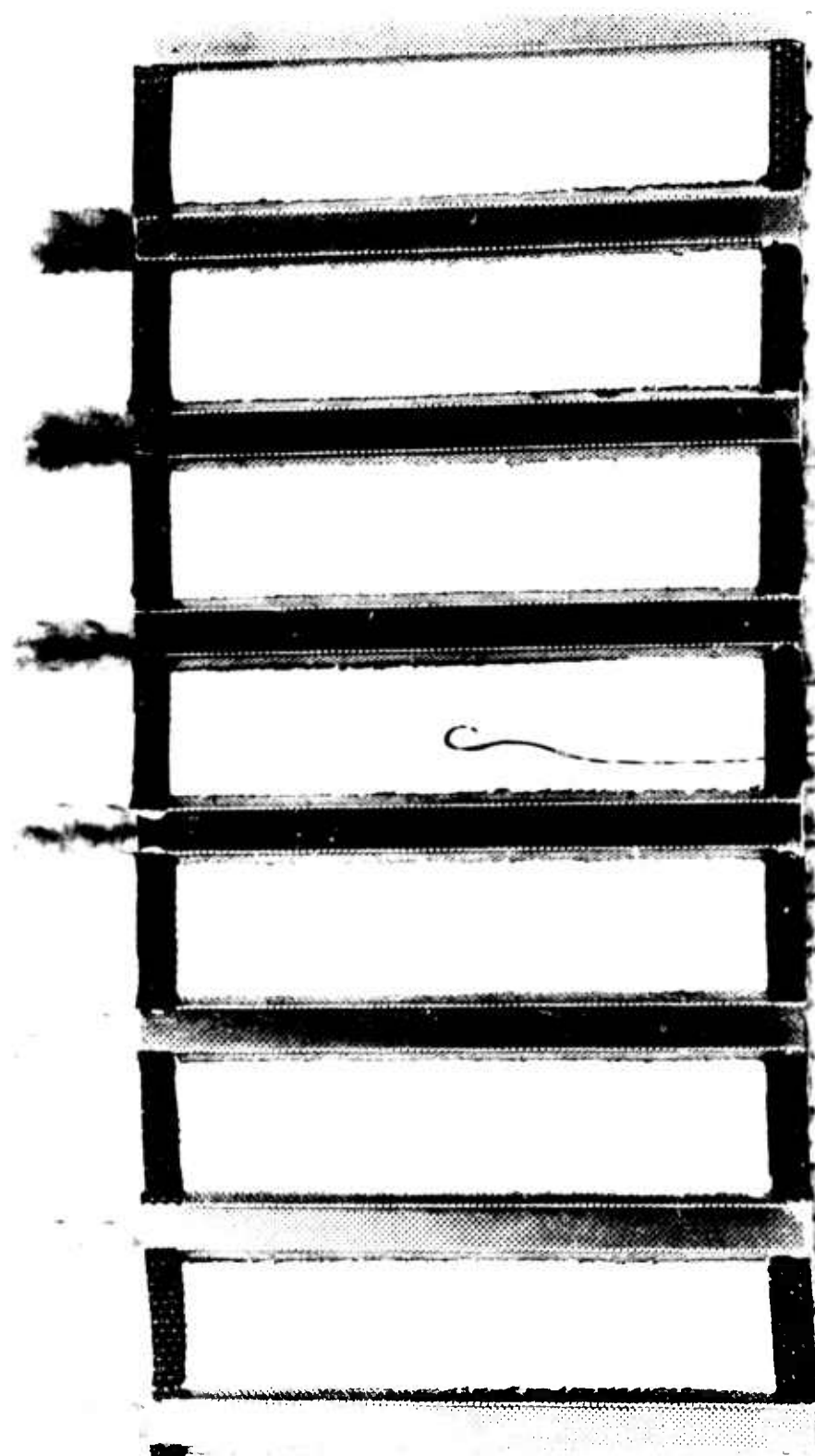
2. Perforated Screen Air Electrode Current Collector

A close-up photograph of the new design perforated metal screen air electrode current collector is shown in Photograph IV-2. This side makes contact with the catalyst by means of the perforated metal flat ribs shown. Air enters the alternate flat rib flow passages perpendicular to the long dimension of the collector, passes through the rib face (45° angle), across the catalyst reaction zone, and reacted air plus product water vapor then passes through the opposite rib face and out the alternate ribs (from the end with the white tabs). The white battery separator material prevents bridging of the air flow passages with product water and aids in its removal from the fuel cell. The dark silicone material is used to form the desired flow pattern. A typical 0.004 in. insulated Pt-Pt-10% Rh thermocouple is shown on the white material. The collector temperature is measured at several points during cell operation.

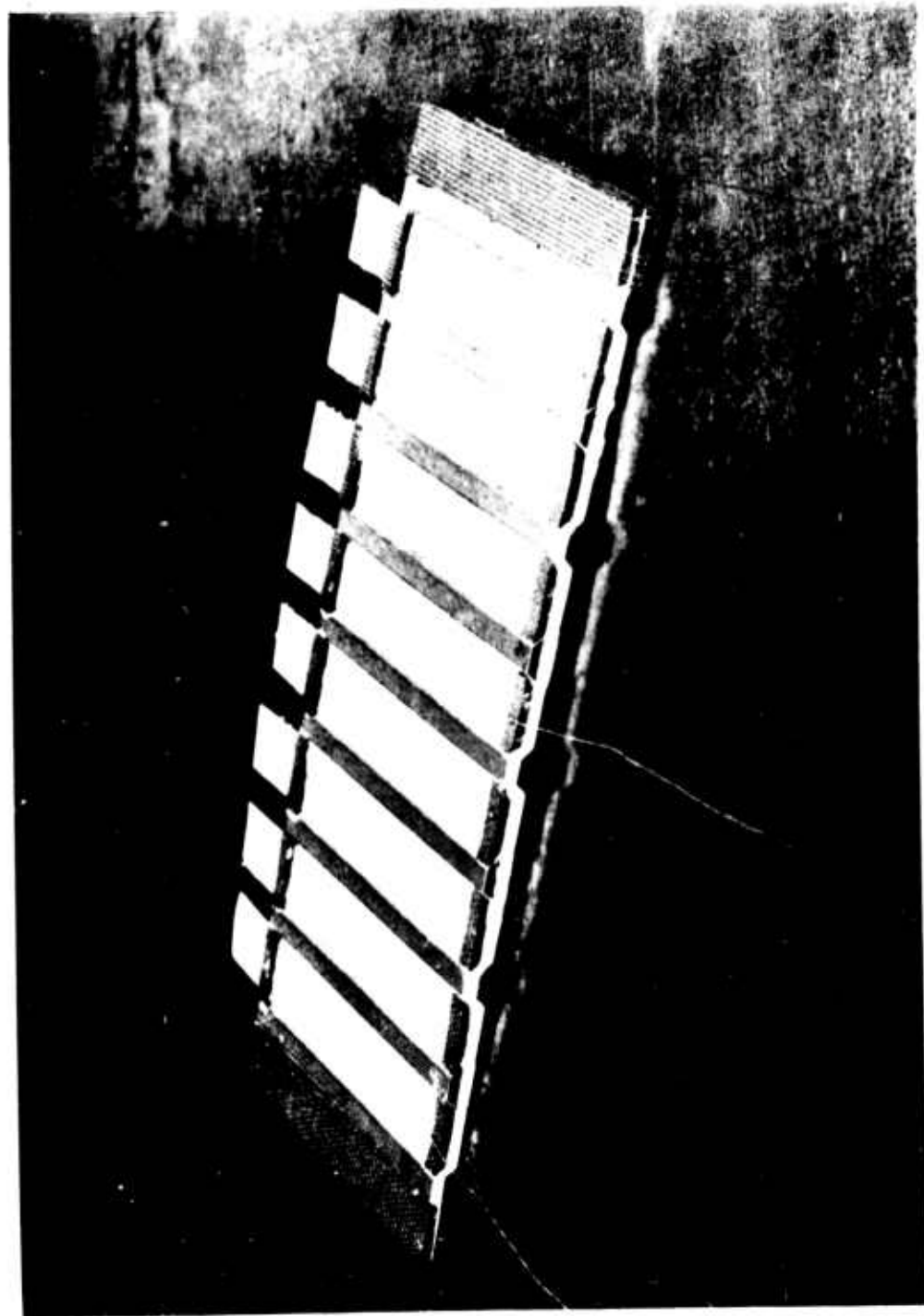
An isometric view of the same collector showing the reaction air side up and the cooling air side down is Photograph IV-3. The alternating pattern of the reaction and cooling air passages is clearly shown. Two collector thermocouples are fixed to the battery separator material with thin transparent tape. Another view is shown at the bottom of Photograph IV-4. An alternate configuration was the cooling air side ribs perpendicular to the reaction air side ribs instead of parallel and permits independent air flow conditions on both sides. Thus a cross-flow heat exchanger is incorporated with each cell. A patent docket has been written for the heat exchanger use and copies will be submitted.



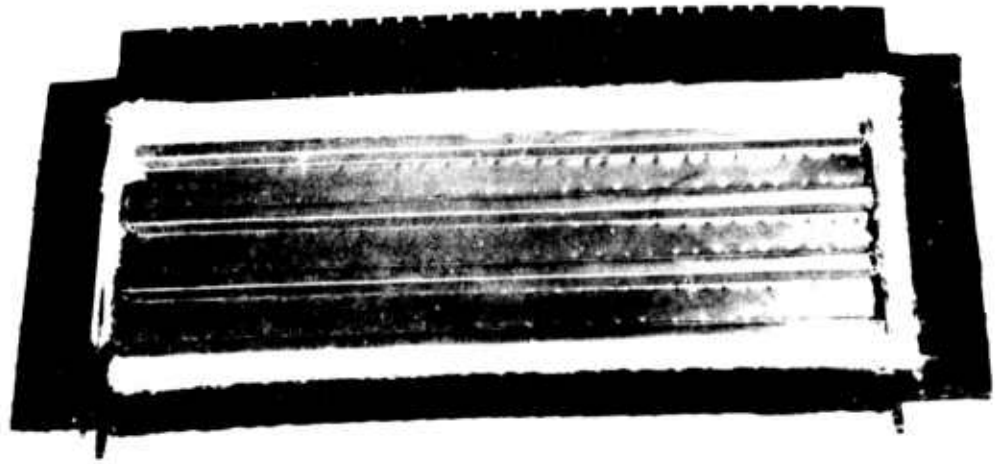
| | | |
|---|---|---|
| Fuel Cell Laboratory DECO-General Electric Company Lynn, Mass. | Photo IV-1 Representative Cross- Section of Perforated Plates (X125) | Semi-Annual Summary Report #2 Contract: DA-039-AMC -00095'E) J. Dankese 6/30/63 |
|---|---|---|



Close-up of Perforated Metal Screen Air Electrode Current Collector



Isometric View of Perforated Metal Screen Air Electrode Current Collector



12728

▲ 12728

FACTUAL DATA (Cont'd)3. Ion Exchange Membrane Fuel Cell - "GPS" Type.

A typical "GPS" ion exchange membrane fuel cell is shown in the center of Photograph IV-4. Two catalyst screen electrodes one on each side are in intimate contact with the membrane.

4. Perforated Metal Screen Hydrogen Electrode Current Collector

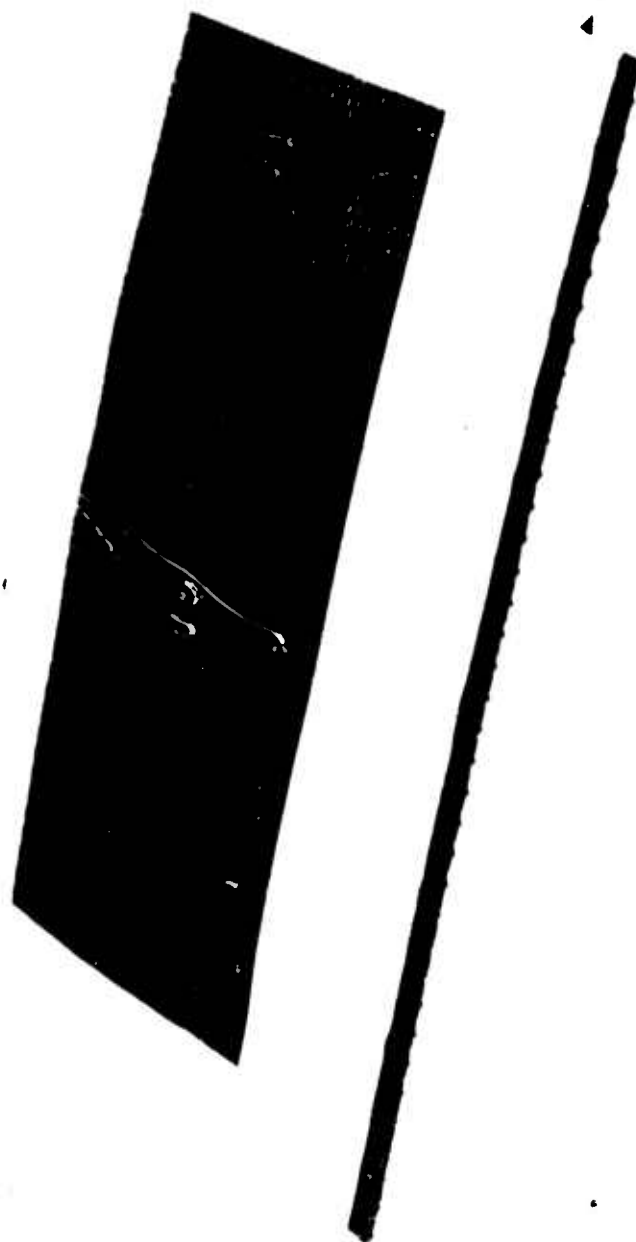
A most recent version of the hydrogen electrode current collector (at the top of Photograph IV-4) incorporates the perforated screen air electrode current collector configuration with manifolds to distribute the hydrogen more uniform during operation of the cell and hydrogen side inert gas purge periods. The battery separator material was not added to the particular collector photographed.

5. Assembled Heat and Mass Transfer Air-Breathing I. E. M. Fuel Cell

Photograph IV-5 presents a "GPS" ion exchange membrane fuel cell in assembled air breathing form, i. e. attached to the hydrogen electrode current collector. Thermocouples for measuring the hydrogen side collector and catalyst temperatures at points opposite those on the air side shown face up are sealed between the frame and membrane. Previous knowledge of the temperature profile across the catalyst surface indicated that the temperature at the extreme sides of the catalyst are the same; hence, only one thermocouple on one side is needed. The reaction zone catalyst area has been marked off with tape to the air electrode geometric area so as to give well defined catalyst active areas for all analyses and accurate current density calculations.

6. Assembled Single Cell I. E. M. and Fixture

The assembled air-breathing I. E. M. fuel cell is placed on top of one current and backup plate and then the air electrode current collector is placed with ribs down on the air side catalyst and finally a second current and backup plate is placed on top of it. Sufficient mechanical pressure is applied by means of small threaded tie-rod screws to give minimum cell electrical resistance. The inlet air end is shown in the photograph. (Ref. Photograph IV-6). This unit is then placed in the white insulated pressure tight box shown in Photograph IV-7 and external load connections are made by means of terminals in the cover which are attached to the cell current plates.



Typical Air Breathing IEM Fuel Cell Assembly

PHOTO IV-5

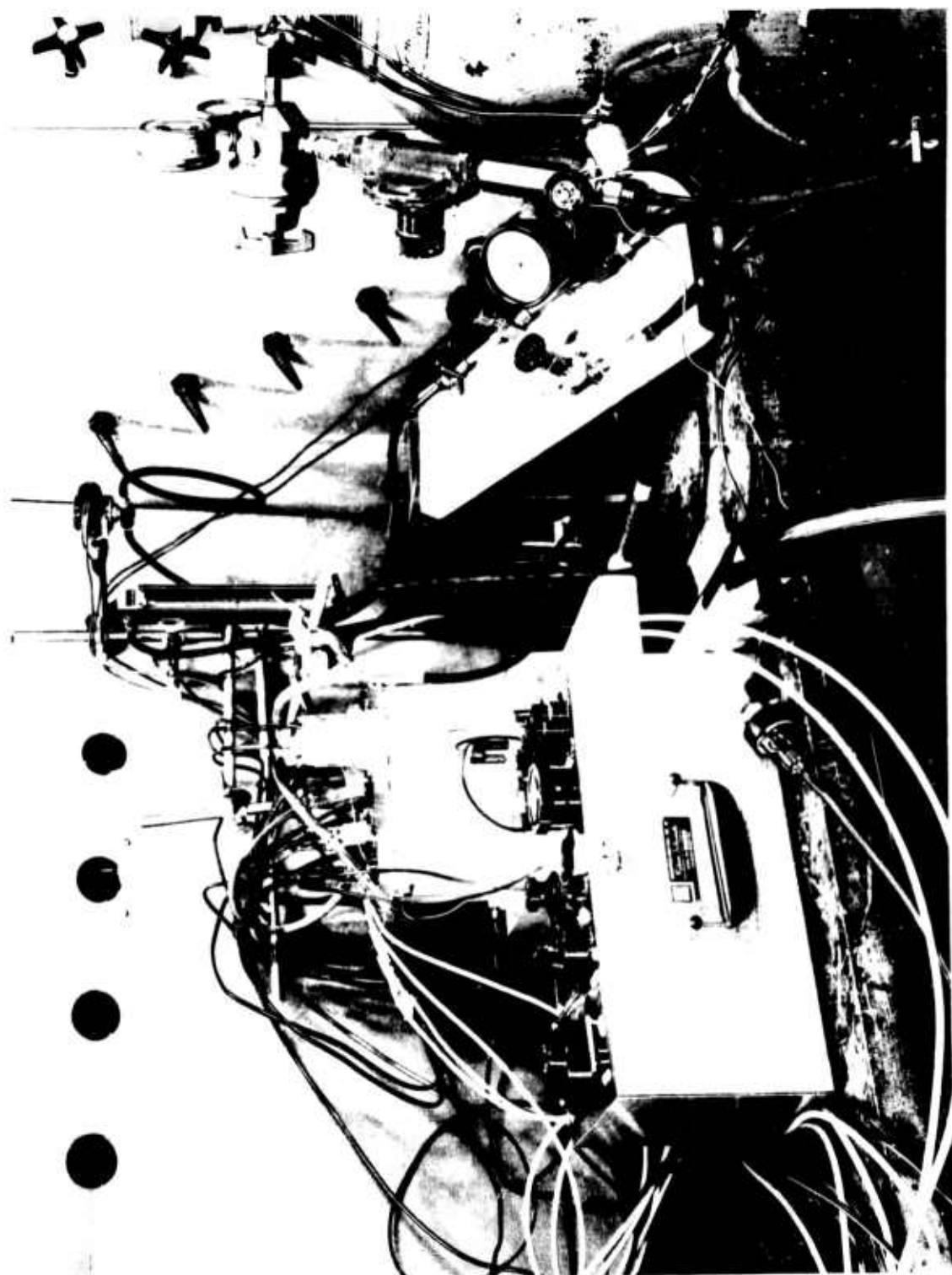
-60-

▲ 12729



Pho 14-6

▲ 12727



Experimental setup for the transfer of data to

4.0 FACTUAL DATA (Cont'd)

4.4.2.2 B. Heat and Mass Transfer Investigations With Electrochemical Reaction

The experimental apparatus used for heat and mass transfer studies with electrochemical reaction is shown in Photographs IV-7 and IV-8. Air at 70° - 80°F and 0% relative humidity is fed from a compressed air bottle at a few inches of water pressure to a calibrated flowmeter and then to the white insulated fuel cell fixture. For higher inlet air humidities, the air is passed from the flowmeter through a gas saturator (as shown in Photograph IV-7) and then to the fixture. Higher air temperatures are obtained by controlling the heat input to a short glass section wrapped with electrical heating tape by means of a rheostat and a thermocouple. Higher cell temperatures are obtained for a given current density in a similar fashion. Reacted air plus product water vapor leaving the fixture passes through a 14" long x 2" diameter silica gel bed to a glass control trap immersed in an acetone-dry ice bath at -70°C located in a Dewar bottle. Boil-off from the bath due to heat conduction is minimized by insulating the top of the bottle with cork wrapped with aluminum foil.

The water balances were achieved by weighing the cell fixture, the silica gel column, the cold trap, the hydrogen bubbler, and in the greater than 0% relative humidity cases, the air saturator before and after operation of the fuel cell at stable current densities of about 42, 62, and 83 amps/ft² for periods of up to eight hours at an air flowrate sufficient to remove 100% of the product water. This air flowrate was determined by monitoring the cell resistance by means of a Kordes-Marko bridge. The air flowrate at which the cell resistance and performance do not vary with time is the 100% removal point. The relative humidity of the inlet air was quantitatively determined by passing the bottled air through the absorption column, by the loss in weight of the air saturator, the air flowrate, and the temperature. Humidity sensors were also used. The relative humidity of the reacted air stream was determined from the temperature of the gas, the change in weight of the fixture, absorption column, and the cold trap, and the air flowrate by using Psychrometric charts. The amount of product water produced was calculated from the current and the length of the run in hours. The over-all water balances were 95 to 99% complete.

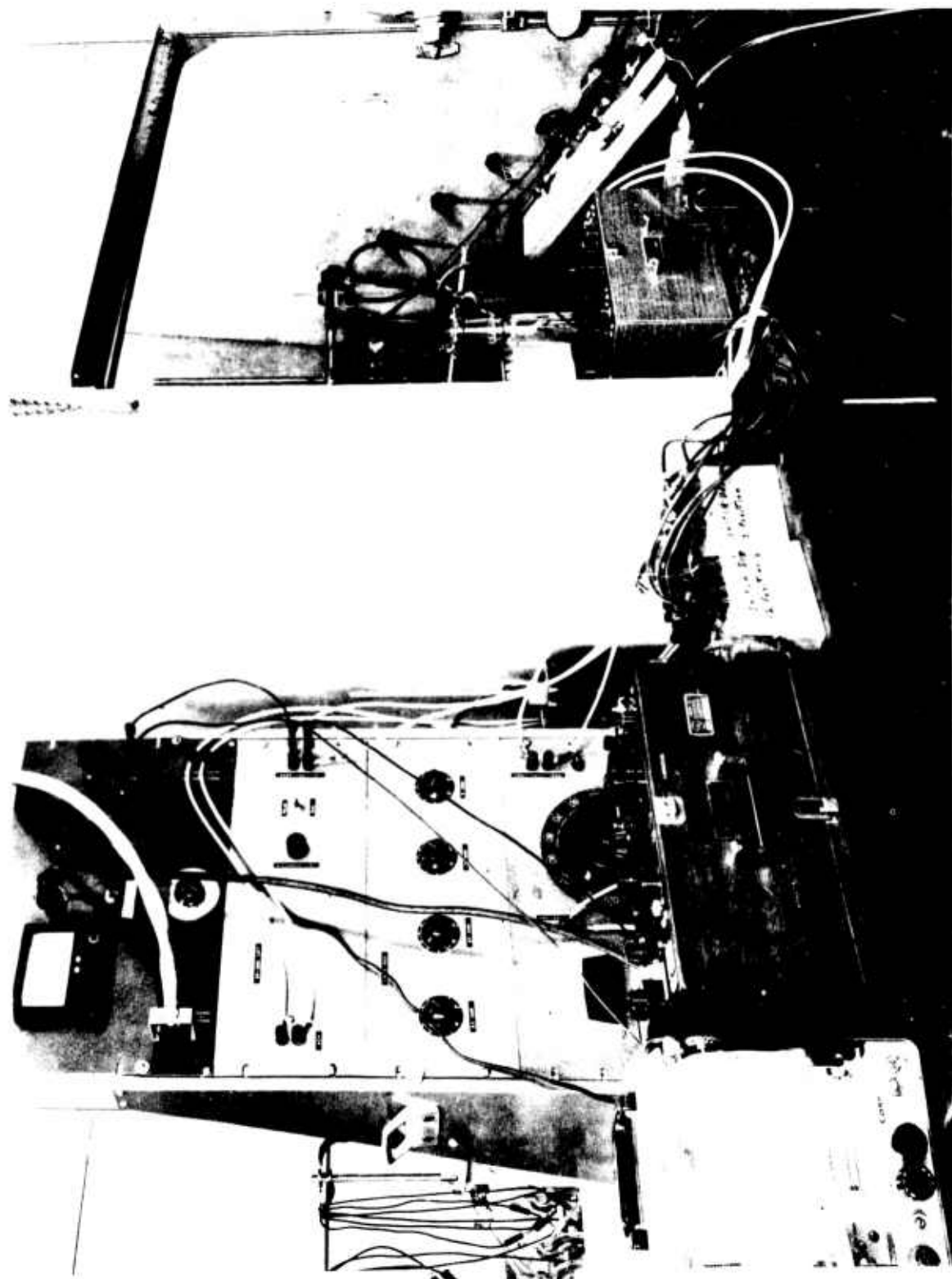


photo IV-1

-21-

A 12601

4.0

FACTUAL DATA (Cont'd)

The heat transfer temperature data were determined using a Honeywell-Rubicon precision millivolt potentiometer (range 0-80 mv) and 0.004 in. Pt - Pt - 10% Rh thermocouples insulated with a coating of a fluoro-carbon resin. These data consisted of measurement of the temperatures across the length and width of the air side catalyst, the middle of a channel to the edge, the collector, and the corresponding temperatures on the hydrogen side. The inlet, ambient, rib outlet, exit bulk, and inlet absorption column air temperatures were also measured as were the face temperatures of the fixture. Data were recorded every 10 to 15 minutes.

Steady-state attainment was determined by a zero rate of change of these temperatures. Usually about 1/2 to 1-1/2 hours were required for conditions to steady-out.

The Kordes-Mark and D. C. voltages were read on a Honeywell-Rubicon potentiometer for cell resistance data while a continuous record of D. C. voltage was obtained with a Varian recorder.

The D. C. voltage could be maintained within ± 10 to 25 m. v. by manual control of the flowrate but attempts at automatically controlling the cell performance were relatively unsuccessful resulting in a progressively more rapid decrease in cell voltage for some yet unexplained reason. In the interest of obtaining heat and mass transfer data under steady conditions manual control was employed.

4.4.2.3 Rates of Water Transport Through and Evaporation from the "GPS" I. E. M. Fuel Cell, Membrane, Catalyst-Electrode, and Pure Water.

A comparison of the relative rates of water transport through and from a "GPS" I. E. M. fuel cell (membrane + 2 catalyst electrodes) and a "GPS" membrane alone was obtained by first taking the air-breathing cell assembly with the hydrogen side filled with water and measuring the loss in weight of the cell assembly sitting on the pan of a precision Mettler balance (± 0.0001 g) under constant ambient conditions of 70-72°F and 56% R. H. every ten minutes until a steady rate was attained. Then the same experiment was performed using a piece of membrane from the same batch number taped to a hydrogen side collector and frame. The relative humidity was determined from the wet and dry bulb temperature readings and the total atmospheric pressure using Psychrometric Tables. The temperature of the ambient air and the catalyst and membrane surfaces were determined by thermocouples both at the start and end of a run. By filling the hydrogen gas compartment with water to a level just equal to the height of the frame, the rate of evaporation of water from a pure water (distilled) surface under the same experimental conditions was determined for comparison.

4.0 FACTUAL DATA (Cont'd)

4.4.2.4 The Effect of Air Velocity on the Water Transport and Evaporation Rates for a "GPS" I. E. M. Fuel Cell

The rates of water transport through and evaporation from the surface of a "GPS" I. E. M. fuel cell as a function of air flowrate were determined by filling the hydrogen gas compartment of the air-breathing cell assembly completely with water (no air bubbles) and then tying-off the inlet and outlet tubes. The cell assembly was weighed and then put into the insulated white fixture and air at 0% R. H. and 72-80°F was passed into the fixture at flowrates which spanned the range of the experimental fuel cell operating conditions and then into the silica gel absorption column and cold trap. The inlet and outlet air, the catalyst surface, the collector, and the fixture face temperatures were recorded every ten minutes. The highest flowrate run was terminated when the temperatures did not vary with time (3.27 hours) and all other runs at lower air flowrates were of this duration. The cell assembly, the fixture, the absorption column, and cold trap were weighed on a precision Seko balance (5000g capacity \pm 0.0005g) after each run. Four air flowrates corresponding to about 3 to 30 times the stoichiometric air requirement for a cell running at a current density of 81 amps/ft² were used.

4.4.3 Results:

4.4.3.1 A Comparison of the Hydrogen-Force Convected Air Performance of "GPS" Ion Exchange Membrane Fuel Cells with the New and Old Design Perforated Screen Air Electrode Current Collector.

Increasing the percentage rib-catalyst contact area from about 1% to about 5% and changing the angle of the rib face from 80° to 45° have resulted in a fuel cell fixture which has an electric resistance of about 0.001 Ω compared to about 0.020 Ω for previous designs and; therefore, a considerably higher performance capability. A comparison between the previous maximum hydrogen-force convected air performance possible with "GPS" ion exchange membrane fuel cells and the present shows that at the 100% product water removal condition the former "hot" (120°F) performance is about equal to the latter cold (85°F) performance, i. e., 0.69 D. C. volt at 50 amps/ft² and 0.59 D. C. volt at 100 amps/ft². However the new design "hot" (120°F) performance is 0.75 and 0.68 volt D. C. at current densities of 50 and 100 amps/ft². Current densities and D. C. voltages in this range have been maintained for periods up to eight hours on a few different cells. The portions of the polarization curves above 110 amps/ft² are shown in broken line form because the points are short time points,

4.0

FACTUAL DATA (Cont'd)

i. e. 15 minutes at 200 A/ft² to 1 minute at 290 amps/ft². The limiting current density for hydrogen and air at 100% removal of product water appears to be 290 amps/ft² compared to 155 amps/ft² for the previous design.

The maximum dead-ended hydrogen-oxygen performance in a standard laboratory fixture is 0.82-0.87 and 0.70 to 0.80 volt D. C. at current densities of 50 and 100 amps/ft², respectively. (Ref. Figure IV-1).

4.4.3.2 Heat and Mass Transfer Analysis

Although the heat transfer data has been taken, the reduction of data and analysis was incomplete at the time of the writing of this report and will, therefore, be included in the Final Report.

The details of a mass transfer analysis of the possible rate limiting mechanisms in the diffusion of oxygen from an air stream to the surface of the oxygen electrode of a "GPS" ion exchange membrane fuel cell appear in Appendix IV. The main results of the analysis are as follows:

1. Counterdiffusion of Oxygen and Water Vapor in the Presence of Inert Nitrogen Gas - Gas Film Controlling. (45, 46, 47, 48, 56)

The rigorous treatment of the simultaneous diffusion of two gases in the presence of a stagnant film of inert gas leads to complex equations even for this relatively simple case. However, useful approximations are obtained by simple relationships which are based upon the assumption that, in a complex system of diffusing gases, the diffusional gradient established for any component A is equal to the sum of the gradients which would result from the separate diffusion of A with each of the other components in separate binary systems in which the concentration and rate are the same as in the complex system. Thus a complicated equation

$$-\frac{\pi}{RT} \frac{dp_A}{dL} = \frac{1}{D_{AB}} (r_{Aa}^{PB} - r_{Ba}^{PA}) + \frac{1}{D_{AR}} (r_{Aa}^{PR} - r_{Ra}^{PA}) + \frac{1}{D_{AS}} (r_{Aa}^{PS} - r_{Sa}^{PA}) + \frac{1}{D_{AI}} r_{Aa}^{PI} \quad (IV-2)$$

for four diffusing gases and an inert gas I reduces to the form

$$r_{Aa} = \frac{D_{Am} \pi}{RT B_{Gf}} [P_A - P_{Ai}] \quad (IV-8)$$

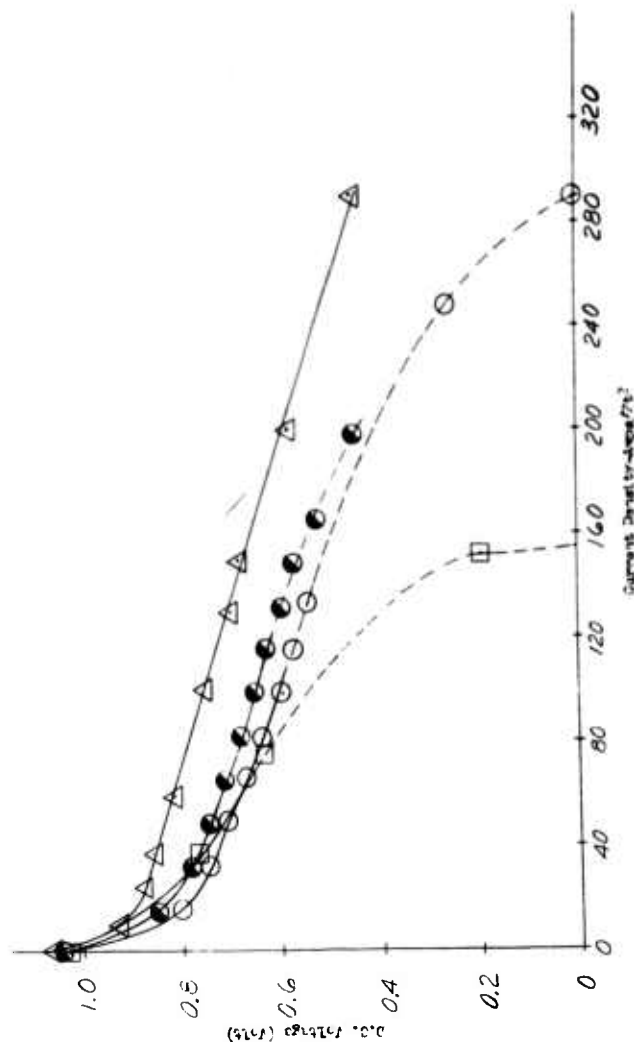
Legend $\frac{R_2}{R_1}$

New Design
Perforated Screen
Perforated Screen
Old Design

D.C. 12007 avg.
D.C. 3507 avg.
D.C.

Lab Cell Fixture $\frac{R_2}{R_1}$
D.C.

1. GHS - Type Membrane
Single Cell-to-Making
2. H_2O Headed-Lab. Cell
Fixture R_2 0.010 A
a. Geometric Catalyst Area =
0.333 ft²
3. H_2 Insulated Air Breathing
Unit R_2 0.015 A
a. Inlet Air 72-80°F at 0.1 A.H.
b. 100% Product Water Vapor
c. Geometric Catalyst Area =
0.333 ft²
4. Perforated Air Electrode Current
Collector (New Design)
b. Total Pressure 1.02 atm



Serial Annual Summary Report #2
Contract DA-36-079-1MC-00095(a)
J.P. Davison 5/70/53

FIGURE IV-1
A COMPARISON OF PRESENT AND PREVIOUS HYDROGEN-AIR PERFORMANCE
WITH SAUDER'S HYDROGEN-OXYGEN PERFORMANCE

Fuel Cell Lab
DECO - G.E. Co.
Lynn, Mass.

FACTUAL DATA (Cont'd)

which can be applied to any diffusing component.

a. Based on Bulk Gas Diffusion Coefficients (45, 46, 47, 48, 56)

On the basis of bulk diffusion coefficients alone, the theoretical limiting current density for the new design perforated metal air electrode current collector operating on air and hydrogen with 100% product water removal is 13,300 amps/ft². based on the maximum bulk rate of diffusion of oxygen. The current density at which the maximum diffusion path for water vapor becomes equal to one half the air gap is 2,430 amps/ft².

The effect of the counterdiffusion of water vapor on the rate of diffusion of oxygen is negligible, i.e., about 1.5%. However, the rate of water vapor diffusion is reduced 12.1% by the counterdiffusion of oxygen.

b. Based on Pore Gas Diffusion Coefficients (50,51, 55)

The problem with calculating rates of gas diffusion in pores is determining whether the flow is in the laminar, intermediate, or Knudsen regimes since the diffusion coefficients depend on the mode of flow. Thus for laminar flow the bulk diffusion coefficient for gases

$$D_B = \left(\frac{0.707}{3 \pi} \right) \left(\frac{\bar{r}}{\sigma^2 C_T} \right) \quad (\text{IV-15})$$

has the range for most gas mixture at atmospheric pressure and 20°C of from 0.1 to 1.0 $\frac{\text{cm}^2}{\text{sec}}$. It is dependent on the total pressure, the total concentration of molecules and the molecular size of the molecules in the mixture. For the Knudsen flow regime the gas pore diffusion coefficient

$$D_k = \frac{2r}{3} \bar{v} \quad (\text{IV-18})$$

has the range of about 0.01 to 1.0 $\frac{\text{cm}^2}{\text{sec}}$ for 0.001 μ and 1 μ pore radii, respectively.

FACTUAL DATA (Cont'd)

Therefore, an expression which shows both the transition between Knudsen and lamihar flow and reduces to these two special cases when $r \ll \lambda$ and $r \gg \lambda$ is needed to calculate the over-all pore diffusion coefficient. Equation (IV-19) in the form

$$D_{(0.A.)} = \left[D_B \left(1 - e^{-2r\bar{v}/3D_B} \right) \right] \quad (IV-19)$$

does just this. The effect of average pore radius on the over-all pore diffusion coefficient for the standard G. E. ion exchange membrane fuel cell catalyst-screen electrode is shown in Figure IV-2. Thus for oxygen

$$D_{O_2m} (0.A.) = 0.227 \left[1 - e^{-1.428 \times 10^5 r} \right]$$

and for water vapor

$$D_{H_2O} (0.A.) = 0.262 \left[1 - e^{-1.238 \times 10^5 r} \right]$$

Based on the pore size distribution

$$D_{O_2m} (0.A.)_{avg.} = 0.1797 \frac{cm^2}{sec} \quad \text{and} \quad D_{H_2O} (0.A.)_{avg.} = 0.1688 \frac{cm^2}{sec.}$$

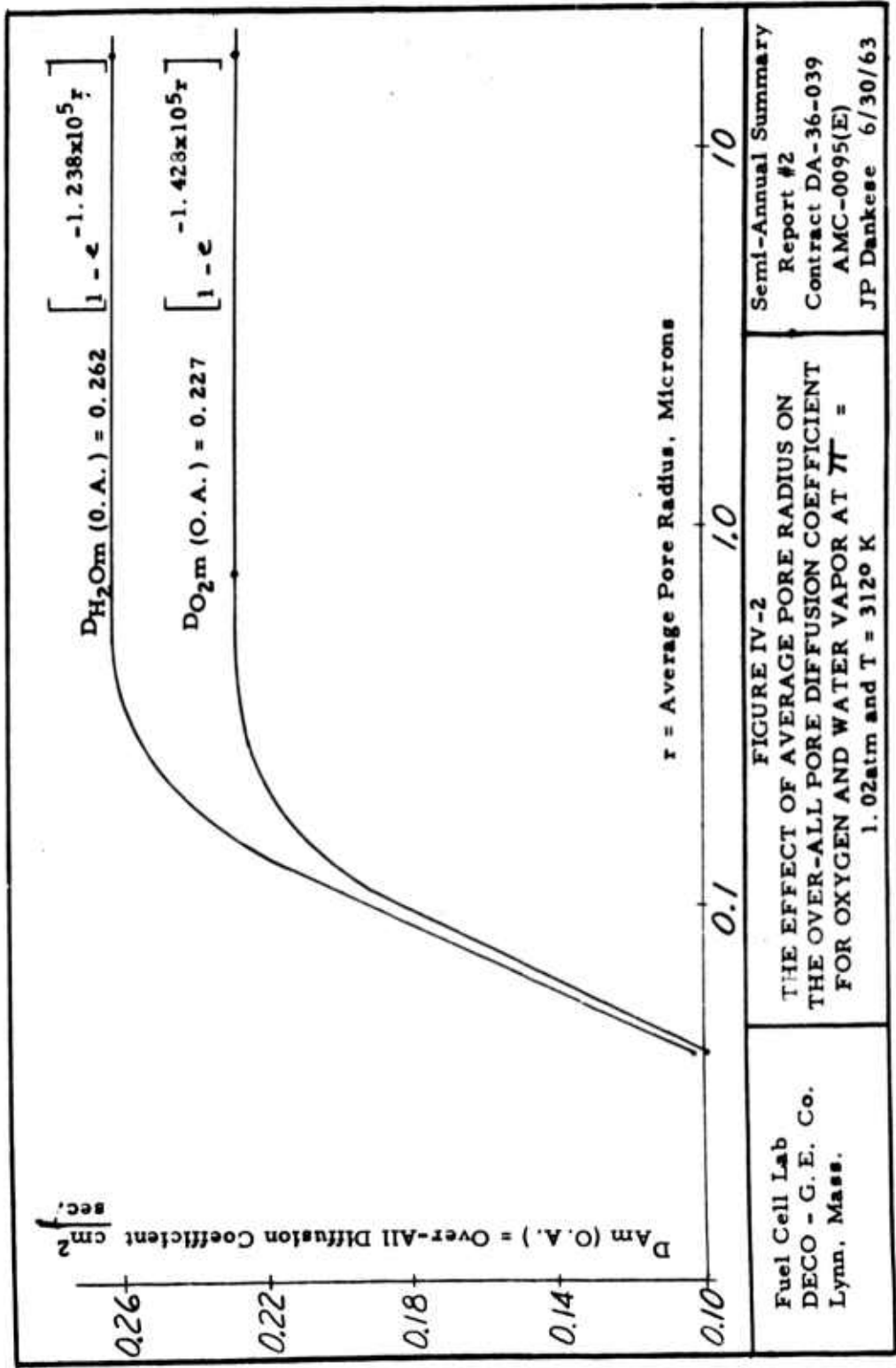
for the catalyst electrode.

Based on the average oxygen pore diffusion coefficient alone, the theoretical limiting current density is 9,600 amps/ft² for the new design perforated metal screen air electrode at 100% removal of product water. Theoretically, the current density at which water vapor diffusion from the bottom of the pores to the air stream becomes the limiting factor in the rate of removal of product water from the pores is 1,450 amps/ft². (Ref. Figure IV-2).

2. Counterdiffusion of Oxygen and Water Vapor in the Presence of Inert Nitrogen Gas - Liquid Film Controlling (45, 46, 47).

Using Fick's law in the form

$$r_{O_{2a}} = D_{O_2-H_2O} \left[\chi_{O_2} - \chi_{O_{2i}} \right] \quad (IV-23)$$



Fuel Cell Lab
 DECO - G. E. Co.
 Lynn, Mass.

FIGURE IV-2
 THE EFFECT OF AVERAGE PORE RADIUS ON
 THE OVER-ALL PORE DIFFUSION COEFFICIENT
 FOR OXYGEN AND WATER VAPOR AT $T =$
 1.02 atm and $T = 312^\circ \text{K}$

Semi-Annual Summary
 Report #2
 Contract DA-36-039
 AMC-0095(E)
 JP Dankese 6/30/63

4.0 FACTUAL DATA (Cont'd)

for the rate of diffusion of oxygen through water, the limiting current density for a "GPS" I. E. M. fuel cell operating on hydrogen and force convected air at 100% product water removal appears to be from 70 amps/ft² for a non wet-proofed electrode to a maximum of 500 amps/ft² for a wet-proofed electrode. Poorly or non-uniformly wet-proofed electrode limiting current densities should fall in between these two limits.

At a current density of 81 amps/ft² the reaction zone appears to occupy about 0.031% of the total pore geometric surface area and from 6.4% to 0.006% of the pore length for the 35 μ and 0.08 μ average pore sizes, respectively. The thickness of the liquid film is about 8.7×10^{-6} cm.

4.4.3.3 Rates of Water Transport Through and Evaporation Rates from the "GPS" I. E. M. Fuel Cell, Membrane, Catalyst-Electrode, and Pure Water. (53)

The results of the measurement of the steady-state rates of water evaporation from the surfaces of a "GPS" I. E. M. fuel cell, membrane, and pure water under the same ambient conditions of 70°-72°F air at 56% relative humidity are shown in Table IV-1. The ambient air velocity varied randomly from 0.25 to 1.0 ft/sec.

TABLE IV-1

| Evaporation Rate (gH ₂ O/Hr) | Geom. Area (cm ²) | k _{H₂O} in g-moles H ₂ O/cm ² -sec | $\frac{(k_{H_2O})_w}{(k_{H_2O})_i}$ | $\frac{P_{H_2O}}{v.p. H_2O}$ |
|--|----------------------------------|---|-------------------------------------|------------------------------|
| Water 1.346 | 104.6 | 1.98×10^{-7} | 1 | 1 |
| Membrane 0.785 | 74.2 | 1.63×10^{-7} | 0.822 | 0.86 |
| Fuel Cell 0.808 | 74.6 | 1.672×10^{-7} | 0.845 | 0.962 |

From the data the evaporation rate of water from a fuel cell (CRM 7) is 84.5% of that observed with pure water and the effective water vapor partial pressure at the surface is 96.2% of the vapor pressure of water at the surface temperature. For the membrane (CRM 7; I. E. C. = 0.64; % water dry basis = 18) alone the water evaporation rate is only

4.0 FACTUAL DATA (Cont'd)

82.2% of the pure water rate and the partial pressure of water vapor at the surface is 86% of the vapor pressure of water at the surface temperature. For the membrane and fuel cell the evaporation rates are equal to the water transport rates through the particular medium also.

Since the rate of water transport and evaporation rate changes only slightly from the fuel cell to the membrane case, the transport and evaporation properties of the catalyst-electrode are assumed to be the same as for pure water.

4.4.3.4 The Effect of Air Velocity on the Water Transport and Evaporation Rates for a "GPS" I. E. M. Fuel Cell.(49, 53)

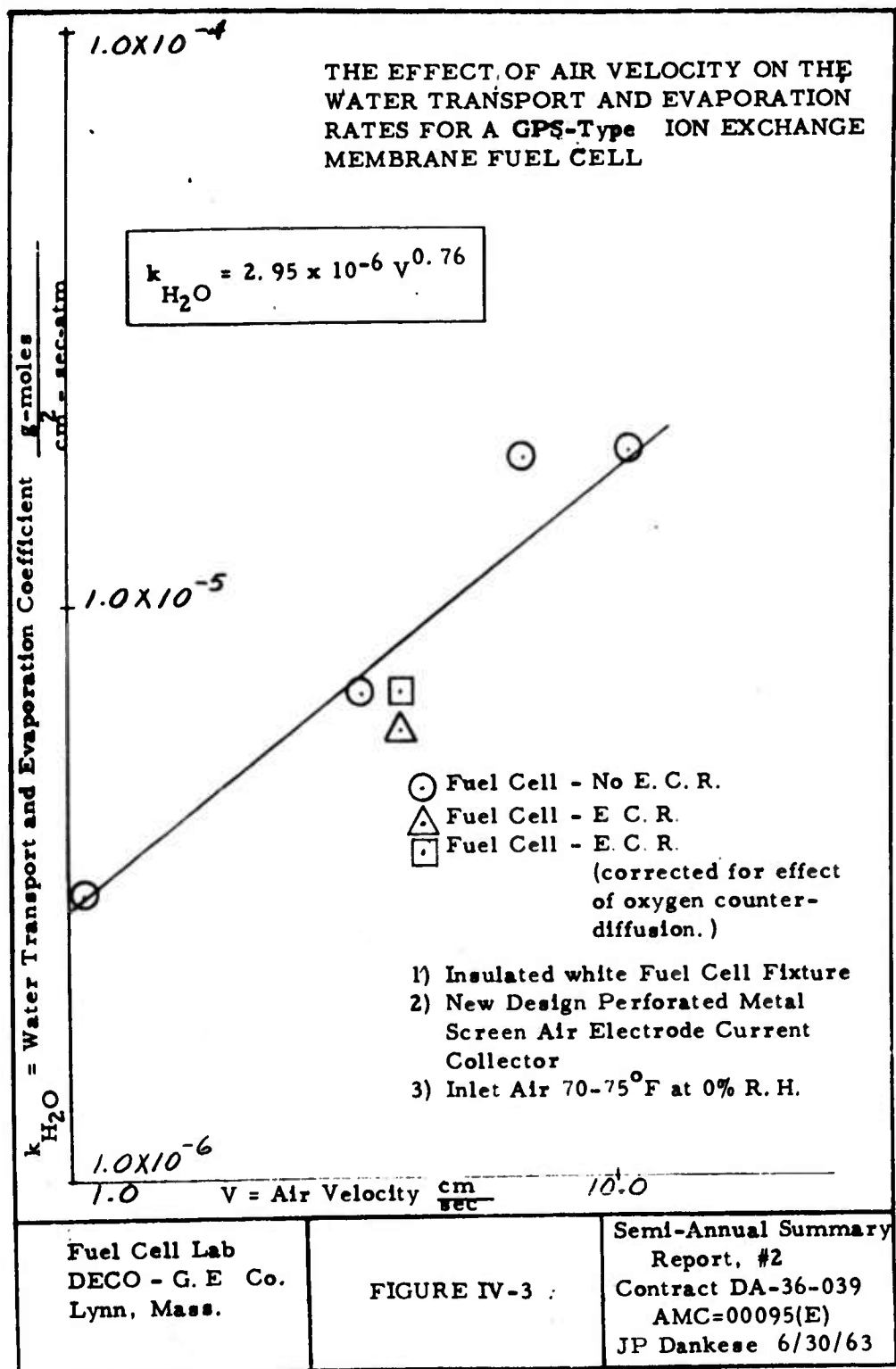
The effect of air velocity on the steady-state water transport and evaporation rates for a "GPS" I. E. M. fuel cell in the absence of electrochemical reaction (No E. C. R.) is shown in Figure IV-3. The range of inlet air, outlet air, and catalyst temperatures were 70° to 80°F, 68° - 73°F, and 66° - 73°F respectively. The inlet air relative humidity was 0% and the average relative humidity in the cells at steady-state conditions was from 28% to 44% for the highest to lowest flowrates which represented from 3 to 30 times the stoichiometric air requirement for a cell operating at a current density of 81 amps/ft². The data were obtained with the fuel cell in the insulated white fixture using the new design perforated metal screen air electrode current collector. The data were corrected for the variable relative humidity conditions by using the data from section 4.4.3.3 and dividing the steady-state rates by the water vapor partial pressure gradient from the catalyst to the air stream to obtain the water transport and evaporation coefficients k_{H_2O} . The data are represented by the empirical equation

$$k_{H_2O} = 2.95 \times 10^{-6} V^{0.76}$$

$$\text{where } k_{H_2O} = \frac{\text{g-moles}}{\text{cm}^2\text{-sec-atm}}$$

$$\text{and } V = \text{avg. linear air velocity} \left(\frac{\text{cm}}{\text{sec}} \right)$$

The data point used in the mass transfer analysis (Ref. Appendix IV) using a different "GPS" I. E. M. fuel cell in the same hardware but at a current density of 81 amps/ft² (E. C. R.) yields a steady-state



4.0 FACTUAL DATA (Cont'd)

evaporation rate at the 100% product water removal point which is very close to the data taken with no E. C. R. Correction for the effect of the counterdiffusion of oxygen brings the data more closely to the no E. C. R. data. The average air temperature was 90°F, the average percent relative humidity was 35%, and the catalyst temperature was 115°F for the E. C. R. point.

4.4.4 Discussion of Results

4.4.4.1 Performance

The main factors contributing to the markedly improved performance observed with the new design perforated metal screen air electrode current collector operating on hydrogen and force-convected air at 70°-80°F and 0% R. H. are believed to be the following: much more uniform removal of product water with the 45° rib face angle as indicated by a maximum variation of catalyst temperature of 1 to 2°F at a current density of 62 amps/ft² and 5°F at 81 amps/ft² compared to 10° to 20°F at 50 amps/ft² for the old design; lower cell resistance; higher air side heat transfer coefficients; and higher current carrying capability. With the present low rib-catalyst contact area, the membrane resistance is the total resistance. Further study above 110 amps/ft² at a constant temperature of about 120°F and 100% water removal is warranted to prove out high current density capability.

4.4.4.2 Mass Transfer Analysis:

The results of the mass transfer analysis which covered both bulk and pore gas diffusion accounting for the counterdiffusion of oxygen and water vapor and gas-liquid diffusion indicate that the maximum current density possible with the present perforated air electrode current collector operating with 100% product water removal is limited by the rate of diffusion of oxygen through a thin film of water at the catalyst-electrolyte interface or reaction zone which covers about 0.03% of the total pore geometric surface area. The estimated range of the limiting current density is 70 to 500 amps/ft². The highest experimentally observed limiting current density is 290 amps/ft² with a catalyst containing about 50% by volume wet-proofing agent. Air flowrate must be of sufficient magnitude to remove 100% of the product water from the oxygen electrode and the air reaction passages. Water vapor diffusion from the pores does not become limiting until a current density of 1,450 amps/ft² is reached, a value which is impossible to reach with air. However, the maximum pure oxygen performance at 100% removal of product water by recirculation of the stream and absorption, conden-

4.0 FACTUAL DATA (Cont'd)

sation, or mechanical separation of product water is estimated to be from 330 to 2,380 amps/ft² based on liquid film control. Since water vapor diffusion from the pores is limiting above 1,450 amp/ft², this current density would appear to be the maximum value for pure oxygen under ideal conditions at temperatures up to 130°F.

On this basis, the present perforated metal screen air electrode current collector has high current density capability and is suitable for large size cells. The mode of removal of product water is adaptable for pure oxygen systems also.

The self-diffusion type air electrode is limited by bulk gas diffusion coefficients to a maximum round shape of 7.0 and 3.5 in. in diameter at current densities of 81 and 162 amps/ft², respectively. The corresponding air gap widths are > 0.007 in. < 0.632 in. and > 0.024 in. < 0.316 in. Therefore, this type device is limiting to small sizes and low current densities.

4.4.4.3 Comparison of Water Transport and Evaporation Coefficients

This data indicates that the "GPS" type membrane fuel cell transports and evaporates water into an air stream at about 85% of the pure water rate. The suppression of water vapor pressure at the surface is about 0.96 times the pure water value. Data in the literature (52) indicate that as little as 1% porosity in a plastic film which does not contain water will cause an evaporation rate equal to 90% of the water rate. Since the I. E. M. contain up to 20% water the experimental data are entirely reasonable. The catalyst layer offers essentially no resistance to the transport of water and acts like a pure water surface.

These results are in agreement with the fact that dry I. E. M. cells (0.250A) have been wet with product water by operating at a low air flowrate (wetting condition) until the cell resistance reduces to normal values (0.015A). By flowing air at a high flowrate, wet cells can be dried very quickly as well known.

4.4.4.4 Air Velocity Effects on Water Transport and Evaporation Rate (46)

The empirical equation $k_{H_2O} = 2.95 \times 10^{-6} V^{0.76}$ which represents

the water transport rate through and evaporation from a "GPS" I. E. M. fuel cell in the absence of and very likely with electrochemical reaction is in agreement with $k_{H_2O} = C V^{0.5}$ for laminar air flow parallel to many surfaces, $k_{H_2O} = C V^{0.65}$ for laminar flow perpendicular to

FACTUAL DATA (Cont'd)

various types of surfaces, and for laminar air flow past a surface facing downstream at an angle of 40° $k_{H_2O} = C V^{0.82}$ which is the maximum value. With the 45° air impingement angle a value of $V^{0.58}$ might be expected on the inlet air side and $V^{0.82}$ on the exit side giving an average value of $V^{0.70}$. The slightly higher value is probably due to the effect of the perforation close to catalyst surface. The close agreement between the no E. C. R. and E. C. R. data further substantiate the observation that the catalyst layer offers no additional resistance to water transport or evaporation as was first shown under C.

In view of the nature of the empirical equation, the conclusions presented under section 4.4.4.2, and previous mass transfer analysis (54) of binary gas systems on phenolic type I. E. M. fuel cells at lower current densities, there exists a distinct possibility that the over-all mass transfer mechanism for the oxygen electrode may be represented by a modified mass transfer factor of the form.

$$j' = C Re^{-0.8} \chi_{O_2}^{-1.0}$$

where C is a const., Re is the Reynold's number, and O_2 is the mole fraction of oxygen gas in the liquid film at the catalyst-electrolyte interface. Using the empirical equation, an expression of the form

$$j' = C k_{H_2O}^{-1.315} \chi_{O_2}^{-b}$$

may apply for force convected air systems or any recirculating gas system which removes 100% of the product water from the oxygen electrode for all practical current densities. If a pure oxygen performance of 1,450 amps/ft² could be obtained, the rate of water evaporation would no longer depend on the gas recirculation rate. The possibility of the existence of a mass transfer correlation of this form will be explored and reported in the Final Report as will a similar heat transfer correlation and an over-all correlation of heat and mass transfer mechanisms, if possible in the time remaining under the contract.

On the basis of the water transport and evaporation coefficients obtained for "GPS" membranes, they may be used in a system to conserve product water and humidify reaction feed air. An invention disclosure will be written along these lines in the immediate future.

4.0 FACTUAL DATA (Cont'd)

4.4.5 Specific Conclusions:

1. The new design perforated metal screen air electrode current collector has permitted substantial increases in "GPS"-type ion exchange membrane fuel cell performance on force-convected air at 70° -100° F and hydrogen, i.e. 0.63-0.68 volt D. C. at a current density of 81 amps/ft² and a limiting current density which appears to be 290 amps/ft² mainly due to more uniform evaporation of product water and decreased fixture resistance.

2. The results of a mass transfer analysis which included bulk gas, pore, and gas-liquid diffusion mechanisms indicate that the limiting current density range for force-convected air at 100% removal of product water is from 70 to 500 amps/ft² depending on whether the catalyst is non, poorly, or well wet-proofed. The maximum current densities appear to be limited by the rate of diffusion of oxygen through a thin aqueous film (which covers about 0.03% of the total geometric pore surface area) at the catalyst-electrolyte interface. The corresponding limiting current density range for pure oxygen appears to be 330 to 2400 amps/ft² at 100% removal of product water but may be limited further to 1,450 amps/ft² by water vapor diffusion from the pores. On this basis, the new design perforated screen air electrode current collector is suitable for large size cells and operation at high current densities.

3. A comparison of the rates of water transport and evaporation for "GPS" I. E. M. fuel cell, membrane, and pure water indicate that the fuel cell and membrane rates are about 85% of the pure water rate and that the catalyst layer rate is substantially 100% of pure water.

4. The effect of air velocity on the rate of evaporation of water from a "GPS" I. E. M. fuel cell with or without electrochemical reaction appears to be represented by an empirical equation of the form

$$k_{H_2O} = 2.95 \times 10^{-6} V^{0.76}$$

Based on past and present work, there exists the possibility that the over-all mass transfer mechanism at the oxygen electrode may be represented by a modified mass transfer factor of the form:

$$j'd = C Re^{-0.8} \chi_{O_2}^{-1.00}$$

or

$$j'd = V^{-0.76} \chi_{O_2}^{-b}$$

4.0 FACTUAL DATA (Cont'd)

$$\text{or } j'd = C k_{\text{H}_2\text{O}}^{-1.315} \times \text{O}_2^{-b}$$

4.4.A Addition to TASK IV

AN OPTIMIZING CONTROL DEVICE FOR USE IN LABORATORY EVALUATION OF HYDROGEN-AIR FUEL CELL OPERATION.

T. Hovious

This Section represents an addition to contract requirements as an off-spring of investigations on water transport in membranes, internal cell resistance and the response to temperature and air flow rate.

4.4.A.1 General

This control device is designed to adjust air flow rate to an operating hydrogen-air fuel cell in such a manner as to maintain near optimum DC output voltage at any given current level.

4.4.A.2 Control Mode

A typical fuel cell DC voltage versus total cell water content is illustrated by Figure 4A-1. Cell voltage for a given current output will be less than the maximum attainable if the fuel cell is either too wet or too dry. The solid line curve of Figure 4A-2 illustrates qualitatively the air flow rate required at any given output current so that the water removal rate just equals the water production rate. An air flow rate greater than that given by the solid line curve will decrease the cell moisture content, whereas a smaller air flow rate will allow the cell moisture content to increase. The effects of variation in quantities such as cell vapor pressure suppression, cell operating temperature, and inlet air relative humidity are neglected in the foregoing description.

To illustrate the mode of control to be used, consider the following assumption. A fixed output current of value I (Figure 4A-2) is established. The control would be adjusted so that either air flow rate A or air flow rate B (Figure 4A-2) could exist for the current of value I. Let it also be assumed that at start-up the cell moisture conditions correspond to that of point W₁ (Figure 4A-1) and that the control supplies an air flow rate equal to point A (Figure 4A-2). Thus, the cell water content is too large, but a drying condition has been applied which causes the total cell water content to decrease with time. The control senses this positive rate of change of output

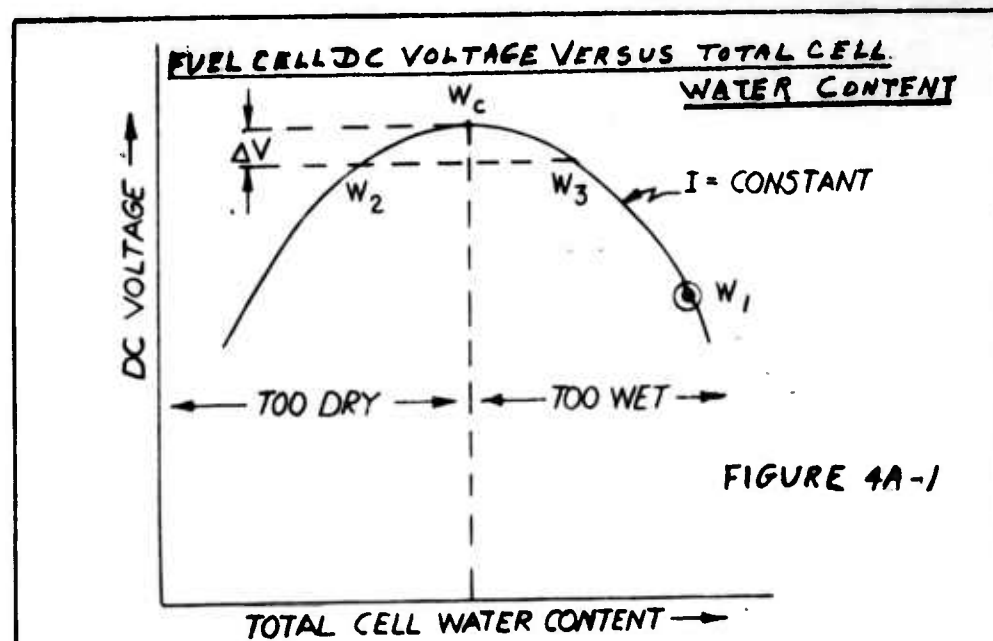


FIGURE 4A-1

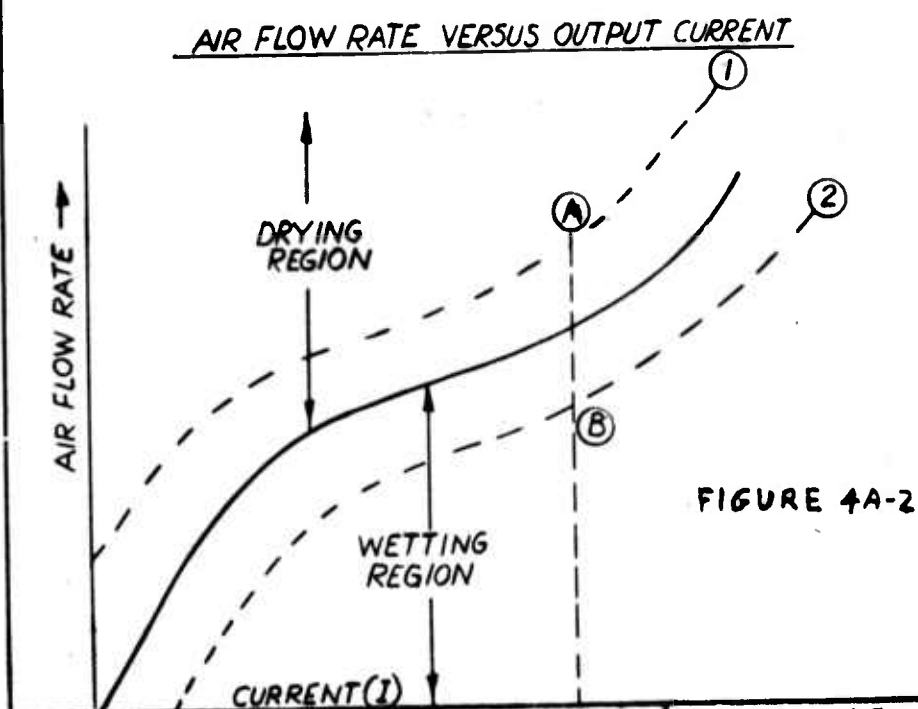


FIGURE 4A-2

Fuel Cell Lab
DECO - G. E. Co.
Lynn, Mass.

FIGURE 4-A

Semi-Annual Summary
Report #2
Contract DA-36-039-
AMC-00095(E)
T. Hevious 6/30/63

FACTUAL DATA (Cont'd)

voltage and maintains the drying air flow rate A (Figure 4A-2). Eventually the cell moisture content decreases to a value W_c (Figure 1) and the output voltage reaches its maximum. As the cell further dries, the output voltage decreases until it has reached an amount equal to ΔV (Figure 4A-1) less than the peak voltage value. This corresponds to a water content W_2 (Figure 4A-1). At this point, the control changes the air flow rate to the wetting condition (point B, Figure 4A-2). The cell water content increases until a water content W_3 (Figure 4A-1) is reached.

At this point, the control flips back to an air flow rate which allows cell drying. Thus, a continuous cycling between cell water content conditions W_2 and W_3 (Figure 4A-1) is maintained. The control will be able to maintain ΔV as small as 0.01 volts if desired.

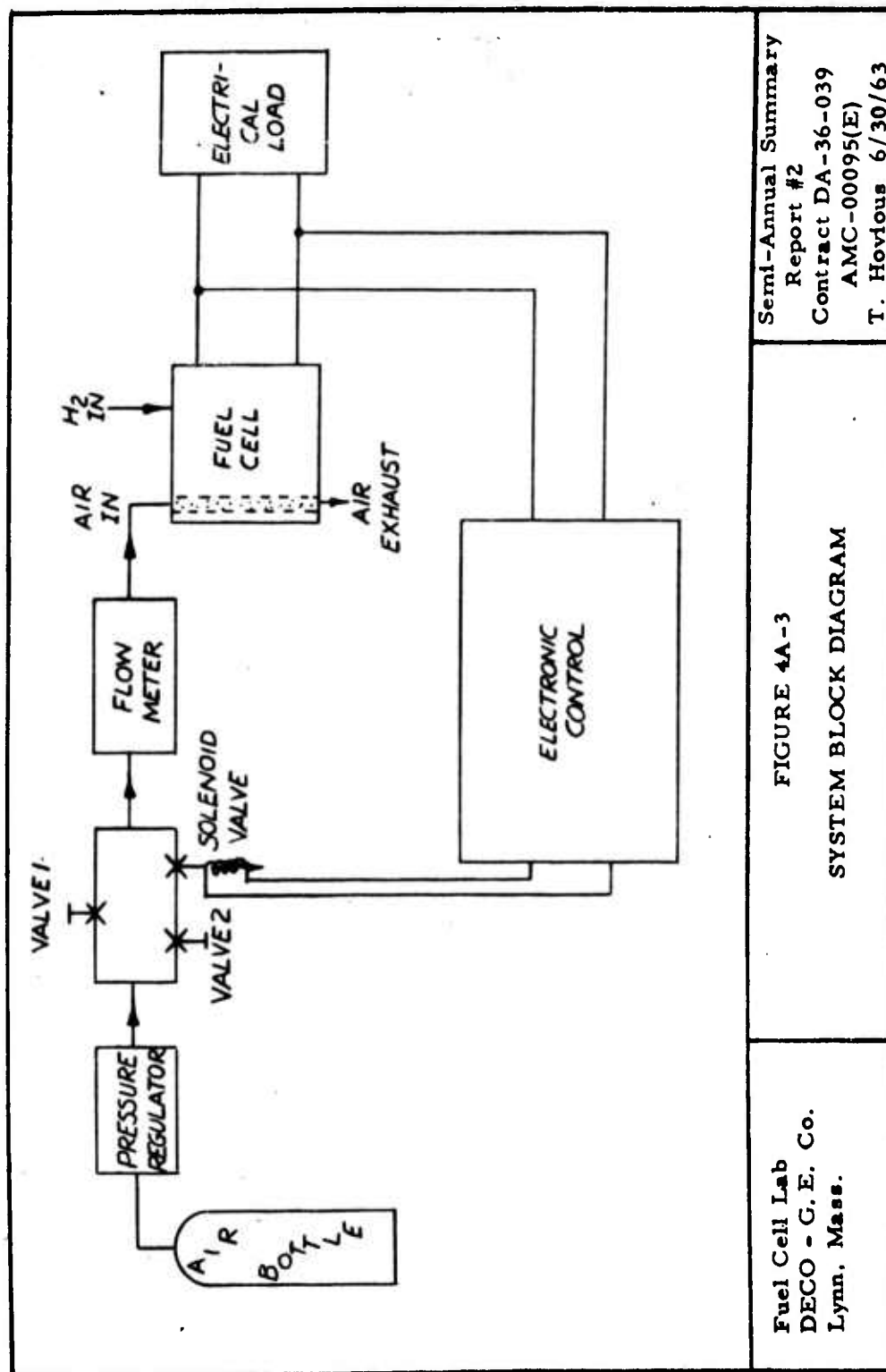
The control also incorporates a timer which operates whenever the rate of change of voltage is negative. If the rate of change of voltage does not become positive within a pre-selected period of time, the control will automatically select the opposite air flow rate condition. This ensures attainment of the proper operating mode when start-up or transient loading upsets the normal control mode.

4.4.A.3

System Description

The system to be used is shown in the block diagram of Figure 4A-3. In using this system, the desired fuel cell output current level is first determined. The drying and wetting air flow rates (points A and B of Figure 4A-2) corresponding to the selected current, I , are then established. The setting air flow rate (point B of Figure 4A-2) is then set by adjustment of valve 1 (Figure 4A-3) with the solenoid operated valve closed. The solenoid operated valve is then opened and valve 2 (Figure 4A-3) is set so that the drying air flow rate (point A of Figure 4A-2) is established. The electronic control will then operate the solenoid valve so as to alternate between drying and wetting air flow rates and maintain the cell water content such as to yield maximum output DC voltage.

This system is simple, and provides for optimizing only at each selected fuel cell output current condition. It does not incorporate automatic adjustment of the air flow rates as the current is varied over a wide range. This air flow rate adjustment must be manually done whenever a major change in output current is made. Automatic compensation for varying electrical loads can be incorporated in the control. The major complication would be that of providing a means of modulating the air flow proportional to an electrical signal.



Semi-Annual Summary
Report #2
Contract DA-36-039
AMC-00095(E)
T. Hovious 6/30/63

FIGURE 4A-3
SYSTEM BLOCK DIAGRAM

Fuel Cell Lab
DECO - G. E. Co.
Lynn, Mass.

4.0 FACTUAL DATA (Cont'd)

4.4.A.4 Operation and Circuitry of the Electronic Control

Operational Control Equations:

The operational equations for amplified A are:

$$\frac{V_A}{V_I} = - \frac{\frac{R_2 \frac{1}{SC_1}}{R_2 + \frac{1}{SC_1}}}{R_1} = \frac{R_2}{R_2 SC_1 + 1} = \frac{R_2}{R_1} \frac{1}{1 + R_2 C_1 S} \quad (\text{IVA-1})$$

where S is the Laplace one-sided operator

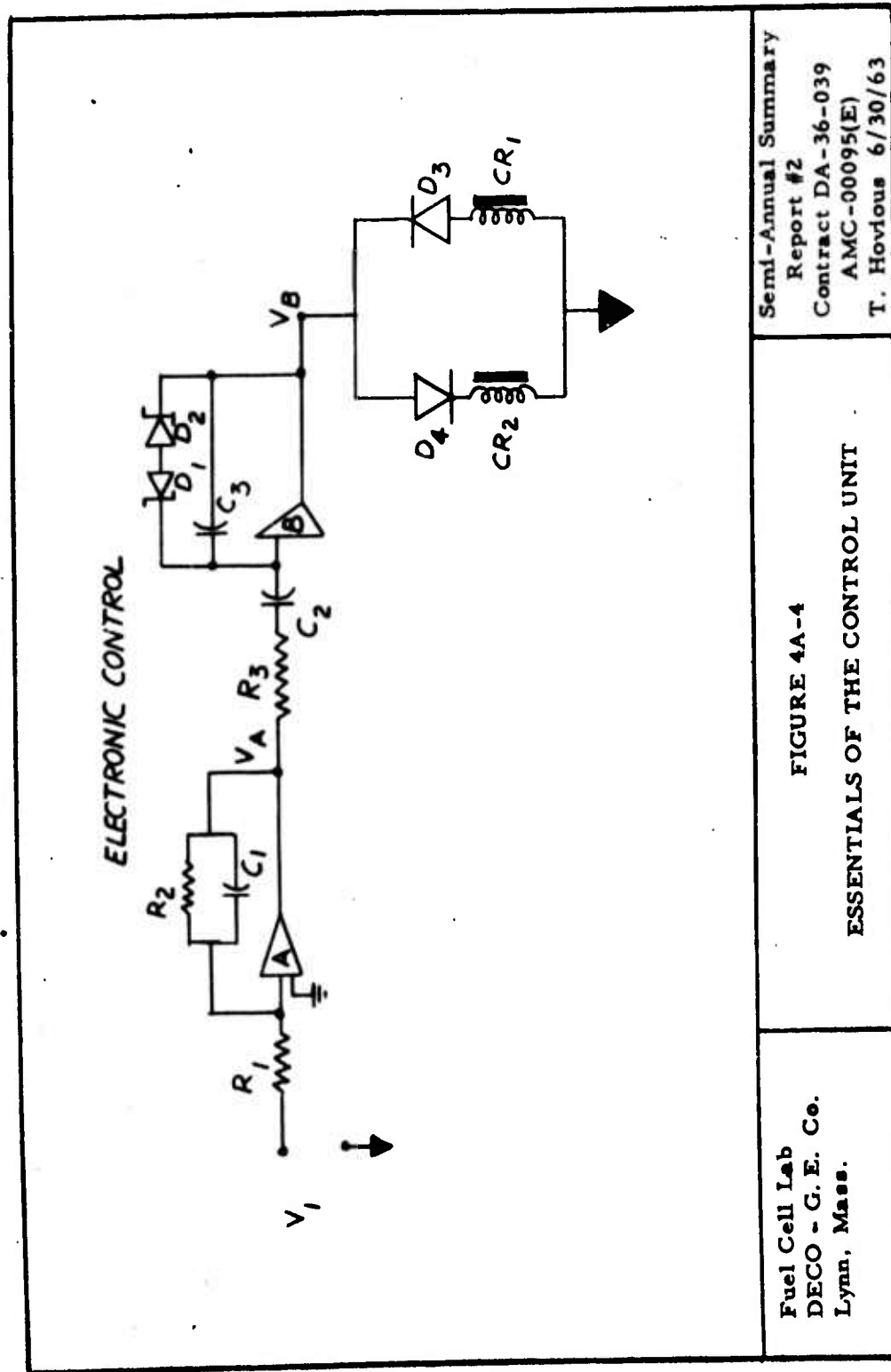
Similarly, where the region of operation is outside of breakdown range of D_1 and D_2 , we conceive the transfer V_B/V_A . Diode D_1 and D_2 are shown in Figure 4A-4 which illustrates the essentials of the control unit.

$$\frac{V_B}{V_A} = - \frac{\frac{1}{SC_3}}{R_3 + \frac{1}{SC_2}} = \frac{1}{SC_3 R_3 + \frac{C_3}{C_2}} = \frac{C_2}{C_3} \left[\frac{1}{SC_2 R_3 + 1} \right] \quad (\text{IVA-2})$$

Consequently, the overall control equation from V_B to V_I is:

$$\frac{V_B}{V_I} = \frac{C_2 R_2}{C_3 R_1} \left[\frac{1}{1 + R_2 C_1 S} \right] \left[\frac{1}{1 + SC_2 R_3} \right] \quad (\text{IVA-3})$$

The transfer function V_B/V_I determines the signal at the logic selection diodes D_3 and D_4 . The gain to DC voltage change is 5000 and this determines the control band sensitivity. A change of 10 millivolts causes V_B to change by 50 volts which is more than sufficient to pull in relay CR_1 or CR_2 depending on the sign of the change in the fuel cell voltage. If the fuel cell voltage increases by 10 millivolts, the relay CR_2 is selected by diodes D_4 and pulls in. Pulling in CR_2 causes no change in the control sequence. When the fuel cell voltage drops by 10 millivolts, diode D_3 selects CR_1 relay and the control sequence begins. Pulling in CR_1 causes the bistable relay LR (Figure 4A-5) to change in state and begins to supply signal power to the time delay circuit composed of the time delay relay TD , the logic diode D_9 and storage



Fuel Cell Lab
DECO - G. E. Co.
Lynn, Mass.

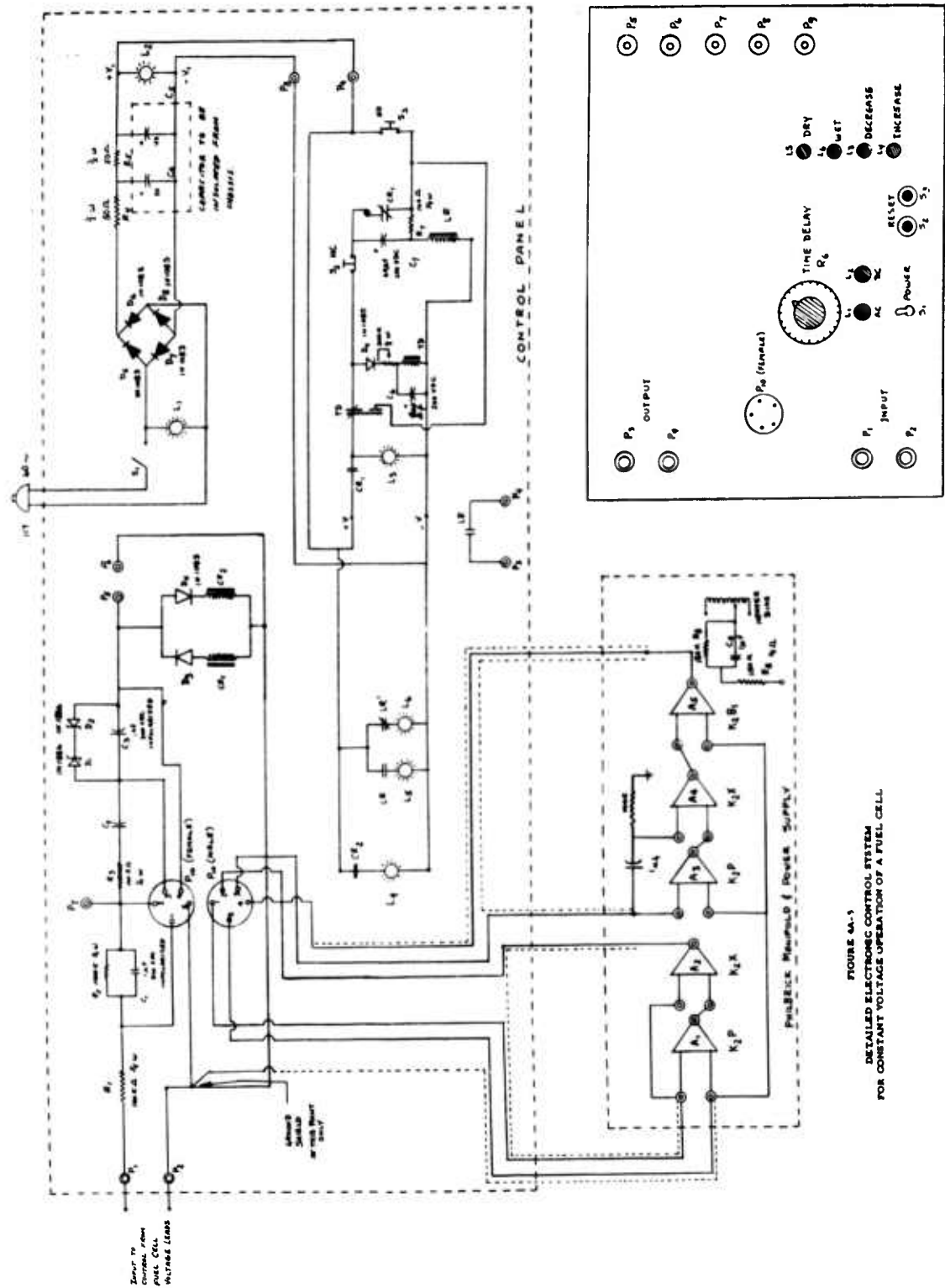


FIGURE 4A-1
DETAILED ELECTRONIC CONTROL SYSTEM
FOR CONSTANT VOLTAGE OPERATION OF A FUEL CELL

CONTROL PANEL LAYOUT

T. C. Hordless
6/30/63

4.0 FACTUAL DATA (Cont'd)

element C₆. If the change in fuel cell voltage reverses sufficiently (i. e. 10 millivolts or greater) to drop out CR₁, then the control returns to its primary state. If the fuel cell voltage continues to drop off for a period greater than the time out period of the time delay, then the time delay relay pulls in, pulsing the bistable relay LR which changes the state of its contacts which changes the air flow rate through activation of the previously mentioned solenoid control valve. This time delayed check is a safety device to insure proper mode of operation under a non steady-state condition. This control is essentially the same as a unit designed and tested to control a hydrogen-oxygen fuel cell by varying mixed water coolant to the cell, thus controlling evaporation of water from the cell. However, the air-breathing cell in the operation described tends to have lower rates of change of voltage with change in control mode than does the hydrogen-oxygen cell described; thus more care was necessary in evaluation of integrator drift problems in the electronic circuitry.

4.5 TASK V:

DESIGN PARAMETERS AFFECTING AIR-OPERATED IEM FUEL CELLS

. D. W. Craft

4.5.1 Introduction:

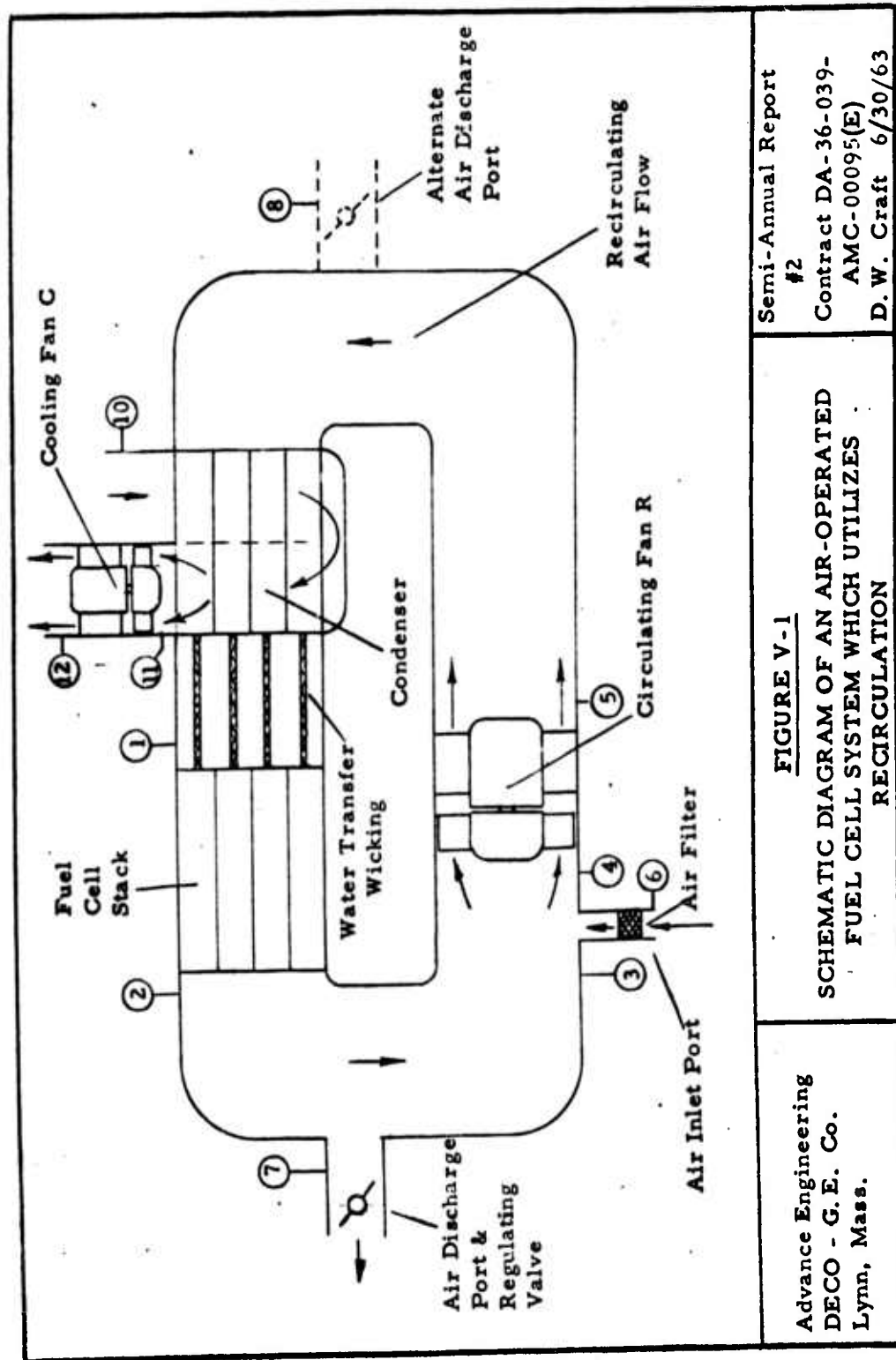
The optimum operation of an IEM fuel cell system on air requires that the following conditions be approached:

1. Removal of the product water from the IEM at the rate of generation.
2. Retention of an optimum water content within the IEM to attain maximum voltage output.
3. Minimization of temperature, partial pressure, water content and voltage gradients within the IEM.

An experimental investigation has been initiated to determine how successful the approach of using a recirculating air flow within a fuel cell system will be in attaining the above requirements.

4.5.2 The Recirculating Air Flow Fuel Cell System

The fuel cell system under consideration is shown in Figure V-1. The gases within the system which are on the air side of the ion exchange



Semi-Annual Report
#2
Contract DA-36-039-
AMC-00095(E)
D.W. Craft 6/30/63

FIGURE V-1
SCHEMATIC DIAGRAM OF AN AIR-OPERATED FUEL CELL SYSTEM WHICH UTILIZES RECIRCULATION

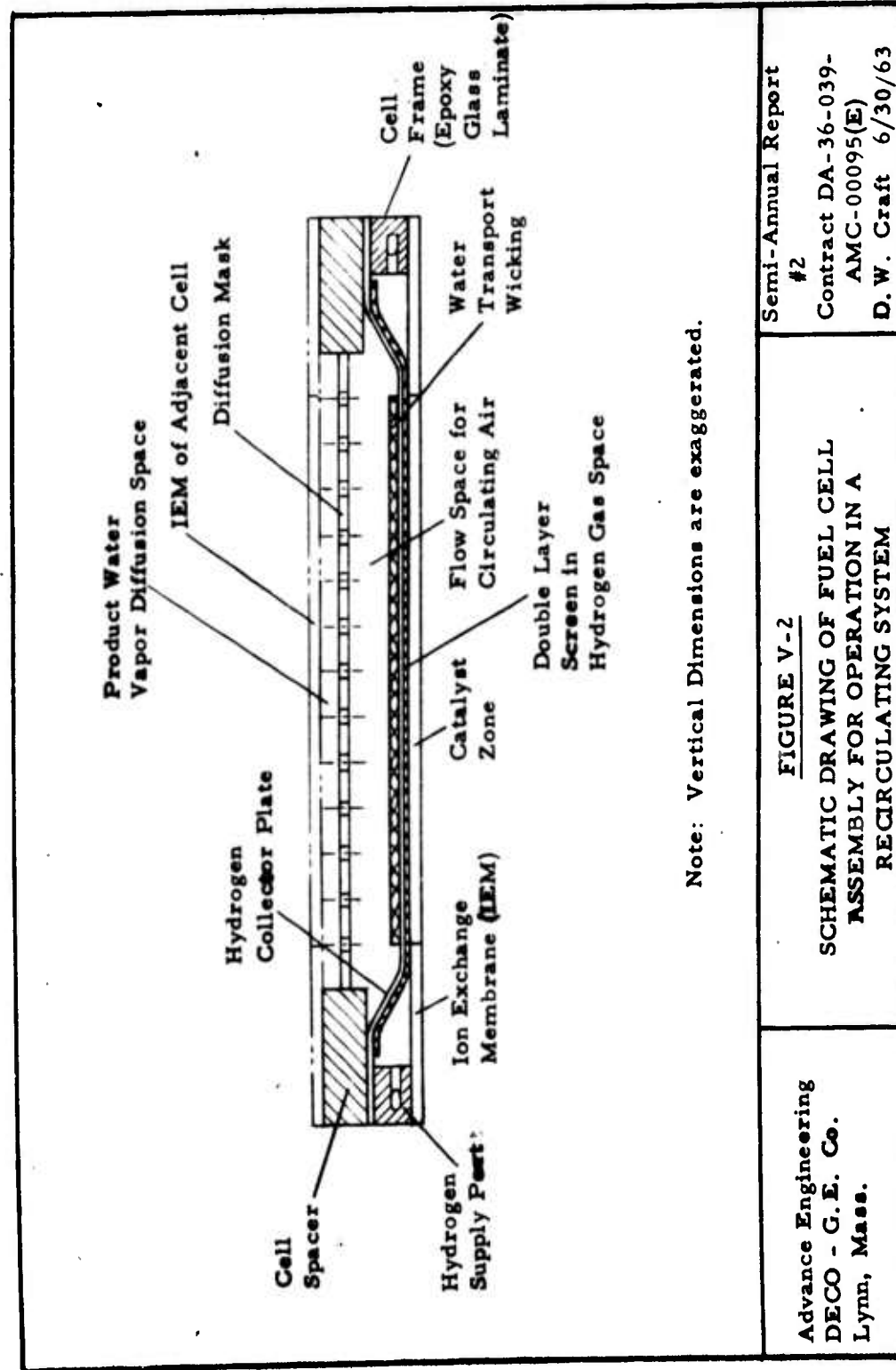
Advance Engineering
DECO - G.E. Co.
Lynn, Mass.

FACTUAL DATA (Cont'd)

membrane (IEM) are continuously recirculated by Fan R in order to minimize temperature and partial pressure gradients and to eliminate the possibility of stagnating the flow in some region of the fuel cell stack.

The gases within the recirculation system will be referred to as air in this discussion since the constituents are the same as air but with a different fractional composition due to the fuel cell reactions. Fan R established static pressures within the recirculating system which are above and below the communicating atmospheric pressure, thus allowing the intake of air at station 6 and the discharge of air at stations 7 or 8. The discharge of air at station 7 is preferable from the standpoint that the oxygen partial pressure is a minimum at this station and therefore represents a minimum flow of oxygen from the system for a given concurrent flow rate of water vapor. Discharge from station 7 allows the establishment of a higher average oxygen partial pressure within the system. The use of station 7 as a discharge location has additional advantages from the standpoint of analysis inasmuch as (1) the recirculation system can be directly compared with a through-flow system (no recirculation or as though there was a blockage at station 3), and (2) the bleed conditions are unaffected by the rate of recirculation. The main reason the recirculation system can minimize the temperature gradients within the fuel cell stack is that the mode of heat rejection is by the evaporation and condensation of water that is retained within the system. The relatively high rate of mass flow in the recirculation circuit (i. e. 100 times the stoichiometric requirement) allows the necessary water for heat rejection to be conveyed in the recirculation loop as water vapor. The air leaving the fuel cell stack is essentially saturated and after additional air is admitted, mixed, and heated by Fan R, the air is still essentially saturated as it enters the condenser. As the recirculation air passes through the condenser, the external cooling air reduces the temperature of the gases and condensation takes place accompanied by a small temperature drop in the recirculating air. The temperature change is small due to the latent heat of vaporization of water.

The water condensed on the condenser surfaces is absorbed by a porous wicking material and the water is transported to the evaporative surfaces of the fuel cell and by capillary conduction through the same wicking material. The evaporative surfaces of the fuel cell assembly, as referred to herein, are the metal current collector plates which form the hydrogen chamber in each fuel cell assembly as shown in Figure V-2. The air side of the IEM is also an evaporative surface, but this surface will not be referred to as such herein,



| | | |
|---|---|--|
| <p>Advance Engineering DECO - G. E. Co. Lynn, Mass.</p> | <p>FIGURE V-2 SCHEMATIC DRAWING OF FUEL CELL ASSEMBLY FOR OPERATION IN A RECIRCULATING SYSTEM</p> | <p>Semi-Annual Report #2 Contract DA-36-039- AMC-00095(E) D.W. Craft 6/30/63</p> |
|---|---|--|

4.0 FACTUAL DATA (Cont'd)

inasmuch as it is planned that in the system under consideration, the rate of evaporation from the IEM will be equal to the rate of product water generation within the air side electrode.

4.5.3 Product Water Management

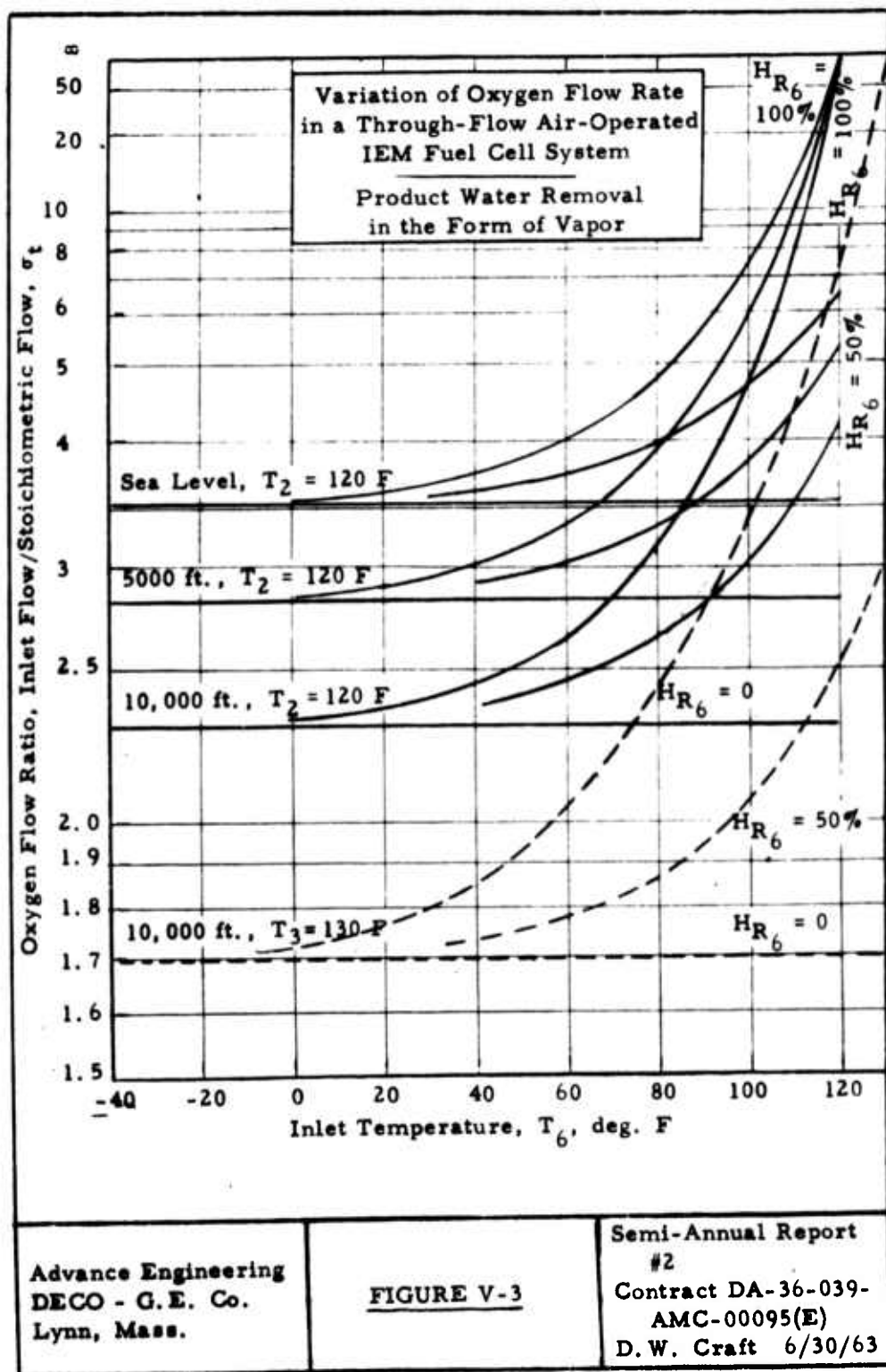
Early air-operated IEM fuel cells required that water be periodically added to the system to offset the excessive drying of the membranes. The excessive drying was caused by a high through-flow rate of air in and out of the system. The high through-flow rate was required for a maximum oxygen partial pressure within the system.

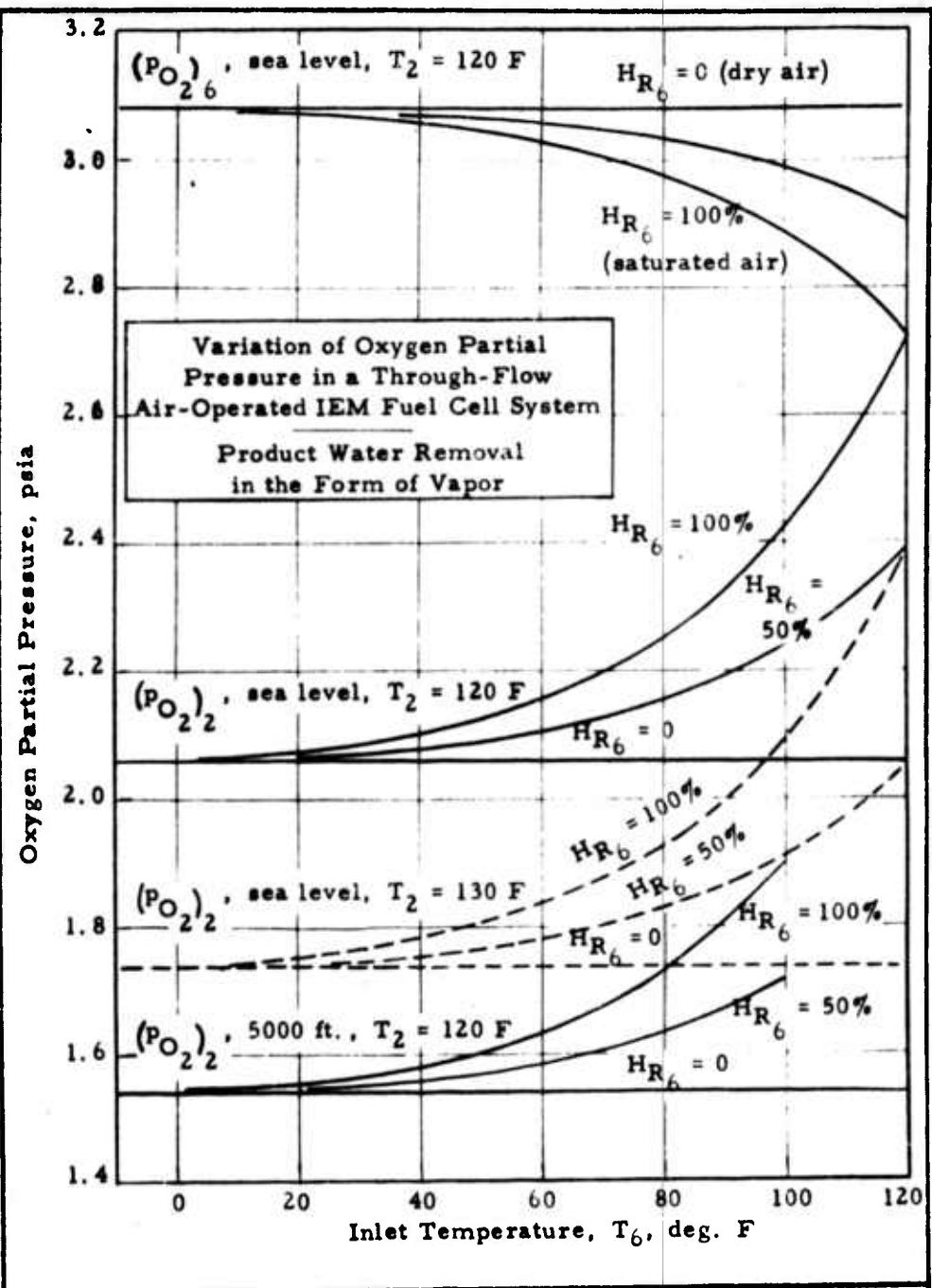
The recirculation system shown schematically in Figure V-1 avoids the necessity for periodic water addition by reducing the through-flow rate of air until the amount of water leaving the system is equal to the rate of product water generation. Appendix V, Sections 1-6, gives an analysis whereby it is shown that the flow rate in and out of the system (through-flow rate) is essentially dependent upon the fuel cell stack operating temperature and the conditions of the entering air.

Figure V-3 shows the variation of the ratio of the through-flow to the stoichiometric air flow with various operating conditions when the product water is removed from the system at the same rate as it is generated. The data in Figure V-3 was calculated from Equation V-22. Figure V-3 shows that if the dry air entered the system, the air flow requirement would only be dependent on altitude (operating pressure) and the stack operating temperature.

The relative humidity HR_6 of the entering air also has considerable influence on the air flow requirement. Figure V-3 is, however, plotted on reciprocal coordinates showing an infinite air flow rate when the stack temperature is equal to the inlet temperature and $HR_1 = 100$ percent. The aforementioned condition is unrealistic since the stack temperature would be above the inlet temperature.

Figure V-4 shows the variation of the oxygen partial pressure at the exit of the fuel cell stack for various air inlet and stack temperature conditions. The data in Figure V-4 was calculated from Equation V-9. Although Equation V-9 is relatively complex, it is shown in Section 5 of Appendix 5 that a linearized version of Equation V-9 (cf Equation V-12 and V-13) is quite accurate.





Advance Engineering
DECO - G.E. Co.
Lynn, Mass.

FIGURE V-4

Semi-Annual Report
#2
Contract DA-36-039-
AMC-00095(E)
D. W. Craft 6/30/63

4.0

FACTUAL DATA (Cont'd)

The linearized versions of Equation V-9 suggest the possibility of providing a control which would (1) compute the oxygen partial pressure required for water balance, (2) sense the true oxygen partial pressure, and (3) adjust the through-flow rate to maintain the proper water balance. The major difficulty of applying Equation V-13, for example, to a control scheme is the complexity of accurately measuring the vapor pressure of the water in the entering air.

A more practical approach which would avoid the necessity of measuring the vapor pressure of water of the entering air would be to alternately produce a wetting and drying condition within the system by controlling the air flow rate. Whether the air flow rate should be increased or decreased could be determined by a measurement of the fuel cell stack internal resistance as a criterion for optimum IEM water content.

4.5.4

Operation of the IEM Fuel Cell in a Uniform Environment

The main benefit of the recirculation of air within the fuel cell system under consideration is to minimize the temperature, partial pressure, water content, and voltage gradients within the IEM. The example given for the heat balance across the fuel cell stack in Section 10 of the Appendix A shows the following conditions entering and leaving the stack for a recirculation rate $\sigma_c = 100$ times the stoichiometric requirement:

$$(p_{O_2})_1 = 2.0897 \text{ psia}$$

$$(p_{O_2})_2 = 2.058 \text{ psia}$$

$$(p_{H_2O})_1 = 1.6023 \text{ psia}$$

$$(p_{H_2O})_2 = 1.6924 \text{ psia}$$

$$t_1 = 118.05 \text{ F}$$

$$t_2 = 120 \text{ F}$$

In a fuel cell system with the same through-flow rate $\sigma_c = 3.42$ as shown by Figure V-3, the oxygen partial pressure at the stack entrance would be $(p_{O_2})_1 = 3.016 \text{ psia}$ as shown in Figure V-4. Also, if all the cooling were done in the system without recirculation with a through-flow rate $\sigma_c = 100$ and no evaporation, the temperature rise would be approximately 13 deg. F rather than 2 deg. F as shown in the above example.

4.0

FACTUAL DATA (Cont'd)

The greatest difficulty in any air operated fuel cell system is to avoid a non-uniform evaporation rate from the IEM since the rate of water redistribution within the IEM is slow and local drying or wetting is to be avoided. Even though the above values of the partial pressure of water vapor seem to differ slightly, the driving force to evaporate water from the IEM is higher at the entrance of the fuel cell stack than it is at the exit. The difference is to be offset by using a mask which has graduated perforations spaced a distance away from the IEM and is to be used for controlling the evaporation rate, thus attaining uniformity. The use of a fixed mask only permits uniformity of evaporation from the IEM at one current density in a given system. Figure V-5 shows a hypothetical polarization curve. The voltage differences at a given current density are proportional to the power output and the heat rejection. Figure V-5 shows that heat rejection due to product water evaporation is proportional to a voltage $\Delta E = 0.228$ volts regardless of current density, whereas the remainder of the heat rejection varies with current density. It is expected that the changes in the required evaporation rates will be offset by the vapor suppression characteristics of the IEM and wicking materials.

4.5.5

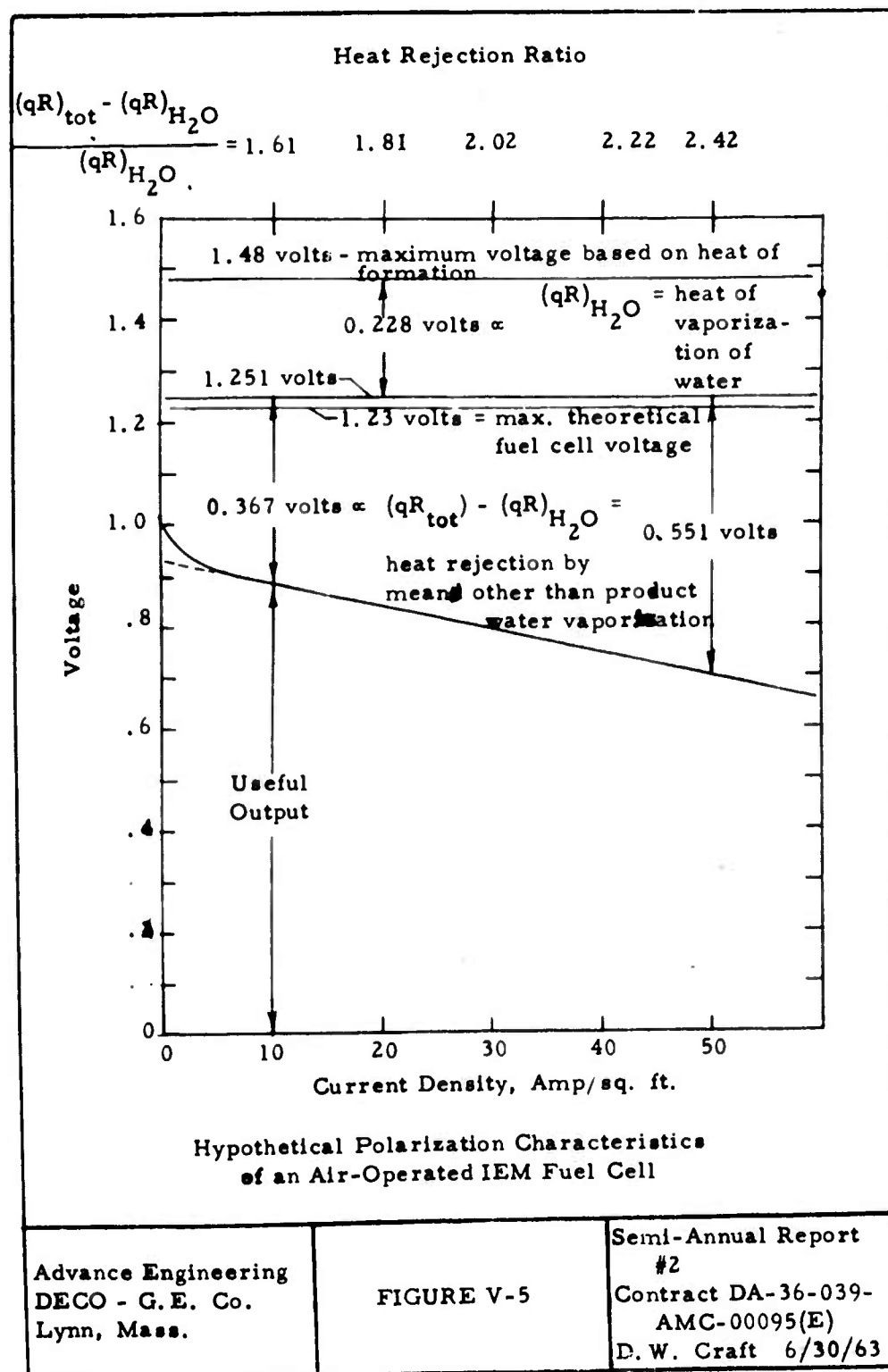
Experimental Equipment for Evaluating the Fuel System with Air Recirculation

Drawings 1076524-536 Sh.1 and Sh.6 show the arrangement of the principal parts of the experimental system for demonstrating the concept of using recirculating air flow.

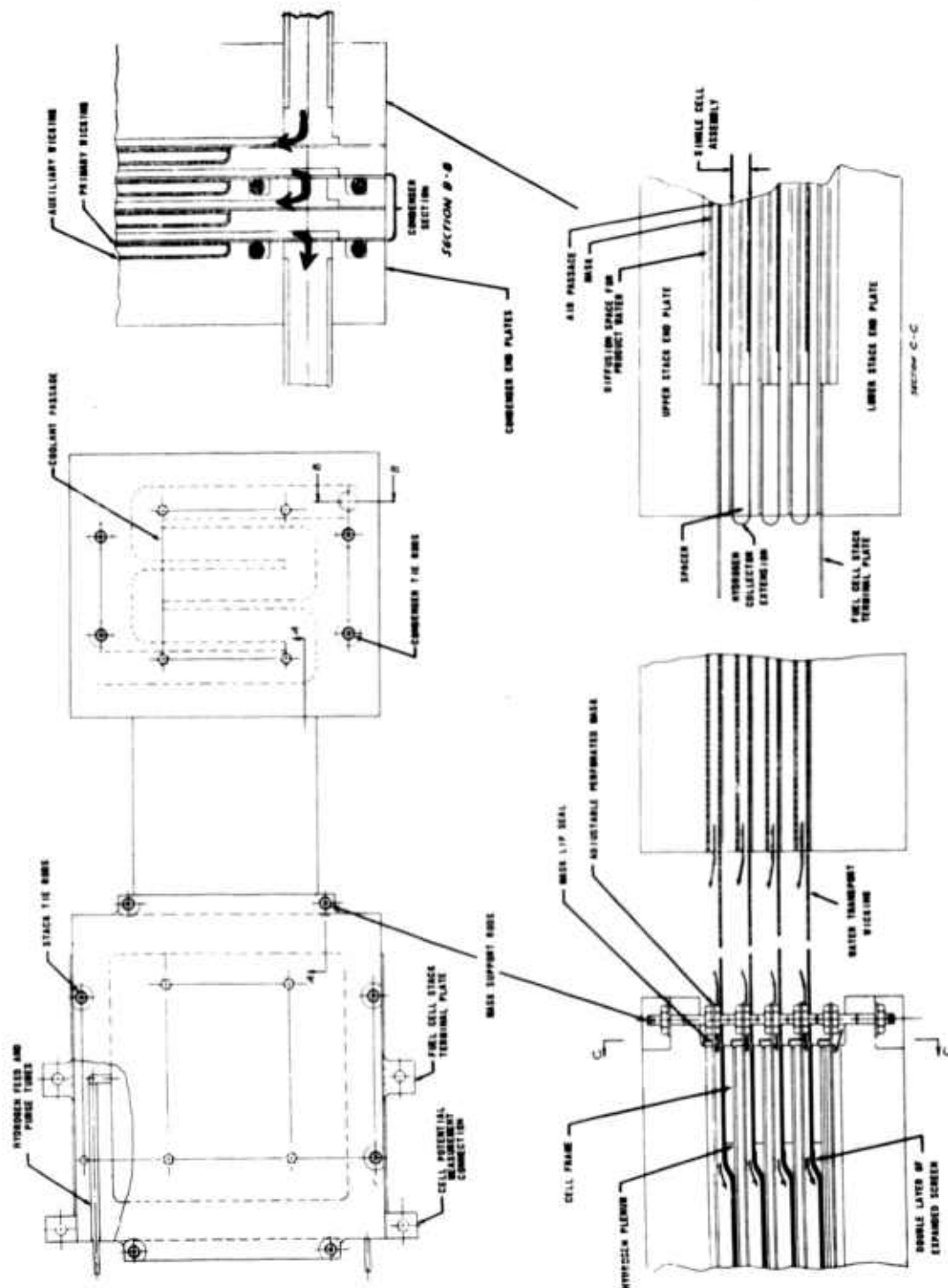
The equipment consists of closed loop air flow system with the air being recirculated by an internal centrifugal fan. The air flow rate can be regulated by adjusting the voltage input to the 6 volt d.c. fan motor. The fan can be located at an alternate position in the system in order to reverse the flow direction of the air through the fuel cell stack and condenser.

The fuel cell stack and the condenser are positioned in a 7 in. I. D. acrylic tube. The recirculation flow path is through a 1.5 in. I. D. acrylic tube which is used to measure the recirculating mass flow.

The fuel stack and condenser units are suspended on circular diaphragms which seal against the 7 in. I. D. acrylic tube where necessary to prevent the recirculating flow from by-passing either unit. Only one sealed diaphragm was needed for the fuel cell stack,







DRWG 1076524-536 SH.6

SECTION A-A

SECTION C-C

EXPERIMENTAL AIR-OPERATED IEM FUEL CELL SYSTEM WITH AIR RECIRCULATION

4.0 FACTUAL DATA (Cont'd)

but two sealed diaphragms were necessary at the condenser to prevent water vapor condensation on the coolant lines and the exterior of the condenser.

Considerable care was taken in the design to insure no uncontrolled air leakage from the system which would make a heat and mass balance difficult. Due to the low power output level of the fuel cell stacks of approximately 9 watts at 50 amps/sq. ft., the closed loop system will be enclosed in a temperature controlled case so that heat leakage will not prevent a reasonably accurate system heat balance.

4.5.5.1 Fuel Cell Stack Design

The experimental fuel cell stack consists of four fuel cells each with 3 in. x 3 in. catalyst areas. Drawing 1076524-536 Sh.6 shows the arrangement of the cells in the stack. The cells are positioned horizontally to facilitate the water transport from the condenser through the wicking.

In order to cool four cells, five air flow passages are required. The uppermost flow passage provides air flow only for cooling the hydrogen collector of the uppermost cell. The lowest air flow passage provides air flow only for evaporating the product water from the lowest cell. A modified mask therefore has to be used for the lowest cell. The two innermost cells will be used for close comparison of performance since the heat transfer conditions for these cells should be reasonably comparable.

4.5.5.2 Fuel Cell Design, Individual Assemblies

The design of individual fuel cell assemblies is best illustrated in Figure V-2 which is actually distorted dimensionally for pictorial purposes. Drawing 1076524-536 Sh.6 shows the details in true proportion.

The hydrogen is supplied through appropriate porting through an epoxy glass laminate frame. A closed hydrogen chamber is formed between a "hat-shaped" titanium-palladium collector plate and the IEM. A standard catalyst and 3 Ta 10-3/0 expanded metal tantalum screens are pressed into each side of the IEM to form the electrode surfaces. The IEM is separated from the hydrogen collector by means of two layers of screens to allow free hydrogen flow to all areas of the anode and provide a minimum distance between the IEM and the cooled hydrogen collector plate.

4.0 FACTUAL DATA (Cont'd)

The air side of the IEM will be maintained at a pressure of approximately 20 in. water above the hydrogen pressure in order to make satisfactory electrical contact between the hydrogen electrode and the double layer of screens.

For a simplified heat transfer analysis, the principal heat generation in the cell may be assumed to be at the air electrode. Approximately one-third of the heat rejection is by means of the evaporation of the product water from the air electrode as shown in Figure V-5. The balance of the heat rejection in the design illustrated in Figure V-2 is by conduction through the IEM, the hydrogen gas gap (approximately 0.007 in.), and the hydrogen collector to the wicking where additional water is evaporated for cooling. At a current density of 50 amps/ft², the temperature drop through the IEM is approximately 0.5 deg. F and the drop through the hydrogen gas gap is approximately 0.05 deg. F.

4.5.5.3 Condenser Design

A water-cooled condenser is used for simplicity in the experimental equipment rather than a more complex gas to gas heat exchanger.

Drawing 1076524-535 Sh.6 shows the outline of one of the coolant passages located in each of four condenser sections. The coolant passages are machined in epoxy glass laminate stock and titanium covers are bonded on to seal the passages against leakage. The condenser coolant passages are connected in series to insure against flow stratification. The individual condenser sections are interconnected by means of "o-ring" seals for easy disassembly and replacement of the wicking. The water coolant flow will only have a temperature rise of 0.1 deg. F with a flow rate of 1 gpm and a fuel cell stack current density of 60 amps/sq. ft.

4.5.5.4 Water Transport Wicking

Woven dacron wicking approximately 0.015 in. thick is used to transport the water from the condenser to the fuel cell stack as shown in Drawing 10765240536 Sh.1 and Sh.6. A continuous strip of wicking is used to transport the water from the metal surface of each condenser passage to the corresponding hydrogen collector plate of each fuel cell passage.

4.0 FACTUAL DATA (Cont'd)

Additional wicking is used to line the epoxy glass laminate surfaces of the condenser flow passages to facilitate the removal of condensed water. The major condensing and evaporative surfaces are arranged on the lower side of the passages to minimize the effects of gravity on the water transport through the wicking. The "hat-shaped" design of the hydrogen collector, however, utilizes gravity to improve the water transport through the wicking.

4.5.5.5 IEM Diffusion Masks

As described in Section 4.5.4, masks with graduated perforations are used to improve the uniformity of evaporation of product water from the entrance to exit of the fuel cell stack. Drawing 1076524-536 Sh.6 shows how the masks are ganged together by supporting screws. The masks can be adjusted uniformly to change the relative spacing of the masks between the evaporative surface and IEM in order to vary the relative evaporation rates from the opposing surfaces.

The masks are made of epoxy glass laminate to eliminate the danger of leakage currents. Lip seals are used on the end of each mask to minimize flow in the vicinity of the IEM.

4.5.5.6 Fuel Cell Stack Current and Voltage Connections

The current collection on the air side is through the tantalum electrode screens. The estimated voltage drop from the center of each cell to the edge is 6 millivolts at 50 amps/ft². The voltage drop would produce a total variation of current density of approximately 5 percent in each cell. It may be possible to later use molybdenum screens to further reduce the current density gradients. This type of current collection is used since the cells are small and maximum freedom of space was desired in the air flow passages for mask change and adjustment. The current collection on the hydrogen side is through the double layer of tantalum screens to the "hat-shaped" hydrogen current collector. The hydrogen current collectors are extended on each side of the cell assemblies and wrapped around the cell assembly spacers to make contact with the screens of the adjacent cells.

Potential connections will be made to each cell in the stack. Cell potential and thermocouple potential connections will be made through a 55 pin, Bendix hermetic connector. The current connections will be made through potted 10-32 threaded posts in the end plate.

4.0 FACTUAL DATA (Cont'd)

4.5.5.7 Mass Flow Measurement

Two alternate methods of measuring the recirculation mass flow rate will be available.

One method will be by means of measuring the pressure drop for a 12 in. distance in a 0.375 in. I. D. tube. A flow rate of 1.5 cfm will produce a pressure drop of approximately 0.1 in. water in this flow meter assuming the flow is essentially laminar.

The alternate device illustrated in Drawing 1076524-536 Sh.6 is a Thomas type meter in which the temperature rise of a heated stream is used to determine the flow rate thermodynamically. The Thomas meter will be constructed of three planes of resistance wire grids. The center grid is to be heated electrically and the additional grids are used as resistance thermometers.

The recirculation mass flow meters are to be calibrated prior to use by means of calibrated rotameters. Rotameters could not be used satisfactorily for measuring the recirculating flow rate due to their relatively high pressure drop.

The flow rate of air into the system is to be measured by a Fischer and Porter Tri-Flat flowmeter with a 0.062 in. dia. spherical float.

4.5.6 Conclusions

The analyses of the air operated IEM fuel cell system with recirculation indicate system feasibility and that a high degree of uniformity of operating conditions can be achieved in this system. More definite conclusions can be made after the experimental results are obtained in the next phase of the work.

4.0 FACTUAL DATA (Cont'd)

4.6 APPENDIXES

- I-1 Micrographs from Adhesion Test
- I-2 The Sharpe and Schonhorn Adhesion Theory
- II-1 No Appendix References
- III-1 Limiting Currents for Various Diffusional Processes
- III-2 Determination of Concentration Distribution in Channels
- III-3 Derivation of Equations for Forced Flow Conditions in Channels with Rectangular Cross-Section.
- IV-1 Heat and Mass Transfer Investigations of the Air-Breathing I. E. M. Fuel Cell
- IV-A No Appendix References
- V-1 through V-10
Heat and Mass Transfer in an Air-Breathing Fuel Cell System with Air Recirculation

4.0 FACTUAL DATA (Cont'd)

APPENDIX I-1

MICROGRAPHS FROM ADHESION TEST

This section comprises additional micrographs of "scratches" made with the adhesion-testing device of Photograph I - 1, and are described in detail in Section 4. 1. 3. 3.

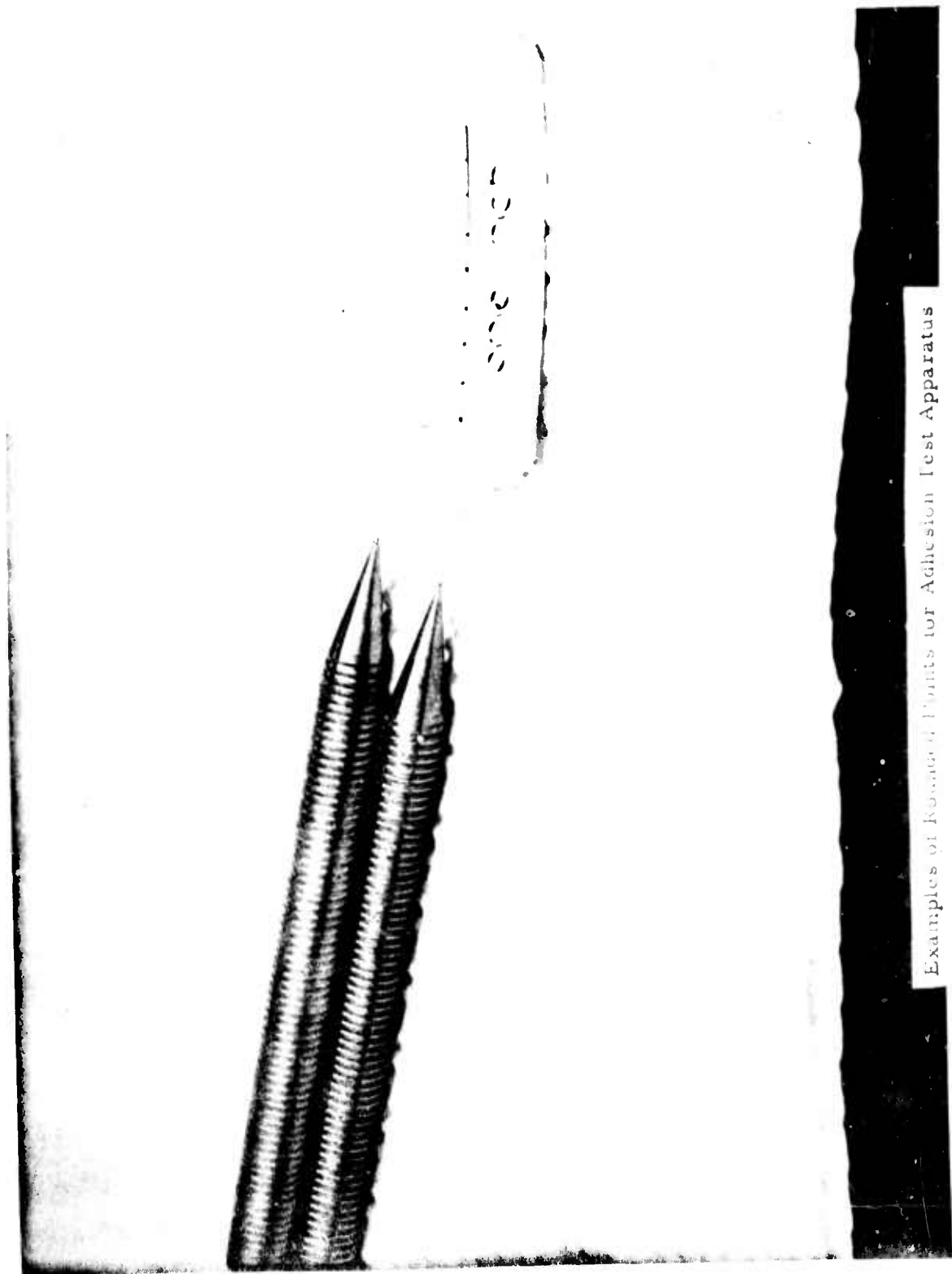
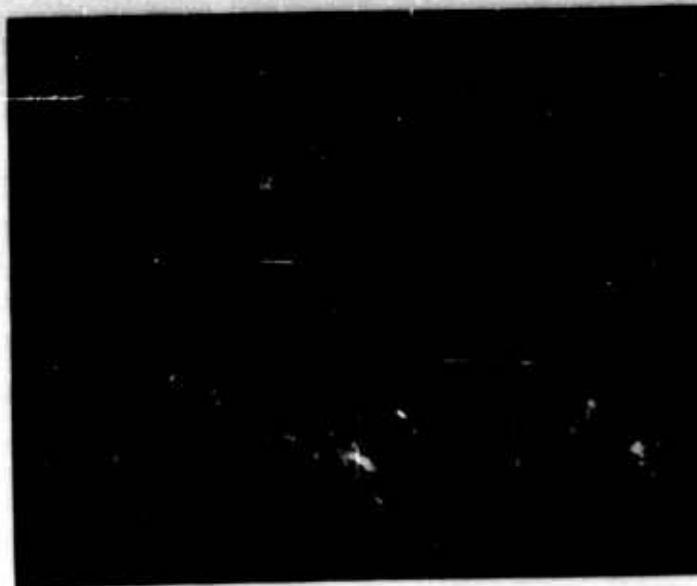


Photo I-8
-132-

A 12602

Examples of Rounded Points for Adhesion Test Apparatus



**Photo I-9
Trans.
Light**



**Photo I-10
Reflected
Light**

Fuel Cell Laboratory
DECO - G. E. Co.
Lynn, Mass.

**Photos I-9 and I-10
Micrographs of
Adhesion Test
Grooves (X200)**

Semi-Annual Summary
Report #2
Contract DA-36-039-
AMC-00095(E)
S. Krumbein 6/30/63



Photo I-11
Trans.
Light
(X80)



Photo I-12
Trans.
Light
(X200)

Fuel Cell Laboratory
DECO - G.E. Co.
Lynn, Mass.

Photos I-11 and I-12
Micrographs of
Adhesion Test
Grooves

Semi-Annual Summary
Report #2
Contract DA-36-039-
AMC-00095(E)
S. Krumbein 6/30/63



Photo I-13
Trans.
Light
(X80)

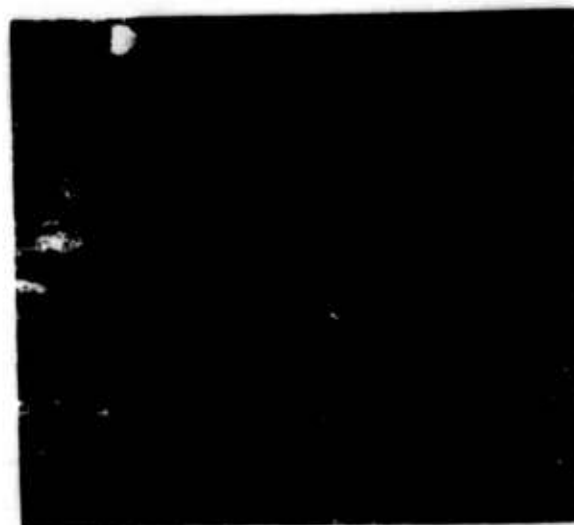


Photo I-14
Reflected
Light
(X200)

Fuel Cell Laboratory
DECO - G. E. Co.
Lynn, Mass.

Photos I-13 and I-14
Micrographs of
Adhesion Test
Grooves

Semi-Annual Summary
Report #2
Contract DA-36-039-
AMC-00095(E)
S. Krumbein 6/30/63

4.0 FACTUAL DATA (Cont'd)

APPENDIX I-2

THE SHARPE AND SCHONHORN ADHESION THEORY

According to Sharpe and Schonhorn (21), there exists a one-to-one correspondence between thermodynamic spreading and strong adhesion. The former concept is usually expressed as requiring the spreading coefficient, S_{sp} to be positive or zero (22). Since:

$$S_{sp} = \gamma_s - (\gamma_{L_2 V_2} + \gamma_{S_1 L_2}) \quad (I-12)$$

the liquid, L_2 , will only spread on the solid, S_1 , if:

$$\gamma_{S_1} \geq \gamma_{L_2 V_2} + \gamma_{S_1 L_2} \quad (I-13)$$

i. e. if the sum of the surface free energies of the liquid, L_2 (in contact with its saturated vapor), and that of the solid/liquid interface is less than that of the solid.

This can be shown, from the Young-Dupre equation (22), to be thermodynamically equivalent to having the work of adhesion, W_{adh} , equalling or exceeding the work of cohesion of the spreading substance, i. e.:

$$W_{adh} \geq W_{coh} \quad (I-14)$$

so that strong adhesion can only occur when the contact angle is zero and the liquid can spread on (or "wet") the solid (21). Since neither γ_{S_1} , nor $\gamma_{S_1 L_2}$ can be directly determined in any satisfactory manner, the empirical, but operationally-useful concept of critical surface tensions (19) was adapted by these authors in the form:

$$\gamma_{c(S_1)} \geq \gamma_{L_2 V_2} \quad (I-15)$$

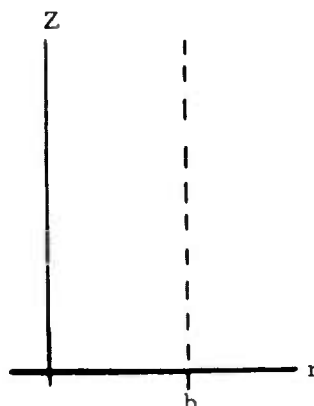
along with the further assumption of approximate equality between γ_c and γ_{LV} for the solid and fluid forms, respectively, of the same material.

APPENDIX III-1

LIMITING CURRENTS FOR VARIOUS DIFFUSIONAL PROCESSES

In order to restrict possibilities of rate-controlled gas diffusional processes, various differential equations have been solved and limiting current calculated for defined systems and for assumed boundary conditions.

1. Cylindrical Diffusion: Linear diffusion of O_2 in the $O_2/N_2/H_2O$ system for electrodes exposed to semi-infinite space, (Figure III- 1B - 1) does not adequately represent the process, since radial diffusion can also occur. For the following boundary conditions:



$$c(r, \infty) = C^0$$

$$C(r, 0) = 0$$

$$C(b, z) = C^0$$

the solution of Laplace's eqn.:

$$\frac{d^2c}{dr^2} + \frac{1}{r} \frac{dc}{dr} + \frac{d^2c}{dz^2} = 0$$

$$C = C^0 \left\{ 1 - 2 \sum_{m=1}^{\infty} \frac{J_0(\lambda_m r/b)}{\lambda_m J_1(\lambda_m)} e^{-\frac{\lambda_m}{b} z} \right\} \quad \text{becomes} \quad \text{(III-20)}$$

where C = partial pressure, i. e. p_{O_2}
 C^0 = bulk partial pressure, p_{O_2}
 λ_m = roots of $J_0(\lambda_m)$

The local current density becomes:

$$j(r) = nFD \left| \frac{dc}{dz} \right|_{z=0} = \frac{2nFDC^0}{b} \sum_{m=1}^{\infty} \frac{J_0(\lambda_m r/b)}{J_1(\lambda_m)} \quad \text{(III-21)}$$

and the total current:

$$I = 2\pi \int_0^b r j(r) dr = 4\pi nFDC^0 \sum_{m=1}^{\infty} \frac{1}{\lambda_m} \quad \text{(III-22)}$$

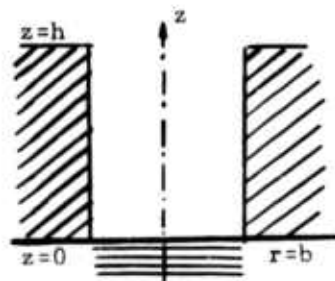
The previous result yield current dependence on electrode diameter rather than surface. In fact, the boundary conditions suggest that a large contribution to electrode current is due to radial diffusion. The thickness of the diffusion layer as determined from:

$$I = nFDA \left. \frac{dc}{dz} \right|_{z=0} = nFDA \frac{C^0 - C}{\delta} \quad (\text{III-23})$$

$$\text{becomes: } \delta = b/4 \quad (\text{III-24})$$

The total current $I = 4000$ mA for an electrode surface of 0.7 cm^2 ($D = 0.25 \text{ cm}^2/\text{sec.}$, $n = 4$, $C^0 = 0.910^{-5}$) and for air, whereas the measured value is ≈ 100 mA.

2. Cylindrical Diffusion In A Pore: Analogous to case 1, would be the cylindrical diffusion in a pore. However, the B. C. now becomes:



$$C(r, h) = C^0$$

$$C(r, 0) = C_0^0$$

$$C(b, z) = 0$$

and the following concentration distribution can be obtained:

$$C = 2 \sum_{m=1}^{\infty} \frac{J_0(\lambda_m r/b)}{\lambda_m J_1(\lambda_m)} \left\{ C_0^0 \cosh(\lambda_m z/b) + \frac{C^0 - C_0^0 \cosh(\lambda_m h/b)}{\sinh(\lambda_m h/b)} \sinh(\lambda_m z/b) \right\} \quad (\text{III-25})$$

where the condition $C_0^0 = 0$ becomes a special case of eqn. III-25.

The local current density becomes:

$$i(z) = -nFD \left. \frac{dc}{dr} \right|_{r=b} = \frac{2nFD}{b} \sum_{m=1}^{\infty} C_0^0 \cosh(\lambda_m z/b) + \frac{C^0 - C_0^0 \cosh(\lambda_m h/b)}{\sinh(\lambda_m h/b)} \times \sinh(\lambda_m z/b) \quad (\text{III-26})$$

and the total pore current becomes, for the case $C_0^0 = 0$

4.0

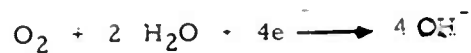
FACTUAL DATA (Cont'd)

$$I(\text{pore}) = 4\pi nFD_e bC^\circ \sum_{m=1}^{\infty} \frac{\cosh(\lambda_m h/b) - 1}{\lambda_m \sinh(\lambda_m h/b)} \quad (\text{III-27})$$

where D_e represents an effective diffusion coefficient. Thus the pore current will depend on pore diameter and on a function of h/b . If the dimensionless group $(\lambda_m h/b)$ is large, eqn. III-27 can be reduced to eqn. III-22 derived above.

3. Diffusion through a liquid layer including particles.

The rate for cathodic oxygen reduction, according to:



can be expressed for large i_c values as:

$$i = nFAk_1 (\text{H}_2\text{O})^2 e^{-\frac{\beta nF}{RT} E} \quad (\text{III-28})$$

In fact, in acidic media for pressures up to 70 atm., Krasilschchikov (35) and Winkelmann (36) have shown that:

$$i_c = kC e^{-\frac{(1-\alpha)F}{RT} E} \quad (\text{III-29})$$

The two eqn. become identical if $k/k_1 = \eta FA (\text{H}_2\text{O})^2$ and if $\beta n = 1 - \alpha = 0.5$ as determined by these authors. Eqn. III-28 can be rewritten, if related to equilibrium conditions, as:

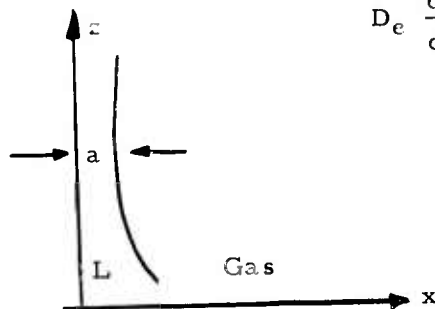
$$I = nFA \left(C_o / C_c \right) C e^{\frac{\alpha nF}{RT} \eta} \quad (\text{III-30})$$

where C = actual O_2 conc.

C_o = equilibrium O_2 conc.

for a one-dimensional analysis:

$$D_e \frac{d^2 c}{dx^2} = \frac{i}{nF} \frac{1}{K} \quad (\text{III-31})$$



D_e = effective diffusion coefficient
 i = current/area
 k = volume/area = cm, represents a property of the medium, as already considered by C. Wagner (40)

4.0

FACTUAL DATA (Cont'd)

$$\text{If: } B^2 = \frac{1}{D_e} \frac{1}{K} \frac{i_e}{C_o} e^{\frac{\alpha n F}{RT} \eta} \quad (\text{III-32})$$

eqn. III-31 becomes:

$$\frac{d^2 c}{dx^2} - B^2 C = 0 \quad (\text{III-33})$$

Solution of eqn. III-33 and subsequent differentiation to determine rates, yields:

$$I = n F D_e S C_o B \tanh (Bd) \quad (\text{III-34})$$

where S represents the transfer area.

If $Bd \gg 0$,

$$I > S = n F (D_e C_o i_o / K)^{1/2} e^{\frac{\alpha n F}{RT} \eta} \quad (\text{III-35})$$

suggesting a current-dependence on $D_e^{1/2}$ and on the electrode property, i.e. thickness of the film or structure of the electrode.

APPENDIX III-2

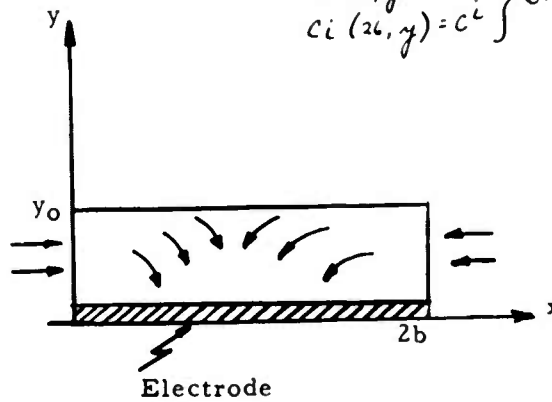
DETERMINATION OF CONCENTRATION DISTRIBUTION IN CHANNELS

$$\nabla^2 C_i = 0 \quad (\text{III-36})$$

$$\sum_i C_i = 1 \quad (\text{III-37})$$

C_i represents partial pressures in the three component systems.
Boundary conditions are:

$$\left. \begin{aligned} C_i(0, y) &= C_i^0 \\ C_i(2b, y) &= C_i^0 \end{aligned} \right\} \text{B.C. 1}$$



$$\left. \begin{aligned} C_{O_2}(x, 0) &= 0 \\ C_{N_2}(x, 0) &= 1 - f(\tau) \\ C_w(x, 0) &= f(\tau) \end{aligned} \right\} \text{B.C. 2}$$

$$\left. \frac{dC_{O_2}}{dy} = \frac{dC_{N_2}}{dy} \right|_{y=y_0} = 0 \quad \text{B.C. 3}$$

$$C_{O_2} + C_{N_2} \Big|_{y=y_0} = 1 - g(\tau) \quad \text{B.C. 4}$$

The concentration of component (i) is related to the partial pressure by:

$$C_i = \frac{n_i}{V} = \frac{P_i}{RT} \quad (\text{III-38})$$

Solution of equation III-36 are, for the different components:

$$C_{O_2} = C^0 \left[1 - \sum_{n=1} A_n \sin \alpha_n x (\cosh \alpha_n y - \tanh \alpha_n y_0 \sinh \alpha_n y) \right] \quad (\text{III-39})$$

$$C_{N_2} = C^0 - \sum_{n=1} A_n \sin \alpha_n x \left[(C^0 - 1 + f(\tau)) \cosh \alpha_n y + \left(\frac{g(\tau) - f(\tau) \cosh \alpha_n y_0}{\sinh \alpha_n y_0} + C^0 \tanh \alpha_n y \right) x \sinh \alpha_n y \right] \quad (\text{III-40})$$

$$C_w = \sum_{n=1} A_n \sin \alpha_n x \left[\frac{g(\tau) - f(\tau) \cosh \alpha_n y_0}{\sinh \alpha_n y_0} \sinh \alpha_n y + f(\tau) \cosh \alpha_n y \right] \quad (\text{III-41})$$

4.0 FACTUAL DATA (Cont'd)

with

$$A_n = \frac{(-1)^{n-1}}{b\alpha_n} \quad \alpha_n = \frac{n\pi}{2b}$$

Local current densities can now be obtained from:

$$j(x) = -nFD \left. \frac{dC_{O_2}}{dy} \right|_{y=0} \quad (\text{III-42})$$

and are, (for O_2 diffusion)

$$j(x)_{O_2} = -n'FDC^0 \sum_{n=1} \alpha_n A_n \sin \alpha_n x \tanh \alpha_n y_0 \quad (\text{III-43})$$

and for H_2O diffusion

$$j(x)_w = -n'FD \sum \alpha_n A_n \sin \alpha_n x \left[\frac{g(r) - f(r) \cosh \alpha_n y_0}{\sinh \alpha_n y_0} \right] \quad (\text{III-44})$$

Average channel current densities are:

$$J_{AVE. O_2} = \frac{n'FDC^0}{b\pi} \sum_{n=1} \frac{[(-1)^{n-1}]^2}{n} \tanh \left(n\pi \frac{y_0}{2b} \right) \quad (\text{III-45})$$

and

$$J_{AVE H_2O} = \frac{n'FD}{b\pi} \sum_{n=1} \frac{[(-1)^{n-1}]^2}{n} \left[\frac{g(r) - f(r) \cosh \alpha_n y_0}{\sinh \alpha_n y_0} \right] \quad (\text{III-46})$$

APPENDIX III-3

DERIVATION OF EQUATIONS FOR FORCED FLOW CONDITIONS
IN CHANNELS WITH RECTANGULAR CROSS-SECTION. DETER-
MINATION OF LIMITING CURRENT DENSITIES.

From a general continuity equation for transport processes:

$$V_x \frac{dc}{dx} + V_y \frac{dc}{dy} = D \left(\frac{d^2c}{dx^2} + \frac{d^2c}{dy^2} \right) \quad (\text{III-47})$$

based on channel geometry described in Figure III-23 and taking into account simplifying assumptions, i. e.

$$V_y \frac{dc}{dy} = \frac{d^2c}{dx^2} = 0 \quad (\text{III-48})$$

a general equation can be obtained to describe diffusional processes in the channel:

$$V_x \frac{dc}{dx} = D \frac{d^2c}{dy^2} \quad (\text{III-49})$$

where V_x is only y -dependent, and has to satisfy the B. C. (Figure III-23):

$$\left. \begin{array}{l} V_y = 0 = V_{y=y_0} = 0 \\ V_{y=y_0/2} = V_{\text{MAX}} \end{array} \right\} \text{B.C. 1}$$

D represents the diffusion coefficient of the binary system N_2/O_2 , the concentration c is related to the partial pressure of oxygen by means of

$$p = cRT \quad (\text{III-50})$$

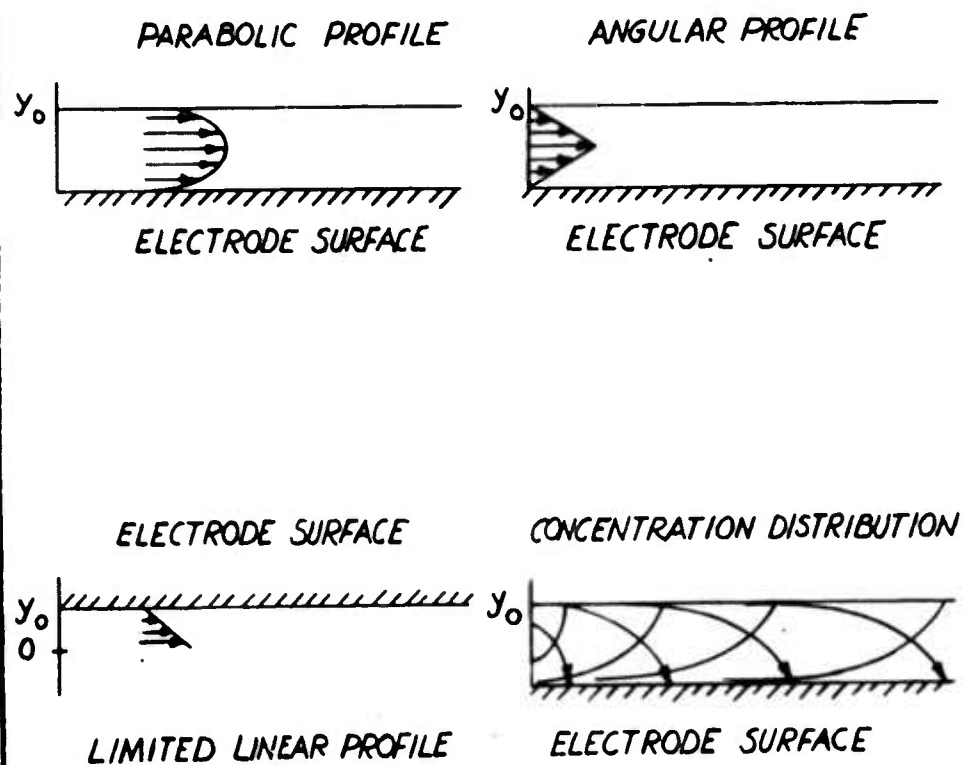
Analytical solutions of eqn. III-49 are possible, in principle, providing V_x is a simple function of y . Different assumptions regarding such velocity profile under laminar flow conditions will be considered.

1. Parabolic Velocity Profile represented by:

$$V = ay(y_0 - y) \quad (\text{III-51})$$

and satisfying B. C. 1, yields:

$$V_{\text{MAX}} = ay_0^2/4 \quad (\text{III-52})$$



Fuel Cell Lab
DECO - G. E. Co.
Lynn, Mass.

FIGURE III-23
VELOCITY PROFILE
AND BOUNDARY
CONDITIONS

Semi-Annual Summary
Report #2
Contract DA-36-039-
AMC-00095(E)
J. A. - H. M. 6/30/63

FACTUAL DATA (Cont'd)

Conservation of volumetric flow rates (nearly correct for already low flow rates):

$$Q = \int_S V_{AVE} ds \quad (III-53)$$

allows to calculate

$$V_{AVE} = \frac{2}{3} V_{MAX} \quad (III-54)$$

yielding the modified eqn.:

$$\frac{6 V_{AVE}}{D y_0^2} y (y_0 - y) \frac{dc}{dx} = \frac{d^2 c}{dy^2} \quad (III-55)$$

The change of variable $y/y_0 = y_1$ and adoption of the dimensionless group:

$$Re Sc \frac{D V_{AVE}}{D} = \frac{4 R_H V_{AVE}}{D} \quad (III-56)$$

where the hydraulic radius

$$R_H = \frac{2 W y_0}{W + y_0} \quad \begin{array}{l} W = \text{channel width,} \\ y_0 = \text{channel height} \end{array} \quad (III-57)$$

yields simplified differential equation III-59.

If $y_0 \ll W$ eqn. III-55 becomes:

$$y_1 (1 - y_1) \frac{dc}{dx} = \frac{1}{3 y_0 (Re Sc)} \frac{d^2 c}{dy_1^2} \quad (III-58)$$

Now with the change of variable: $X_1 = x/y_0$, and defining $3 Re Sc = N$;

$$y_1 (1 - y_1) \frac{dc}{dX_1} = \frac{1}{N} \frac{d^2 c}{dy_1^2} \quad (III-59)$$

with the following B. C.:

$$\left. \begin{array}{l} c = 0 \text{ at } y_1 = 0 \text{ and } X_1 \gg 0 \\ c = c^0 \text{ at } X_1 < 0 \text{ and any } y_1 \end{array} \right\} \text{B.C. 2 a}$$

Eqn. III-59 does not yield an analytical solution. However, numerical solutions by iteration techniques would be possible. No attempt has been made to apply such techniques.

4.0

FACTUAL DATA (Cont'd)

Simpler differential equations can be derived if non-parabolic velocity profiles are assumed.

2. Angular Velocity Profile

Close approximation to parabolic profiles are obtained from:

$$V = V_{MAX} (1 - y_1^2) \quad (III-60)$$

(see figure III-23)

$$\text{where: } V_{AVE} = \frac{2}{3} V_{MAX} \quad (III-61)$$

For $X_1 = X/y_0$ and $\frac{3}{16} (ReSc) = N$, an eqn. similar to eqn. III-58 can be derived:

$$(1 - y_1^2) \frac{dc}{dx_1} = \frac{1}{N} \frac{d^2c}{dy_1^2} \quad (III-61)$$

with the following B. C.

$$\left. \begin{array}{l} c = 0 \text{ at } y_1 = +1 \text{ and } x_1 \geq 0 \\ c = c^0 \text{ at } x_1 < 0 \text{ and any } y_1 \end{array} \right\} \text{B.C.2}$$

By rearrangement of variables, the dimensionless group N can be eliminated to yield

$$(1 - y_1^2) \frac{dc}{dx_2} = \frac{d^2c}{dy_1^2} \quad (III-62)$$

This differential eqn. allows to separate variables to yield:

$$\frac{X'}{X} = \frac{Y''}{(1 - y_1^2)Y} = -\lambda \quad (III-63)$$

requiring the solution of:

$$Y'' + \lambda(1 - y_1^2)Y = 0 \quad (III-64)$$

with: $Y(1) = Y'(1) = 0$, which could be appreciably simplified if $Y(\pm 1) = Y''(\pm 1) = 0$ suggesting a plane of symmetry at $y_1 = 0$. Practically, this would suggest to determine limiting current densities for two parallel flat electrodes. If now,

4.0

FACTUAL DATA (Cont'd)

$$y^2 = \pi \text{ and } Y = \pi^{-\frac{1}{4}} Z \quad (\text{III-65})$$

it is possible to show that equation III-66:

$$\frac{d^2 Z}{d\pi^2} + \left(-\frac{\lambda}{4} + \frac{\lambda}{4\pi} + \frac{3}{16\pi^2} \right) Z = 0 \quad (\text{III-66})$$

is a Whittaker-type differential equation (41):

$$\frac{d^2 Z}{d\psi^2} + \left(-\frac{1}{4} + \frac{\sqrt{\lambda}}{4\psi} + \frac{3}{16\psi^2} \right) Z = 0 \quad (\text{III-67})$$

where $\psi = \sqrt{\lambda} \pi$

Solutions of this eqn. III-67 are available. Additional work will be required to show applicability to reported experimental results.

3. Linear Velocity Profile

Assumption of linear profiles yield, in essence, simpler differential equations and as a result have been the subject of investigations on heat and mass transfer processes. If, as represented in figure III-23,

$$V = Ky_i \text{ for } y_i \geq 0 \quad (\text{III-68})$$

the following eqn. can be derived:

$$\frac{dc}{dx} = \frac{D}{Ky_o^2} \frac{1}{y_i} \frac{d^2 c}{dy_i^2} \quad (\text{III-69})$$

with:

$$c = 0 \text{ at } y_i = 0 \text{ and any } x$$

$$c = c^o \text{ at } x \leq 0 \text{ and } y_i \geq 0$$

FACTUAL DATA (Cont'd)

Development of eqn. III-69 depends on the velocity gradient K . For laminar flow:

$$\left(\frac{dV}{dy}\right)_{y=0} = K = \frac{g\delta}{\mu} \quad (\text{III-70})$$

where:

$$\delta = \left(\frac{3Q\mu}{g}\right)^{1/3} \quad (\text{III-71})$$

δ = film thickness; Q = flow rate, μ = kinematic viscosity,
 g = acceleration in the x-direction

For eqn. III-60

$$\frac{D}{Ky_0^2} = \frac{2}{3} \frac{\delta^2}{Re Sc} \frac{1}{y_0^2} \quad (\text{III-72})$$

and if $\delta = \alpha y_0$;

$$\frac{D}{Ky_0^2} = \frac{2/3 \alpha^2}{Re Sc} \quad (\text{III-73})$$

For small flow rates: $\alpha \approx 1/2$

and eqn. III-69 becomes:

$$\frac{dc}{dx} = \frac{1}{N} \frac{1}{y_1} \frac{d^2c}{dy_1^2} \quad (\text{III-74})$$

For the change of variables: $C^* = C - C_0$ eqn. III-74 becomes:

$$\frac{dc^*}{dx} = \frac{1}{N} \frac{1}{y_1} \frac{d^2c^*}{dy_1^2} \quad (\text{III-75})$$

with the B. C.:

$$C^* = 0 \text{ for } x \leq 0 \text{ and } y_1 \geq 0$$

$$C^* = C_0 \text{ for } x > 0 \text{ and } y_1 = 0$$

This type of equation has been studied by Kramers & Kreyger (42).
 The rate of transport at the interface can be shown to be:

$$\left(\frac{dc^*}{dy_1}\right)_{y_1=0} = \frac{\pi 3}{\Gamma(1/3)} C_0 \left(\frac{gx}{N}\right)^{-1/3} \quad (\text{III-76})$$

FACTUAL DATA (Cont'd)

In terms of original variables, eqn. III-76 becomes:

$$\left(\frac{dc}{dy}\right)_{y=0} = \frac{-3}{r^{(1/3)}} \frac{C_0}{y_0} \left(\frac{3x}{2ReSc}\right)^{-1/3} \quad (\text{III-77})$$

The position-dependent current can be derived as:

$$i_L = -nFD \left(\frac{dc}{dy}\right)_{y=0} = \frac{3nFD}{r^{(1/3)}} \frac{C_0}{y_0} \left(\frac{3x}{2ReSc}\right)^{-1/3} \quad (\text{III-78})$$

In terms of the experimental variables for operation on air, at constant n, D, C_0 :

$$i_L(x) = 2nFD^{2/3} W^{-1/3} C_0 \left(\frac{Q}{xy_0^3}\right)^{1/3} \quad (\text{III-79})$$

Eqn. III-79 does not describe limiting currents at $X = Q$. If the function is normalized by taking $i_L(0) = 130 \text{ mA/cm}^2$ (as determined from limiting current density measurements for flow and non-flow conditions of air) linear relationship should be obtained between

$$\log [i_L(x)/i_L(0)] \text{ and } (Q/xy_0^3)^{1/3}$$

Constant flux at the Electrode

In the case of galvanostatic techniques, constant and uniform current distribution are obtained, corresponding to $(dc/dy)_{y=0} = \text{Const.}$ Under such conditions, equation III-75 can be rewritten:

$$\frac{d^2 C^*}{dy_1 dx} = \frac{1}{N} \frac{d}{dy_1} \left(\frac{1}{y_1} \frac{d^2 C^*}{dy_1^2} \right) \quad (\text{III-80})$$

$$\text{and if } (dc^*/dy_1) = \psi$$

(III-81)

$$\frac{d\psi}{dx} = \frac{1}{N} \frac{1}{dy_1} \left(\frac{1}{y_1} \frac{d\psi}{dy_1} \right)$$

FACTUAL DATA (Cont'd)

Eqn. III-81 has been studied in the case of heat transfer for non-Newtonian liquids for laminar flow (43). Now, the B. C. becomes:

$$\begin{aligned} x < 0 : \psi &= 0 \\ y_1 = 0 : \psi^* &= 1 \\ y_1 = \infty : \psi &= 0 \end{aligned} \quad \text{providing } \psi^* = \frac{(dc^*/dy_1)y_1}{(dc^*/dy_1)_{y_1=0}}$$

If
$$\pi = \frac{y_1}{(gx/N)^{1/3}} \quad (\text{III-82})$$

it can be shown that:

$$\pi \psi^{*''} + (3\pi^2 - 1) \psi^{*'} = 0 \quad (\text{III-83})$$

B. C.
$$\begin{aligned} \pi = 0 : \psi^* &= 1 \\ \pi = \infty : \psi^* &= 0 \end{aligned}$$

Eqn. III-83 admits the solution:

$$\psi^* = \frac{3}{\Gamma(2/3)} \int_{\pi}^{\infty} \pi e^{-\pi^3} d\pi \quad (\text{III-84})$$

Thus,

$$\int_{c^*}^0 dc^* = \int_{y_1}^{\infty} \psi_{y_1} dy_1 = \psi_{y_1=0} \int_{y_1}^{\infty} \psi^* dy_1 = \psi_{y_1=0} \left(\frac{gx}{N}\right)^{1/3} \int_{\pi}^{\infty} \psi^* d\pi \quad (\text{III-85})$$

And

$$-\frac{C^*}{\psi_0} = \left(\frac{gx}{N}\right)^{1/3} \left[\frac{e^{-\pi^3}}{\Gamma(2/3)} - \pi \left\{ 1 - \frac{\Gamma(2/3 \pi^3)}{\Gamma(2/3)} \right\} \right] \quad (\text{III-86})$$

For $y_1 = 0$;

$$-\frac{C_{\text{WALL}}^*}{\psi_0} = \left(\frac{gx}{N}\right)^{1/3} \frac{1}{\Gamma(2/3)} \quad (\text{III-87})$$

4.0

FACTUAL DATA (Cont'd)

$$\psi_o = (C_o - C_{WALL}) \left(\frac{gx}{N} \right)^{-1/3} \Gamma(2/3) \quad (\text{III-88})$$

For limiting conditions, when $C_{wall} = 0$, eqn. III-89:

$$\psi_{o,L} = C_o \left(\frac{gx}{N} \right)^{-1/3} \Gamma(2/3) \quad (\text{III-89})$$

can be compared with eqn. III-76. If relations of the type:

$$\ln(1 - i/i_L) = \alpha(E^\circ - E) = \alpha\eta_d \quad (\text{III-90})$$

are descriptive of the polarization curves, and in fact represent $\ln(C_w/C_o)$; the overall curve can be established if α and i_L are known. However, since α has physical significance, values of $i_L(x)$ as defined by eqn. III-79 are, in principle, sufficient to describe the current - voltage relationships.

In addition, wall concentration of oxygen can be calculated as a function of concentration gradients near the electrode, i.e. local currents.

APPENDIX IV

IV-1 MASS TRANSFER ANALYSISAnalysis of the Possible Rate Limiting Mechanisms in the Diffusion of Oxygen from an Air Stream to the Surface of the Oxygen Electrode in a G. E. "GPS" Type Ion Exchange Membrane Fuel Cell

The rate at which mass may be transferred in a fluid is determined by the physical properties of the fluid, its state of motion, and the driving potential.(44, 45,57) When the fluid in which mass transfer is occurring is stagnant or is in laminar motion normal to the direction of mass transfer, the mechanism of transfer is that of molecular diffusion which has been defined as the spontaneous intermingling of miscible fluids placed in mutual contact accomplished without the aid of mechanical stirring. The shear stresses in fluids in laminar motion (transfer of momentum) exist through the action of viscosity. At the interface, the fluid velocity relative to the solid surface is substantially zero while at increasing distances from the interface the velocity progressively increases. In effect, the fluid may be considered as composed of thin layers which follow the contours of the surface without mixing with the adjacent layers except as mingling results from molecular diffusion.

Even under the conditions of turbulent flow there is always a layer of fluid at the interface in which laminar flow is maintained. The thickness of this laminar layer or film depends upon the conditions of flow and becomes less as the velocity is increased. At the low Reynold's numbers (10 to 150) observed in this experimental investigation, the laminar layer includes the entire stream.

On the basis of the film concept mass transfer is considered as resulting from molecular diffusion across the effective film under the influence of a concentration gradient.

1-A. Countercurrent Diffusion of Oxygen from an Air Stream to the Oxygen Electrode and Water Vapor from the Oxygen Electrode to the Air Stream in the Presence of an Electrochemical Reaction. (45)

In order to determine whether the diffusion of oxygen from an air stream to the oxygen electrode is limited by a stagnant gas film, or by the countercurrent diffusion of water vapor into the air stream, or by gas diffusion into pores, or by a liquid film in the electrode an analysis of these mechanisms was made as follows.

A-1. Diffusion in Complex Systems - Gas - Gas

"In heterogeneous chemical reactions two or more components may diffuse to and from an interface in the presence or absence of a film of inert gas. The transfer may be equimolal in both directions or may correspond to an increase or decrease in the number of moles." (45)

Quoted from (45):

"For the general gaseous reaction $aA + bB \rightleftharpoons rR + sS$ proceeding in the presence of an inert gas I the following equation which includes the effect of all components present applies. Thus for the diffusion of A,

$$-RT \frac{dC_A}{dL} = - \frac{dp_A}{dL} = \alpha_{AB} C_A C_B (U_A - U_B) + \alpha_{AR} C_A C_R (U_A - U_R) + \alpha_{AS} C_A C_S (U_A - U_S) + \alpha_{AI} C_A C_I (U_A)$$

where $-\frac{dp_A}{dL}$ = partial pressure gradient of component A in the direction of diffusion L

$\alpha_{AB}, \alpha_{AR}, \alpha_{AS}, \alpha_{AI}$ = proportionality factors

C_A, C_B, C_R, C_S, C_I = molal concentrations of A, B, R, S, and I, resp.

U_A, U_B, U_R, U_S = linear velocities of diffusion of A, B, R, S in the direction of diffusion of A

An alternate equation is,

$$-\frac{\pi}{RT} \frac{dp_A}{dL} = \frac{1}{D_{AB}} (r_{Aa} p_B - r_{Ba} p_A) + \frac{1}{D_{AR}} (r_{Aa} p_R - r_{Ra} p_A) + \frac{1}{D_{AS}} (r_{Aa} p_S - r_{Sa} p_A) + \frac{1}{D_{AI}} r_{Aa} p_I$$

where π = total pressure (atm)

R = gas constant $\left(82.06 \frac{\text{cm}^3 \cdot \text{atm}}{\text{g-mole} \cdot ^\circ \text{K}} \right)$

4.0 FACTUAL DATA (Cont'd)

| | |
|----------------------|---|
| T | = absolute temperature ($^{\circ}\text{K}$) |
| D_{AB}, AR, AS, AI | = diffusion coefficients $\left(\frac{\text{cm}^2}{\text{sec.}}\right)$ characteristic of the pair of components AB, AR, AS, and AI |
| r_{Aa}, Ba, Ra, Sa | = the average molal rate of diffusion of A, B, R, and S $\left(\frac{\text{g-moles}}{\text{cm}^2\text{-sec.}}\right)$ |
| P_A, B, S, I | = partial pressure of A, B, S, and I (atm) |
| L | = distance in the direction of diffusion of A (cm) |

The terms U_I and r_I do not appear since there is no net diffusion of inert gas.

Because of the uncertainty of the proportionality factors and the corresponding diffusivities in mixtures of several components and because of the complications resulting in attempting to apply different values for each binary pair, an average diffusivity D_{Am} will be used to replace the separate values recorded in Equation IV-2. The average value of the diffusion coefficient will be taken as the weighted mean of the values for each pair. Thus for component A,

$$(1-N_A) D_{Am} = N_B D_{AB} + N_R D_{AR} + N_S D_{AS} + N_I D_{AI} \quad (\text{IV-3})$$

where N_A, N_B, \dots = average mole fractions of components A, B, ... in the diffusional film.

From the stoichiometry of the general reaction,

$$r_{Ba} = \left(\frac{b}{a}\right) r_{Aa}; r_{Ra} = -\left(\frac{r}{a}\right) r_{Aa}; r_{Sa} = -\left(\frac{s}{a}\right) r_{Aa} \quad (\text{IV-4})$$

Substituting Equation IV-4 in IV-2 and replacing each diffusion coefficient with the average value D_{Am} gives

$$-\frac{\pi}{RT} \frac{dp_A}{dL} = \frac{1}{D_{Am}} r_{Aa} \left[p_B + p_R + p_S + p_I - p_A \frac{(b-r-s)}{a} \right] \quad (\text{IV-5})$$

or, since $\pi = p_A + p_B + p_R + p_S + p_I$

4.0

FACTUAL DATA (Cont'd)

$$r_{Aa} dL = - \frac{D_{Am} \pi}{RT} \left[\frac{dp_A}{\pi - p_A \left(\frac{a+b-r-s}{a} \right)} \right] \quad (IV-6)$$

$$= - \frac{D_{Am} \pi}{RT} \left(\frac{dp_A}{\pi + p_A \delta_A} \right)$$

$$\text{where } \delta_A = \frac{r+s-a-b}{a}$$

Integrating between the film boundaries L (bulk) and L (interface) corresponding to an effective film thickness B_G gives

$$r_{Aa} = \frac{D_{Am} \pi}{RT B_G} \left(\frac{1}{\delta_A} \right) \ln \left(\frac{\pi + p_A \delta_A}{\pi + p_{Ai} \delta_A} \right) \quad (IV-7)$$

Equation (IV-7) also may be written in the form

$$r_{Aa} = \frac{D_{Am} \pi}{RT B_G p_f} (p_A - p_{Ai}) \quad (IV-8)$$

$$\text{where } p_f = \frac{(\pi + \delta_A p_A) - (\pi + \delta_A p_{Ai})}{\ln \left(\frac{\pi + \delta_A p_A}{\pi + \delta_A p_{Ai}} \right)} \quad (IV-9)$$

B_G = effective film thickness (cm)

p_f = Film Factor (atm)

Equation IV-9 is the logarithmic mean value of $(\pi + \delta_A p_A)$ over the boundary limits of the gas film. Thus, for diffusion of A,

$$p_f = \left[\pi + \delta_A p_A \right]_{lm} \quad (IV-10)$$

Similarly, for S

$$p_f = \left[\pi - \delta_S p_S \right]_{lm} \quad (IV-11)$$

where $\delta_S = \frac{r + s + \dots - a - b - \dots}{s}$

Where the ratio of $\left(\frac{\pi + \delta_A p_A}{\pi + \delta_A p_{Ai}} \right)$ is small,

for example less than 1.2, the arithmetic mean is in close agreement with the logarithmic mean and may be used for most purposes.

For equimolal diffusion it may be recognized from Equation (IV-10) that $p_f = \pi$ and Equation (IV-8) reduces to the form

$$r_{Aa} = -r_{Ba} = \frac{-D_{AB}}{RT} \frac{d p_A}{L} \quad (IV-12)$$

which is the fundamental equation for diffusion of gases but is directly applicable only to the case of equimolal countercurrent diffusion of a binary mixture of A and B.

For the diffusion of only one component in the presence of a stagnant gas, δ_A in Equation IV-9 is equal to -1, and the value of p_f becomes that given by the following equation

$$p_f = \frac{\frac{p_{B2} - p_{B1}}{2}}{\ln \left(\frac{p_{B2}}{p_{B1}} \right)} = \left(p_{B2} - p_{B1} \right)_{lm}$$

p_f = logarithmic mean of p_{B2} and p_{B1}

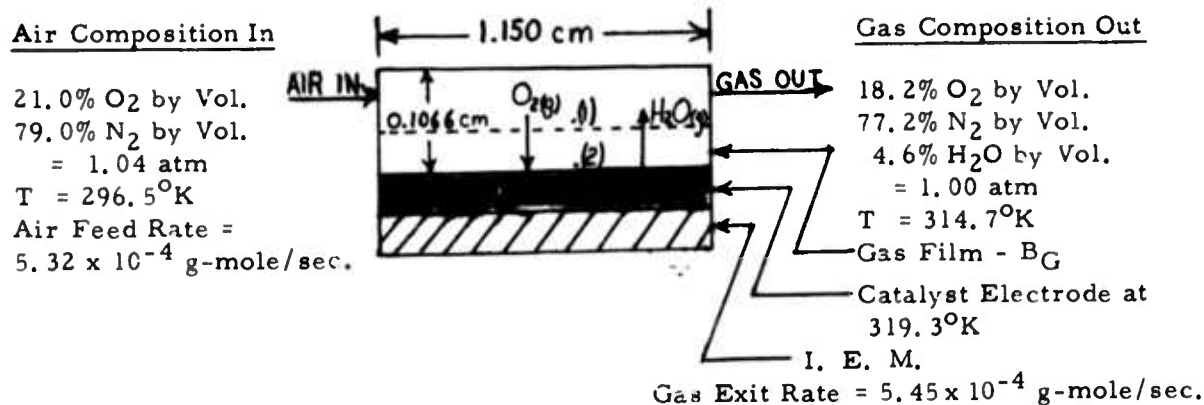
Subscript 1 = refers to the bulk value

Subscript 2 = refers to the interface value

FACTUAL DATA (Cont'd)

Equation (IV-8) and (IV-9) also can be applied where multicomponent diffusion takes place without stoichiometric relations. For example, in the countercurrent adsorption of one gas and desorption of another the constants a and s may be taken as the actual molal rates of adsorption and desorption, respectively, and the ratio $\frac{s}{a}$ may assume any value.

Equation (IV-1) indicates that for a given concentration gradient, the rate of diffusion of A is favored by the presence of another component diffusing in the same direction and retarded by another component diffusing in the opposite direction. Approximate values of a and s may be obtained in such a case by calculating the rate at which each component would diffuse under the conditions of the system if the other were absent." End of quote of (45). These principles will be applied to fuel cell systems.

1A-2 Bulk Diffusion - Gas Film Controlling (45).System:Basis: (1) G. E. I. E. M. Fuel Cell

- (2) Current = 4.85 amps
- (3) Current Density = 86.7 ma/cm² (80.7 amps/ft²)
- (4) Geometric Catalyst Area = 56.0 cm² (0.0602 ft²)
- (5) Product Water Evaporation Rate = 2.51 x 10⁻⁵ g-mole/sec.
= 100% at Indicated Air Flow which is 8.9 times the stoichiometric requirement
- (6) Oxygen Consumption Rate = 1.254 x 10⁻⁵ g-mole/sec.
- (7) Air Gap = 0.1066 cm

4.0

FACTUAL DATA (Cont'd)

$$\% \text{O}_2 \text{ avg.} = \text{avg. Oxygen Percentage in Bulk (1)} = \frac{21.0 + 18.2}{2} = \underline{\underline{19.6\%}}$$

A linear gradient of oxygen concentration from the inlet to the outlet of the reaction zone is justified because of the shortness of the path.

$$\pi_{\text{avg.}} = \text{Avg. Total Pressure} = \left(\frac{1.04 + 1.00}{2} \right) = \underline{\underline{1.02 \text{ atm}}}$$

$$P_{\text{O}_2(1)} = \text{Avg. Oxygen Partial Pressure in Bulk} = 0.196 (1.02) = \underline{\underline{0.200 \text{ atm}}}$$

$$P_{\text{O}_2(2)} = \text{Avg. Oxygen Partial Pressure at interface} = \underline{\underline{0 \text{ atm}}}$$

The oxygen gas partial pressure at the catalyst interface can be assumed to be negligible compared to the bulk oxygen partial pressure; therefore, in order to approximate the oxygen partial pressure gradient, $P_{\text{O}_2(2)}$ is set equal to zero.

$$P_{\text{H}_2\text{O}(1)} = \text{Avg. water vapor partial pressure in Bulk} = \left[\frac{0 + 0.70(0.0796)}{2} \right] = \underline{\underline{0.0278 \text{ atm.}}}$$

Linear gradient taken for same reason as for $\% \text{O}_2 \text{ avg.}$

$$P_{\text{H}_2\text{O}(2)} = \text{Avg. water vapor partial pressure at interface} = \underline{\underline{0.101 \text{ atm}}}$$

1A-2a. Counterdiffusion of Oxygen and Water Vapor in Presence of Inert (45, 46, 47, 48, 56) Nitrogen Gas - Bulk Diffusion Coefficients

$$D_{\text{O}_2-\text{N}_2} = D_{\text{O}_2-\text{N}_2} \left(\frac{T}{T_0} \right)^{1.75} \left(\frac{1.00}{1.02} \right) = 0.181 \left(\frac{312.4}{273} \right)^{1.75} (0.980) = 0.223 \text{ cm}^2/\text{sec.}$$

312.4°K 273°K
1.02 atm 1.00 atm

$$D_{\text{O}_2-\text{H}_2\text{O}} = 0.290 \left(\frac{1.00}{1.02} \right) = 0.284 \text{ cm}^2/\text{sec.}$$

312.4°K 312.4°K
1.02 atm 1.00 atm

4.0

FACTUAL DATA (Cont'd)

$$D_{\text{H}_2\text{O} - \text{N}_2} = 0.266 \frac{1.00}{1.02} = 0.260 \text{ cm}^2/\text{sec.}$$

$$\begin{array}{cc} 312.4^\circ\text{K} & 312.4^\circ\text{K} \\ 1.02 \text{ atm} & 1.00 \text{ atm} \end{array}$$

Calculation of the Arithmetic Mean Composition of the Gas FilmAt Interface - = 1.02 atmIn Bulk - π = 1.02 atm

$$P_{\text{O}_2(2)} = 0 \text{ atm}$$

$$P_{\text{O}_2(1)} = 0.200 \text{ atm}$$

$$P_{\text{N}_2(2)} = 0.919 \text{ atm}$$

$$P_{\text{N}_2(1)} = 0.792 \text{ atm}$$

$$P_{\text{H}_2\text{O}(2)} = 0.101 \text{ atm}$$

$$P_{\text{H}_2\text{O}(1)} = 0.0278 \text{ atm}$$

$$\text{Mean Mole Fraction of O}_2 \text{ in Gas Film} = \left(\frac{0 + 0.200}{2} \right) / 1.02 = \underline{\underline{0.0980}}$$

$$\text{Mean Mole Fraction of N}_2 \text{ in Gas Film} = \left(\frac{0.919 + 0.792}{2} \right) / 1.02 = \underline{\underline{0.839}}$$

$$\text{Mean Mole Fraction of H}_2\text{O vapor in Gas Film} = \left(\frac{0.101 + 0.0278}{2} \right) / 1.02 = \underline{\underline{0.0630}}$$

Calculation of the Average Diffusion Coefficients for Oxygen, $D_{\text{O}_2\text{m}}$, and Water Vapor, $D_{\text{H}_2\text{O}\text{m}}$

Using Equation (IV-3)

$$\begin{aligned} D_{\text{O}_2\text{m}} &= \frac{N_{\text{N}_2} D_{\text{O}_2-\text{N}_2} + N_{\text{H}_2\text{O}} D_{\text{O}_2-\text{H}_2\text{O}}}{1 - N_{\text{O}_2}} \\ &= \frac{(0.839)(0.223) + (0.0630)(0.284)}{1 - 0.0980} = \underline{\underline{0.227 \text{ cm}^2/\text{sec.}}} \end{aligned}$$

$$\begin{aligned} \text{and } D_{\text{H}_2\text{O}\text{m}} &= \frac{N_{\text{N}_2} D_{\text{H}_2\text{O}-\text{N}_2} + N_{\text{O}_2} D_{\text{H}_2\text{O}-\text{O}_2}}{1 - N_{\text{H}_2\text{O}}} \\ &= \frac{(0.839)(0.260) + (0.0980)(0.284)}{1 - 0.0630} = 0.262 \text{ cm}^2/\text{sec.} \end{aligned}$$

4.0

FACTUAL DATA (Cont'd)Calculation of Film Factors p_f

Using Equations (10) and (11)

$$p_{fO_2} = \frac{\left[\pi + \delta_{O_2} p_{O_2} \right]_{lm} \left[\pi + \delta_{O_2} p_{O_2(1)} \right] - \left[\pi + \delta_{O_2} p_{O_2(2)} \right]}{\ln \left[\frac{\pi + \delta_{O_2} p_{O_2(1)}}{\pi + \delta_{O_2} p_{O_2(2)}} \right]}$$

$$\text{where } \delta_{O_2} = \frac{r_{O_2a} - r_{H_2Oa}}{r_{O_2a}} = \frac{2.24 \times 10^{-7} - 4.48 \times 10^{-7}}{2.24 \times 10^{-7}} = \underline{\underline{-1}}$$

$$\text{then } p_{fO_2} = \frac{\left[1.02 + (-1)(0.200) \right] - \left[1.02 + (-1)(0) \right]}{\ln \left[\frac{1.02 + (-1)(0.200)}{1.02 + (-1)(0)} \right]} = \underline{\underline{0.917 \text{ atm}}}$$

$$\text{also } p_{fH_2O} = \frac{\left[\pi + \delta_{H_2O} p_{H_2O} \right]_{lm} \left[\pi + \delta_{H_2O} p_{H_2O(1)} \right] - \left[\pi + \delta_{H_2O} p_{H_2O(2)} \right]}{\ln \left[\frac{\pi + \delta_{H_2O} p_{H_2O(1)}}{\pi + \delta_{H_2O} p_{H_2O(2)}} \right]}$$

$$\text{Where } \delta_{H_2O} = \frac{r_{H_2Oa} - r_{O_2a}}{r_{H_2Oa}} = \frac{4.48 \times 10^{-7} - 2.24 \times 10^{-7}}{4.48 \times 10^{-7}} = \underline{\underline{0.5}}$$

$$\text{then } p_{fH_2O} = \frac{\left[1.02 + (0.5)(0.0278) \right] - \left[1.02 + 0.5(0.101) \right]}{\ln \left[\frac{1.02 + (0.5)(0.0278)}{1.02 + (0.5)(0.101)} \right]} = \underline{\underline{-1.058 \text{ atm}}}$$

4.0

FACTUAL DATA (Cont'd)Calculation of the Rates of Diffusion of Oxygen and Water Vapor in the Presence of Each Other

Using Equation (IV-8):

$$r_{O_2ac} = \frac{D_{O_2m} \pi}{RT B_{G_{O_2}} P_{f_{O_2}}} \left[P_{O_2(1)} - P_{O_2(2)} \right]$$

$$2.24 \times 10^{-7} = \frac{(0.227) (1.02) (0.200 - 0)}{(82.06) (312) (B_{G_{O_2}}) (0.917)}$$

$$\text{thus } B_{G_{O_2}} = \underline{8.77 \text{ cm}}$$

$$\text{also } r_{H_2Oac} = \frac{D_{H_2Om} \pi \left[P_{H_2O(1)} - P_{H_2O(2)} \right]}{RT B_{G_{H_2O}} P_{f_{H_2O}}}$$

$$-4.48 \times 10^{-7} = \frac{(0.262) (1.02) [0.0278 - 0.10]}{(82.06) (312) (B_{G_{H_2O}}) (1.058)}$$

$$\text{thus } B_{G_{H_2O}} = \underline{1.607 \text{ cm}}$$

1A-2b. Estimation of the Percentage Error Introduced by Calculating the Diffusion Rates of Oxygen and Product Water Vapor Neglecting the Effect of Counterdiffusion of Each Component - Based on Bulk Gas Diffusion Coefficients. (45, 46, 47, 48, 56)

If water vapor and nitrogen gas are considered as a stagnant component and the effect of water vapor is neglected, the rate of diffusion of oxygen from the air stream to the oxygen electrode is obtained as follows:

$$r_{O_{2a}} = \frac{D_{O_2 - N_2} \pi}{RT P_{f_{O_2}} B_{G_{O_2}}} \left[P_{O_2(1)} - P_{O_2(2)} \right]$$

4.0 FACTUAL DATA (Cont'd)

$$\text{where } p_{f_{O_2}} = \frac{p_{N_2(2)} - p_{N_2(1)}}{\ln \left(\frac{p_{N_2(2)}}{p_{N_2(1)}} \right)} = \frac{1.020 - 0.820}{\ln \left(\frac{1.020}{0.820} \right)} = \underline{\underline{0.917 \text{ atm}}}$$

$$\text{and } r_{O_2a} RTB_{GO_2} = \frac{(0.223) (1.02) (0.200 - 0)}{(0.917)} = 4.95 \times 10^{-2}$$

$$\text{Ratio of Countercurrent Diffusion} = \frac{r_{O_2ac} RTB_{GO_2}}{\text{No Countercurrent Diffusion } r_{O_2a} RTB_{GO_2}} = \frac{5.04 \times 10^{-2}}{4.95 \times 10^{-2}} = \underline{\underline{1.015}}$$

$$\therefore \text{Percentage Error in } r_{O_2a} = \underline{\underline{-1.59\%}}$$

Calculation of the Rate of Diffusion of Water Vapor Neglecting the Effect of the Counterdiffusion of Oxygen Gas.

If oxygen and nitrogen gas are now considered as a stagnant component and the effect of oxygen gas is neglected, the rate of diffusion of water vapor from the oxygen electrode to the air stream may be obtained as follows:

$$-r_{H_2Oa} = \frac{D_{H_2O-N_2} \pi \left[p_{H_2O(1)} - p_{H_2O(2)} \right]}{RT p_{f_{H_2O}} B_{GH_2O}}$$

$$\text{where } p_{f_{H_2O}} = \frac{p_{N_2(2)} - p_{N_2(1)}}{\ln \left(\frac{p_{N_2(2)}}{p_{N_2(1)}} \right)} = \frac{0.919 - 0.992}{\ln \left(\frac{0.919}{0.992} \right)} = \underline{\underline{0.935 \text{ atm}}}$$

$$\text{then } r_{H_2Oa} RTB_{GH_2O} = \frac{-(0.260) (1.02) (0.0278 - 0.1010)}{(0.935)} = \underline{\underline{2.08 \times 10^{-2}}}$$

$$\text{Ratio of Counterdiffusion Diffusion} = \frac{r_{H_2Oa} RTB_{GH_2O}}{\text{No Countercurrent Diffusion } r_{H_2Oa} RTB_{GH_2O}} = \frac{1.855 \times 10^{-2}}{2.08 \times 10^{-2}}$$

$$\therefore \text{Percentage Error in } r_{H_2Oa} = \underline{\underline{+12.12\%}} = \underline{\underline{0.893}}$$

FACTUAL DATA (Cont'd)

Result: Neglecting the effect of water vapor counterdiffusion on the rate of diffusion of oxygen gas from the air stream to the oxygen electrode causes an error of -1.6% in the rate calculation. Therefore, the rate of diffusion of oxygen gas from the air stream to the oxygen electrode is not appreciably affected by the rate of counterdiffusion of water vapor from the oxygen electrode to the air stream. The error in the rate of diffusion of water vapor from the oxygen electrode to the air stream is +12.1% when the effect of the counterdiffusion of oxygen gas is neglected.

1A-3 Conclusions:

1A-3.1. Oxygen Diffusion from a Force-Convected Air Stream Flowing at a Rate Sufficient to Remove 100% of the Product Water From the Oxygen Electrode Considering the Counterdiffusion of Water Vapor - Based on Bulk Gas Diffusion Coefficients.

The calculated gas film thickness of 8.77 cm represents the maximum distance that oxygen gas can diffuse from a force-convected air stream to an oxygen electrode against the counterdiffusion of product water vapor at the 100% removal rate with an oxygen partial pressure gradient of 0.200 atm and the experimental conditions of cell temperature and total pressure and maintain a current density of 80.7 amp/ft². Since in the experimental hardware the average diffusion path or gas film thickness is only $\frac{0.1066}{2} = 0.0533$ cm or 1/164 the maximum path, the rate of oxygen diffusion is not limited by a stagnant gas film based on bulk phase diffusion coefficients. The effect of the counterdiffusion of water vapor on the diffusion of oxygen is negligible. Theoretically, on this basis alone a limiting current density of about 13,300 amp/ft² could be maintained under the same operating conditions. At one time the stoichiometric air requirement the limiting current density would be 10,200 amps/ft². Therefore, the recently invented perforated air electrode current collector is suitable for large size cells and operation at high current densities.

By comparison the size of a self-diffusion type air electrode with an air gap of sufficient magnitude (> 0.007 in) to supply oxygen at the required rate would be limited to a round shape 7.0 in. in diameter to operate a current density of 80.7 amps. ft² at the same conditions of temperature and total pressure. The size cell at 162 amps/ft² would be limited to a 3.5 in. diameter. The air gap would have to be greater than 0.024". Much larger gaps are required in practice to maintain the average oxygen pressure gradient at the 0.200 atm. level required to maintain an average current density at these levels (Ref. Task III). On the basis of bulk gas diffusion coefficients, this type cell design is limited to small sizes and low current densities.

1A-3.2. Product Water Vapor Diffusion from the Oxygen Electrode to an Air Stream Flowing at a Sufficient Rate to Remove 100% of the Product Water Against the Counterdiffusion of Oxygen - Based on Bulk Diffusion Coefficients.

Since the actual air gap width is small $\frac{0.1066}{2} = 0.0533$ cm compared to the calculated gas film of 1.607 cm, the rate of diffusion of water vapor to the air stream from the oxygen electrode under the experimental conditions is not limited by diffusion through a stagnant gas layer at the electrode surface at a current density of 80.7 amps/ft². However, the rate of removal of water vapor from the air electrode gas compartment and, therefore, the oxygen electrode to ambient conditions is dependent on the air flowrate, i. e. it must be sufficient to remove 100% of the product water by maintaining the water vapor partial pressure gradient. On the basis of bulk gas diffusion coefficients alone, the current density at which the stagnant gas film for water vapor diffusion would be equal to 0.0533 cm is 2430 amps/ft² at the same experimental conditions of temperature and pressure and 100% removal of product water.

By contrast, a self-diffusion type cell would be limited to a maximum 7.0 in. diameter round shape with an air gap > 0.007 in. and < 0.632 in. in order to avoid an oxygen electrode product water removal problem at 80.7 amps/ft². At a current density of 162 amps/ft², the maximum diameter would be 3.50 in. and the air gap > 0.024 in. and < 0.316 in.

1A-3.3. Gas Diffusion into Pores Controlling

In order to determine whether the diffusion of oxygen from the air stream into the pores of the oxygen electrode limits the rate of diffusion of oxygen an analysis was made as follows:

Basis:

- (1) "GPS" - Type I. E. M. Fuel Cell
- (2) Standard Pt black Catalyst Screen Electrode Loading of 0.223 g/in.²
- (3) Geometric Catalyst Area = 56.0 cm²
- (4) Electrode Thickness 0.0045 in.
- (5) Catalyst Porosity 33.5% by the Mercury Penetrometer Method
- (6) Pore Size Distribution by the Mercury Penetrometer Method

FACTUAL DATA (Cont'd)

Three Distinct Pore Diameter Groups:

| <u>Range</u> | <u>%</u> | <u>Avg. Pore Diameter</u> |
|-------------------|----------|---------------------------|
| 18 - 90 μ | 35.6 | 35 μ |
| 0.15 - 18 μ | 27.4 | 1.5 μ |
| 0.15 - 0.06 μ | 37.0 | 0.08 μ |

- (7) Bulk Density of Catalyst = 3.40 g/cm³
- (8) Total Surface Area of Catalyst = 16 m²/g
- (9) Diffusion Tortuosity Factor = 1.50
- (10) Assume pores free of liquid water except at the membrane-catalyst interface at the bottom of the pores

1A-3.3a Diffusion Tortuosity Factors (46, 50, 51)

Experimental data and a survey of the literature reported by Leonard Benjamin Rothfeld (51) indicated that diffusion tortuosity factors for unconsolidated media such as catalyst layers produced by compressing powders are from 1.4 to 3.0, for consolidated synthetic media as high as 5.3 and for naturally occurring rocks up to 10. He concludes that previously reported factors as large as 10 for pelleted catalyst were probably based on an incorrectly assumed diffusion mechanism and that no sound experimental evidence is available to support the contention that the tortuosity of catalyst particles is this high. He further states that diffusion tortuosities are about 20% larger than flow tortuosities.

Air permeability data reported by the National Carbon Co. (Ref. p. 1550, Chem. Eng. Hd. Bk.) for porous compressed carbon and graphite slabs avg. pore sizes from 5 to 190 μ yield flow tortuosities which level off at 1.50 for very small pore diameters at 48% porosity and at 1.23 for 36% porosity. The corresponding diffusion tortuosities are estimated as 1.80 and 1.48, respectively.

The experimental facts are in good agreement with a theoretical tortuosity factor of 1.41 based on a "random" direction assumption by Ahlborn Wheeler (58).

Finally, on this basis a diffusion tortuosity of 1.50 is assumed for the experimental catalyst. That is the average length of the gas diffusion path be assumed to be 1.50 times the catalyst electrode thickness.

4.0 FACTUAL DATA (Cont'd)

1A-3.3b Gas Phase Diffusion Coefficients in Catalyst Pores (50, 51)

(1) Laminar Flow Regime

The magnitude of the gas bulk diffusion coefficient in pores of 10,000 Å⁰ (1 μ) radius or larger in contact with one atmosphere of gas pressure is independent of the pore radius and inversely proportional to the total gas pressure. Because under these conditions the mean free path of a gas molecule is about 1/10 (oxygen = 9.940 × 10⁻⁶ cm = 994 Å⁰ = 0.0994 μ at 20°C) the pore radius and molecules will collide much more often with each other than with the pore wall. Laminar or stream-line flow will predominate. The kinetic theory gives the following approximate formula for the diffusion coefficient for a mixture of gases of similar mass and molecular diameter

$$D_B = \frac{1}{3} \bar{v} \lambda$$

where D_B = bulk diffusion coefficient for gases, cm²/sec. (IV-13)

\bar{v} = arithmetic average molecular velocity, cm/sec.

λ = mean free path (cm)

An explicit equation for D_B in terms of molecular quantities and the concentration or pressure is obtained by substituting

$$\lambda = \frac{0.707}{\pi \sigma^2 C_T} \quad (IV-14)$$

where π = total gas pressure (atm)

σ = molecular diameter (cm)

C_T = total concentration (molecules/cm³)

eqn. IV-14 into eqn. IV-13

$$\text{whence } D_B = \frac{0.707}{3\pi} \frac{\bar{v}}{\sigma^2 C_T} \quad (IV-15)$$

The range of values for D_B for most gas mixtures at atmospheric pressure and a 20°C temperature are 0.1 to 1.0 cm²/sec.

(2) Knudsen Flow Regime

When a catalyst contains pores of 1000 Å (0.1 μ) radius or less Knudsen or molecular flow rules the rate of gas transport at moderate pressures. Under these conditions, the mean free path between intermolecular collisions will be greater than the pore diameter. As a result a molecule within the pore structure will, in general, strike a pore wall before it strikes another molecule. Intermolecular collisions may thus be neglected, and a molecule travels within a pore by a series of "random flights" interrupted by collisions with a pore wall. The "resistance" to diffusion is due to the fact that after collision with the pore wall, the molecule is just as apt to reverse its direction as it is to proceed in the direction of the previous flight. Knudsen showed that under these conditions the flow of molecules through a capillary of length ΔX cm. is governed by the equation:

$$\frac{dn}{dt} = \frac{8}{3} \frac{\pi r^3}{\sqrt{2\pi m k_B T}} \left(\frac{\Delta p}{\Delta X} \right) \quad (\text{IV-16})$$

where $\frac{dn}{dt}$ = gas flowrate $\frac{\text{molecules}}{\text{sec.}}$

m = mass of a single molecule (g)

k_B = Boltzmann Const. (1.38×10^{-16} ergs/°K/molecule)
(i. e., the gas divided by Avogadro's Number)

T = absolute temperature (°K)

r = radius of the capillary (cm)

ΔP = pressure difference between ends of the capillary
(dynes/cm²)

Knudsen's equation shows that flow or diffusion of a particular molecular species in small pores is independent of the total gas pressure, is independent of the pressure or absence of other types of molecules, and depends only on the partial pressure gradient of that species. Because each molecule travels completely independently of its neighbors, there is no such thing in small pores at moderate gas pressures as a "mass" or "hydrodynamic" flow in which molecules are carried along in propor-

4.0 FACTUAL DATA (Cont'd)

tion to their concentration, such as occurs in ordinary streamline flow. A Knudsen diffusion coefficient can be defined by using the perfect gas law

$$p = c k_B T$$

and defining this coefficient for molecular species in a pore by the equation of def:

$$\frac{dn}{dt} = A D_k \left(\frac{\Delta C}{\Delta x} \right) \quad (IV-17)$$

where A is the cross-sectional area of the pore then

$$D_k = \frac{2r}{3} \sqrt{\frac{8k_B T}{\pi m}} = \frac{2r}{3} \bar{v} \left(\frac{\text{cm}^2}{\text{sec.}} \right) \quad (IV-18)$$

For a molecule of average molecular weight \bar{M} is about 10^5 cm/sec and D_k has the numerical range of values of about 0.01 cm²/sec for 10 Å (0.001 μ) to 1.0 cm²/sec for 10,000 Å (1 μ) pores.

(3) Over-All Equation for Gas Diffusion Coefficients in Pores

Wheeler (58) proposes two semi-empirical over-all equations for gas diffusion coefficients in pores as follows:

$$D = \frac{1}{3} \bar{v} \lambda \left(1 - 2 \frac{\bar{v}}{\lambda} \right) \quad (IV-19)$$

$$\text{and } D = \frac{1}{3} \bar{v} \lambda \left(\frac{2r/\lambda}{1 + 2r/\lambda} \right) \quad (IV-20)$$

both have the property of showing the transition between Knudsen and ordinary diffusion and of reducing to the two special cases; eqn. IV-18 when r is much less than λ and eqn. IV-13 when r is much greater than λ . Equation IV-19 shows a more gradual transition between the two type of diffusion than does IV-20, yet he prefers equation IV-19 since the physical problem is surely connected with the relative probability of a molecule striking the pore wall vs. striking a second molecule and the bracketed expression in IV-19 is exactly the probability that a molecule will have a collision with a second molecule before traveling a distance equal to the pore diameter.

4.0

FACTUAL DATA (Cont'd)

Over-all diffusion coefficients calculated using equation IV-19 in the form $D = D_B (1 - e^{-2r\bar{v}/3D_B})$ were within 10% and 0.5% of the values determined experimentally by Rothfeld (51) on N_2 -He and N_2 - A counterdiffusing mixtures, respectively. It is expected that for mixtures of oxygen and nitrogen and water vapor with molecular weights and sizes much less different than the pairs Rothfeld reported on that the use of equation IV-19 will permit calculation of over-all diffusion coefficients within less than 10% of the actual values.

(4) Application of Equations

System: Same as (1) Bulk Diffusion - Gas Film Controlling

(a) Calculation of Over-All Diffusion Coefficients for Each of the Three Average Pore Size Ranges (45, 46, 47, 50, 55, 56)

$$\begin{aligned} \text{now } D_{O_2m} (0.A) &= D_{O_2m} \left(1 - e^{-2r\bar{v}/3D_{O_2m}} \right) \\ &\quad \begin{matrix} 312.4^\circ K \\ \pi = 1.02 \text{ atm} \end{matrix} \quad \begin{matrix} 312.4^\circ K \\ 1.02 \text{ atm} \end{matrix} \\ \text{and } \bar{v} \propto \sqrt{\frac{T}{\pi}} \quad \bar{v}_{O_2} &= 44,000 \sqrt{\left(\frac{1.00}{1.02} \right) \left(\frac{312.4}{293.0} \right)} = \underline{45,000 \text{ cm/sec.}} \\ &\quad \begin{matrix} 312.4^\circ K \\ \pi = 1.02 \text{ atm} \end{matrix} \\ \bar{v}_{N_2} &= 47,100 (1.022) = \underline{48,200 \text{ cm/sec.}} \\ \bar{v}_{H_2O} &= 58,700 (1.022) = \underline{60,000 \text{ cm/sec.}} \\ \bar{v}_{avg.} &= N_{O_2} \bar{v}_{O_2} + N_{N_2} \bar{v}_{N_2} + N_{H_2O} \bar{v}_{H_2O} \\ &= (0.0980) (45,000) + (0.839) (48,200) + 0.0630 (60,000) = \underline{48,690 \text{ cm/sec.}} \end{aligned}$$

(b) then for 35 μ avg. pore diameter

$$\begin{aligned} D_{O_2m} (0.A.) &= 0.227 \left[\frac{-2(1.75 \times 10^{-3}) (4.869 \times 10^4)}{3 (0.227)} \right] \\ &\quad \begin{matrix} 312.4^\circ K \\ \pi = 1.02 \text{ atm} \end{matrix} \quad \begin{matrix} 1 - e \end{matrix} \\ &= D_{O_2m} = \underline{0.227 \text{ cm}^2/\text{sec.}} \end{aligned}$$

FACTUAL DATA (Cont'd)(c) also for 1.5 μ avg. pore diameter

$$D_{O_2m}(0.A.) = 0.227 \left[1 - \frac{-2(7.5 \times 10^{-5})(4.869 \times 10^4)}{3(0.227)} \right]$$

$$\pi = 1.02 \text{ atm} \quad 312.4^\circ\text{K} \quad = D_{O_2m} = \underline{0.227} \text{ cm}^2/\text{sec.}$$

(d) Finally for a 0.08 μ avg. pore diameter

$$D_{O_2m}(0.A.) = 0.227 \left[1 - \frac{-2(4 \times 10^{-6})(4.869 \times 10^4)}{3(0.227)} \right]$$

$$= \underline{0.0992} \text{ cm}^2/\text{sec.} \quad < D_{O_2m} = \underline{0.227} \text{ cm}^2/\text{sec.}$$

$$\text{and } D_{H_2Om}(0.A.) = 0.262(0.391) = \underline{0.1024} \frac{\text{cm}^2}{\text{sec.}} < D_{H_2Om} = \underline{0.262} \frac{\text{cm}^2}{\text{sec.}}$$

Note:

For the 0.08 μ avg. pore diameter, the over-all pore diffusion coefficient is 56.5% less than the bulk diffusion value for oxygen and 60.9 less for water vapor.

1A-4 Maximum Current Density Limitations Due to Gas Pore Diffusion Mechanism (45, 50, 51)

The use of the over-all gas pore diffusion coefficients for oxygen and water vapor to estimate the maximum current density possible for "GPS" I. E. M. fuel cell with the standard catalyst electrode operating on force-convected air under the same conditions stated for the bulk diffusion case is as follows:

Since the screen of the catalyst-electrode occupies about 16% of the geometric surface area of the electrode-membrane interface and penetrates to about 1/3 the thickness of the catalyst, the average pore length will be somewhat longer 0.01728 cm vs. 0.01712 cm to the reaction zone which is assumed to occur in the limit at the bottom of the pores at the catalyst-electrolyte interface. The maximum rate of diffusion and of current density will then be determined by a weighted average of the rates of diffusion through the two sections of different length and area.

4.0

FACTUAL DATA (Cont'd)

Now the total gas flowrate $\left(\frac{\text{g-moles}}{\text{sec.}}\right)$ is the same for both sections

$$\text{hence } r_{\text{O}_2\text{a}(0.\text{A.}) \text{ avg.}} = \frac{\left(\frac{1.5}{1.0}\right) + \left(\frac{3.0}{0.84}\right)}{\left(\frac{4.5}{1}\right)} r_{\text{O}_2\text{a}(0.\text{A.})_1}$$

$$= \underline{\underline{1.127}} r_{\text{O}_2\text{a}(0.\text{A.})_1} \text{ g-moles/cm}^2\text{-sec.}$$

$$\text{also } r_{\text{H}_2\text{Oa}(0.\text{A.}) \text{ avg.}} = 1.127 r_{\text{H}_2\text{Oa}(0.\text{A.})_1}$$

$$D_{\text{O}_2\text{m}(0.\text{A.}) \text{ avg.}} \pi \left[P_{\text{O}_2(1)} - P_{\text{O}_2(2)} \right]$$

$$\therefore r_{\text{O}_2\text{a}(0.\text{A.}) \text{ avg.}} = \frac{RT \quad p_f \quad B_{\text{G}_{\text{O}_2}(0.\text{A.}) \text{ avg.}}}{}$$

treating the $D_{\text{O}_2\text{m}(0.\text{A.})}$ for the three different average pore size as conductances in parallel.

$$\begin{aligned} \underline{\underline{D_{\text{O}_2\text{m}(0.\text{A.}) \text{ avg.}}}} &= (\text{pore fraction})_{35\mu} D_{\text{O}_2\text{m}(0.\text{A.})} + (\text{pore fraction})_{1.5\mu} \times \\ &D_{\text{O}_2\text{m}(0.\text{A.})} + (\text{pore fraction})_{0.08\mu} D_{\text{O}_2\text{m}(0.\text{A.})} \\ &= 0.356 (0.227) + 0.274 (0.227) + 0.370 (0.0992) \\ &= \underline{\underline{0.1797 \text{ cm}^2/\text{sec.}}} \end{aligned}$$

$$\text{and } \underline{\underline{D_{\text{H}_2\text{Om}(0.\text{A.}) \text{ avg.}}}} = (0.63) (0.262) + (0.37) (0.1024) = \underline{\underline{0.1688 \text{ cm}^2/\text{sec.}}}$$

$$\begin{aligned} \text{then } \underline{\underline{B_{\text{G}_{\text{O}_2}(0.\text{A.}) \text{ avg.}}}} &= \frac{(0.1797) (1.02) (0.200 - 0)}{(82.06) (312) (0.917) \frac{(2.24 \times 10^{-7})}{0.335} (1.127)} = \underline{\underline{2.06 \text{ cm}}} \\ &\text{at } 80.7 \text{ amps/ft}^2 \end{aligned}$$

4.0 FACTUAL DATA (Cont'd)

$$\text{also } B_{\text{GH}_2\text{O}} (0. A.)_{\text{avg.}} = \frac{(0.1688)(1.02)(0.101 - 0.0278)}{(82.06)(312)(1.052) \left(\frac{4.48 \times 10}{0.335} \right) (1.127)}$$

$$= \underline{\underline{0.310 \text{ cm}}}$$

Since the length of the diffusional path is only 0.01728 cm in the experimental hardware and the calculated stagnant gas film thickness is 2.06 cm for oxygen, the rate of diffusion of oxygen to the bottom of the catalyst pores is not limited by the rate of diffusion through this film and neither is the current density of 80.7 amps/ft² at the experimental conditions of 100% product water removal, temperature, and pressure. In fact, on the basis of oxygen pore diffusion coefficients alone, the theoretical limiting current density would be 9,600 amps/ft². The rate of product water vapor diffusion from the bottom of the catalyst pores to the air stream is not limited by diffusion through a stagnant gas film in the pores at a current density of 80.7 amps/ft². Theoretically, the current density at which water vapor pore diffusion does become limiting is 1,450 amps/ft² with 100% product water removal and the same conditions of temperature and pressure. However, the rate of removal of water vapor from the oxygen electrode and from the air electrode gas compartment does depend on the air flowrate, i.e. it must be sufficient to remove 100% of the product water under the experimental conditions of temperature, water vapor partial pressure gradient, and total pressure.

1-B. Oxygen Diffusion Rate From An Air Stream to the Oxygen Electrode Limited by Gas Diffusion Across a Liquid Film at This Surface. (45, 46, 47)

The basic equation for gas diffusion through a liquid is given by Fick's law

$$r_{Aa} = -D_{AB} \frac{dc_A}{dL} \quad (\text{IV-21})$$

where r_{Aa} = rate of diffusion of A (g-moles/sec-cm²)

C_A = concentration of A (g-moles/cm³)

4.0

FACTUAL DATA (Cont'd)

D_{AB} = diffusion coefficient of gas A in the liquid phase ($\text{cm}^2/\text{sec.}$)

$$\text{since } C_A = \frac{X_A}{\bar{V}_m}$$

where X_A = Mole fraction of A in the liquid phase (g-moles/g-moles)

\bar{V}_m = average molal volume of liquid phase ($\text{cm}^3/\text{g-mole}$)

d_L = effective liquid film thickness (cm)

Subscript i = refers to properties at the interface

Equation 21 becomes:

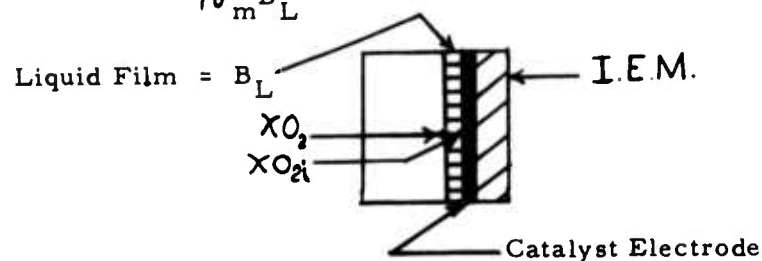
$$r_{Aa} = - \frac{D_{AB}}{\bar{V}_m} \frac{dx_A}{dL} \quad (\text{IV-22})$$

Equation IV-22 may be integrated over a film thickness B_L to give:

$$r_{Aa} = \frac{D_{AB}}{\bar{V}_m B_L} (X_A - X_{Ai}) \quad (\text{IV-23})$$

This equation may be applied to the diffusion of oxygen through a liquid film using the same air data as in the bulk gas diffusion case

$$\text{then } r_{O_{2a}} = \frac{D_{O_2-H_2O}}{\bar{V}_m B_L} (X_{O_2} - X_{O_{2i}})$$



$$D_{O_2 - H_2O} = 1.98 \times 10^{-5} \frac{\text{cm}^2}{\text{sec.}} + (28.3^\circ\text{C}) (0.03 \frac{1}{^\circ\text{C}}) (1.98 \times 10^{-5})$$

(at 319.3°K) (at 291°K)

$$= 3.66 \times 10^{-5} \frac{\text{cm}^2}{\text{sec.}} \quad (\text{Ref. Int. Crit. Tables Vol. V})$$

4.0

FACTUAL DATA (Cont'd)

X_{O_2} at the average conditions of the surface of the liquid film is estimated using Henry's law which is followed by oxygen at low and moderate pressures.

$$p_{O_2} = K_{O_2 - H_2O} X_{O_2} \quad (IV-24)$$

where K depends only on the solute-solvent pair and the temperature. It is independent of the pressure up to 5 atms.

$$\text{therefore } X_{O_2} = \frac{0.200}{5.70 \times 10^4} = 3.51 \times 10^{-6} \text{ (g-moles/g-moles)}$$

(at 319.3°K)

$$\text{also } X_{O_{2i}} = 0$$

The oxygen gas mole fraction at the catalyst-electrolyte interface can be safely assumed to be negligible compared to the bulk mole fraction; therefore, to approximate the oxygen concentration gradient $X_{O_{2i}}$ is set equal to zero.

$$\text{and } \bar{V}_m = \bar{V}_{mH_2O} = 18.20 \frac{\text{cm}^3}{\text{g-mole}} \text{ the molal volume of water since}$$

the molal volumes of oxygen and nitrogen in the liquid phase can be neglected.

then $r_{O_{2am}}$ (0. A.) avg. (based on a 33.5% catalyst porosity and correction for screen)

$$= \frac{(1.127)(2.24 \times 10^{-7})}{(0.335)} = \frac{(3.66 \times 10^{-5})(3.51 \times 10^{-6} - 0)}{18.20 \bar{B}_L}$$

$$\therefore \underline{\underline{\bar{B}_L}} = \underline{\underline{8.69 \times 10^{-6} \text{ cm}}}$$

at a current density of 80.7 amps/ft².

4.0 FACTUAL DATA (Cont'd)

The significance of this liquid film thickness may be estimated as follows:

| <u>Avg. Pore Diameter</u> | <u>% of Total Pores</u> | <u>Total Pore Geom. Surface Area</u> | <u>% of Total</u> | <u>Ratio $2B_L$ Pore Diam</u> | <u>Area of Reaction Zone, cm^2</u> | <u>Length of Reaction Zone, cm</u> |
|--|-------------------------|--------------------------------------|-------------------|--|--|------------------------------------|
| $35\mu = 3.5 \times 10^{-3} \text{cm}$ | 35.6 | $1.108 \times 10^2 \text{cm}^2$ | 0.2 | 0.00487 | 7.12 | 1.108×10^{-3} |
| $1.5\mu = 1.5 \times 10^{-4} \text{cm}$ | 27.4 | $1.993 \times 10^3 \text{cm}^2$ | 3.7 | 0.1158 | 5.47 | 4.75×10^{-5} |
| $0.08\mu = 8.0 \times 10^{-6} \text{cm}$ | 37.0 | $5.05 \times 10^4 \text{cm}^2$ | 96.1 | 2.00 | 3.21 | 1.10×10^{-6} |

The liquid film thickness represents 0.487%, 11.58%, and 200% of the diameters of the 35μ , 1.5μ , and 0.08μ average pore sizes, respectively. Also, the geometric surface area of this film must be equal to 15.80 cm^2 from the diffusion equation. It will be instructive then to compare this value first with the total pore geometric surface area and the reaction zone area for each pore size with the total area for each size and second the length of the reaction zone with the pore length for each pore size.

$$\begin{aligned} \text{the number of } 35\mu \text{ pores } n &= \frac{(0.356) (0.335) (56.0) (0.84) (0.01728)}{\frac{\pi}{4} (3.50 \times 10^{-3})^2 (0.01728)} \\ &= \underline{\underline{5.84 \times 10^5}} \text{ pores} \end{aligned}$$

$$\text{and the number of } 1.5\mu \text{ pores} = (0.274) (0.335) (56.0) (0.84) = \frac{\pi}{4} (1.5 \times 10^{-4})^2$$

$$\underline{\underline{n_{1.5\mu} = 2.45 \times 10^8}} \text{ pores}$$

$$\text{finally } \underline{\underline{n_{0.08\mu}}} = \frac{(0.370) (0.335) (56.0) (0.84)}{(0.785) (8.0 \times 10^{-6})^2} = \underline{\underline{1.162 \times 10^{11}}} \text{ pores}$$

The total geometric pore surface area is

$$\begin{aligned} &= A_{35\mu} + A_{1.5\mu} + A_{0.08\mu} \\ &= (5.84 \times 10^5) (\pi) (3.5 \times 10^{-3}) (1.728 \times 10^{-2}) + (2.44 \times 10^8) (\pi) (1.5 \times 10^{-4}) \\ &\quad (1.728 \times 10^{-2}) \\ &\quad + (1.162 \times 10^{11}) (\pi) (8.0 \times 10^{-6}) (1.728 \times 10^{-2}) = \underline{\underline{5.25 \times 10^4 \text{ cm}^2}} \end{aligned}$$

4.0 FACTUAL DATA (Cont'd)

A comparison between this number and the liquid film area shows that the entire diffusion of oxygen and reaction occurs at

$$\frac{15.80}{5.25 \times 10^4} = \underline{\underline{0.0301\%}} \text{ of the total geometric pore surface area.}$$

The liquid film surface area for each average pore size is estimated from both the individual cross-sectional pore area fractions and the pore diffusion coefficients. Whence

$$\begin{aligned} \text{Liquid Film Area for } 35\mu \text{ pore size} &= 7.12 \text{ cm}^2 \\ &1.5\mu \text{ pore size} = 5.47 \text{ cm}^2 \\ &0.08\mu \text{ pore size} = 3.21 \text{ cm}^2 \end{aligned}$$

Thus the percentage total pore geometric surface area occupied by the liquid film reaction zone is 6.4%, 0.27%, and 0.006% for the 35 μ , 1.5 μ , and 0.08 μ average pore sizes, respectively.

The length of the reaction zone is estimated as follows:

$$35\mu \text{ pore diameter } m\pi dl = 7.12$$

$$\underline{\underline{l_{35\mu}}} = \frac{7.12}{(5.84 \times 10^5) (3.14) (3.5 \times 10^{-3})} = \underline{\underline{1.108 \times 10^{-3} \text{ cm}}}$$

$$\underline{\underline{l_{1.5\mu}}} = \frac{5.47}{(2.45 \times 10^8) (3.14) (1.5 \times 10^{-4})} = \underline{\underline{4.75 \times 10^{-5} \text{ cm}}}$$

$$\underline{\underline{l_{0.08\mu}}} = \frac{3.21}{(1.162 \times 10^{11}) (3.14) (8.0 \times 10^{-6})} = \underline{\underline{1.10 \times 10^{-6} \text{ cm}}}$$

These values represent 6.42%, 0.275%, and 0.00638% of the 35 μ , 1.5 μ , and 0.08 μ pore lengths, respectively.

Conclusions:

The reaction zone varies from 1.108×10^{-3} cm to 1.10×10^{-6} cm in length and covers from 6.4% to 0.006% of the individual pore areas or about 0.03% of the total geometric pore surface area.

FACTUAL DATA (Cont'd)

Theoretically, the minimum thickness for this film is the thickness of a monomolecular layer of water = 2.7×10^{-8} cm but data in the literature indicate that water vapor adsorption on platinum is multimolecular and consists of from 51 to 380 layers or from 1.375×10^{-6} cm to 1.025×10^{-5} cm at the saturation pressure for water vapor. This would appear to be the range of thicknesses for the liquid film in the catalyst pores at the reaction zone. Hence the limiting current density could range from about 68 amp/ft² for a non wet-proofed or non-uniformly wet-proofed catalyst to as high as 510 amps/ft² in the ideal wetproofed catalyst case both operating at 100% removal of product water. Therefore, the maximum rate of oxygen diffusion from an air stream to the oxygen electrode catalyst-electrolyte interface and the maximum current density possible at 100% product water removal on an ion exchange membrane fuel cell are limited by the diffusion of the oxygen through a thin liquid film on the walls of the pores at the catalyst-electrolyte interface.

4.0 FACTUAL DATA (Cont'd)

APPENDIX V-1

Heat and Mass Transfer in an Air-Breathing Fuel Cell System with Air Recirculation

V-1 Introduction

In the analysis which follows, reference will be made to various flow stations which are shown in Figure V-1 which is a schematic drawing of the system. The reader is referred to Section 4.4.2 for a description of the basic system.

V-2 Air Composition and Properties

The following composition of dry atmospheric air was used:

Table V-1 - Standard Composition of Dry Air

| <u>Constituent</u> | <u>Notation</u> | <u>Molecular Weight, m</u> | <u>Mole Fraction, X</u> |
|--------------------|-----------------|----------------------------|-------------------------|
| Nitrogen | N ₂ | 28.016 | 0.7809 |
| Oxygen | O ₂ | 32.000 | 0.2095 |
| Argon | Ar | 39.944 | 0.0093 |
| Carbon Dioxide | CO ₂ | 44.010 | 0.0003 |
| Dry Air | | 28.966 | 1.000 |

Since nitrogen, argon, and carbon dioxide do not enter into the reactions, they may be considered diluent gases and lumped together for mathematical convenience.

V-3 Mass Flow Balance

Assuming that the flow is one-dimensional at any flow station in the system, the mass rate of flow of any constituent can be represented by the following expression:

$$W_j = \frac{m_j p_j A_k V_k}{1545.32 T_k} \quad (\text{lb. m/sec.}) \quad (1)$$

4.0 FACTUAL DATA (Cont'd)

where: W_j = mass flow rate of any constituent
(j = O₂, H₂ or D)

m_j = molecular weight of the constituent

p_j = partial pressure of the constituent, psia

A_k = flow cross-sectional area, sq. in.
(k = station 1, 2, 3, etc.)

V_k = velocity, fps

T_k = absolute temperature, deg. R

V-4 Product Water Mass Flow Balance

The increase in mass rate of flow of water flowing through the system rate of generation of product water if the bleed flow rate through the system is controlled such that product water is carried off in the bleed system at the same rate at which it is generated. The product water generation rate is a function of the oxygen consumption rate and since $2H_2 + \rightarrow 2H_2O$

$$\frac{(W_{H_2O})_7 - (W_{H_2O})_6}{m_{H_2O}} = \frac{2[(W_{O_2})_6 - (W_{O_2})_7]}{m_{O_2}} \quad (V-2)$$

and substituting Equation (V-1) into Equation (V-2)

$$\left[\frac{A_7 V_7}{T_7} (P_{H_2O})_7 - \frac{A_6 V_6}{T_6} (P_{H_2O})_6 \right] = 2 \left[\frac{A_6 V_6}{T_6} (P_{O_2})_6 - \frac{A_7 V_7}{T_7} (P_{O_2})_7 \right] \quad (V-3)$$

and solving Equation V-3 for $\left(\frac{A_6 V_6}{A_7 V_7} \right) \left(\frac{T_7}{T_6} \right)$ gives:

$$\left(\frac{A_6 V_6}{A_7 V_7} \right) \left(\frac{T_7}{T_6} \right) = \frac{(P_{H_2O})_7 + 2(P_{O_2})_7}{(P_{H_2O})_6 + 2(P_{O_2})_6} \quad (V-4)$$

4.0 FACTUAL DATA (Cont'd)

V-5 Diluent Mass Flow Balance

The mass flow rate of the diluent gases in and out of the system must equal in order for equilibrium conditions to prevail or:

$$(W_D)_7 = (W_D)_6 \quad (V-5)$$

$$(p_D)_7 = p_7 - (p_{H_2O})_7 - (p_{O_2})_7 \quad (V-6)$$

$$(p_D)_6 = p_6 - (p_{H_2O})_6 - (p_{O_2})_6$$

where p_6 and p_7 represent the summation of all the static partial pressures at the two stations; then from Equations V-1 and V-5:

$$\left(\frac{A_6}{A_7}\right)\left(\frac{V_6}{V_7}\right)\left(\frac{T_7}{T_6}\right) = \frac{p_7 - (p_{H_2O})_7 - (p_{O_2})_7}{p_6 - (p_{H_2O})_6 - (p_{O_2})_6} \quad (V-7)$$

If Equations V-4 and V-7 are equated and expanded, several terms cancel out giving:

$$\begin{aligned} p_7 (p_{H_2O})_6 + (p_{O_2})_6 \left[2p_7 - (p_{H_2O})_7 \right] = \\ p_6 (p_{H_2O})_7 + p_{O_2 7} \left[2p_6 - (p_{H_2O})_6 \right] \end{aligned}$$

and solving Equation V-8 for $p_{O_2 7}$ gives: (V-8)

$$(p_{O_2})_7 = \frac{\left[p_7 - 0.5(p_{H_2O})_7 \right] (p_{O_2})_6 - 0.5 \left[p_6 (p_{H_2O})_7 - p_7 (p_{H_2O})_6 \right]}{\left[p_6 - 0.5(p_{H_2O})_6 \right]} \quad (V-9)$$

But for the atmospheric air entering the system:

$$(p_{O_2})_6 = 0.2095 \left[p_6 - (p_{H_2O})_6 \right] \quad (V-10)$$

4.0 FACTUAL DATA (Cont'd)

and Equation (V-9) becomes:

$$(P_{O_2})_7 = \frac{0.2095 [p_7 - 0.5(p_{H_2O})_7] [p_6 - (p_{H_2O})_6] - 0.5 [p_6(p_{H_2O})_7 - p_7(p_{H_2O})_6]}{[p_6 - 0.5(p_{H_2O})_6]} \quad (V-11)$$

Equation (V-11) is a quasi-rigorous expression for the relationship showing that the oxygen partial pressure at the discharge of a fuel cell stack is essentially a function of the fuel cell operating temperature and the atmospheric conditions when the amount of water leaving the system is equal to the amount entering plus the amount generated.

A simplified version of Equation (V-11) which is more suitable for computation in a control system may be developed by multiplying and dividing Equation (V-11) by $[p_6 + 0.5(p_{H_2O})_6]$, letting $p_6 = p_7$, and neglecting all terms where the product of two values of vapor pressure occurs gives:

$$(P_{O_2})_7 = \frac{0.2095 [p_6 - 0.5(p_{H_2O})_7] [p_6 - (p_{H_2O})_6] [p_6 + 0.5(p_{H_2O})_6] - 0.5 [p_6 (p_{H_2O})_7 - (p_{H_2O})_6] [p_6 + 0.5(p_{H_2O})_6]}{[p_6 - 0.5(p_{H_2O})_6] [p_6 + 0.5(p_{H_2O})_6]}$$

which first reduces to:

$$(P_{O_2})_7 \approx 0.2095 p_6 - 0.60475(p_{H_2O})_7 + 0.39525(p_{H_2O})_6 \quad (V-12)$$

A test of the accuracy of Equation (V-12) may be made by comparing the results of an extreme example with Equation (V-11). Let $p_6 = p_7 = 14.696$, $t_6 = 120$ F, and $t_7 = 130$ F where for saturated conditions $(p_{H_2O})_6 = 1.6924$ psia and $(p_{H_2O})_7 = 2.2225$ psia.

| Relative Humidity | Vapor Press. at Inlet | Oxygen Partial Press. at Outlet | $(P_{O_2})_7$, psia | Error-Per cent |
|-------------------|-----------------------|---------------------------------|----------------------|----------------|
| H_{R1} | $(p_{H_2O})_6$, psia | Eq. (11) | Eq. (12) | |
| 0 | 0 | 1.7348 | 1.7348 | 0.0 |
| 1.0 | 1.6924 | 2.3909 | 2.4037 | 0.53 |

4.0 FACTUAL DATA (Cont'd)

Equation (V-12) can be made still more accurate by adjusting the last constant from 0.3952 to 0.3877 or:

$$(P_{O_2})_7 \approx 0.2095 p_6 - 0.6048 (P_{H_2O})_7 + 0.3877 (P_{H_2O})_6 \quad (V-13)$$

V-6 Oxygen Mass Flow Rate

It is instructive to compare the oxygen mass flow rate through the system with the rate of consumption. Let the through-flow oxygen equivalence ratio σ_t be the ratio of the mass flow rates of oxygen entering the system and oxygen consumed within the system. Then:

$$\sigma_t = \frac{(W_{O_2})_6}{(W_{O_2})_6 - (W_{O_2})_7} \quad (V-14)$$

or:

$$(\sigma_t - 1) (W_{O_2})_6 = \sigma_t (W_{O_2})_7 \quad (V-14A)$$

and using Equation V-1):

$$(\sigma_t - 1) (P_{O_2})_6 \frac{A_6 V_6}{T_6} = \sigma_t (P_{O_2})_7 \frac{A_7 V_7}{T_7} \quad (V-15)$$

Rearranging Equation (V-15) and equating to Equation V-4) gives:

$$\frac{(P_{H_2O})_7 + 2(P_{O_2})_7}{(P_{H_2O})_6 + 2(P_{O_2})_7} = \left(\frac{\sigma_t}{\sigma_t - 1} \right) \frac{(P_{O_2})_7}{(P_{O_2})_6} \quad (V-16)$$

When solved for $(P_{O_2})_7$, it becomes:

$$(P_{O_2})_7 = \frac{(\sigma_t - 1) (P_{H_2O})_7 (P_{O_2})_6}{\sigma_t (P_{H_2O})_6 + 2(P_{O_2})_6} \quad (V-17)$$

4.0 FACTUAL DATA (Cont'd)

Equations which are similar to Equations (V-16) and (V-17) can be developed from Equations (V-7) and (V-15); thus:

$$\frac{P_7 - (P_{H_2O})_7 - (P_{O_2})_7}{P_6 - (P_{H_2O})_6 - (P_{O_2})_6} = \left(\frac{\sigma_t}{\sigma_t - 1} \right) \frac{(P_{O_2})_7}{(P_{O_2})_6} \quad (V-18)$$

when solved for $(P_{O_2})_7$ becomes:

$$(P_{O_2})_7 = \frac{(\sigma_t - 1) [P_7 - (P_{H_2O})_7] (P_{O_2})_6}{\sigma_t [P_6 - (P_{H_2O})_6]} \quad (V-19)$$

Setting Equation (V-17) equal to Equation (V-19) and eliminating common factors gives:

$$\frac{(P_{H_2O})_7}{\sigma_t (P_{H_2O})_6 + 2(P_{O_2})_6} = \frac{[P_7 - (P_{H_2O})_7]}{\sigma_t [P_6 - (P_{H_2O})_6]} \quad (V-20)$$

and solving for σ_t gives:

$$\sigma_t = \frac{2 [P_7 - (P_{H_2O})_7] (P_{O_2})_6}{P_6 (P_{H_2O})_7 - P_7 (P_{H_2O})_6} \quad (V-21)$$

and since $(P_{O_2})_6 = 0.2095 [P_6 - (P_{H_2O})_6]$, Equation (V-21) becomes:

$$\sigma_t = \frac{0.419 [P_7 - (P_{H_2O})_7] [P_6 - (P_{H_2O})_6]}{P_6 (P_{H_2O})_7 - P_7 (P_{H_2O})_6} \quad (V-22)$$

Equation (V-22) shows that the ratio of through-flow rate through the system to the stoichiometric oxygen flow rate requirement is entirely a function of the static pressures and water vapor pressures in and out of the fuel cell system

4.0 FACTUAL DATA (Cont'd)

V-7 Heat and Mass Balance of Flow Through the Fuel Cell Stack

The heat and mass balance of the flow through the fuel cell stack is an iterative type of solution. Certain assumptions can, however, be made that give a reasonably accurate initial solution. A second solution can correct for any discrepancies. The assumptions used in the following analysis are:

1. One-dimensional, steady-state flow through the air passages.
2. The initial temperature of the water evaporated into the air stream is equal to the inlet gas temperature.
3. All of the stack heat losses are rejected to the gas stream by means of sensible heat losses and evaporation.
4. The gas is saturated with water vapor at the entrance and exit of the stack.

Regarding the last assumption, when the recirculating air flow rate is . . . 100 times that necessary to provide the stoichiometric oxygen requirement, approximately 72 per cent of the heat rejection is by means of evaporation. A small error in the final gas temperature would therefore have a small effect on determining the amount of water needed to provide the necessary heat rejection.

V-7-1 Diluent Mass Flow Balance

Equation (V-7) can also be applied to the conditions entering and leaving the fuel cell stack, or for constant area flow.

$$\left(\frac{V_1}{V_2} \right) \left(\frac{T_2}{T_1} \right) = \frac{P_2 - (P_{H_2O})_2}{P_1 - (P_{H_2O})_1} \left(\frac{P_{O_2}}{P_{O_2}} \right)_2 \quad (V-23)$$

V-7-2 Oxygen Mass Flow Balance

The amount of recirculation is related to the stoichiometric oxygen requirement by the ratio \sqrt{c} as follows:

4.0 FACTUAL DATA (Cont'd)

V.7.2 Oxygen Mass Flow Balance

The amount of recirculation is related to the stoichiometric oxygen requirement by the ratio σ_c as follows:

$$\sigma_c = \frac{(W_{O_2})_2}{(W_{O_2})_1 - (W_{O_2})_2} \quad (V-24)$$

where: $(W_{O_2})_2$ = oxygen flow rate leaving the fuel cell stack

$(W_{O_2})_1 - (W_{O_2})_2$ = oxygen consumption in the fuel cell stack

or rewriting Equation (V-24):

$$(W_{O_2})_1 = \left(\frac{\sigma_c + 1}{\sigma_c} \right) (W_{O_2})_2 \quad (V-25)$$

and using Equation (V-1) for the continuity expression for constant area flow:

$$(P_{O_2})_1 \frac{V_1}{T_1} = \left(\frac{\sigma_c + 1}{\sigma_c} \right) (P_{O_2})_2 \frac{V_2}{T_2} \quad (V-26)$$

Rewriting Equation (V-26) gives:

$$\left(\frac{V_1}{V_2} \right) \left(\frac{T_2}{T_1} \right) = \left(\frac{\sigma_c + 1}{\sigma_c} \right) \frac{(P_{O_2})_2}{(P_{O_2})_1} \quad (V-27)$$

4.0 FACTUAL DATA (Cont'd)

The partial pressure of the oxygen at the stack entrance can be found by setting Equation (V-23) equal to Equation (V-27), or:

$$\frac{P_2 - (P_{H_2O})_2 - (P_{O_2})_2}{P_1 - (P_{H_2O})_1 - (P_{O_2})_1} = \left(\frac{\sigma_c + 1}{\sigma_c} \right) \frac{(P_{O_2})_2}{(P_{O_2})_1} \quad (V-28)$$

which reduces to the following expression when solved for $(P_{O_2})_1$:

$$(P_{O_2})_1 = \frac{(\sigma_c + 1) [P_1 - (P_{H_2O})_1] (P_{O_2})_2}{\sigma_c [P_2 - (P_{H_2O})_2] + (P_{O_2})_2} \quad (V-29)$$

Substituting Equation (V-29) for $(P_{O_2})_1$ in Equation (V-27) gives:

$$\left(\frac{V_1}{V_2} \right) \left(\frac{T_2}{T_1} \right) = \frac{\sigma_c [P_2 - (P_{H_2O})_2] + (P_{O_2})_2}{\sigma_c [P_1 - (P_{H_2O})_1]} \quad (V-30)$$

V. Temperature Change with Saturated Conditions

If the gas is saturated, the partial pressure of the water vapor is only a function of gas temperature. A change in temperature is approximately proportional to the change in the partial pressure of the water vapor for small temperature changes. The approximation can be expressed as follows:

4.0 FACTUAL DATA (Cont'd)

$$T_2 - T_1 \approx \frac{(p_{H_2O})_2 - (p_{H_2O})_1}{\left(\frac{\partial p_{H_2O}}{\partial T}\right)_{sat}} \quad (V-31)$$

The evaluation of $(\partial p_{H_2O}/\partial T)_{sat}$ from Keenan and Keyes is as follows for the temperature interval from 118 F to 120 F:

$$\left(\frac{\partial p_{H_2O}}{\partial T}\right)_{sat} \approx \frac{1.6924 - 1.6006}{120.0 - 118.0} = \frac{0.0918}{2.0} = 0.0459 \frac{\text{psi}}{\text{deg. F}} \quad (V-32)$$

and from Equation (V-31):

$$\frac{T_1}{T_2} \approx 1 - \frac{(p_{H_2O})_2 - (p_{H_2O})_1}{\left(\frac{\partial p_{H_2O}}{\partial T}\right)_{sat} T_2} \quad (V-33)$$

Substituting for T_1/T_2 in Equation (V-30) using Equation (V-33) gives:

$$\left(\frac{V_1}{V_2}\right) = \left\{ \frac{\sigma_c [p_2 - (p_{H_2O})_2] + (p_{O_2})_2}{\sigma_c [p_1 - (p_{H_2O})_1]} \right\} \left[1 - \frac{(p_{H_2O})_2 - (p_{H_2O})_1}{\left(\frac{\partial p_{H_2O}}{\partial T}\right)_{sat} T_2} \right] \quad (V-34)$$

V.9 Fuel Cell Stack Heat Balance

At 120 deg. F the heat of formation of condensed water is $H_f = 68,204$ cal/gm-mole which corresponds to an ideal voltage of $E_i = 1.478$ volts using the Faraday equation. The fuel cell thermodynamic efficiency η_{FC} can be expressed as the ratio of the output voltage E and E_i or;

4.0 FACTUAL DATA (Cont'd)

$$\eta_{FC} = \frac{E}{E_i} = \frac{E}{1.478} \quad (V-35)$$

The amount of heat rejected by the fuel cell stack q_R can be related to the amount of oxygen consumption by following equation using the reaction $2H_2 + O_2 = 2H_2O$.

$$q_R = (1 - \eta_{FC}) 68,204 \frac{\text{cal}}{\text{gm-mol } H_2O} \left(\frac{2 \text{ gm-mol } H_2O}{32 \text{ gm } O_2} \right) \cdot (1.798823) \frac{\text{BTU/lb.}}{\text{cal/gm}} \cdot \left[(W_{O_2})_1 - (W_{O_2})_2 \right] \frac{\text{lb-} O_2}{\text{sec.}} \quad (V-36)$$

or:

$$q_R = 7660 (1 - \eta_{FC}) \left[(W_{O_2})_1 - (W_{O_2})_2 \right], \text{ BTU/sec.} \quad (V-37)$$

The heat rejected from the stack is assumed to be absorbed by evaporation of water (product water plus additional water wicked from the condenser) and by increasing the enthalpy of the circulating gas,

or:

$$\begin{aligned} & \left[(W_{H_2O})_2 - (W_{H_2O})_1 \right] (h_{fg})_1 + (c_{p_{O_2}}) \left[(W_{O_2})_2 T_2 - (W_{O_2})_1 T_1 \right] \\ & + (c_{p_D}) (W_D) (T_2 - T_1) + (c_{p_{H_2O}}) \left[(W_{H_2O})_2 T_2 - (W_{H_2O})_1 T_1 \right] \\ & = 7660 (1 - \eta_{FC}) \left[(W_{O_2})_1 - (W_{O_2})_2 \right] \end{aligned} \quad (V-38)$$

4.0 FACTUAL DATA (Cont'd)

Assuming a constant flow area, rewriting Equation (V-38) by using the equation for continuity, Equation (V-1) gives:

$$\begin{aligned}
 & m_{H_2O} \left[(p_{H_2O})_2 \frac{V_2}{T_2} - (p_{H_2O})_1 \frac{V_1}{T_1} \right] (h_{fg})_1 + (C_{p_{O_2}}) \\
 & \left[(p_{O_2})_2 V_2 - (p_{O_2})_1 V_1 \right] + (C_{p_D}) (p_D) [V_2 - V_1] \\
 & + (C_{p_{H_2O}}) \left[(p_{H_2O})_2 V_2 - (p_{H_2O})_1 V_1 \right] \\
 & = 7660 (1 - \eta_{FC}) \left[(p_{O_2})_1 \frac{V_1}{T_1} - (p_{O_2})_2 \frac{V_2}{T_2} \right] m_{O_2} \quad (V-39)
 \end{aligned}$$

Multiplying Equation (V-39) by T_2/V_2 gives:

$$\begin{aligned}
 & m_{H_2O} \left[(p_{H_2O})_2 - (p_{H_2O})_1 \left(\frac{V_1}{V_2} \right) \left(\frac{T_2}{T_1} \right) \right] (h_{fg})_1 + (C_{p_{O_2}}) T_2 \\
 & \left[(p_{O_2})_2 - (p_{O_2})_1 \left(\frac{V_1}{V_2} \right) \right] + (C_{p_D}) T_2 p_D \left[1 - \left(\frac{V_1}{V_2} \right) \right] + (C_{p_{H_2O}}) T_2 \\
 & \left[(p_{H_2O})_2 - (p_{H_2O})_1 \left(\frac{V_1}{V_2} \right) \right] \\
 & = 7660 (1 - \eta_{FC}) m_{O_2} \left[(p_{O_2})_1 \left(\frac{V_1}{V_2} \right) \left(\frac{T_2}{T_1} \right) - (p_{O_2})_2 \right] \quad (V-40)
 \end{aligned}$$

4.0 FACTUAL DATA (Cont'd)

The terms in Equation (V-40) containing the oxygen partial pressure can be simplified by using Equation (V-27) or:

$$\begin{aligned}
 y = & m_{H_2O} \left[(p_{H_2O})_2 - (p_{H_2O})_1 \left(\frac{V_1}{V_2} \right) \left(\frac{T_2}{T_1} \right) \right] (h_{gf})_1 \\
 & + (C_{PO_2}) T_2 \cdot \left[1 - \left(\frac{\sigma_c + 1}{\sigma_c} \right) \left(\frac{T_1}{T_2} \right) \right] (p_{O_2})_2 \\
 & + (C_{PD}) T_2 \left[p_2 - (p_{H_2O})_2 - (p_{O_2})_2 \right] \cdot \left[1 - \left(\frac{V_1}{V_2} \right) \right] \\
 & + (C_{PH_2O}) T_2 \left[(p_{H_2O})_2 - (p_{H_2O})_1 \left(\frac{V_1}{V_2} \right) \right] \\
 & - \frac{7660 (1 - \eta_{FC}) m_{O_2} (p_{O_2})_2}{\sigma_c} = 0
 \end{aligned} \tag{V-40A}$$

Equations (V-27), (V-29), (V-30) and (V-34) are then used to eliminate all unknowns in Equation (V-40) except $(p_{H_2O})_1$ assuming that the conditions at station 2, the exit of the stack, are known.

4.0 FACTUAL DATA (Cont'd)

$$\begin{aligned}
 & m_{H_2O} \left[(P_{H_2O})_2 - \frac{\sigma_c [P_2 - (P_{H_2O})_2] (P_{H_2O})_1 + (P_{O_2})_2 (P_{H_2O})_1}{\sigma_c [P_1 - (P_{H_2O})_1]} \right] (h_{fg})_1 \\
 & + (C_{P_{O_2}}) T_2 (P_{O_2})_2 \left\{ 1 - \left(\frac{\sigma_c + 1}{\sigma_c} \right) \left[1 - \frac{(P_{H_2O})_2 - (P_{H_2O})_1}{\left(\frac{\partial P_{H_2O}}{\partial T} \right)_{sat} T_2} \right] \right\} \\
 & + (C_{P_D}) T_2 [P_2 - (P_{H_2O})_2 - (P_{O_2})_2] \left\{ 1 - \frac{\sigma_c [P_2 - (P_{H_2O})_2] + (P_{O_2})_2}{\sigma_c [P_1 - (P_{H_2O})_1]} \right. \\
 & \quad \left. \cdot \left[1 - \frac{(P_{H_2O})_2 - (P_{H_2O})_1}{\left(\frac{\partial P_{H_2O}}{\partial T} \right)_{sat} T_2} \right] \right\} + (C_{P_{H_2O}}) T_2 \\
 & \cdot \left\{ (P_{H_2O})_2 - (P_{H_2O})_1 \frac{\sigma_c [P_2 - (P_{H_2O})_2] + (P_{O_2})_2}{\sigma_c [P_1 - (P_{H_2O})_1]} \left[1 - \frac{(P_{H_2O})_2 - (P_{H_2O})_1}{\left(\frac{\partial P_{H_2O}}{\partial T} \right)_{sat} T_2} \right] \right\} \\
 & - 7660 (1 - \eta_{FC}) m_{O_2} \left[\left(\frac{\sigma_c + 1}{\sigma_c} \right) - 1 \right] (P_{O_2})_2 = 0 \quad (V-41)
 \end{aligned}$$

Equation (V-41) is quite complex to attempt to solve analytically; therefore, the solution was sought by making an initial estimate $(P_{H_2O})_1^{(1)}$ for the partial pressure of the water vapor at the exit of the fuel cell stack and then determine a more refined value $(P_{H_2O})_1^{(2)}$ by the Newton-Raphson method which is expressed as follows:

4.0 FACTUAL DATA (Cont'd)

$$(p_{H_2O})_1^{(2)} = (p_{H_2O})_1^{(1)} - \frac{y^{(1)}}{\left[\frac{\partial y}{\partial (p_{H_2O})_1} \right]^{(1)}} \quad (V-42)$$

where: (1), (2) indicate values based on successive estimates

y = residual equation (residual is essentially zero when a satisfactory solution is obtained)

To use Equation (V-42), Equation (V-41) must be different with respect to $(p_{H_2O})_1$, or:

$$\begin{aligned} \frac{\partial y}{\partial (p_{H_2O})_1} = & - (C_{p_{O_2}}) \left(\frac{\sigma_c + 1}{\sigma_c} \right) \frac{(p_{O_2})_2}{\left(\frac{\partial p_{H_2O}}{\partial T} \right)_{sat}} - \left\{ \frac{\sigma_c [p_2 - (p_{H_2O})_2] + (p_{O_2})_2}{\sigma_c [p_1 - (p_{H_2O})_1]^2} \right\} \\ & \cdot \left\{ p_1 m_{H_2O} (h_{fg})_1 + (C_{p_D}) T_2 [p_2 - (p_{H_2O})_2 - (p_{O_2})_2] \right. \\ & \left. \left[1 + \frac{p_1 - (p_{H_2O})_2}{\left(\frac{\partial p_{H_2O}}{\partial T} \right)_{sat} T_2} \right] + (C_{p_{H_2O}}) T_2 \right. \\ & \left. \left[p_1 - \frac{p_1 (p_{H_2O})_2 - 2 [p_1 - 0.5 (p_{H_2O})_1] (p_{H_2O})_1}{\left(\frac{\partial p_{H_2O}}{\partial T} \right)_{sat} T_2} \right] \right\} \quad (V-43) \end{aligned}$$

4.0 FACTUAL DATA (Cont'd)

V. 10 Example of Solution to Heat Balance of Flow through the Fuel Cell Stack

The following example is used to illustrate the solution to the heat balance equations for the fuel cell stack

Given:

$$P_1 = P_2 = 14.711 \text{ psia}$$

$$C_{P_{O_2}} = 7.042 \frac{\text{B}}{\text{lb}_m \cdot \text{mol}}$$

$$t_2 = 120^\circ \text{F} = 579.7 \text{ R}$$

$$C_{P_D} = 6.934$$

$$(P_{H_2O})_2 = 1.6924 \text{ psia}$$

$$C_{P_{H_2O}} = 8.045$$

$$n_c = 100 \quad \eta_{FC} = 0.5$$

$$(h_{fg})_1 = 1026.3 \text{ B/lb}_m$$

$$E = 0.739 \text{ volts}$$

Dry air enters system

$$\left(\frac{\partial P_{H_2O}}{\partial T} \right)_{sa}^{(1)} = 0.0459 \frac{\text{psi}}{\text{deg R}}$$

Initial assumption

$$t_1^{(1)} = 118^\circ \text{F}, (P_{H_2O})_1^{(1)} = 1.6006$$

The gas composition at station 7 is the same as at station 2, therefore,

$$P_6 \approx P_2 \text{ and } (P_{H_2O})_7 = (P_{H_2O})_2. \text{ Since the entering air is dry,}$$

$(P_{H_2O})_6 = 0$. The partial pressure of the oxygen leaving the fuel cell stack from Equation (V-12) is found as follows:

$$(P_{O_2})_2 = 0.2095(14.711) - 0.6048(1.6924) = 2.058 \text{ psia}$$

Equation (V-40A) is used to determine γ . Miscellaneous terms within

Equation (V-40A) are determined as follows:

4.0 FACTUAL DATA (Cont'd)

$$\frac{T_1}{T_2} = \frac{459.7 + 118}{459.7 + 120} = \frac{1}{1.00346}$$

$$P_1 - (P_{H_2O})_2 = 14.711 - 1.6924 = 13.0186 \text{ psia}$$

$$P_1 - (P_{H_2O})_1 = 14.711 - 1.6006 = 13.1104 \text{ psia}$$

$$(P_{O_2})_1 = \frac{101(13.1104)(2.0580)}{100(13.0186) + 2.0580} = 1.01553(2.058)$$

$$= 2.0900 \text{ psia} \quad (V-29)$$

$$\frac{V_1}{V_2} \left(\frac{T_2}{T_1} \right) = \frac{1.01}{1.01553} = \frac{1}{1.005475} \quad (V-27)$$

$$\frac{V_1}{V_2} = \frac{1}{1.005475(1.00418)} = \frac{1}{1.00968}$$

$$\frac{\sigma_c + 1}{\sigma_c} \left(\frac{T_1}{T_2} \right) = \frac{1.01}{1.00346} = 1.00651$$

$$P_2 - (P_{H_2O})_2 - (P_{O_2})_2 = 14.711 - 1.6924 - 2.0580 = 10.961 \text{ psia}$$

$$1 - \frac{V_1}{V_2} = \frac{0.005475}{1.005475} = 0.00545$$

$$(P_{H_2O})_2 - (P_{H_2O})_1 \left(\frac{V_1}{V_2} \right) \left(\frac{T_2}{T_1} \right) = 1.6924 - \frac{1.6006}{1.005475} = 0.1004$$

$$(P_{H_2O})_2 - (P_{H_2O})_1 \left(\frac{V_1}{V_2} \right) = 1.6924 - \frac{1.6006}{1.00895} = 0.1061$$

4.0 FACTUAL DATA (Cont'd)

Substituting in Equation (V-40A):

$$y = 18.016(1026.3)(0.1004) \\ + 579.7 \left[7.042(-0.00651)(2.058) + 6.934(10.961) \cdot (0.00545) + 8.045(0.1072) \right] \\ - \frac{7660(0.5)(32)(2.058)}{100}$$

$$y = 1856 + 681 - 2520 = +17$$

Equation (V-43) is now evaluated in order to correct the assumed value of

$$(P_{H_2O})_1^{(1)} = 1.6006 \text{ psia, or:}$$

$$\frac{\partial y}{\partial (P_{H_2O})_1} = - \frac{7.042(1.01)(2.058)}{0.0459} - \left[\frac{100(13.0186) + 2.058}{100(13.1094)^2} \right] \\ \left\{ 14.711(18.016)(1026.3) \right. \\ \left. + 6.934(579.7)(10.961) \cdot \left[1 + \frac{13.0186}{0.0459(579.7)} \right] \right. \\ \left. + 8.045(579.7) \right. \\ \left. \cdot \left[14.711 - \frac{14.711(1.6924) - 2(14.711 - 0.8003)(1.6006)}{0.0459(579.7)} \right] \right\}$$

$$\frac{\partial y}{\partial (P_{H_2O})_1} = - 318.6 - \frac{272,000 + 65,600 + 72,050}{13.2}$$

$$= - 318.6 - 31,000 = - 31,319$$

4.0 FACTUAL DATA (Cont'd)

From the Newton-Raphson relationship equation:

$$(P_{H_2O})_1^{(2)} = 1.6006 - \left(\frac{+17}{-31,319} \right) = 1.6011 \text{ psia}$$

A repetition of the above series of calculations does not produce a significant improvement in the value for $(P_{H_2O})_1$.

From Keenan and Keyes the temperature corresponding to $(P_{H_2O})_1 = 1.6011 \text{ psia}$ is $t_1 = 118.01 \text{ deg. F.}$

The first term in Equation (V-40A) is proportional to the amount of heat rejected by the evaporation of water; the term is evaluated as follows:

$$P_1 - (P_{H_2O})_1 = 14.711 - 1.6011 = 13.1100 \text{ psia}$$

$$\begin{aligned} (P_{O_2})_1 &= \frac{101(13.1100)(2.0580)}{100(13.0186) + 2.058} = 1.01548(2.0580) \\ &= 2.0897 \text{ psia} \end{aligned} \quad (V-29)$$

$$\frac{V_1}{V_2} \left(\frac{T_2}{T_1} \right) = \frac{1.01}{1.01548} = \frac{1}{1.005425} \quad (V-27)$$

$$(qR)_{H_2O} \approx 18.016(1026.3) \left[1.6924 - \frac{1.6011}{1.005425} \right] = 1828$$

4.0 FACTUAL DATA (Cont'd)

The total heat rejection is proportional to the last term in

Equation (V-40A) which was evaluated previously as $(qR)_{\text{tot}} \approx 2520$.

The percent heat rejection by evaporation of water is then found as follows:

$$\begin{aligned}\text{Percent heat rejection by evaporation} &= \frac{(qR)_{\text{H}_2\text{O}}}{(qR)_{\text{tot}}} \times 100 \\ &= \frac{1848(100)}{2520} = 73.4 \text{ percent}\end{aligned}$$

CONCLUSIONS

In order to satisfy the multiple requirements necessary to be fulfilled in a broad approach at IEM fuel cell battery designs, systematic investigations have been undertaken, emphasizing determinations of rates as related to the electrochemical reaction, the transport of water in ion exchange membranes, detailed heat and mass transport across interfaces and overall systems analysis.

The program included applied research as well as development activities in an attempt to apply experimental results and concepts immediately to single cell investigations. Appreciable improvements in air-operated IEM fuel cell capabilities have results from this type of approach.

Properties of the electrolyte (IEM)/electrode interface have become important parameters in establishing an analytical model descriptive of interfacial processes and describing the nature and quality of the 2-phase bond. Because of systems complexity and the limited amount of published work in the literature, novel measurement techniques need investigating and improving before definite conclusions will become available.

Water transport in ion exchange membranes can be induced by various gradients, of which pressure gradient effects have been determined. Classical equations for transport in porous media, accounting for membrane properties have yielded a general correlation to describe transfer rates. This result will suggest structural membrane modifications in order to control water transport rates compatible with overall heat and mass transfer processes.

Detailed rate-controlling mechanisms for the air-breathing IEM/Pt black electrodes still remain to be elucidated and will require more experimental work beyond the scope of the present program. However, the semi-empirical relationships derived for self-breathing and forced-flow conditions in air-channels have yielded parametric influences of gas properties (temperature, partial pressures of oxygen, water and nitrogen) operating conditions (electrode surface temperature, air flow rate) and systems geometry (channel length and height). The results suggested new designs allowing for quasi-uniformity of the main parameters, i. e., electrode temperature, partial pressures of oxygen and water.

A broad approach to battery design aimed at the multitude of air-operated applications is now possible, as a result of the establishment of the importance of major parameters.

A novel current collector design, allowing for short air-channels, resulting in better surface distribution of the oxidant (air) and more uniform surface and channel properties (temperature, water removal, thermal conductivity, etc...) has resulted in systems stability and high power capabilities (50 watts/ft²). Availability of experimental results, for steady state operation, will suggest further modifications and applicability of cell voltage control devices.

Fast electrode surface temperature and cell resistance response to varying load conditions and air flow rates has allowed the design of a control device which can maintain cell voltage quasi time-independent. Since, specific fuel cell batteries may require controlling devices for unattended operation, the designed system is now becoming the object for such investigations.

Preliminary designs now available for a system based on the control of water partial pressure, according to parametric influences determined in single channel studies, display over-all simplicity and expected system stability without appreciable effects of variations of environmental conditions. Such a system shows promising applicability to multiple air-operation applications.

Presently, sufficient experimental data, information and knowledge are available to allow for confidence in the successful design of air-operated IEM Fuel Cell Batteries.

PROGRAM FOR NEXT INTERVAL

Planned work up to the Final Technical Report (covering the period from October 1, 1962 to September 30, 1963) will remain in agreement with the Technical Guidelines, EPP No. 58-238 of July 17, 1962, and include:

Task I: Interfacial Membrane/Electrode Properties

Limited additional work is planned for the purpose of testing conclusions with hydrophobic binders possessing critical surface tension values between those of TFE and Kel-F. Additional work will be conducted on sample preparation techniques for optical and electron microscopy observations.

Task II: Water Transport through Membranes

Additional work on hydrodynamic as well as vapor permeabilities will be conducted on other membrane systems. Work on electro-osmotic rates of water transport will be continued.

Task III: Electrochemical Oxygen Reduction

No additional experimental work is planned. Limited data analysis, as required to interpret results, will be conducted.

Task IV: Heat and Mass Transfer Investigations

Limited additional experimental work is planned. Emphasis will be placed on analysis of heat transfer data and interpretation of experimental results obtained on single cells.

Task V: Design Parameters Affecting Air-Operated Fuel Cells

An extensive experimental program is planned, associated with testing and evaluation of the preliminary design, described in detail in this Report.

Task VI: Ion Exchange Membranes

Sporadic supporting activities will be associated with experimental work of Tasks I and II. New membranes will be investigated as electrolyte, as suggested by Contract Officers of the USAELRDL.

IDENTIFICATION OF KEY PERSONNEL

During the period covering January 1, 1963 to June 30, 1963, the following principal investigators have been associated with the program tasks:

Dr. J. R. Boyack - Water Transport in Ion Exchange Membranes
 Mr. D. W. Craft - Design Parameters - Air-Operated IEM Fuel Cells
 Mr. J. Dankese - Heat and Mass Transfer - Air-Operated IEM Cell
 Dr. S. J. Krumbein - Interface Structure and Interfacial Properties
 Dr. H. J. Maget - Kinetics of the Electrochemical Oxygen Reduction

Detailed Time Distribution (January 1 to June 30, 1963)*A. Principal Investigators

| | |
|---|-------------------|
| Dr. J. R. Boyack, Physical Chemist & Electrolytes | 511 hrs. |
| Mr. D. W. Craft, Senior Preliminary Design Engineer | 543 hrs. |
| Mr. J. Dankese, Laboratory Chemical Engineer | 918 hrs. |
| Dr. S. J. Krumbein, Physical Chemist-Electrochemistry | 481 hrs. |
| Dr. H. J. Maget, Senior Chemical Engineer | 732 hrs. |
| | <u>3 185 hrs.</u> |

B. Supporting Laboratory Specialists and Technicians

| | |
|---|-------------------|
| Mr. J. Amore, Specialist - Fuel Cell Electrode | 909 hrs. |
| Mr. W. Armstrong, Specialist - Instrumentation | 132 hrs. |
| Mr. R. Donovan, Technician - Laboratory | 471 hrs. |
| Mr. E. Glosl, Technician - Polyelectrolyte Physics | 287 hrs. |
| Mr. J. Huss, Fuel Cell Evaluation Lab. Technician | 1 022 hrs. |
| Others with individual contribution less than 100 hours | 473 hrs. |
| | <u>3 294 hrs.</u> |

C. Reports and Drafting

| | |
|----------------------------|---------|
| Mr. E. P. Breau and others | 431 hrs |
|----------------------------|---------|

* Data available up to June 16 and extrapolated to June 30, 1963.

The technical background of principal investigators is presented in the following résumés:

IDENTIFICATION OF KEY PERSONNEL (Cont'd)James R. Boyack, Ph. D. - Electrolyte Physical Chemist

Dr. Boyack completed all his work for a Ph. D. from the University of Utah in November 1961, (degree June 1962) and joined the Fuel Cell Laboratory of General Electric's Aircraft Accessory Turbine Department in December 1961. He received his B.S. in Chemistry in 1958 at the University of Utah. His doctoral thesis was concerned with zone diffusion and mobility in paper electrophoresis. Included in his background is a summer as research assistant at Eastman Kodak Company.

Since joining General Electric, Dr. Boyack has been working with electrolyte transport mechanisms in various systems such as ion-exchange polymers, gels, etc.

D. W. Craft - Senior Preliminary Design Engineer

Mr. Craft holds B.S.M.E. and M.S.M.E. degrees from Purdue University, 1945 and 1949 respectively. His principal fields are thermodynamics and fluid mechanics.

From 1949 to 1954 he was on the teaching and research staff at Purdue University where he instructed a senior aeronautical engineering course in gas turbines and jet propulsion and was engaged in gas turbine and rocket engine research.

He joined General Electric in 1954 and was originally concerned with the field of turbomachinery. He conceived and developed a high speed dynamometer which uses a turbine as its primary element - now used as standard for small turbine development. He also developed a theory for the compressible flows through drag turbines and compressors. He designed and developed a high suction specific speed fuel pump. Other important contributions were in design of supersonic nozzles, mass flow meters and the preparation of digital computer programs for thermodynamic and fluid dynamic analyses.

His fuel cell experience, since 1961, has been primarily in the field of mass transfer. His efforts have been instrumental in the development of a passive system utilizing a fixed pressure gradient imposed across a porous plate, for the delivery of water from a condensing system under zero gravity conditions. Under his leadership this principle was successfully applied to a production version of a hydrogen-oxygen fuel cell system in which product water is recovered from the fuel cell for the potable water supply in a manned spacecraft. In addition, a patent has been applied for in his name for a method removing entrained liquid from a gas stream.

IDENTIFICATION OF KEY PERSONNEL (Cont'd)

Currently, Mr. Craft is applying heat and mass transfer theory to air-breathing solid electrolyte fuel cells. He is investigating methods of maintaining an optimum water balance in the electrolyte while operating at high current density.

Mr. Craft is a member of ASME, Tau Beta Pi, Pi Tau Sigma, and Sigma Xi.

Joseph P. Dankese - Laboratory Chemical Engineer

Mr. Dankese received his B.S. in Chemical Engineering from the Massachusetts Institute of Technology in 1954, and has done graduate work at Northeastern University.

Before joining General Electric in early 1961, he accumulated a wide background in chemical engineering work at Microwave Associates, Ionics, Inc., Dewey and Almy Chemical Co., and A. D. Little, Inc. This included studies of conductive coatings, glass to metal seals, and high temperature sintering of metals; design of the electrical and hydraulic systems for ion-exchange membrane electrodialysis equipment and field testing of the final product; process design and development for the vinyl chloride and butadiene type copolymer plants; developed a battery separator for electric storage batteries (U.S. Patent No. 3, 026, 366-March 20, 1963); analysis and process design of the liquid oxygen and hydrocarbon fueling system for the Tital missile - this work involved heat transfer, mass transfer and thermodynamics; conducted experimental studies on the effect of radiation on the reactivity of gaseous hydrocarbon in fuel cells; surveyed various power sources including batteries, fuel cells, thermoelectric and thermionic devices.

In General Electric's Direct Energy Conversion Laboratory, he had conducted mass and heat transfer studies and authored a G. E. Technical Report No. 62DE-2 on Mass Transfer and Voltage Control in Fuel Cells, investigated new fuels and submitted two joint patent disclosures on borohydride and methanol liquid fuels, improved electrode structures, advanced ion exchange membranes for fuel cells (GPS Membranes), and developed a modified air-electrode current collector for use with I. E. M. fuel cells for which a patent disclosure will be submitted.

Mr. Dankese is a registered professional engineer in Massachusetts and a member of the Boston Chapter of the American Institute of Chemical Engineering.

IDENTIFICATION OF KEY PERSONNEL (Cont'd)Simeon J. Krumbein, Ph.D. - Physical Chemist - Electrochemistry

Dr. Krumbein, received his Ph.D. in Physical Chemistry from New York University in October 1961 and joined the Fuel Cell Laboratory of General Electric's Direct Energy Conversion Operation immediately thereafter. In addition to being a research assistant at New York University from 1957 to 1959, he had been working for the past two years under a National Science Foundation Fellowship. His doctoral thesis dealt with the effects of proteins on the electro-metric behavior of simple inorganic ions.

Prior to this, he worked in the laboratory of the Technical Research Group (TRG), Inc., where he conducted analysis of the properties of materials.

Since coming to the Direct Energy Conversion Operation, Dr. Krumbein has been primarily concerned with fundamental electrochemical mechanisms as they exist in fuel cell applications.

Henri J.R. Maget, D.Sc. - Senior Chemical Engineer

Dr. Maget has a background combining organic chemistry and chemical engineering. He holds degrees: B.S. and Licence es Sciences from University of Strasbourg, France, 1950 where he majored in Chemistry; M.S. in Petroleum Engineering from Petroleum School, Paris, 1953; M.S. in Chemical Engineering from University of Michigan, 1956; and D.Sc. from University of Toulouse, France, 1959. He joined the Aircraft Accessory Turbine Department in August 1960.

His background includes two years of research at the University of Michigan as an exchange scientist. This was followed by two years of research work at Institut du Genie Chimique in France and more recently as research scientist at Yale University. His specialization leading to his doctorate was chemical kinetics and polymerization of epoxides.

Since he joined the General Electric Company, Dr. Maget has been working on physico-chemical properties of electrochemically active catalysts, and is investigating the relationship between these properties and the performance of fuel cells.

8.0 LITERATURE REFERENCES

1. "Ion Exchange Membrane Fuel Cell Report No. 2", ARPA Order No. U.S. Army Signal Corps Res. and Dev. Lab., Ft. Monmouth, N.J., Jan. - June, 1962.
2. "Ion Exchange Membrane Fuel Cell Report No. 3", ARPA Order No. 80-61, U.S. Army Signal Corps Res. and Dev. Lab., Ft. Monmouth, N.J., Oct. 1961-1962.
3. D.C. Grahame, J. Electrochem. Soc., 99, 3700 (1952).
4. K. Kordesch, in "Fuel Cells", G.J. Young, ed., Chap. 2, Reinhold Publishing Corp., New York, 1960.
5. "Fuel Cell Electrode Materials", Report No. 1, U.S. Electronic Res. and Dev. Lab., Fort Monmouth, N.J., Contract No. DA-36-039-SC-88954. March, 1962.
6. D.L. Hillhouse and H.W. Kline, I & E Transactions on Instrumentation, I - 9, No. 2, Sept. 1960.
7. D.L. Hillhouse, Private Communication.
8. D.C. Grahame, J. Am. Chem. Soc., 68, 301 (1946).
9. O.S. Heavens, J. Phys. Radium, 11, 355 (1950).
10. P. Benjamin and C. Weaver, Proc. Royal Soc. (London), A 254, 163 (1960).
11. F.P. Bowden and O. Tabor, "The Friction and Lubrication of Solids", Clarendon Press, Oxford, 1958, Chapt. V.
12. D. Tabor, Proc. Royal Society (London), A 251, 378 (1959).
13. Reference 11, Chapter I.
14. R.F. King and D. Tabor, Proc. Phys. Soc. (London), 66B, 728. (1953).
15. "Compressive Properties of Rigid Plastics", ASTM D 695-61T, ASTM Standards, 1961, Part 9, p. 349.
16. F.P. Bowden and D. Tabor, Proc. 2nd Internat. Cong. of Surface Activity. Vol. III, Butterworths Scientific Publications, London, 1957, p. 386.

8.0 LITERATURE REFERENCES (Cont'd)

17. A. M. Glauert, in "Techniques for Electron Microscopy", Chapt. VIII, ed. D. Kay, Blackwell Scientific Publications, Oxford, 1961, p. 174
18. e.g. M. W. Breiter, J. Am. Chem. Soc., 109, 42 (1962); S. Gilman, *ibid.*, In Press.
19. H. W. Fox and W. A. Zisman, J. Colloid Sci., 7, 109 (1952); 5, 514 (1950).
20. W. A. Zisman, NRL Report 5699, November 29, 1961.
21. L. H. Sharpe and H. Schonhorn, "A Comprehensive Theory of Adhesion", presented at the 144th Meeting of The American Chemical Society, Los Angeles, Calif., April 3, 1963.
22. J. T. Davies and E. K. Rideal, "Interfacial Phenomena", Academic Press, London, 1961, Chap. I.
23. C. W. Carr, R. McClintock, K. Sollner, J. Electrochem. Soc. 109, 251 (1962).
24. N. W. Rosenberg, J. H. B. George, W. D. Potter, J. Electrochem. Soc. 104, 111 (1957).
25. D. Mackay and P. Meares, Trans. Faraday Soc. 55, 122 (1959).
26. R. J. Stewart and W. F. Graydon, J. Phys. Chem. 61, 164 (1957).
27. A. S. Tombalakian, H. J. Barton, and W. F. Graydon, J. Phys. Chem. 66, 1006 (1962).
28. R. Schlogl and U. Schodel, Z. Physik. Chemie (Frankfurt) 5, 372 (1955).
29. For a description of the apparatus see Ion Exchange Fuel Cell Report No. 2, June 30, 1962, ARPA Order No. 80-61, pg. 210.
30. S. B. Twiner, Diffusion and Membrane Technology, Rheinhold Publishing Co., New York (1962).
31. D. Mackay and P. Meares, Trans. Faraday Soc. 55, 1221 (1959).
32. J. H. Wang, C. V. Robinson and I. S. Edelman, J. Am. Chem. Soc. 75, 466 (1943).
33. Calculated from viscosity data in International Critical Tables, Vol. V, McGraw-Hill Book Co., Inc. New York and London (1939).

LITERATURE REFERENCES (Cont'd)

34. M. G. Clark, "Performance Studies with Porous Oxygen Electrodes"
Paper presented at the Boston Meeting of the Electrochem. Society, 1962.
35. A. I. Krasilschchikov, J. phys. Chem., USSR 26, 216 (1952).
36. D. Winkelman, . Electrochem., 60, 731 (1956).
37. R. Paul and I. B. Srivastava, Indian J. Phys., 35, 465-74 (1961).
38. International Critical Tables.
39. F. T. Bacon, "The Medium Temperature H_2/O_2 (Air) cell" Paper presented at the New Orleans Meeting of the A.I.Ch.E., April 1963.
40. C. Wagner, unpublished.
41. Whittaker & Watson, "Modern Analysis" Cambridge Un. Press, 1952.
42. H. Kramers & P. J. Kreyger, Chem. Eng. Sci., 6, 42-8 (1956).
43. R. B. Bird, Chemie Ing. Techn. 9, 569-72 (1959).
44. Brown, "Unit Operations", John Wiley & Sons, Inc., New York, 1955.
45. Hougen and Watson, "Chemical Process Principles Part Three - Kinetics and Catalysis", John Wiley & Sons, Inc., New York, 1957.
46. Perry, "Chemical Engineer's Handbook", McGraw-Hill Book Company, Inc., New York, 1950.
47. "International Critical Tables", Vol. V.
48. Reid and Sherwood, "The Properties of Gases and Liquids", McGraw-Hill Book Company, Inc., New York, 1958.
49. Johnson, "Nomography and Empirical Equations", John Wiley & Sons, New York, 1952.
50. Frankenburg, Rideal, Komarewsky, "Advances in Catalysis - Vol. III", Academic Press, Inc., New York, 1951.
51. Rothfeld, "Diffusion and Flow of Gases in Porous Catalysts", Thesis University of Wisconsin, 1961.
52. LaMer, "Chemical Engineering", McGraw-Hill Publishing Co., New York, June 10, 1963.

8.0 LITERATURE REFERENCES (Cont'd)

- 53. Marvin, "Psychrometric Tables", U.S. Government Printing Office, Washington, 1941.
- 54. Dankese, "Study of Mass Transfer of Hydrogen and Oxygen in Binary Mixture with Inert Gases as Related to Performance of the General Electric Ion Exchange Membrane Fuel Cell", Lynn, 1962.
- 55. Hodgman, Weast, Selby, "Handbook of Chemistry and Physics", Chemical Rubber Publishing Co., Cleveland, 1955.
- 56. Mason and Monchick, "Transport Properties of Polar-Gas Mixtures", J. Chem. Phys. 36, No. 10, May 15, 1962.
- 57. Knudsen and Katz, "Fluid Dynamics and Heat Transfer", McGraw-Hill Book Company, Inc., New York, 1958.
- 58. Wheeler A., "Advance in Catalysis", Vol. III - Academic Press, Inc., New York, 1951.

CONTRACT DISTRIBUTION LIST

SECOND SEMI-ANNUAL REPORT
CONTRACT NO. DA 36-039-AMC-00095(E)

Commanding Officer
U. S. A. Electronics Research and
Development Laboratory
Fort Monmouth, N. J.
ATTN: Logistics Division
(MARKED FOR PROJECT
ENGINEER) (20)
ATTN: SELRA/P (1)
ATTN: Dir of Research/Engr. (1)
ATTN: File Unit #1 (1)
ATTN: Technical Document Cent. (1)

OASD (R&D), Rm. 3E1065
ATTN: Technical Library
The Pentagon
Washington 25, D. C. (1)

Chief of Research and Development
OCS, Department of the Army
Washington 25, D. C. (1)

Commanding General
U. S. A. Electronics Command
ATTN: AMSEL-AD
Fort Monmouth, N. J. (3)

Director
U. S. Naval Research Laboratory
ATTN: Code 2027
Washington 25, D. C. (1)

Commanding Officer and Director
U. S. Naval Electronics Laboratory
San Diego 52, California (1)

Air Force Cambridge Research
Laboratories
ATTN: CRZC
L. G. Hanscom Field
Bedford, Massachusetts (1)

Commanding Officer
Harry Diamond Laboratories
ATTN: Library, Room 211, Bldg. 92
Connecticut Ave & Van Ness St., N. W.
Washington, D. C. (1)

Commanding Officer
U. S. A. Electronics Material Support
Agency
ATTN: SELMS-ADJ
Fort Monmouth, N. J. (1)

Deputy President
U. S. A. Security Agency Board
Arlington Hall Station
Arlington 12, Virginia (1)

Director
Defense Documentation Center
ATTN: TISIA
Cameron Station
Alexandria, Virginia (10)

Chief
U. S. A. Security Agency
Arlington Hall Station
Arlington 12, Virginia (2)

Commander
Aeronautical Systems Division
ATTN: ASAPRL
Wright-Patterson Air Force Base
Ohio (1)

Air Force Cambridge Research Laboratories
ATTN: CRXL-R
L. G. Hanscom Field
Bedford, Massachusetts (1)

CONTRACT DISTRIBUTION LIST (CONT.)

| | | | |
|--|-----|--|-----|
| Rome Air Development Center ATTN: RAALD Griffiss Air Force Base, N. Y. | (1) | Headquarters U. S. A. Material Command Research and Development Directorate ATTN: AMCRD-DE-MO Washington 25, D. C. | (1) |
| Commanding General U. S. A. Electronics Research and Development Activity ATTN: Technical Library Fort Huachuca, Arizona | (1) | Commanding General U. S. A. Electronics Command ATTN: AMSEL-RE-A Fort Monmouth, N. J. | (1) |
| Commanding General U. S. A. Combat Developments Command ATTN: CDCMR-E Fort Belvoir, Virginia | (1) | Dr. Sidney Magram Physical Sciences Division Army Research Office 3045 Columbia Pike Arlington, Virginia | (1) |
| Commanding Officer U. S. A. Communications and Electronics Combat Development Agency Fort Huachuca, Arizona | (1) | Dr. Ralph Roberts Head, Power Branch Office of Naval Research (Code 429) Department of the Navy Washington 25, D. C. | (1) |
| Director Fort Monmouth Office U. S. A. Communications and Electronics Combat Development Agency Fort Monmouth, N. J. | (1) | Mr. Bernard B. Rosenbaum Bureau of Ships (Code 340) Department of the Navy Washington 25, D. C. | (1) |
| Air Force Systems Command Scientific/Technical Liaison Office U. S. Naval Air Development Center Johnsville, Pennsylvania | (1) | Mr. George W. Sherman Aeronautical Systems Division ATTN: ASRMFP Wright-Patterson Air Force Base Ohio | (1) |
| Director USAE GIMRADA ATTN: ENGGM-SS Fort Belvoir, Virginia | (1) | Dr. John H. Huth Advanced Research Projects Agency The Pentagon, Room 3E157 Washington 25, D. C. | (1) |
| Marine Corps Liaison Office U. S. A. Electronics Research and Development Laboratory Fort Monmouth, N. J. | (1) | Lt. Col. George H. Ogburn, Jr. Auxiliary Power Branch (SNAP) Division of Reactor Development U. S. Atomic Energy Commission Washington 25, D. C. | (1) |

CONTRACT DISTRIBUTION LIST (CONT.)

| | |
|--|---|
| AFSC Scientific/Technical Liaison Office U. S. A. Electronics Research and Development Laboratory Fort Monmouth, N. J. (1) | Mr. Walter C. Scott National Aeronautics & Space Administration 1520 H. Street, N.W. Washington 25, D. C. (1) |
| USAELRDL Liaison Office Rome Air Development Center ATTN: RAOL Griffiss Air Force Base, N. Y. (1) | Institute for Defense Analysis 1666 Connecticut Avenue, N. W. Washington 25, D. C. ATTN: Dr. Szego & Mr. Hamilton (1) |
| Power Information Center Moore School Building 200 South Thirty-Third Street Philadelphia 4, Pennsylvania (1) | Director Advanced Research Projects Agency Washington 25, D. C. (6) |
| Union Carbide Corporation Union Carbide Consumer Products Co. 270 Park Avenue New York 17, New York ATTN: Mr. R. B. Klopfenstein (1) | Commanding Officer U. S. A. Electronics Research and Development Laboratory ATTN: SELRA/DR, ARPA Coordinator Fort Monmouth, N. J. (1) |
| United Aircraft Corporation Pratt & Whitney Aircraft Division East Hartford 8, Connecticut ATTN: Mr. J. M. Lee (1) | Dr. H. P. Gregor 150 Lakeview Avenue Leonia, N. J. (1) |
| Melpar, Inc. 3000 Arlington Boulevard Falls Church, Virginia ATTN: Mr. R. T. Foley (1) | Magna Corporation R&D Laboratories 1001 South East Street Anaheim, California ATTN: Dr. Silverman (1) |
| University of Pennsylvania John Harrison Laboratory of Chemistry Philadelphia 4, Pennsylvania ATTN: Dr. J. Bockris (1) | Engelhard Industries, Inc. Military Service Department 113 Astor Street Newark 2, N. J. ATTN: Mr. V. A. Forlenza (1) |
| Speer Carbon Company Research Laboratory Packard Road & 47th Street Niagara Falls, N. Y. ATTN: Dr. W. E. Parker (1) | Mr. R. A. Osteryoung Atomics International Canuge Park, California (1) |

CONTRACT DISTRIBUTION LIST (CONT.)

| | | | |
|---|-----|--|-----|
| Dr. David M. Mason Stanford University Stanford, California | (1) | Dr. E.A. Oster General Electric Co., DECO Lynn, Massachusetts | (1) |
| Dr. Howard L. Recht Astropower Inc. 2968 Randolph Avenue Costa Mesa, California | (1) | Dr. Arthur J. Rosenberg TICO, Incorporated Materials Research Laboratory Bear Hill Waltham 54, Massachusetts | (1) |
| Mr. L.R. Griffith California Research Corp. 576 Standard Avenue Richmond, California | (1) | Prof. Herman P. Meissner Massachusetts Institute of Technology Cambridge 39, Massachusetts | (1) |
| Dr. Ralph G. Gentile Monsento Research Corp. Boston Laboratories Everett 49, Massachusetts | (1) | Mr. Donald P. Snowden General Atomics P.O. Box 608 San Deigo 12, California | (1) |
| Mr. Ray M. Hurd Texas Research Associates 1701 Guadalupe Street Austin 1, Texas | (1) | Dr. C. Tobias Chemistry Department University of California Berkeley, California | (1) |
| Dr. C.E. Heath Esso Research & Engineering Co. Box 51 Linden, N.J. | (1) | Mr. Y.L. Sandler Westinghouse Research Laboratories Pittsburg, Pennsylvania | (1) |
| Dr. Richard H. Leet American Oil Company Whiting Laboratories P.O. Box 431 Whiting, Indiana | (1) | | |
| Dr. Douglas W. McKee General Electric Company Research Laboratories Schenectady, N.Y. | (1) | | |

GENERAL ELECTRIC DISTRIBUTION

Fuel Cell Lab - 1-70

J Boyack
P Chludzinski
J Dankese
R Dempsey
A Fickett
A Fragala
R Hodgdon, Jr.
SJ Krumbein
HJ Maget (2)
EA Oster
PV Popat
G Wheeler
H Young

Bldg. 2-74A

W Aker
J Bartas
EP Breau (2)
C Christianson
R Fain
T Hovious
R Kegan
JJ O'Connor
DW Puffer
H Rondeau
A Syska

Bldg. 1-74A

DL Douglas
R Flais
TK Johnson (5)
SS Nielsen
GA Phillips
J Wright

Bldg. 2-74A

R Blackmer
R Fowler
P Rigopulos
JL Schanz

AAT Library (2) 3-74

H Levey 2-74A

Research Lab., Schenectady, NY

HA Liebhafsky

GE Representative

Mr. Arthur Glenn
45 West Front Street
Red Bank, New Jersey

ATL

C Kent

| AD NO. | ACCESSION NO. | UNCLASSIFIED | AD NO. | ACCESSION NO. | UNCLASSIFIED |
|---|---------------|--|---|---------------|--|
| GENERAL ELECTRIC COMPANY DIRECT ENERGY CONVERSION OPERATION LYNN, MASSACHUSETTS SECOND SEMI-ANNUAL TECHNICAL REPORT ON ION EXCHANGE MEMBRANE FUEL CELLS (U) PERIOD: JANUARY 1, 1963 - JUNE 30, 1963 213 PAGES INCLUDING ILLUSTRATIONS ARPA ORDER NUMBER 80 WATER TRANSPORT AND MEMBRANE/ELECTRODE INTERFACIAL PROPERTIES OF CATION EXCHANGE MEMBRANES, FOR FUEL CELL APPLICATIONS, HAVE BEEN INVESTIGATED. CURRENT DENSITIES IN AIR CHANNELS ARE CONTROLLED BY GAS- DIFFUSION. A NEW AIR CURRENT COLLECTOR DESIGN HAS ALLOWED OPERATION AT 85 AMPS/FT ² ON HYDROGEN AND AIR. NEW DESIGNS ARE BEING INVESTIGATED. | | <p>I. RESEARCH ON ION EXCHANGE MEMBRANE FUEL CELLS</p> <p>1. FUEL CELL LAB. STAFF</p> <p>II. U.S. ARMY ELECTRONICS RESEARCH AND DEVELOPMENT LABORATORY</p> <p>III. CONTRACT DA36-039- AMC-00095(E)</p> | GENERAL ELECTRIC COMPANY DIRECT ENERGY CONVERSION OPERATION LYNN, MASSACHUSETTS SECOND SEMI-ANNUAL TECHNICAL REPORT ON ION EXCHANGE MEMBRANE FUEL CELLS (U) PERIOD: JANUARY 1, 1963 - JUNE 30, 1963 213 PAGES INCLUDING ILLUSTRATIONS ARPA ORDER NUMBER 80 WATER TRANSPORT AND MEMBRANE/ELECTRODE INTERFACIAL PROPERTIES OF CATION EXCHANGE MEMBRANES, FOR FUEL CELL APPLICATIONS, HAVE BEEN INVESTIGATED. CURRENT DENSITIES IN AIR CHANNELS ARE CONTROLLED BY GAS- DIFFUSION. A NEW AIR CURRENT COLLECTOR DESIGN HAS ALLOWED OPERATION AT 85 AMPS/FT ² ON HYDROGEN AND AIR. NEW DESIGNS ARE BEING INVESTIGATED. | | <p>I. RESEARCH ON ION EXCHANGE MEMBRANE FUEL CELLS</p> <p>1. FUEL CELL LAB. STAFF</p> <p>II. U.S. ARMY ELECTRONICS RESEARCH AND DEVELOPMENT LABORATORY</p> <p>III. CONTRACT DA36-039- AMC-00095(E)</p> |
| GENERAL ELECTRIC COMPANY DIRECT ENERGY CONVERSION OPERATION LYNN, MASSACHUSETTS SECOND SEMI-ANNUAL TECHNICAL REPORT ON ION EXCHANGE MEMBRANE FUEL CELLS (U) PERIOD: JANUARY 1, 1963 - JUNE 30, 1963 213 PAGES INCLUDING ILLUSTRATIONS ARPA ORDER NUMBER 80 WATER TRANSPORT AND MEMBRANE/ELECTRODE INTERFACIAL PROPERTIES OF CATION EXCHANGE MEMBRANES, FOR FUEL CELL APPLICATIONS, HAVE BEEN INVESTIGATED. CURRENT DENSITIES IN AIR CHANNELS ARE CONTROLLED BY GAS- DIFFUSION. A NEW AIR CURRENT COLLECTOR DESIGN HAS ALLOWED OPERATION AT 85 AMPS/FT ² ON HYDROGEN AND AIR. NEW DESIGNS ARE BEING INVESTIGATED. | | <p>I. RESEARCH ON ION EXCHANGE MEMBRANE FUEL CELLS</p> <p>1. FUEL CELL LAB. STAFF</p> <p>II. U.S. ARMY ELECTRONICS RESEARCH AND DEVELOPMENT LABORATORY</p> <p>III. CONTRACT DA36-039- AMC-00095(E)</p> | GENERAL ELECTRIC COMPANY DIRECT ENERGY CONVERSION OPERATION LYNN, MASSACHUSETTS SECOND SEMI-ANNUAL TECHNICAL REPORT ON ION EXCHANGE MEMBRANE FUEL CELLS (U) PERIOD: JANUARY 1, 1963 - JUNE 30, 1963 213 PAGES INCLUDING ILLUSTRATIONS ARPA ORDER NUMBER 80 WATER TRANSPORT AND MEMBRANE/ELECTRODE INTERFACIAL PROPERTIES OF CATION EXCHANGE MEMBRANES, FOR FUEL CELL APPLICATIONS, HAVE BEEN INVESTIGATED. CURRENT DENSITIES IN AIR CHANNELS ARE CONTROLLED BY GAS- DIFFUSION. A NEW AIR CURRENT COLLECTOR DESIGN HAS ALLOWED OPERATION AT 85 AMPS/FT ² ON HYDROGEN AND AIR. NEW DESIGNS ARE BEING INVESTIGATED. | | <p>I. RESEARCH ON ION EXCHANGE MEMBRANE FUEL CELLS</p> <p>1. FUEL CELL LAB. STAFF</p> <p>II. U.S. ARMY ELECTRONICS RESEARCH AND DEVELOPMENT LABORATORY</p> <p>III. CONTRACT DA36-039- AMC-00095(E)</p> |

| AD NO. | ACCESSION NO. | UNCLASSIFIED | AD NO. | ACCESSION NO. | UNCLASSIFIED |
|--|---------------|--|--|---------------|--|
| GENERAL ELECTRIC COMPANY DIRECT ENERGY CONVERSION OPERATION LYNN, MASSACHUSETTS SECOND SEMI-ANNUAL TECHNICAL REPORT ON ION EXCHANGE MEMBRANE FUEL CELLS (U) PERIOD: JANUARY 1, 1963 - JUNE 30, 1963 213 PAGES INCLUDING ILLUSTRATIONS ARPA ORDER NUMBER 80 | | I. RESEARCH ON ION EXCHANGE MEMBRANE FUEL CELLS II. U.S. ARMY ELECTRONICS RESEARCH AND DEVELOPMENT LABORATORY III. CONTRACT DA36-039- AMC-00095(E) | GENERAL ELECTRIC COMPANY DIRECT ENERGY CONVERSION OPERATION LYNN, MASSACHUSETTS SECOND SEMI-ANNUAL TECHNICAL REPORT ON ION EXCHANGE MEMBRANE FUEL CELLS (U) PERIOD: JANUARY 1, 1963 - JUNE 30, 1963 213 PAGES INCLUDING ILLUSTRATIONS ARPA ORDER NUMBER 80 | | I. RESEARCH ON ION EXCHANGE MEMBRANE FUEL CELLS II. U.S. ARMY ELECTRONICS RESEARCH AND DEVELOPMENT LABORATORY III. CONTRACT DA36-039- AMC-00095(E) |
| WATER TRANSPORT AND MEMBRANE/ELECTRODE INTERFACIAL PROPERTIES OF CATION EXCHANGE MEMBRANES, FOR FUEL CELL APPLICATIONS. HAVE BEEN INVESTIGATED. CURRENT DENSITIES IN AIR CHANNELS ARE CONTROLLED BY GAS- DIFFUSION. A NEW AIR CURRENT COLLECTOR DESIGN HAS ALLOWED OPERATION AT 85 AMPS/FT ² ON HYDROGEN AND AIR. NEW DESIGNS ARE BEING INVESTIGATED. | | | WATER TRANSPORT AND MEMBRANE/ELECTRODE INTERFACIAL PROPERTIES OF CATION EXCHANGE MEMBRANES, FOR FUEL CELL APPLICATIONS. HAVE BEEN INVESTIGATED. CURRENT DENSITIES IN AIR CHANNELS ARE CONTROLLED BY GAS- DIFFUSION. A NEW AIR CURRENT COLLECTOR DESIGN HAS ALLOWED OPERATION AT 85 AMPS/FT ² ON HYDROGEN AND AIR. NEW DESIGNS ARE BEING INVESTIGATED. | | |
| AD NO. | ACCESSION NO. | UNCLASSIFIED | AD NO. | ACCESSION NO. | UNCLASSIFIED |
| GENERAL ELECTRIC COMPANY DIRECT ENERGY CONVERSION OPERATION LYNN, MASSACHUSETTS SECOND SEMI-ANNUAL TECHNICAL REPORT ON ION EXCHANGE MEMBRANE FUEL CELLS (U) PERIOD: JANUARY 1, 1963 - JUNE 30, 1963 213 PAGES INCLUDING ILLUSTRATIONS ARPA ORDER NUMBER 80 | | I. RESEARCH ON ION EXCHANGE MEMBRANE FUEL CELLS II. U.S. ARMY ELECTRONICS RESEARCH AND DEVELOPMENT LABORATORY III. CONTRACT DA36-039- AMC-00095(E) | GENERAL ELECTRIC COMPANY DIRECT ENERGY CONVERSION OPERATION LYNN, MASSACHUSETTS SECOND SEMI-ANNUAL TECHNICAL REPORT ON ION EXCHANGE MEMBRANE FUEL CELLS (U) PERIOD: JANUARY 1, 1963 - JUNE 30, 1963 213 PAGES INCLUDING ILLUSTRATIONS ARPA ORDER NUMBER 80 | | I. RESEARCH ON ION EXCHANGE MEMBRANE FUEL CELLS II. U.S. ARMY ELECTRONICS RESEARCH AND DEVELOPMENT LABORATORY III. CONTRACT DA36-039- AMC-00095(E) |
| WATER TRANSPORT AND MEMBRANE/ELECTRODE INTERFACIAL PROPERTIES OF CATION EXCHANGE MEMBRANES, FOR FUEL CELL APPLICATIONS. HAVE BEEN INVESTIGATED. CURRENT DENSITIES IN AIR CHANNELS ARE CONTROLLED BY GAS- DIFFUSION. A NEW AIR CURRENT COLLECTOR DESIGN HAS ALLOWED OPERATION AT 85 AMPS/FT ² ON HYDROGEN AND AIR. NEW DESIGNS ARE BEING INVESTIGATED. | | | WATER TRANSPORT AND MEMBRANE/ELECTRODE INTERFACIAL PROPERTIES OF CATION EXCHANGE MEMBRANES, FOR FUEL CELL APPLICATIONS. HAVE BEEN INVESTIGATED. CURRENT DENSITIES IN AIR CHANNELS ARE CONTROLLED BY GAS- DIFFUSION. A NEW AIR CURRENT COLLECTOR DESIGN HAS ALLOWED OPERATION AT 85 AMPS/FT ² ON HYDROGEN AND AIR. NEW DESIGNS ARE BEING INVESTIGATED. | | |

UNCLASSIFIED

UNCLASSIFIED